



**HAL**  
open science

# Submillimetric magnets made of nanoparticles for portable magnetic devices

Lise-Marie Lacroix

► **To cite this version:**

Lise-Marie Lacroix. Submillimetric magnets made of nanoparticles for portable magnetic devices. Physics [physics]. Université Toulouse 3 - Paul Sabatier, 2018. <tel-04075440>

**HAL Id: tel-04075440**

**<https://hal.science/tel-04075440v1>**

Submitted on 20 Apr 2023

**HAL** is a multi-disciplinary open access archive for the deposit and dissemination of scientific research documents, whether they are published or not. The documents may come from teaching and research institutions in France or abroad, or from public or private research centers.

L'archive ouverte pluridisciplinaire **HAL**, est destinée au dépôt et à la diffusion de documents scientifiques de niveau recherche, publiés ou non, émanant des établissements d'enseignement et de recherche français ou étrangers, des laboratoires publics ou privés.



HAL Authorization



Université  
de Toulouse



## Habilitation à Diriger des Recherches

présentée par

Lise-Marie Lacroix

Maitre de conférences à l'Université Toulouse III, Paul Sabatier

Submillimetric magnets made of nanoparticles for portable  
magnetic devices

Rapportrices :

Dr Nora DEMPSEY,	Institut Néel, Grenoble
Dr Maria del Puerto MORALES,	Instituto de Ciencia de Materiales, Madrid
Dr Véronique PIERRON-BOHNES,	Institut de Physique et Chimie des Matériaux de Strasbourg

Membres du jury :

Dr Bruno CHAUDRET	Laboratoire de Physique et Chimie des Nano-Objets, Toulouse
Pr Michel GOIRAN	Laboratoire National des Champs Magnétiques Intenses, Toulouse
Pr Clément SANCHEZ	Collège de France, Laboratoire Chimie de la Matière Condensée, Paris
Pr Guillaume VIAU	Laboratoire de Physique et Chimie des Nano-Objets, Toulouse

Janvier 2018



• **TABLE OF CONTENTS**

<b>↗ Curriculum Vitae</b>	4
Education, Positions, Awards, Fellowships	4
Science promotion	5
Teaching activities	6
Supervision of students, Research activity	7
Institutional responsibilities, Commission of trust, Collaborations	9
<b>↗ Introduction</b>	10
<b>↗ Summary of research activity</b>	11
I. <i>Synthesis of nano-objects exhibiting controlled sizes and shapes</i>	
1. <i>Fe nanoparticles</i>	11
2. <i>FeCo NPs : towards a composition control</i>	16
3. <i>Noble metal nanoparticles</i>	21
II. <i>Physical study of model objects</i>	
1. <i>Magnetic configuration in nano-objects</i>	27
2. <i>Magnetic hyperthermia</i>	31
3. <i>Electronic transport measurements</i>	32
III. <i>Controlled assembly and integration of nanostructured materials : towards applications</i>	
1. <i>FeCo NPs for RF filters</i>	39
2. <i>Dense assemblies of Co NRs as rare-earth free permanent magnets</i>	42
<b>↗ Research project : submillimetric magnets</b>	45
<b>↗ Publications</b>	63
<b>↗ Selection of publications</b>	72

## PERSONAL INFORMATION

Lacroix, Lise-Marie  
20<sup>th</sup> March 1982, French  
University Toulouse III, LPCNO (UMR 5215)

Married, 1 daughter (26/04/2012)  
Associate Professor,

### • EDUCATION

- 2008 **PhD in Nanophysics**, “Synthesis of optimized Fe(0) NPs for magnetic hyperthermia using an organometallic approach”.  
Laboratoire de Physique et Chimie des Nano-Objets (LPCNO), Institut National des Sciences Appliquées (INSA) Toulouse, France.  
PhD Supervisors : Bruno Chaudret, Julian Carrey
- 2005 **Master’s degree in NanoPhysics**, Département Génie Physique, INSA Toulouse, France (Rank : 1<sup>st</sup>)
- 2005 **Engineer’s degree in Physics**, INSA Toulouse, France (Rank : 1<sup>st</sup>)
- 2003 – 2004 **VULCANUS in Japan**, EU-Japan Center, Tokyo (Japan)

### • CURRENT POSITIONS

- 2009 – **Permanent Associate Professor** Département de Physics - LPCNO,  
Université Toulouse III-Paul Sabatier, France
- 2014 – **Co-head of the Transpyrenean Associated Laboratory for Electron Microscopy** (TALEM), France-Spain

### • PREVIOUS POSITIONS

- 2015 **Invited professor**, Victoria University, Wellington, New Zealand
- 2010 – 2012 **Head of the Master’s degree** “Maths Physique Chimie pour l’Enseignement”
- 2008 – 2009 **Post-Doctoral position** Chemistry Department, Brown University (Supervision : Pr. Shouheng Sun)

### • AWARDS

- 2016 **Young Investigator** Award, Institut de Chimie de Toulouse, France
- 2014 **Paul Sabatier** Award, Académie des Sciences et des Belles Lettres de Toulouse, France
- 2011 **Novela** Award, Toulouse, France
- 2009 **PhD** award, French Chemical Society – Physical-Chemistry speciality, France
- 2008 **PhD** award, Association Française des Femmes Diplômées des Universités, France
- 2008 **Poster presentation** award, 12<sup>th</sup> Louis Neel colloque, France
- 2007 **Poster presentation** award, 11<sup>th</sup> Louis Neel colloque, France
- 2006 **Oral presentation** award, French Chemical Society – Journées Jeunes Chercheurs, France

### • FELLOWSHIPS

- 2016 – 2020 **Research and supervision** Fellowship, National University Comity (CNU-28), France
- 2015 – 2017 **Délégation CNRS Fellow** (Visiting scientist position), Physics Institute of CNRS, France
- 2015 – 2016 **Dumont d’Urville Fellowship** - Royal Society of New Zealand and the French Ministry of Foreign Affairs
- 2012 – 2016 **Scientific Excellence Fellowship**, National University Comity (CNU-28), France
- 2008 – 2009 **Post doctoral Scholarship DGA** (Direction Générale de l’Armement), Ministry of Defense, France
- 2007 **Student travel fellowship**, 52<sup>nd</sup> Magnetism and Magnetic Material Conference, USA
- 2005 – 2008 **PhD Scholarship from the Ministry of National Education**, France
- 2005 **EU-Joint Research Center Scholarship**, IHCP-JRC, Italy
- 2004 – 2005 **“Bourse Master d’excellence”** Scholarship, INSA Toulouse, France
- 2003 – 2004 **Vulcanus in Japan Scholarship** from EU-Japan Center, Belgium-Japan

I have a dual physics and engineering educational background. I ranked 1<sup>st</sup> in the Physics department at INSA Toulouse, after spending 1 year in Japan in 2003 working for Canon Research Center on flexible electronic devices (Vulcanus in Japan fellowship). In parallel I ranked 1<sup>st</sup> from a master degree in “Nanophysics, Nanocomponents, Nanomeasurement” in 2005 after a 6 month trainee in the Institute for Health and Consumer Protection of the Joint Research Center (Ipsra, Italy) working on biosensors (3 publications, 1 patent).

Having obtained a PhD fellowship from the French Ministry of Research, I joined the Laboratory of Physics and Chemistry of Nano-Objects (LPCNO) to work on the synthesis of Fe nanoparticles with tunable sizes and shapes for hyperthermia applications. Under the supervision of Bruno Chaudret and Julian Carrey, I worked on organometallic synthesis and studied nanomagnetism combining magnetometry, micromagnetic simulations and electron holography. Thanks to magnetic and spectroscopic characterizations I could unravel the complex growth mechanism leading to the predictive synthesis of metallic Fe NPs. I designed the hyperthermia set-up, which is still currently used. This work obtained several awards, among which the 2009 Physical Chemistry Section PhD award of the French Chemistry Society. (9 publications)

In 2008, I obtained a postdoctoral fellowship from the French Ministry of Defence, to work on magnetic biosensors at Brown University (USA) under the supervision of Pr. Shouheng Sun, who pioneered the work on magnetic nanoparticle synthesis. To enhance the detection sensitivity I optimized i) the surface modification of the biosensors to favor the specific anchoring of magnetic nanoparticles and ii) the properties of the particle used. By incorporating halides ions into the thermodecomposition approach previously developed in the lab, I could fine tune the precursor reactivity and thus synthesize for the first time single crystalline Fe particles. Since then, the use of halides has further been generalized to other metallic NPs by Pr. Sun. (4 publications)

In 2009, I was ranked 1<sup>st</sup> by the selection committee of the Université Toulouse III and returned to the LPCNO as an associate-professor, benefiting from the unique multidisciplinary environment that LPCNO provides. Since then, I have been teaching physics (~200h/year) from Bachelor’s to Master’s level and recently become in charge of the magnetometry service at LPCNO. I have developed on new thematic fields on original nanoparticles synthesis, controlled assembly and deposition (11 publications), and initiated international collaborations, rewarded by a Dumont d’Urville grant. In 2014, I received the Paul Sabatier prize and in 2016 the Young Investigator Award. I was the PI of the ELECTRON project involving 5 partners on the electronic properties of original NPs (4 publications), and the leader of the “elaboration of model systems” task of the EMMA project aiming at yielding quantitative magnetic measurements using electron microscopy (3 publications). I was involved in two industrial projects (Siemens, ST Microelectronics) and two large FP7 projects (Nanodiatream, Refreepermag) on magnetic nanoparticles (6 publications, 1 book chapter).

Since 2009, I have also take part in different actions to promote science towards society and children, for instance through democratization lectures, secondary school partnerships and practical lab visits.

#### • SCIENCE PROMOTION

Sept 2017 -	CithEtique, workshop on ethical questions Nanoparticle thematic on a dedicated session for engineers	~50 person
May 2017 -	Pint of Science Speaker for the thematic night : “Nanoparticles as medical treatment?”	~50 person/night
Since 2014 –	European Researchers night Speed searching : 10min discussions with 5 persons Bouche à oreille : fast description of research activity Responsible for a practical lab for children “The red gold”	~30 person/night ~20 person/night ~200 children/night
Since 2014 –	Responsible for a high school program, consisting in 3 visits (lectures+lab work) to motivate scientific careers	~ 35 pupils/year
Since 2013 –	Invited lectures on nanoparticles Science association, INSA, French Regional Chamber of Commerce and Industry ...	50-300 person/lecture
2010 – 2015	Participation in “Prof dans les labos”, aiming at sensitizing high school teachers to research	~ 30 teachers /year
Interviews in local newspapers (La Dépêche), and radio (France Bleu Toulouse, Radio Campus FM)		

- **TEACHING ACTIVITIES**

2009 – **Permanent Associate Professor** – Université Toulouse III-Paul Sabatier, France - ~200 h/year

2005 – 2008 **Sessional Lecturer** (Moniteur) – INSA Toulouse, France – 64h/year

In the past 5 years I have been teaching lectures (CM-Cours magistraux), practical tutorials (TD-Travaux Dirigés) and practical labs (TP-Travaux pratiques) at bachelor (L-Licence) and master level (M) as summarized in the following table. In the last 2 years I obtained a 6 month-CNRS delegation fellow. This fellowship corresponds to a teaching reduction of 96h/year.

	Université Toulouse III – Paul Sabatier						INSA		Total	
	CM		TD		TP		Total UPS	TD-APP		TP
	L	M	L	M	L	M		L		L
<b>2012-2013</b>	27	18	29	8	38	42	<b>162</b>	35	42	<b>239</b>
<b>2013-2014</b>	24	7	45	8	48	24	<b>156</b>	21	15	<b>192</b>
<b>2014-2015</b>	24	7	47	8	62	33	<b>181</b>	21	15	<b>217</b>
<b>2015-2016</b>	24	7	8	8	16	33	<b>96</b>	0	0	<b>96 (1/2 CNRS)</b>
<b>2016-2017</b>	29	16	15	16	0	30	<b>106</b>	0	0	<b>106 (1/2 CNRS)</b>

Since 2009, I have been teaching general physics courses as follow :

Bachelor : Physics : Optics, Mechanics (solids, fluids), Electromagnetism

Chemistry : Scientific interviews, Societal and Technological risks

Master : Physics : Fluid Mechanics, Teachers formation (preparation Agregation), Nanotechnology, Vacuum techniques.

Among these different courses, I have been in charge of the creation of practical labs on **vacuum techniques for the Joint European Master in Space Science and Technology**. My course was articulated around theoretical lectures on the different equipments (gauges, pumps...), and practical labs on (ultra-) high vacuum chambers (turbomolecular and cryogenic pumps, Penning gauges). Low temperature, low pressure and high ionization conditions were simulated to study the damages on the satellites' electronic circuits. The course and the practical labs were done in English, the number of students varying with years from 22 to 32.

I also created a 12h **course on nanotechnology for the Master's degree "Condensed Matter Physics"**. The main objective consisted in giving a general overview of the different techniques used to prepare nano-objects, through physical or chemical means. Then, several applications of nanostructured materials were discussed, ranging from electronic transport to biomedical applications. The number of students varied between 8 and 12. Two master students (Anaïs Loubat, Marc Pousthomis) who followed this course joined our laboratory as trainee and later as PhD students.

Since 2011, I gave general **physics lectures** (optics – fluid mechanics - radioactivity, ~20h/year) to fresh students (1<sup>st</sup> year of Bachelor's degree ~150 students/course). At the same time I joined the pedagogic team of the **"Agregation" preparation**. The aim is to prepare Master students to become high school teachers in physics and chemistry. I take part in theoretical lectures, in practical labs, to strengthen the students' experimental skills, and in practical courses which reproduce the exams conditions (the students have to present a course on a given topic during 50 min - leçon de physique).

Having both a master's degree and an engineer's degree, I have been involved in two selective bachelor's degrees which are preparing the students for engineer or long scientific studies. I gave practical tutorials on physics (solid mechanics, electromagnetism) and chemistry (scientific interviews) to prepare students for the **Concours Commun Polytechnique** (26h, ~36 students/year) and in the new bachelor degree **"Parcours Spéciaux"**. The selected students follow intensive courses and perform multiple research internship..

Aside from the regular scientific teaching, I am also involved in the **promotion of scientific careers**, she gives lectures on nanoparticle synthesis and applications for 3<sup>rd</sup> year bachelor students (~2h, 50 students/year) and 1<sup>st</sup> year master students (3h, 30 students/year), I participate to Campus Tours and students information sessions (Info Sup', Journées Portes Ouvertes), and debates on engineer's career (~2h, 30 students/debate)

- **SUPERVISION OF GRADUATE STUDENTS AND POSTDOCTORAL FELLOWS**

Since 2009 – I supervised or cosupervised 20 persons (6 PhD, 8 Postdocs and 6 Masters students)

**PhD Students : 4 completed / 2 on-going**

- 2010-2014 : Anais Loubat (presently engineer at Institut Lavoisier, France),  
Co-supervised (60%) with B. Raquet (LNMCI, Toulouse)  
“Chemical growth and electronic transport properties of gold nanowires”  
PRES-Région Midi Pyrénées grant *4 co-signed publications*
- 2012-2016 : Marc Pousthomis (presently engineer at NEXdot company, France),  
Co-supervised (50%) with G. Viau (LPCNO)  
“From chemical synthesis of nanoparticles to nano-structured magnetic materials : A bottom-up approach for rare-earth free permanent magnets”  
Siemens fellowship *4 co-signed publications, 1 book chapter*  
*Best PhD Award, Académie des Sciences-Toulouse*
- 2013-2016 : Evangelia Anagnostopoulou (presently Technical Sales Specialist at Kinesis Ltd, UK),  
Co-supervised (50%) with G. Viau (LPCNO)  
“Synthesis of magnetic nanoparticle for rare-earth free permanent magnets”  
FP7 project Refreepermag *6 co-signed publications, 1 book chapter*
- 2013-2016 : Cyril Garnero (presently post-doc at Institut de Chimie des Milieux et des matériaux de Poitiers, France)  
Co-supervised (50%) with B. Chaudret (LPCNO)  
"Synthesis of magnetic nanoparticles : towards integrated inductors"  
ST Microelectronics fellowship *1 co-signed publication, 4 in preparation*
- 2016- : Pierre Moritz,  
Co-supervised (50%) with T. Leïchlé (LAAS, Toulouse)  
“Integrated Nanostructured Magnets for the electromagnetic actuation of biosensors”  
IDEX grant
- 2016- : Déborah De Masi,  
Co-supervised (50%) with B. Chaudret (LPCNO)  
“Synthesis of bimetallic nanoparticles for photoinduced catalytic reactions”  
ERC Monacat fellowship

**Postdoctorates : 6 completed**

- 2014-2016 : Dominikus Heift (presently junior research fellow, Durham University, England),  
co-supervised (30%) with B. Chaudret  
“Synthesis of FeS nanoparticles”, ERC fellowship *1 paper in preparation*
- 2014-2015 : Udishnu Sanyal (presently post-doc, Technische Universität München , Germany),  
co-supervised (50%) with G. Viau  
“Synthesis of Co@CoSb nanorods”, FP7 project Refreepermag fellowship *2 co-signed papers*
- 2014-2015 : Francisco Bonilla (presently post-doc, CIC Energigune, Spain),  
co-supervised (30%) with T. Blon (LPCNO)  
“Micromagnetic simulation of Fe nanocubes”, ANR fellowship *2 co-signed papers*
- 2015-2016 : Said El-Nouh (presently associate professor, Egypt), co-supervised (40%) with G. Viau  
“Synthesis of ultrathin Au nanowires”, Egypt-France fellowship *1 co-signed paper, 1 in preparation*
- 2015-2016 : Bruno Camargo (presently associate professor, Institute of Physics, Poland),  
co-supervised (30%) with W. Escoffier (LNCMI)  
“Electronic transport on Pt nanostars”, Labex NEXT fellowship *1 co-signed paper*
- 2015-2017 : Mathieu Lepasant (presently post-doc, CNES, France), co-supervised (70%) with P. Fau (LCC)  
“Integration of FeCo nanoparticles on microelectronics”, ST Microelectronic fellow *3 papers in preparation*

**Master Students** : 8 completed (5 pursued as PhD, 1 became an engineer).

2017 : Ségolène Combettes, Synthesis and integration of nanostructured magnets, co-supervised (50%) with G. Viau  
2016 : Jean-Claude Mbouta-Nzau, Synthesis and self assembly of Co nanorods, co-supervised (50%) with G. Viau  
2015 : Baptiste Martin, Nanoparticles for spring magnet elaboration, co-supervised (50%) with G. Viau  
2014 : Antoine Robert, Synthesis and self assembly of Au nanowires, co-supervised (50%) with G. Viau  
2013 : Romain Lemeur, Synthesis of soft magnetic nanoparticles, supervised  
2012 : Marc Pousthomis, Synthesis of hard magnetic nanoparticles for permanent magnets, co-supervised (50%) with G. Viau  
2012 : Chris Starkey, Synthesis of Plasmonic Nanoparticles for Surface Enhanced Raman Spectroscopy, co-supervised (50%) with G. Viau  
2010 : Anaïs Loubat, Electronic properties of Au nanowires chemically grown, co-supervised (50%) with B. Raquet

2008 – 2009 During my post-doc at **Brown University** I helped Pr. Sun in supervising **2 PhD students** (1 professor – China, 1 engineer – intellectual property) and **1 Master Student** (PhD at Harvard)

## • RESEARCH ACTIVITIES

Few indicators are listed below, the details of these activities will be developed in the next section

**47 PUBLICATIONS** in peer-reviewed scientific journals (Sum of the times cited : **1060** - WoK, Aug. 2017)

Among which **4** invited papers

**12** publications as first author, **8** publications as last and/or corresponding author in different journals :

*Chemistry* : J. Am. Chem. Soc., Angew. Chem. Int. Ed., Chem. Comm., Chem. Phys. Lett., Chem. Cat. Chem.

*Material science* : Nano Lett., ACS Nano, Adv. Funct. Mater., Nanoscale, J. Phys. Chem. C, Langmuir, Small, Nano. Res.

*Physics*: Phys. Rev. B, J. Magn. Magn. Mater., J. Appl. Phys., Rev. Sci. Instrum.

*Nanobiotechnology* : Interf. Foc., IEEE Biodetection, Curr. Top. Med. Chem.

**2 CHAPTERS** in collective volume

1. Soft chemistry nanowires for permanent magnet fabrication, in *Magnetic nano- and microwires*. Edited by Manuel Vazquez, Woodhead publishing Series in Electronic and Optical Materials (2016)
2. Organometallic Nanoparticles in *Advances in Organometallic Chemistry and Catalysis* Edited by Armando J.L. Pombeiro, John Wiley and Sons (2014)

**1 GRANTED PATENT**

Process for controlling surface wettability WO/2007/087900

**DISSEMINATION OF FINDINGS**

**16** oral presentations in international conferences – **5** invitations

**8** oral presentations in national conferences – **3** invitations

**11** invited seminars (New Zealand, Spain, USA, Ireland, France)

**RESEARCH GRANT**

Writing of 10 national and European grants (ERC Starting grant, ranked B), 3 were successful

2013-2017 ANR EMMA (Electron Microscopy for MAgnetism), Work-Package leader, 570k€

2014-2016 Labex NEXT ELECTRON (Electronic Transport in Original Nanoparticles), PI, 100k€

2016-2018 AAP IDEX Nanobiomag, PI, 120k€

- **INSTITUTIONAL RESPONSIBILITIES**

- 2017 **Co-writer** with R. Poteau and X. Marie of the EUR Graduate School of Nanoscale Science and Engineering project
- Since 2016 **Member of the Executive Committee**, NEXT Laboratory of Excellence, France
- Since 2014 **Co-head**, Associated International Laboratory TALEM, France
- Since 2013 **Member of the Scientific Council**, Université Toulouse III, France
- 2011 – 2016 **Member of the Laboratory Council**, LPCNO, France

- **COMMISSIONS OF TRUST**

- 2017 **Reviewer** for the French national funding agency (ANR) – Generic and Momentum Calls
- 2016 **Examiner for PhD thesis** (Dr. Andrew McGrath), University of Wellington, New Zealand
- 2016 **Reviewer** for the Newton International Fellowship, the Royal Society, Great Britain
- Since 2015 **Selection Committee** (member) for the promotion of associate professors, Université Toulouse III-Paul Sabatier, France
- Since 2014 **Selection Committee** (member or vice-president) for 3 permanent positions of associate professor, Université Toulouse III-Paul Sabatier, France
- Since 2009 **Reviewer** for ~15 papers per year for 20 journals (Nature Comm., JACS, Angew. Chem., Nanoscale, ACS Nano, Small, Langmuir...)
- 2009 **Reviewer** for the National Academies, Chemistry section, USA
- 2009 **Chairman** ACS Fall Meeting (Washington DC, 16-20 August 2009), Functional Nanomaterials for Energy and Biomedicine Applications session

- **ORGANISATION OF SCIENTIFIC MEETINGS**

- 2019 **Louis Neel conference**, Organising committee, ~200 participants, Toulouse, France
- 2016 **PMSE** (Molecular Plasmonic and Exalted Spectroscopy) **Summer school**, Organising committee, 56 participants, Toulouse, France
- 2016 **TALEM** (Transpyrenean Associated Laboratory for Electron Microscopy) **workshop**, Organiser, 28 participants, Banyuls, France
- 2015 **JSI** (Surface and Interface days) **workshop**, Organising committee in charge of the exhibitors, 130 participants, Toulouse, France
- 2006 **JMC10** (Condensed Matter) **conference**, Organising committee, 850 participants, Toulouse

- **MAJOR COLLABORATIONS**

- Richard Tilley**, Nanoparticle synthesis, Chemistry Department, University of New South Wales, Australia  
*1 submitted paper, joint Dumont d'Urville grant*
- James Watkins**, Surface modification, University of Massachusetts, USA  
*1 on-going project on Co NRs*
- Raul Arenal**, Electronic tomography, Instituto de Nanociencia de Aragon, University of Zaragoza, Spain  
*4 papers, 2 submitted, TALEM laboratory*
- Etienne Snoeck, Christophe Gatel and Bénédicte Warot-Fonrose**, Electronic microscopy, CEMES-CNRS, France  
*7 publications, EMMA project*
- Marianne Imperor-Clerc** Small Angle X-Ray Scattering, LPS-CNRS, France  
*3 papers, common synchrotron and neutron proposal*
- Frédéric Ott**, Neutron Scattering and micromagnetic simulations, LLB-CEA, France  
*4 papers, 1 submitted, 1 book chapter, REFREPERMAG European Project, neutron proposal*
- Dorota Koziej**, EXAFS measurements, University of Hambourg, Germany  
*common synchrotron proposal, on-going project on FeCo NPs*
- Thierry Leïchlé**, MEMS-Biosensors, LAAS-CNRS, France  
*1 paper, joint PhD student*

## Introduction

The fabrication and integration of sub-millimeter magnetic materials into predefined circuits is of major importance for portable magnetic devices for the telecommunications, automotive, biomedical and space applications, but remains highly challenging. The present state-of-the-art is not satisfactory given either the poor magnetic properties of the components (e.g. low magnetization of ferrites) or their societal drawbacks (e.g. rarity, toxicity, environmental costs or geopolitical dependence of the rare-earth based magnets).

There is therefore a need and an opportunity for a process to prepare magnets in the sub-millimeter range for new developments in microelectronics, nanobiotechnology, energy conversion... Top-down approaches using sputtering deposition could lead to relatively thick magnetic films, patterned through microelectronics processes,<sup>1</sup> or laser induced thermopatterning.<sup>2,3</sup> The bottom-up approach, which consists in assembling single-domain nanoparticles into dense materials,<sup>4,Ch2</sup> is the other alternative of primary choice for integrated permanent magnets providing that the nanoparticles (NPs) building blocks exhibit a sufficient coercivity.<sup>5</sup> Recently, patterning of magnetic polymers by inkjet,<sup>6</sup> imprinting<sup>7</sup> or photolithography,<sup>8</sup> or electroplating through masks<sup>9,10</sup> have been investigated to design integrated magnets compatible with microelectronic processes.<sup>11</sup> These approaches suffer from a low magnetic fraction, which drastically reduce the magnetization ( $M_S$ ), as well as fairly soft magnetic constituents, with a low anisotropy ( $K$ ).

Thus, one approach to solve the problem of performant integrated PM consists in **synthetizing optimized building blocks, assembling them into dense metamaterials through a generic deposition technique.**

I aim at overpassing this challenge in the coming years, taking benefit from my previous experience at the interface between chemistry and physics. Since 2005, my researches have been based on three main axes:

- The **liquid phase synthesis** of nano-objects exhibiting controlled size and shape. This objective requires a fundamental study of the reaction mechanisms involved in order to optimize the experimental parameters in a predictive way.
- The **study of their physical properties** (in particular their magnetic and electronic transport properties) going from isolated nanoparticles to interacting ones. In this aim, efforts have been devoted to the local deposition of particles.
- Finally, the **controlled assembly** of the particles to form new materials, which exhibit unique properties due to their nanostructuration, and the further **integration** of these nanostructured materials as active elements in microelectronic components.

In this manuscript, I will review my research activities following these three main themes, overlooking most of my publications. Having used several characterization techniques, such as electron microscopy, magnetic measurements and Mössbauer spectroscopy, I did perform occasionally analysis for collaborators. My scientific contribution being limited, the resulting publications on Co complexes and Al, FeC and FeS NPs will not be developed here.

I will finally present my research project on integrated magnets for portable magnetic devices and the main strategies I plan to follow.

## I. Synthesis of nano-objects exhibiting controlled sizes and shapes

Among the multiple approaches developed for the synthesis of NPs in the past decades, chemical synthesis in liquid phase yielded nano-crystals with tuneable sizes and shapes.<sup>12</sup> The general strategy followed relies on the decomposition/reduction of a precursor, typically a salt or an organometallic compound to yield free atoms. These atoms tend to aggregate to form small seeds during the nucleation step. Once formed, these seeds then grow yielding the final NPs by successive addition of atoms or by coalescence, according to the classical models (Figure 1).<sup>13,14</sup> To prevent NPs from aggregation and sintering, organic molecules (surfactants) or polymers are added to ensure steric hindrance or electrostatic repulsion.

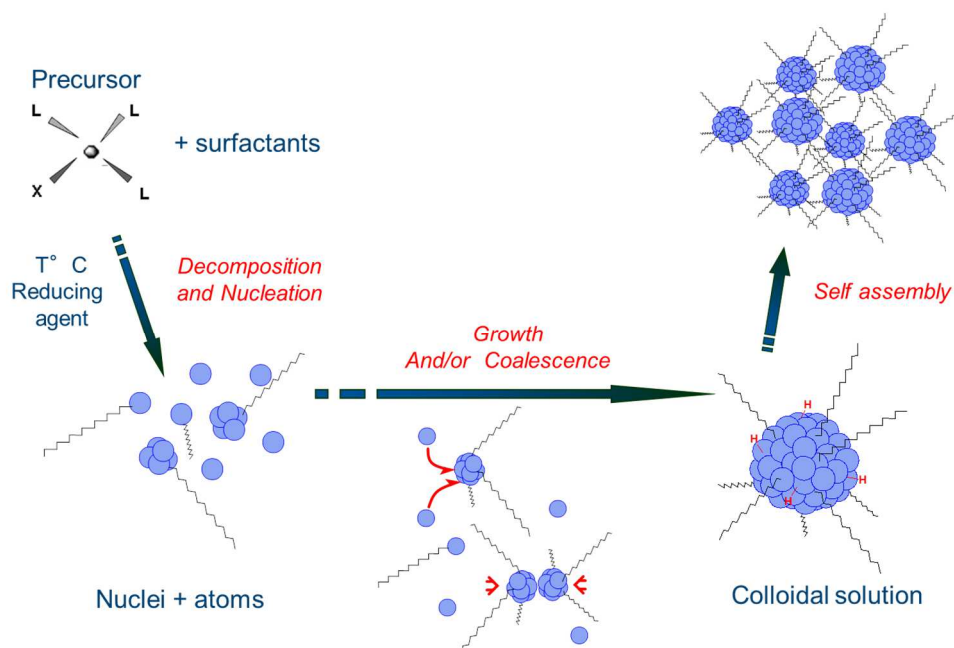


**Figure 1.** Schematic view of the synthesis of nanoparticles through a liquid-phase approach.

Since physical properties depend on the size, size distribution and shape of NPs, the challenge of any chemical synthesis thus consists in controlling the nucleation and growth steps to yield NPs with optimized properties. Monodisperse NPs (with a narrow size distribution  $\sigma < 10\%$ ) could be prepared via a burst nucleation, fast and limited in time, followed by a homogeneous growth.<sup>15</sup> Nucleation and growth steps extent depends of experimental parameters such as reaction time, temperature, nature of the precursors and surfactants, thus careful optimization of these parameters are usually required.<sup>16</sup> Eventually, the nanoparticles can self-assemble, thanks to a delicate balance between attractive and repulsive forces,<sup>17,18</sup> yielding macroscopic supercrystals.<sup>19</sup>

Since 2005, I have been interested in understanding the growth mechanism hidden behind the nanoparticle synthesis, in order to reach a predictive and fine tuning of their properties. During my PhD and post-doc I studied mostly Fe nanoparticles. Since 2009, I kept on working on Fe-based NPs (Fe, FePt, FeCo, FeS...) and started to study nanoparticles with original physical properties (ultrafine gold nanowires, Pt stars or Co nanorods).

### 1. Synthesis of metallic Fe nanoparticles

Iron nanoparticles (NPs) are promising candidates for a wide range of applications, ranging from magnetic data storage to chemical or biomedical uses, such as contrast agents for sensitive magnetic resonance imaging (MRI)<sup>A21</sup> or efficient heater media for magnetic fluid hyperthermia (MFH).<sup>A10</sup> Iron indeed combines a high saturation magnetization ( $M_S$ ) at room temperature ( $212 \text{ A.m}^2.\text{kg}^{-1}$ )<sup>20</sup> and a presumably low toxicity. Nevertheless, to achieve optimum operation conditions, these NPs should

have well-controlled magnetic properties and biological functionalities, which are strongly dependent of the surface states, sizes and shapes of NPs. Thus, a strict control of the NPs synthesis is required.

A widely used approach to synthesize Fe NPs consists in thermal decomposition of  $\text{Fe}(\text{CO})_5$  in the presence of long-chain surfactants.<sup>21</sup> The NP size can be tuned from 4 to 20 nm by controlling reaction parameters.<sup>22,23</sup> However, the magnetic properties of these NPs are usually degraded compared to bulk values due to CO contamination and partial carburization, i.e. introduction of C atoms within the Fe crystals. To prevent such carburization,  $\text{Fe}(\text{CO})_5$  can be replaced by iron salts or organometallic compounds whose decomposition did not yield any carbon source. Due to their high stability, the reduction of iron salts required harsh conditions. For instance,  $\text{FeCl}_2$  could be reduced in water by sodium borohydride, but boron contamination has been found to decrease the NP moment.<sup>24</sup>

In order to avoid such surface contaminations and their drastic effects on magnetic properties, an organometallic approach could be advantageous since controlled decomposition under mild conditions can be achieved.

#### a) Organometallic approach using $\{\text{Fe}[\text{N}(\text{SiMe}_3)_2]_2\}_2$

*PhD performed under the supervision of Sébastien Lachaize, Marc Respaud and Bruno Chaudret, in collaboration with Andrea Falqui. These results were reported in 3 papers (AC1, A6, A19) and 1 book chapter (Ch1), 2 papers are currently in preparation.*

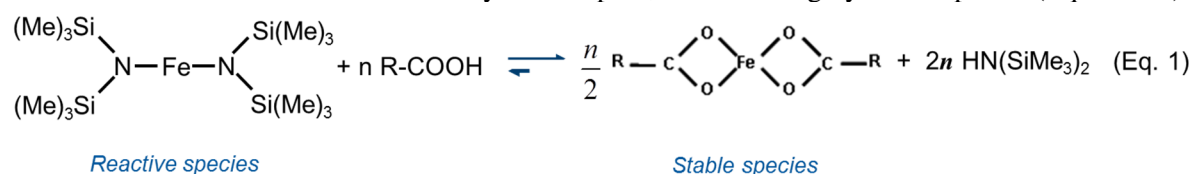
Through intensive prospective work, our team determined that amido precursors such as  $\text{Fe}[\text{N}(\text{SiMe}_3)_2](\text{THF})$  ( $\text{Me} = \text{CH}_3$ ,  $\text{THF} = \text{tetrahydrofuran}$ )<sup>25</sup> or the dimer  $\{\text{Fe}[\text{N}(\text{SiMe}_3)_2]_2\}_2$ <sup>26</sup> can yield unoxidized iron magnetic NPs under mild conditions. These precursors exhibit a good compromise between stability, to be stored once prepared, and reactivity, to be decomposed under mild and reductive conditions.

To demonstrate the pertinence of the precursor choice, ultra-small Fe NPs (< 2nm) have been prepared by solely decomposing the dimer in mesitylene solvent under 3 bars of  $\text{H}_2$  at  $150^\circ\text{C}$  (Figure 2a).<sup>AC1</sup> This demonstrates that  $\text{HN}[\text{Si}(\text{CH}_3)_3]_2$  or some derivatives of it released during the synthesis are able to stabilize the NPs surface. Furthermore, these NPs exhibit a magnetization closed to the bulk value. The magnetic properties of ultra-small NPs being drastically affected by pollutants, one can conclude that by-products of the precursor reduction do not alter the surface states. Moreover, these nanoparticles can be used as catalysts for alkene hydrogenation, evidencing a clean surface state.<sup>27</sup>

- Surfactant addition : the role of the acid concentration

In order to grow larger NPs, displaying a higher potential for further applications, we have developed a rational approach for the synthesis of Fe(0) NPs by reducing the  $\{\text{Fe}[\text{N}(\text{SiMe}_3)_2]_2\}_2$  complex, under mild conditions ( $150^\circ\text{C}$ ,  $\text{H}_2$  pressure) in the presence of a mixture of acid/amine ligands with 16 carbons, namely hexadecylamine (HDA) and palmitic acid (PA).<sup>A6</sup>

The effect of several experimental parameters, including the reaction time, the temperature, and the surfactant concentrations, has been investigated. By coupling different characterization techniques (magnetic measurements, Mössbauer spectroscopy, Transmission Electron Microscopy - TEM) we highlighted the key role played by the acid concentration. This ligand was not only involved in the stabilization of the NPs formed but also in the modification of the reactive Fe precursor. We indeed evidenced the in-situ formation of carboxylate complex, which are highly stable species (Equation 1).



By tuning the acid concentration, we could therefore control the relative amount of reactive species, the  $\{\text{Fe}[\text{N}(\text{SiMe}_3)_2]_2\}_2$  initially introduced, which is decomposed during the nucleation step, as well as

the stable carboxylate species formed, which is delivered all along the growth step. Therefore, we could tune the number of seeds created during the nucleation and thus, control the final NP size in the range 1.5 nm - 21 nm (Figure 2a). This size increase is concomitant with the modification of the NPs shapes (Figure 2b-c): spherical below 1.4 equiv. acid per mol of iron atoms (eq.), and cubic above.

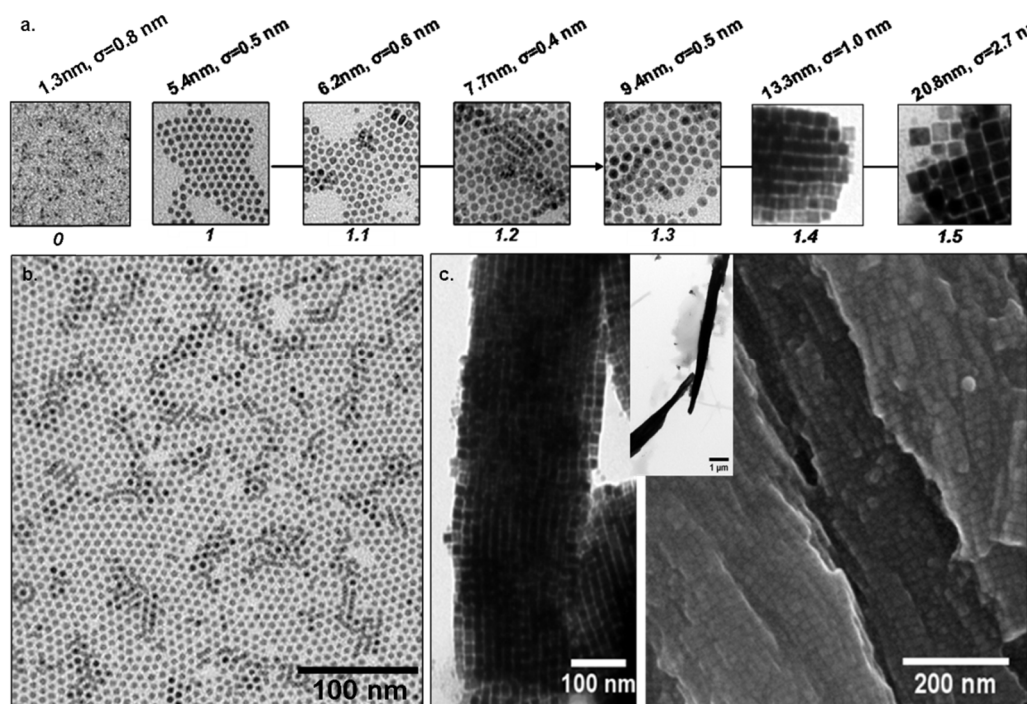


**Figure 2.** Transmission Electron Microscopy (TEM) images of Fe NPs. a) Size evolution as a function of the acid concentration between 0 and 1.5 eq. b) 5.5nm nanospheres and c) 13.3nm nanocubes obtained with respectively 1 eq. and 1.4 eq. of acid. Nanocubes self-organized into micrometric wires.<sup>A6</sup>

- A complex nucleation/growth mechanism

Such shape control could be understood in the framework of an environmentally dependent growth process. Above 1.4 eq. of acid, the presence of organic super-structures filled with iron(II) carboxylate species could be observed at the very beginning of the reaction. These structures are fairly similar to the final super-structure of cubes finally obtained (Figure 3a-d).

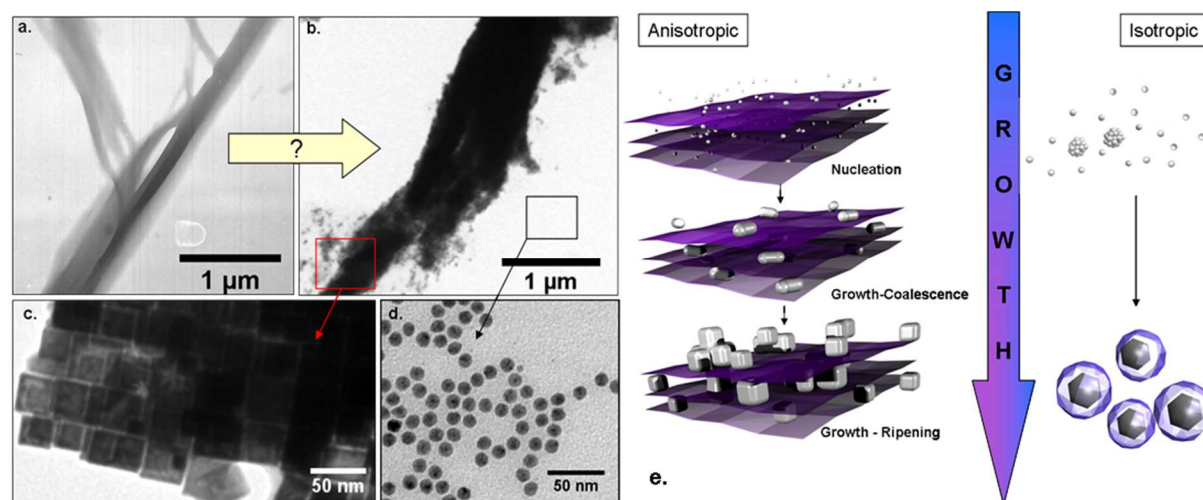


**Figure 3.** TEM images of a) organic super structure before decomposition and b) self assemblies obtained after 48h; they are filled with c) nanocubes while d) nanospheres are found outside of these micrometric organizations. e) Schematic view of the environment-dependent growth mechanism proposed.

Based on a combined morphologic, magnetic and spectroscopic study of the reaction advancement, we proposed that the nucleation and growth can occur either outside these organic soft templates, *i.e.* in an isotropic environment, or inside them, *i.e.* in an anisotropic environment (Figure 3e). In the first case, we obtain spherical polycrystalline NPs of mean sizes increasing with the carboxylic acid concentration, as expected. In the second case, the reaction monitoring reveals several steps: (i) nucleation, (ii) growth and coalescence favoured by an amine-rich environment, followed by (iii) growth and repair mechanisms in a carboxylate-rich environment. These 3 main steps lead to cubic NPs organized into super-structures. The evolution of the environment from amine- to carboxylate-rich is directly correlated to the decomposition of the iron(II) carboxylate species.

- Extension towards a broader size and shape control

Work in collaboration with *Bénédicte Warot-Fonrose (CEMES, Toulouse)* and *Florian Hüe (Cambridge)*

Providing that our hypothesis of a complex growth mechanism in 3-steps was correct, one should be able to change the morphology of the nanoparticles obtained by changing the kinetic of iron(II) carboxylate decomposition. By decreasing the reaction temperature (down to 120°C) or by changing the mixture of surfactant used (dodecylamine / lauric acid), we could slow down the carboxylate release and thus extent the coalescence step. Nanoparticles with unique features such as anisotropic stars (Figure 4a) or porous nanocubes, as revealed by electron tomography (Figure 4b-d), could be obtained.

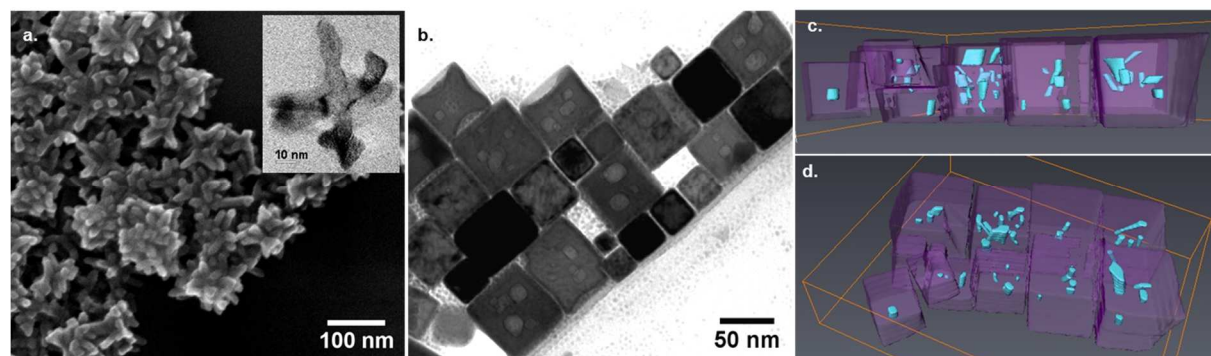


**Figure 4.** a) Scanning electron microscopy (SEM) image of nanostars. As inset, TEM image of a single star. b) TEM image of porous nanocubes, obtained with dodecylamine/lauric acid surfactants. c-d) 3D reconstruction of the nanocubes obtained from electron tomography study, the defects embedded within the objects are represented in blue, the outer surface of the cubes in light violet.<sup>A19</sup>

To go beyond these results, gaining control on the nucleation step was mandatory. In the literature, the use of preformed seeds, in the so-called seeded-growth process,<sup>28,29</sup> has been widely used to strictly separate the nucleation and growth process. Pt seeds have been used for instance to promote the heterogeneous growth of Fe NPs by thermodecomposition of  $\text{Fe}(\text{CO})_5$ .<sup>22,30</sup> Recently, we reported the overgrowth of Fe cubes onto preformed Co nanorods using  $\{\text{Fe}[\text{N}(\text{SiMe}_3)_2]_2\}_2$ .<sup>A25</sup> We developed a simple approach where ultrasmall iron(0) NPs of 1.5 nm,<sup>AC1</sup> were used both as seeds and as Fe source (Figure 5), the idea behind consisting in taking advantage of the ripening step observed in the synthesis.

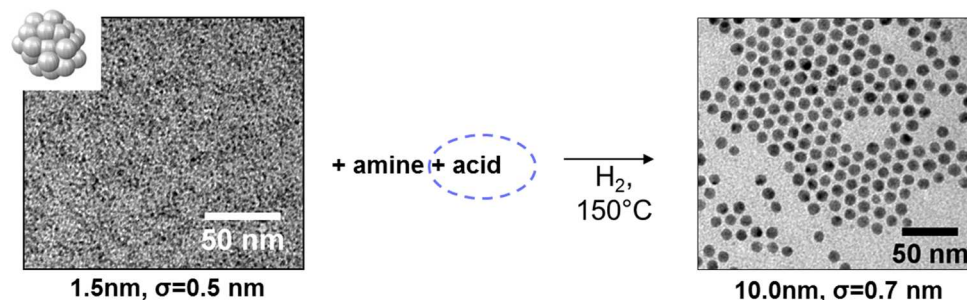


**Figure 5.** Schematic view of the ripening based synthesis using ultrasmall Fe NPs as Fe source.

The key role played by the hydrogen in this ripening process could be evidenced by a combined transmission electron microscopy (TEM) and Mössbauer spectroscopy study.

Finally, replacing carboxylic acid (R-COOH) by ammonium chloride salt (R-NH<sub>3</sub><sup>+</sup>, Cl<sup>-</sup>) changed the iron intermediates formed and thus fastened the reaction kinetic both in the direct synthesis or in the ripening-based approach, yielding larger spheres and cubes.<sup>A4,31</sup>

Thanks to these different approaches, a unique size control ranging from 1.5 to 11 nm for spheres and from 7 to 90 nm for cubes was for the first time reached for metallic Fe nanoparticles (Figure 6).

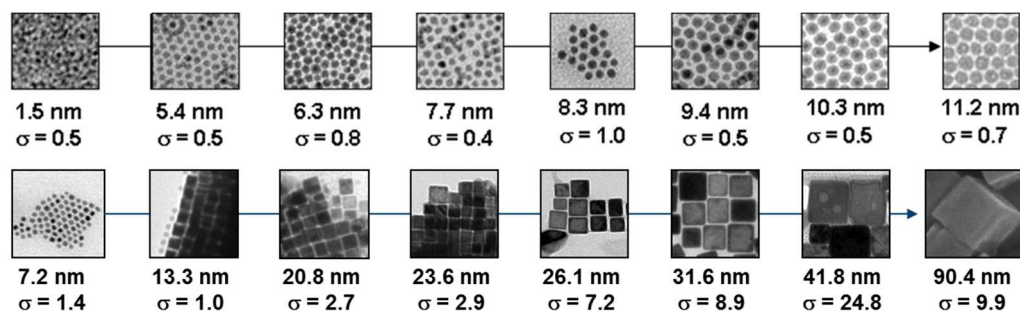


**Figure 6.** Size and shape control of Fe(0) nanoparticles.

*The application of these model NPs for magnetic field hyperthermia and fundamental magnetic and magnetotransport measurements will be further described in section II.*

#### b) Using Fe(CO)<sub>5</sub> precursor

*Post-doc performed under the supervision of Pr. Shouheng Sun, in collaboration with Don Ho, Natalie Frey and Kai Cheng. These results were reported in 1 paper and 2 review articles (A10, A13, A17).*

Though highly toxic, Fe(CO)<sub>5</sub> is still commonly used. Contrarily to the Fe silylamide precursor used during my PhD, it is less reactive and thus do not require to be stored and manipulated in glove box. Furthermore, Fe atoms are already reduced (oxidation degree 0), therefore no reducing agent (such as H<sub>2</sub> or NaBH<sub>4</sub>) are needed. After joining Pr. Shouheng Sun team in Brown University (Providence, USA), I was therefore in charge of developing a new synthesis approach to yield air-stable Fe nanoparticles starting from Fe(CO)<sub>5</sub> for future biomedical application.

However, making monodisperse Fe NPs stable in ambient and biological environments remained an extremely challenging task. A promising way to stabilize the high moment metallic NPs is via core/shell structures. Although noble metals such as gold or silver are considered as good candidates, their controlled growth on the preformed metallic NPs is not simple.<sup>32</sup> Alternative solutions for the formation of this protective shell include carbon<sup>33</sup> or oxide coating.<sup>23</sup>

We developed a facile synthesis of crystalline Fe/Fe<sub>3</sub>O<sub>4</sub> nanoparticles from the thermal decomposition of Fe(CO)<sub>5</sub>. Different from all previous Fe(CO)<sub>5</sub>-based syntheses, where amorphous and partly carburized Fe nanoparticles (amor-Fe) are obtained, we could for the first time modify the decomposition pathway of Fe(CO)<sub>5</sub> precursor to prevent the CO dissociation. The key point consisted in adding halides ions, in the form of an alkyl ammonium chloride salt (the hexadecylammonium chloride salt I previously studied), leading single crystalline Fe particles of 15 nm.<sup>A13</sup> The exact growth mechanism was however not elucidated due to the limited period of my post-doc (9 months) and the absence of spectroscopy techniques.

Once exposed to air, these particles were only partially oxidized and the resultant 15 nm core/shell bcc-Fe/Fe<sub>3</sub>O<sub>4</sub> particles (Figure 7a) were stable in air over months while keeping a high magnetization value (164 A.m<sup>2</sup>.kg<sub>Fe</sub><sup>-1</sup>).

These core/shell nanoparticles could be further functionalized by classical ligand-interlock procedure (using amphiphilic oleylamine-polyethylene glycol) and dispersed in water or phosphate buffered saline without showing any sign of deep oxidation in the testing periods up to a month.

These Fe/Fe<sub>3</sub>O<sub>4</sub> NPs exhibit enhanced magnetic imaging contrast ( $r_2 = 220 \text{ s}^{-1} \cdot \text{mM}^{-1}$ , Figure 4b) and heating effects compared to the iron oxide NPs commonly used or even to the amorphous Fe/Fe<sub>3</sub>O<sub>4</sub> NPs generally prepared using Fe(CO)<sub>5</sub>. Thus, the crystalline Fe/Fe<sub>3</sub>O<sub>4</sub> NPs could serve as robust probes for simultaneous magnetic resonance imaging (MRI) and magnetic fluid hyperthermia (MFH) applications.

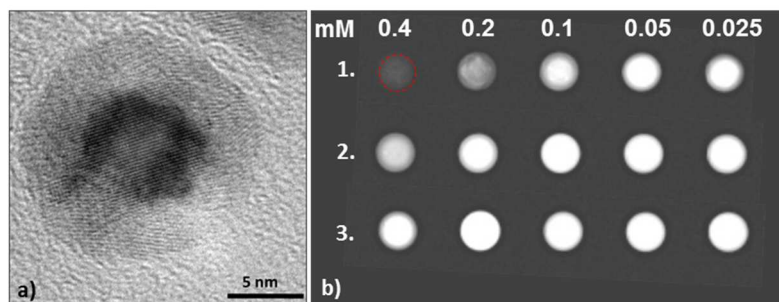


**Figure 7.** a) High Resolution (HR) TEM images of the Fe NPs, b) T<sub>2</sub>-weighed images of the bcc-Fe/Fe<sub>3</sub>O<sub>4</sub> NPs (1), amorphous-Fe/Fe<sub>3</sub>O<sub>4</sub> NPs (2) and 16 nm Fe<sub>3</sub>O<sub>4</sub> NPs (3).

The use of halide ions has further been generalized to other metallic NPs by Pr. Sun's group.

## 2. FeCo NPs : towards a composition control

While controlling the size and the shape of monometallic nanoparticles is already challenging, it is even more complicated for bimetallic alloys. Different mixing patterns such as core-shell, onion-like or dumbbells have so far been mostly obtained (Figure 8).<sup>34</sup>

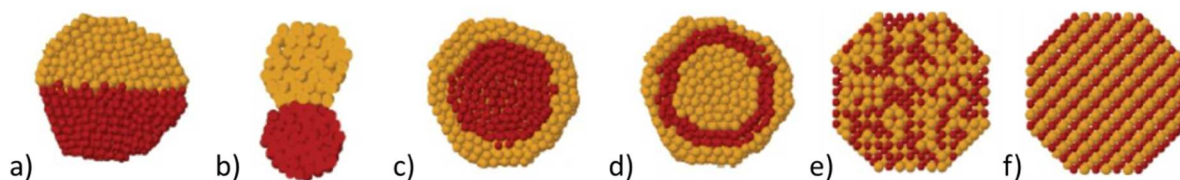


**Figure 8.** Schematic view of the different bimetallic structure obtained a-b) janus-type; c) core-shell, d) onion-like, e) disordered alloy, f) ordered alloy. Reprinted from<sup>34</sup>

Among the different magnetic material, the FeCo alloy exhibit the highest saturation magnetization ( $M_S = 245 \text{ A} \cdot \text{m}^2 \cdot \text{kg}^{-1}_{\text{FeCo}}$ ) combined with a low anisotropy constant ( $K_{\text{Fe}_{50}\text{Co}_{50}} = 1,5 \cdot 10^4 \text{ J} \cdot \text{m}^{-3}$ ).<sup>20</sup> Therefore, this alloy is a material of primary choice for numerous products ranging from RF filters to biomedical applications.<sup>35</sup> Despite important efforts to develop liquid phase synthesis, including thermal decomposition<sup>36</sup>, polyol process<sup>37</sup>, hydrothermal synthesis<sup>38-40</sup> and sonochemical method<sup>41,42</sup>, crystalline FeCo nanoparticles (NPs) could never been achieved directly. Indeed, the difference of reactivity of the precursors and the mild temperature of reaction used lead to poorly crystallized nanoparticles with inhomogeneous chemical structure, which therefore exhibit a reduced saturation magnetization. A high temperature annealing process is then mandatory to achieve the desired bulk magnetic properties, but at the expense of the size and shape control of the nanoparticles due to sintering.

I worked on two different approaches, that I will briefly overview, to reach an accurate chemical control of this alloy.

### a) Sequential approach : interfacial diffusion in Co/Fe core/shell NPs.

Work performed during my post-doc, in collaboration with Shen Peng, Chao Wang and under the supervision of Pr. Shouheng Sun. These results were reported A9.

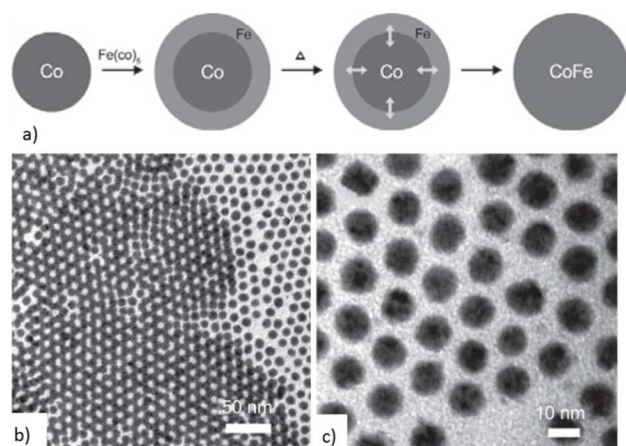


**Figure 9.** a) Schematic view of the interfacial diffusion-based synthesis protocol. TEM images of b) 8 nm Co seeds and d) 11 nm FeCo NPs.

Pr. Shouheng Sun pioneered the work on FePt alloy.<sup>43</sup> His group reported that interfacial diffusion between the core and the shell in core/shell structured particles is a successful approach to various alloy NPs. For example, ferromagnetic FePt NPs were made by high-temperature reductive annealing of FePt/Fe<sub>3</sub>O<sub>4</sub> NPs,<sup>44</sup> and AuAg alloy NPs were synthesized from Ag/Au core/shell NPs.<sup>45</sup>

Therefore, we studied the possibility to make core/shell structured Co/Fe NPs from Co seeds and further convert them into CoFe NPs by high temperature aging.<sup>A9</sup>

Co NPs were first prepared by thermodecomposition of Co<sub>2</sub>(CO)<sub>8</sub> precursor at 210°C in presence of oleic acid and

diethylamine. After removing the excess of surfactants, a Fe shell was further grown by the thermodecomposition of Fe(CO)<sub>5</sub> at 180°C. The interfacial diffusion was then promoted in liquid-phase by heating the colloidal solution of Co/Fe core/shell NPs at 250°C for 15 min. An excess of oleylamine was added to prevent any coalescence of the particles. Polycrystalline NPs exhibiting the expected bcc structure were obtained, but with reduced magnetization.

The key point of this approach was the promotion of the interfacial diffusion thanks to thermal heating. However, we have latter shown on Co nanorods that the organic solvent and the surfactants can be partially decomposed at such a high temperature leading to the carbidization of the NPs, and thus to the reduction of the magnetic properties.<sup>A22</sup>

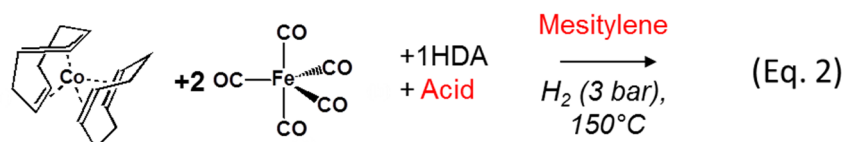
### b) Direct synthesis : co-reduction of organometallic complexes

- Fe(CO)<sub>5</sub> and Co(COD)(COT)

Work initiated during my PhD, in collaboration with Céline Desvaux, under the supervision of Bruno Chaudret and continued after 2009, in collaboration with Pier-Francesco Fazzini

During her PhD under the supervision of Bruno Chaudret, Céline Desvaux reported the synthesis of 15 nm FeCo NPs, which self-organize into millimeter supercrystals, by the co-decomposition of Fe(CO)<sub>5</sub> and Co(η<sup>3</sup>-C<sub>8</sub>H<sub>13</sub>)(η<sup>4</sup>-C<sub>8</sub>H<sub>12</sub>) under dihydrogen at 150°C in toluene.<sup>46-48</sup> The particles exhibited however a magnetization limited to 160 A.m<sup>2</sup>.kg<sup>-1</sup><sub>FeCo</sub> due to a chemically inhomogeneous structure and a partial carburization due to CO byproducts.<sup>49</sup>

I slightly adapted the procedure to use mesitylene as solvent (Equation 2) in order to reduce the overpressure risk. In presence of 1 equivalent of oleic acid (an unsaturated acid with 16 carbons), monodispersed nanoparticles of 13 nm with a Fe<sub>60</sub>Co<sub>40</sub> composition were obtained. However, in presence of 1 eq. of both oleic and stearic acids, two populations of 16 and 27 nm were obtained (Figure 10). These particles are Co-rich (Fe<sub>20</sub>Co<sub>80</sub>), the iron being stabilized in stable molecular species as evidenced by Mossbauer spectroscopy.



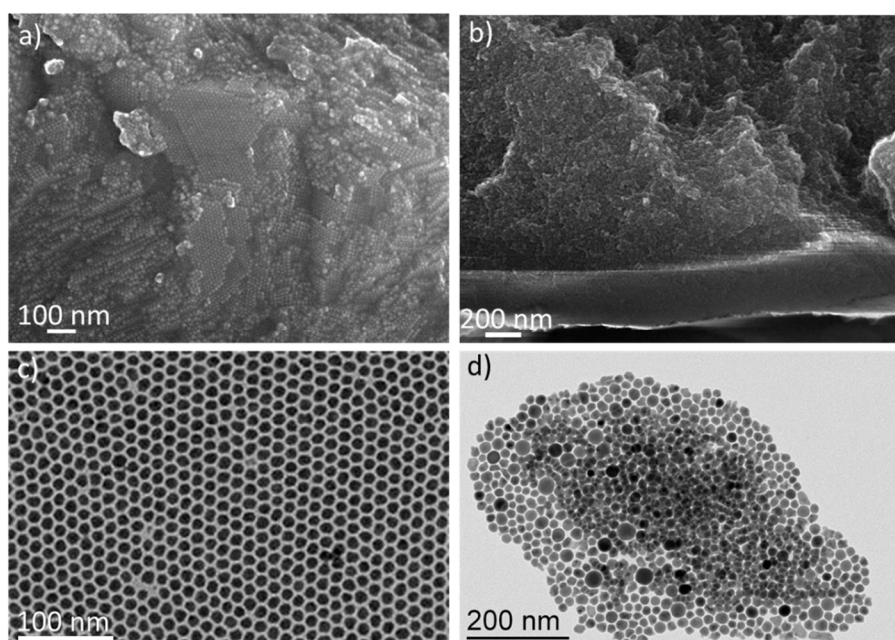


**Figure 10.** a-b) Scanning Electron Microscopy (SEM) of supercrystals and c-d) TEM images of the constituting FeCo NPs prepared in presence of a-c) 1 eq. of oleic acid and b-d) 1 eq. of oleic and stearic acids.

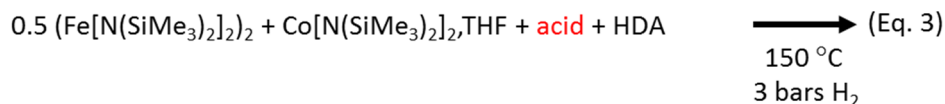
These particles have been further used for magnetic field hyperthermia and magnetotransport measurements as described in the next sections.

- $\{\text{Fe}[\text{N}(\text{SiMe}_3)_2]_2\}_2$  and  $\text{Co}[\text{N}(\text{SiMe}_3)_2]_2, \text{THF}$

Work performed with Cyril Garnero, Katarina Soulantika and Bruno Chaudret, in collaboration with Raul Arenal (INA, Saragosse), Bénédicte Warot-Fonrose and Cécile Garcia (CEMES, Toulouse), Yoleemin Shin and Christian Meny (IPCMS, Strasbourg). 1 manuscript is in preparation

Despite important efforts, the control of the FeCo alloy could not be reached with the previous precursors, annealing being mandatory to reach the bulk magnetic properties. Thus, since 2010 I started to work on extending the synthesis of Fe NPs to FeCo NPs using silylamides precursors. After obtaining promising preliminary results, a PhD thesis was funded in the framework of an industrial project (Tours 2015).

FeCo nanoparticles (NPs) were obtained by decomposing  $\{\text{Fe}[\text{N}(\text{SiMe}_3)_2]_2\}_2$  (with  $\text{Me} = \text{CH}_3$ ) and  $\{\text{Co}[\text{N}(\text{SiMe}_3)_2]_2, \text{THF}\}$  at  $150^\circ\text{C}$  under  $\text{H}_2$  (Equation 3). As previously observed in the synthesis of Fe NPs, the acid reactant governs the final NP size and shape through its concentration and its nature.



In presence of hexadecylammonium chloride salt, large particles of  $11,4 \pm 0,7$  nm NPs, which exhibit a truncated octahedral shape are obtained after only few hours of reaction (Figure 11a-b). However, the reaction is much slower in presence of palmitic acid, leading after 48 h of reaction to nanocubes with a mean size of  $8,3 \pm 0,9$  nm (Figure 11c-d). Both type of particles were highly crystalline and exhibited the expected bcc structure as revealed by high resolution transmission electron microscopy and X-Ray Diffraction (Figure 11e). The crystallite sizes could be extracted using the Scherrer formula and are respectively of 9,9 nm and 7,4 nm, in good agreement with the TEM mean size. While a thin oxide shell is clearly observed on the HRTEM images, XRD patterns do not exhibit any extra peaks due to oxide phases.

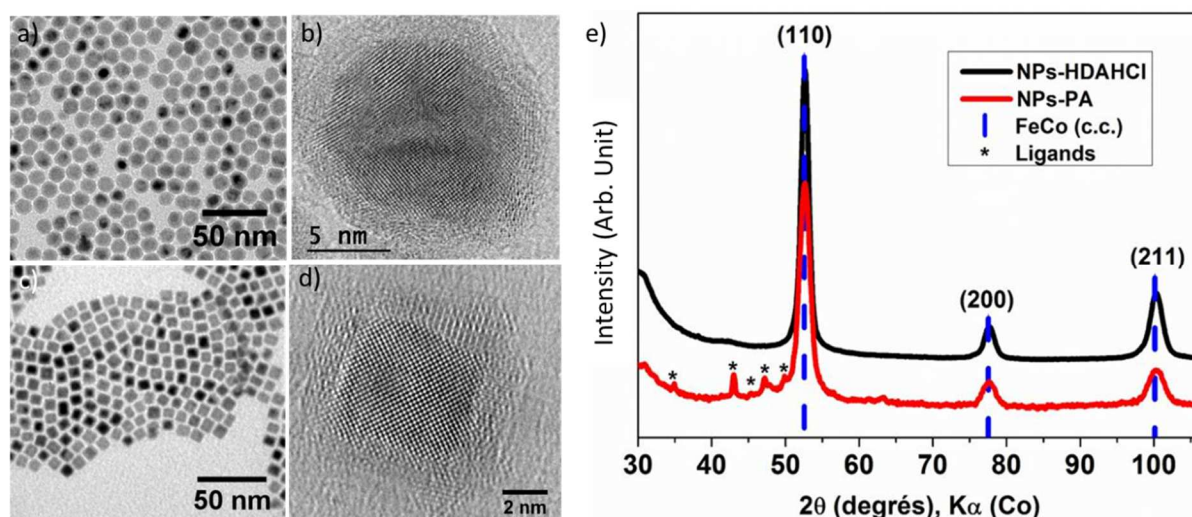


**Figure 11.** a-c) TEM and b-d) HRTEM images of FeCo NPs synthesized in presence of HDAHCl (a-b) or palmitic acid (PA, c-d) and e) the corresponding XRD patterns in black and red respectively.

The determination of the chemical structure of the obtained NPs was fairly challenging. Indeed, oxidation was encountered during the introduction of the NPs into the aberration-corrected microscope. Local chemical analysis with atomic resolution were done in collaboration with Raul Arenal, Bénédicte Warot-Fonrose and Cécile Marcelot. For both type of particles a demixion between Fe and Co was observed, leading mostly to a Co-rich core surrounded by a  $\text{Fe}_3\text{O}_4$  shell (Figure 12). In the case of the NPs prepared in presence of HDAHCl, a statistical study based on Energy Electron Loss Spectroscopy (EELS) revealed the presence of three main types of particles : Co pure core, a Co-rich FeCo core or a janus-type structure.

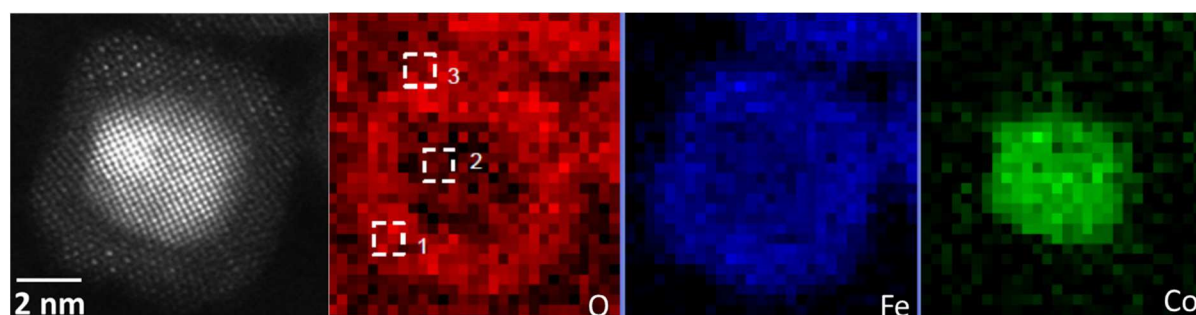


**Figure 12.** High Angle Annular Dark Field (HAADF) and the corresponding O, Fe and Co mapping determined by EELS.

The chemical environment of Fe atoms and Co atoms were probed using Mössbauer spectroscopy and 0-field Nuclear Magnetic Resonance (0-field  $^{59}\text{Co}$  NMR), in collaboration with Christian Meny and Yooleemin Shin (ICPMS, Strasbourg). Fe-based molecular species are still detected after 48h of reaction in presence of palmitic acid, confirming the slow kinetic of decomposition of the carboxylate-based species (Figure 13). The broad peak observed by NMR can be fitted by a continuous composition gradient varying from a pure Co environment in the core of the particle to a Fe environment at the NP surface.

The particles prepared in presence of HDAHCl exhibit a very different feature. The decomposition reaction is over after 24h of reaction, molecular species being no longer detected in that case. The three peaks in the NMR spectrum corresponds respectively to a bcc-Co (~200 MHz), a Co-rich FeCo alloy (~220 MHz) and the chemically ordered  $\text{B}_2$  alloy with a stoichiometric composition (290 MHz) and slightly Fe-rich composition (310 MHz knee). These three environments may correspond to the three types of particles detected by EELS.

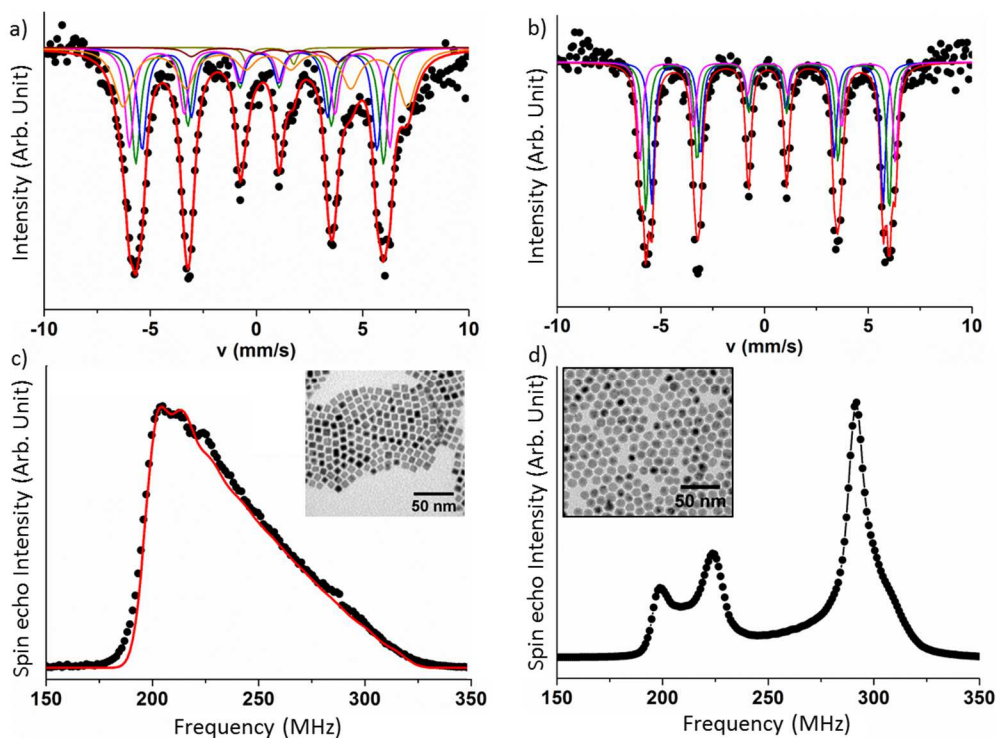
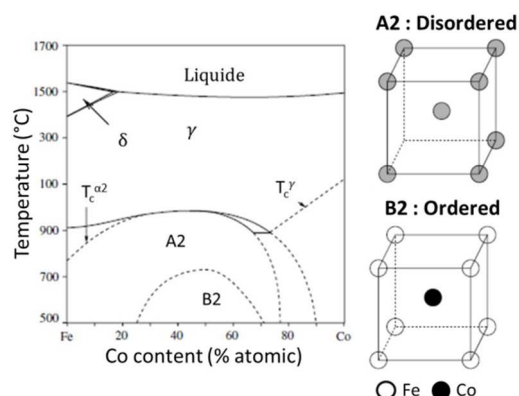


**Figure 13.** a-b) Mössbauer spectroscopy and c-d) O-field  $^{59}\text{Co}$  NMR of FeCo NPs prepared with a-c) PA and b-d) HDAHCl surfactant.

To my knowledge, this is the first report of the direct stabilization of the thermodynamic phase  $B_2$  in nanoparticles. This phase, which consists in the regular stacking of Fe and Co planes, is generally obtained after thermal annealing from the disordered bcc-structure, referred to as the  $A_2$  phase (Figure 14).

**Figure 14.** Phase diagram of FeCo alloy and schematic view of the  $A_2$  and  $B_2$  structure



In conclusion, the control of the precursor-surfactant interaction was once more crucial to govern the reactivity of the species formed in-situ. In presence of carboxylates, the Fe and Co species decompose at a slightly different rate, leading to a concentration profile within the particles. In presence of halides, the reactivity of the Fe and Co species become very similar, allowing for the partial stabilization of the chemically ordered FeCo alloy.

The obtained particles have been further used for RF-filters application (section III) and are currently investigated for magnetically-activated catalysis. Preliminary experiments of EXAFS and anomalous XRD will be pursued to confirm the partial  $B_2$  ordering.

### 3. Noble metal nanoparticles with complex shapes

In 2009, our colleagues from the LNCMI-Toulouse, Bertrand Raquet and Walter Escoffier, were interested in studying the electronic transport in metallic analogous of carbon nanotubes. The requirements seemed fairly complex to achieve by a liquid-phase synthesis approach:

- A diameter of few nanometers to reach a quasi one-dimensional confinement
- A micrometric length to allow their connection by conventional microelectronic processes

We obtained a PhD funding from the University of Toulouse in 2010 to work at the interface between physics and chemistry on the synthesis and the electronic transport properties of gold nanowires. Anaïs Loubat shared her time between our laboratory and the LNCMI.

#### a) Ultrathin Au Nanowires : a unique anisotropic growth

Work performed with Anaïs Loubat and Guillaume Viau, in collaboration with Romuald Poteau, Raul Arenal (INA, Saragosse), Marianne Imperor-Cler and Brigitte Pansu (LPS, Orsay). These results have been published in 4 papers (A26, A28, A30, A43).

Ultrathin gold nanowires (Au NWs), exhibiting sub-2 nm diameter and micrometric length, were firstly reported by Halder and Ravishankar.<sup>50</sup> An expanding interest immediately appeared for these objects due to their unique properties, among which one can cite high surface to volume ratio, mechanical flexibility and remarkable conductivity properties.<sup>51</sup> These features open the perspective towards various applications such as analyse sensors,<sup>52,53</sup> fuel cell anodes,<sup>54</sup> elastic coiled springs,<sup>55,56</sup> or transparent electrodes.<sup>57,58</sup> To be competitive with the existing technologies, the developed alternatives should rely on cost-effective synthesis of Au NWs, i.e. with high yield and limited post-treatment requirements. Since the pioneer work in 2007,<sup>50</sup> two main routes have been followed to synthesize Au NWs: the first one involves the precipitation of an intermediate solid phase assuming that it acts as a soft-template for the wire growth,<sup>59,60,61,62,63</sup> while the second one is a direct reaction in an isotropic solution (Figure 15).<sup>50,64,65,66</sup> These two approaches lead to ultrathin Au NWs along with other nanoparticles such as spheres or rods. The quantitative analysis of the different populations, and therefore the Au NWs yield estimation, though crucial, cannot be easily addressed. Moreover, the growth mechanism remained unclear.

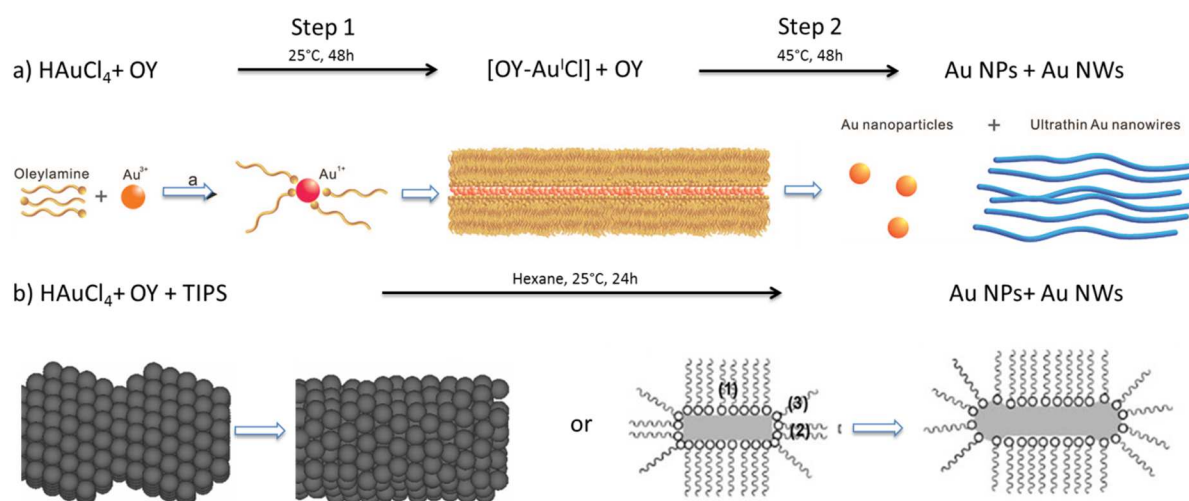


**Figure 15.** Schematic view of the two approaches for the synthesis of ultrathin Au nanowires using a) a soft-template or b) a direct reaction in a isotropic solution. The proposed growth mechanism by soft-templating, oriented attachment and micellar growth are reprinted from the references <sup>60,50</sup> and <sup>67</sup> respectively. OY = oleylamine, TIPS = Triisopropylsilane

Thus, we studied quantitatively the two approaches to determine which one was the most promising for large scale synthesis and investigated the driving force responsible for such an anisotropic growth.

- In-situ study : coupled TEM-SAXS investigations

While TEM is the technique of choice to characterize the particles morphologies, we could not obtain reliable estimation of the relative yield of Au NWs and spheres due to sampling issues. On the contrary, Small Angle X-Ray Scattering (SAXS) is a state-of-art *in situ* technique which can shed light on the growth mechanism,<sup>68,69,70</sup> and the synthesis yield of metallic nanoparticles.<sup>A26,71</sup> The quantitative analysis of SAXS data on an absolute scale enables to determine the number of particles and their size and shape. Indeed, spheres are characterized by a plateau, known as the Guinier region, followed by a knee whose position is inversely proportional to their diameter ( $q=2\pi/d$ ). In the case of wires, the scattering profile is mainly characterized by a  $q^{-1}$  slope as evidenced in Figure 16.

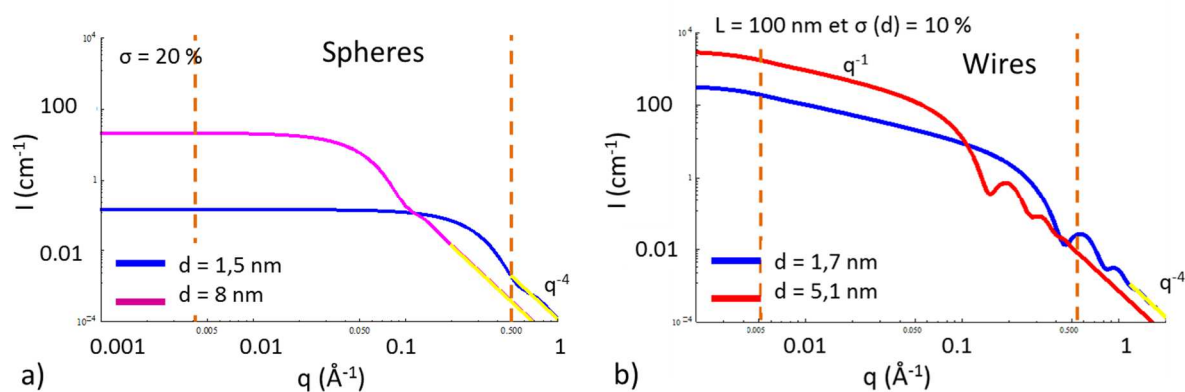


**Figure 16.** Simulated profile for a) spheres of 1.5 nm (in blue) and 8 nm (in pink) of diameters and b) 100 nm long wires of 1.7 (blue) or 5.1 nm (red) of diameters.

In the case of monodisperse nanoparticles, SAXS analysis is therefore fairly straightforward,<sup>72</sup> but for more complex populations, the interpretation becomes non univocal due to the averaging of several scattering profiles.<sup>73,74</sup> Coupled TEM and SAXS characterizations enable to obtain unambiguously quantitative analysis even on polymorphic nanoparticles.<sup>75,76</sup>

- Soft-template approach

The lamellar phase formed after the first reaction step was carefully analysed by structural, spectroscopic and computational techniques, confirming the formation of linear Au<sup>I</sup> complexes (Figure 17).<sup>A30</sup>

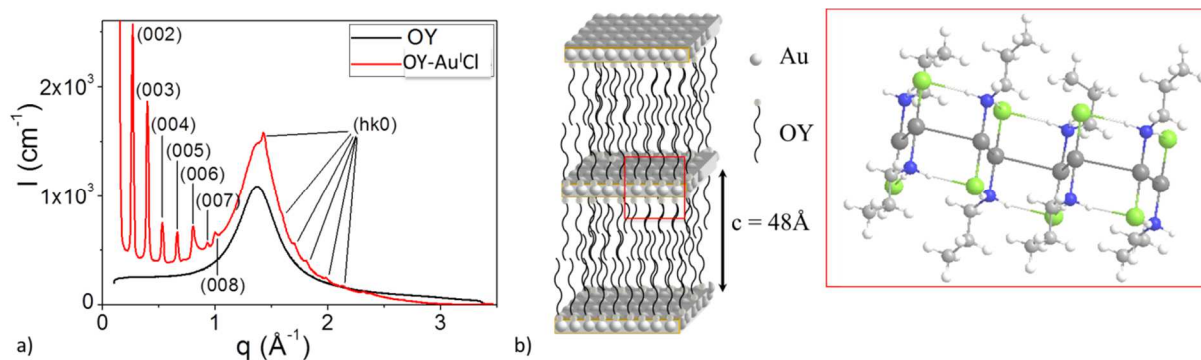
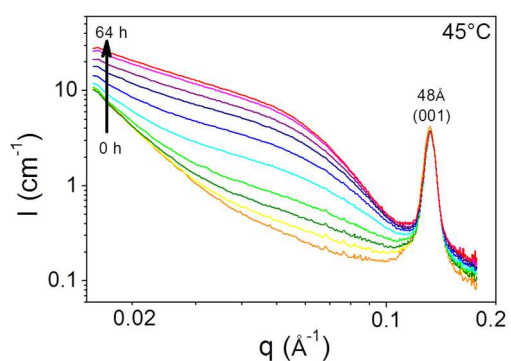


**Figure 17.** a) SAXS pattern of the free oleylamine (black) and the lamellar phase obtained after the first reaction step (red). b) Schematic view of the lamellar phase with an interlamellar distance of 48Å. As inset, DFT calculation of the stable configuration of Cl-Au<sup>I</sup>-RNH<sub>2</sub> complexes. 3 carbons alkyl chain amines were considered due to computational time limitation. In green : Cl, blue : N, Grey : C, White : H, Black : Au<sup>I</sup>.



However, its prevalence as driving force towards unidimensional growth is questioned. Indeed, the in-situ SAXS study did not evidence its consumption during the Au NWs growth, the characteristic peak, corresponding to the interlamellar distance, remaining constant over the whole 64h. Moreover, the reaction yield of Au NWs is limited to 4%, neither the reaction time, nor the temperature allowing any significant increase of it.

**Figure 18.** Time evolution of the SAXS pattern at 45°C.

- *Direct reaction in isotropic environment*

This synthesis approach relies on a one step liquid phase reaction, where the gold chloride salt is solubilised in hexane in presence of oleylamine (OY) and reduced by triisopropylsilane (TIPS). An optimization of the experimental parameters allowed us to obtain wires after only few hours at 40°C (Equation 4).



We followed the growth of Au NWs by ex-situ TEM and in-situ SAXS.<sup>A26</sup> After 15 min of reaction at 40°C, small spheres are formed and short wires with a mean length of ~100nm are observed (Figure 19a). After 45 min, the wires length increases to ~500 nm to reach a micrometric length after 3h of reaction (Figure 19b-c). The SAXS study performed at the beam line SWING at the synchrotron Soleil evidenced a fast reaction kinetic. At t=0, i.e. just after the addition of the reducing agent, a Guinier region characteristic of small spheres is already observed. With time, the SAXS profile evolved revealing a  $q^{-1}$  slope characteristic of the wire growth (Figure 19d). By fitting the experimental profile, Marianne Imperor-Cler could determine the volume fraction of spheres, whose diameter was determined to be 1.7 nm, and of wires, which exhibit the exact same diameter (Figure 19e).

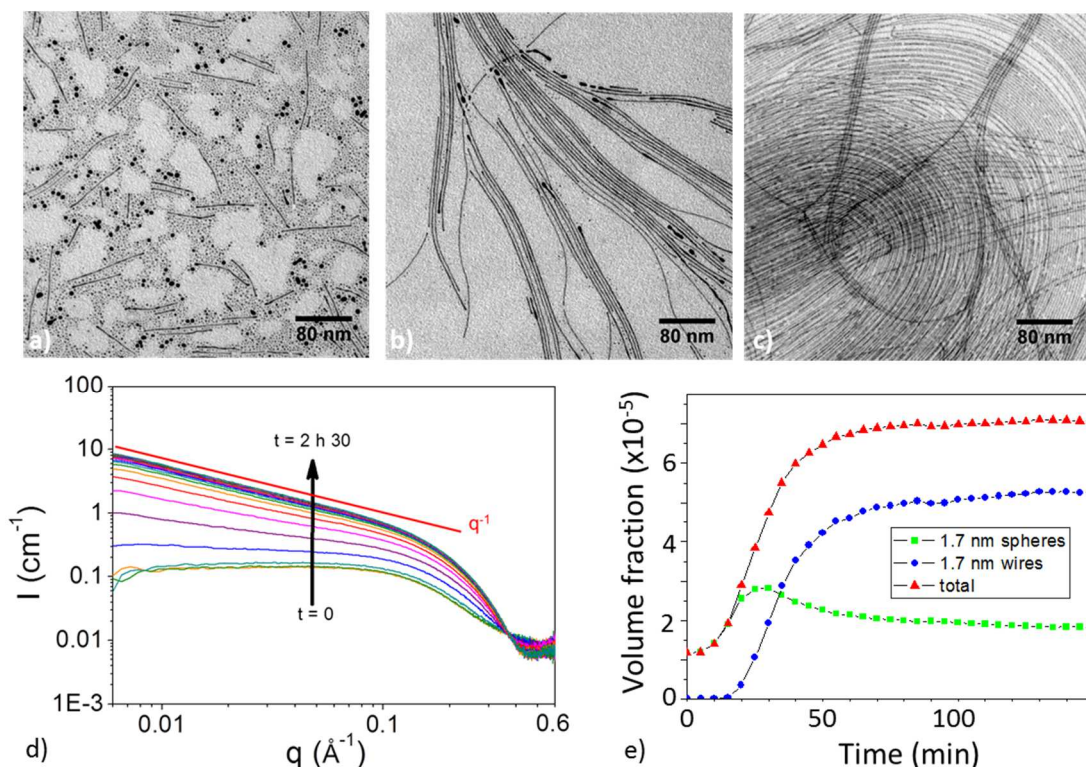


**Figure 19.** TEM images of Au nano-objects obtained after a) 15 min, b) 45 min and c) 3h of reaction at 40°C. d) Time evolution of the SAXS profile and e) the corresponding volume fraction evolution.

The reduction  $\text{Au}^{\text{III}} - \text{Au}^0$  is total after only 90 min of reaction at  $40^\circ\text{C}$ , the yield of Au NWs being of 75%, far above the 4% obtained with the soft-template route.

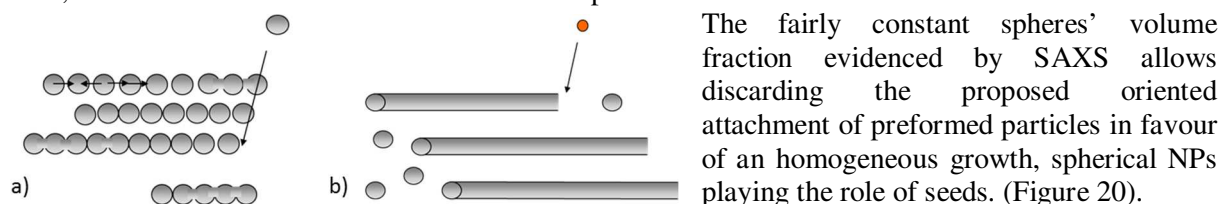


**Figure 20.** Schematic view of a) the oriented attachment and b) the atom by atom growth

After few additional hours at  $40^\circ\text{C}$ , ultrathin Au NWs self-organize into a hexagonal super-lattice, as revealed by additional Bragg peaks in the SAXS profile. This super-lattice exhibits a very large lattice parameter corresponding to an interwire distance of 8 nm (Figure 21). Such large value can be explained by the presence of a bilayer at the surface of each nanowires. NMR and XPS studies revealed that the bilayer is composed of oleylamine and oleylammonium chloride.

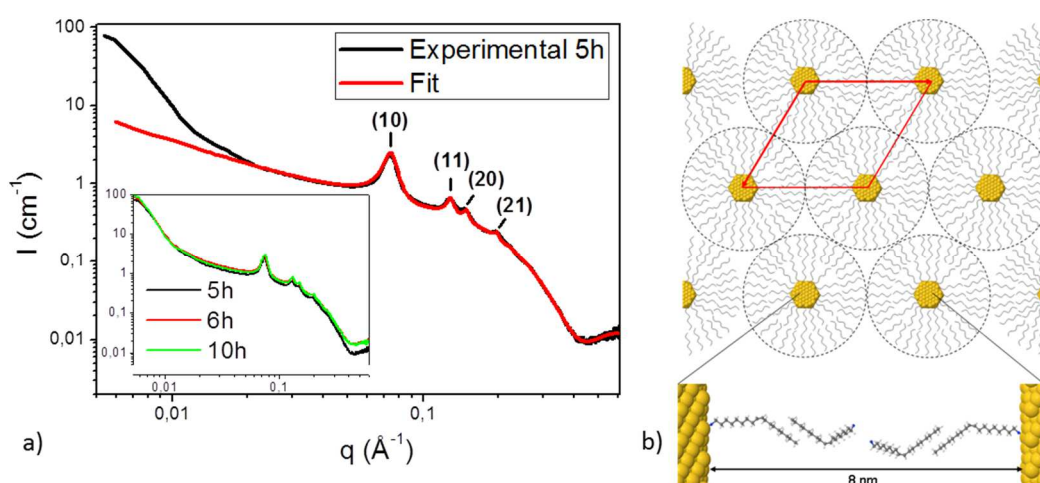


**Figure 21.** a) Experimental and fitted SAXS profiles after 5h at  $40^\circ\text{C}$ , as inset, the time evolution up to 10h. The peaks indicative of a long-range positional order are labelled. b) the corresponding schematic view of the hexagonal phase observed. Each Au NW being surrounded by a bilayer of surfactants.

- Driving force towards the anisotropic growth

To understand the growth mechanism responsible for such a unique growth we studied further the reaction, in particular through the effect of the oleylamine concentration (Figure 22). In presence of only 20 mM of oleylamine, corresponding to 2 equivalents per mole of gold, only small spheres were obtained. When the oleylamine concentration was increased to 50 mM, small rods were observed after 3h but tend to dissociate with time. Stable wires were only observed for a minimal concentration of 100 mM.

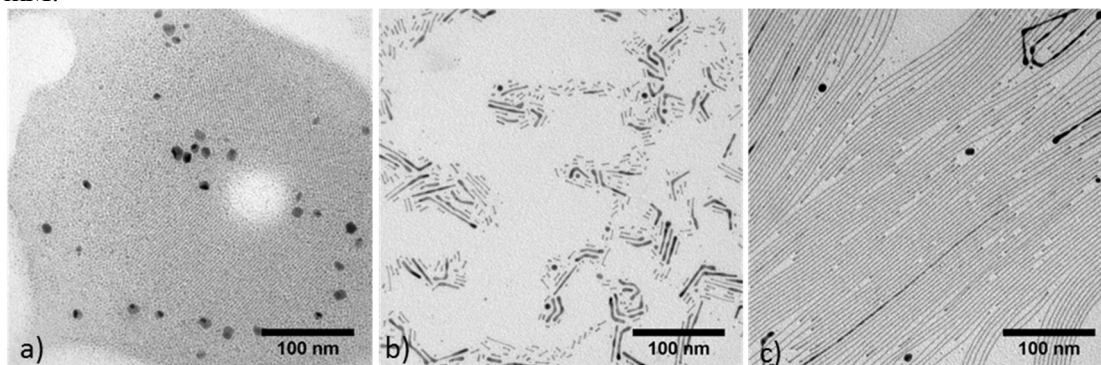
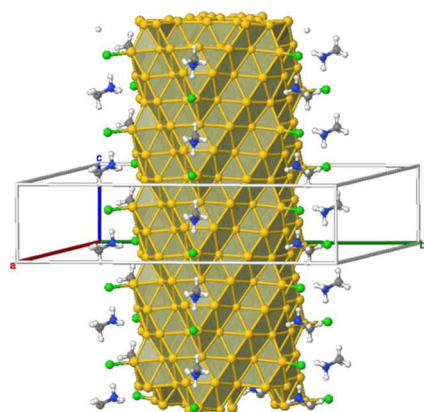


**Figure 22.** TEM images of Au nano-objects formed after 3h of reaction at  $40^\circ\text{C}$  in presence of a) 20 mM, b) 50 mM and c) 100 mM of oleylamine.

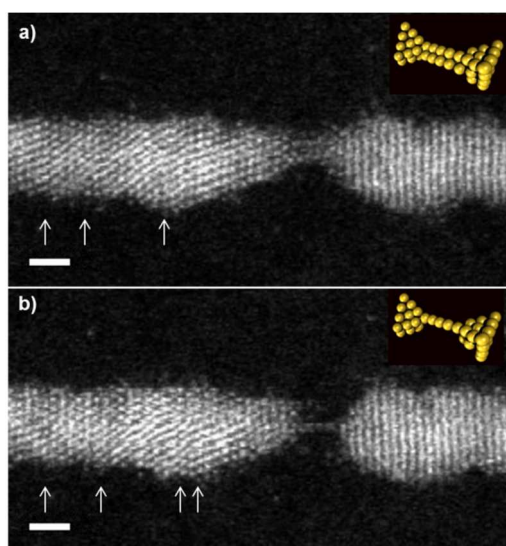
Such concentration effect on the shape evolution of the Au nanoparticles, combined with the presence of ligands bilayer at the surface of the wires, reminds the phase diagram of surfactants like CTAB in aqueous media and the critical micellar concentration associated with the transition from spherical to cylindrical micelles. All these observations suggest that a micellar growth mechanism drives the one-dimensional growth.<sup>77</sup>

- A cooperative absorption and organisation of ligands at the Au NWs surface?



Catherine Murphy evoked a cooperative effect between surfactants organisation and Au reduction, previously described as a “zip” mechanism for the growth of Au nanorods in water.<sup>78</sup> Though our reaction occurs in apolar solvent, DFT calculations of the energetic stabilisation by polar heads (oleylamine vs. oleylammonium chloride) were performed by Romuald Poteau to investigate this hypothesis. Due to computational limitation, the alkyl chain was limited to one carbon. Methylammonium chloride ion pair adsorption was found to be energetically favoured compared to methylamine absorption, providing a simultaneous adsorption of both  $\text{NH}_3^+$  and  $\text{Cl}^-$  ion pairs on the surface (Figure 23).

**Figure 23.** DFT geometry of a gold nanowire stabilized by methylammonium chloride (the unitcell is highlighted, as well as the faceting of the NW resulting from the low-index surface cleavage). In green : Cl, blue : N, Grey : C, White : H, Yellow : Au.



The absorption being strongly dependant on the crystallographic surface exposed, intensive structural characterizations have been performed. Authors have mostly concluded on a fcc structure of the Au NW with a growth direction along the  $\langle 111 \rangle$  direction. However, the Au NWs evolved under the electron beam leading first to a recrystallization and then to their fragmentation into chain of spheres, which tend to diminish their surface/volume ratio (Figure 24).<sup>A28</sup> Thus, the determination of the crystalline structure of the wire is still unclear.

**Figure 24.** HAADF image of a single Au nanowire undergoing a) an irreversible recrystallization and b) a fragmentation with a single-atom thick chain as transient state. As inset, schematic view of the breaking junction. White arrows indicate twin planes in the fcc structure.

X-Rays are a promising alternative to electron beam to determine the structure of the wires without inducing any artefacts. We recently obtained a 3-day beamtime at the Argonne synchrotron to perform an in-situ study using Wide Angle X-Ray Scattering (WAXS) and X-ray Atomic Pair Distribution Function (PDF) techniques to determine the structural evolution of the objects. Preliminary results evidenced a non-compact structure of the Au NWs, thus in contradiction with the fcc structure usually reported in the literature. The further data analysis is however still on-going, in collaboration with Romuald Poteau, Pierre Lecante (CEMES, Toulouse) and Valeri Petkof (Central Michigan University, USA), to conclude on the exact structure of the wires.

*Fundamental studies on the stabilization of the wires are currently pursued using in-house SAXS, in collaboration with Pierre Roblin and Sébastien Teychenné (LGC, Toulouse). Moreover, a proposal for combined EXAFS-SAXS measurements at synchrotron Soleil has been submitted.*

## b) Extension towards other metals : the case of Pt

Work performed with Guillaume Viau and reported in 3 papers (A18, A44 and NA2).

We studied the possibility to transpose this unique anisotropic growth observed on ultrathin Au NWs to other metals. Having in mind the possible importance of the bilayer micelles and the ions pairs we studied the reduction of different chloride salt ( $\text{AgCl}$ ,  $\text{RuCl}_3$ ,  $\text{FeCl}_2$ ,  $\text{H}_2\text{PtCl}_6$ ) in presence of oleylamine. However none of them led to anisotropic objects whatever the experimental conditions used. If we keep on investigating the reason of such a failure, the reduction of the platinum salt ( $\text{H}_2\text{PtCl}_6$ ) under a dihydrogen atmosphere in pure oleylamine led to quasi single-crystalline Pt nanoparticles with peculiar morphologies –cubic dendrites, planar tripods and 5-fold stars - (Figure 25).<sup>A18</sup> Such Pt objects exhibit a large surface/volume ratio and controlled crystallographic faces. These features are of primary importance for developing various applications such as ultra-sensitive sensors<sup>79</sup> or highly active catalysts.<sup>80</sup> Indeed, surface atoms with pending bounds are highly active sites for specific adsorption and consequently for selective catalytic reactions.<sup>81</sup>

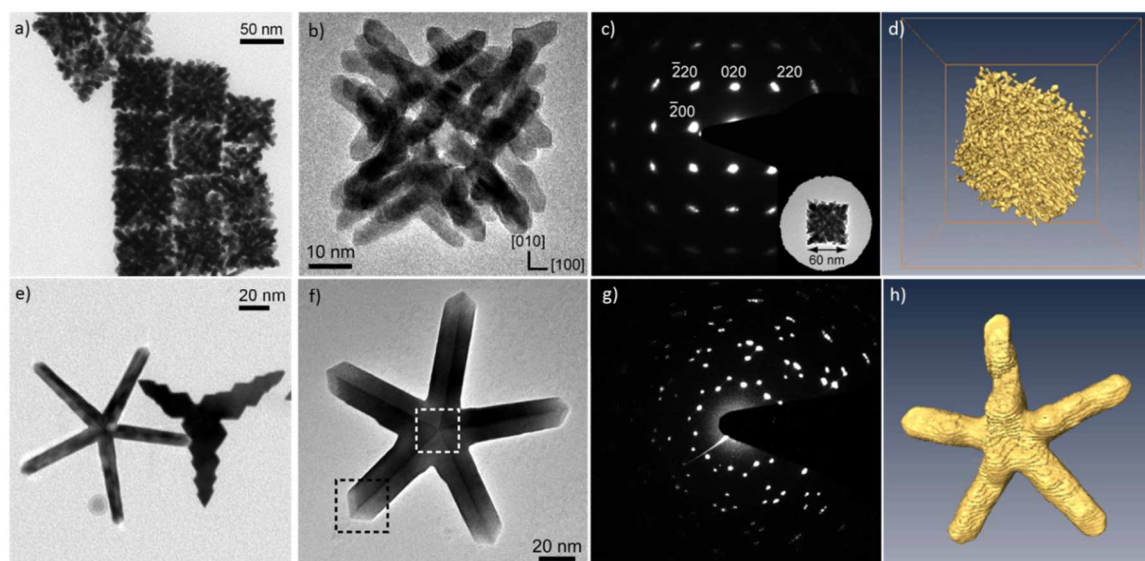


**Figure 25.** a,e) TEM, b,f) HRTEM, c,g) Selective Area Electron Diffraction – SAED, and d,h) 3D models reconstructed from electron tomography of a-d) cubic dendrites and e-h) Pt stars.

If intensive empirical optimizations had been devoted to the shape control of noble-metal nanocrystals,<sup>12,82,83</sup> we reported a simple strategy, whose reaction kinetics could be easily controlled by experimental parameters such as Pt concentration, reaction temperature and dihydrogen pressure.

A fast reaction, occurring in few minutes, leads to cubic seeds and thus to a dendritic growth (Figure 26). The peculiarity of these objects is their high crystallinity, their outer cubic shape and the unprecedented size control of their envelope. Such dendritic cubes display a high surface-to-volume ratio (estimated by electron tomography to  $2.4 \times 10^4 \text{ m}^2/\text{kg}$ ), while their cubic shape enables their self-assembly on surfaces.

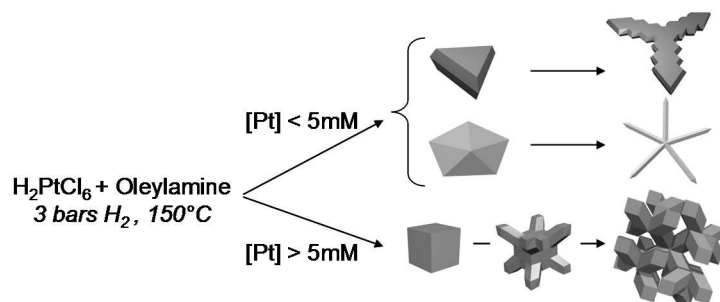


**Figure 26.** Schematic view of the shape control obtained

On the contrary, a slow reaction leads to twinned seeds which evolve into highly crystalline planar tripods (3-fold stars) and 5-fold stars. Such multiply twinned NPs are unique for Pt and result from a multi-step process, a second nucleation and growth occurring at the reactive sites of the preformed twinned seeds.

*The exact growth mechanism is still under investigation, we suppose that the autocatalytic reduction of  $\text{H}_2\text{PtCl}_6$  on  $\langle 100 \rangle$  facets plays a major role in the fast dendritic growth.*

## II. Physical study of model objects

Having a dual physics and chemistry educational background, my major motivation arises from multidisciplinary studies. Once the synthesis of nanoparticles is well mastered, I like taking part in the characterization of their physical properties. Of course, these studies are always made in collaboration with physic experts that I would like to specifically acknowledge.

Among the different properties encountered in particles of reduced sizes, I mostly worked on magnetism and electronic transport properties, as summarized below.

### 1. Magnetic configuration in nano-objects : experimental and theoretical study

*Work initiated during my PhD and pursued since 2009 with Thomas Blon, Francisco Bonilla, Anca Meffre and Marc Respaud, in collaboration with Etienne Snoeck and Christophe Gatel (CEMES, Toulouse). These results have been reported in 4 papers (A4, A19, A33, A41).*

The magnetic configuration in a magnet of a given volume, i.e. the orientation of the magnetic moment (or spin) of each atoms, results from the minimization of its total energy. This total energy is the sum of three different contributions : the magneto-crystalline anisotropy,  $E_{mc}$ , which tends to align the spins along a specific crystallographic direction (referred to as the easy-axis), the exchange energy,  $E_{ex}$ , which tends to align adjacent spin parallel to each other, and the magneto-static energy,  $E_{dipol}$ , which tends to close the magnetic flux within the material to prevent the appearance of magnetic poles. As a result, three typical magnetic configurations can be encountered in a magnetic material at

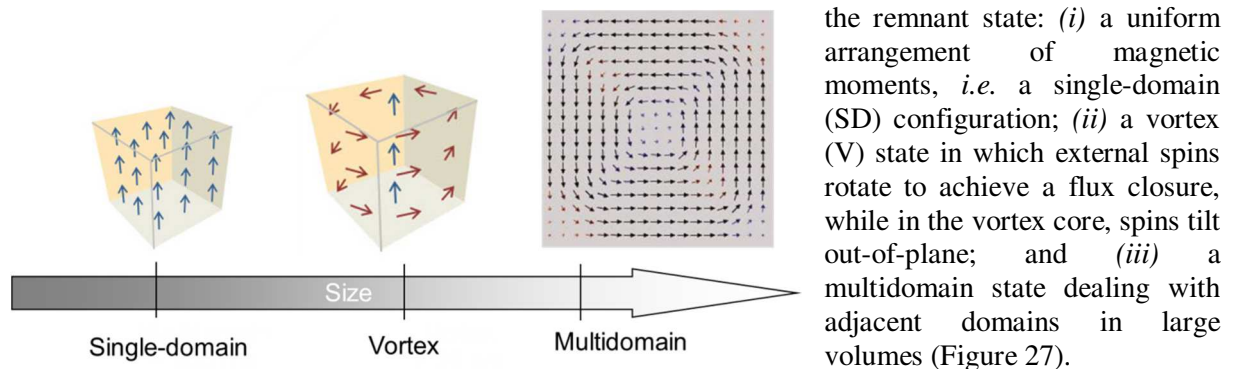


**Figure 27.** Schematic view of the magnetic configurations expected as a function of the particle size.

These different magnetic configurations are currently pursued for technological applications such as magnetic racetrack memories,<sup>84</sup> magnetic hyperthermia<sup>A10</sup> or microwave signal-processing.<sup>85</sup> Therefore, detailed knowledge of the magnetic behavior of magnets becomes of primary importance.

#### a) Determination of the single-domain/vortex transition in isolated magnets

Though largely investigated numerically, the experimental determination of the single-domain/vortex limit in a nanoparticle had never been experimentally reported, even for nano-objects with the simplest geometries. Single crystalline Fe nanocubes (NCs) we synthesized (see section I.1) represent model systems for such a study. These defect-free objects exhibit indeed controlled and reproducible magnetic properties over the whole size range available between 7 and 90 nm.

During my PhD, we could evidence for the first time the presence of a vortex-state in a 30 nm cube combining Electron Holography (EH) and micromagnetic simulations, using OOMF.<sup>A4</sup> Off-axis EH is an interferometric technique that measures the phase shift of a high-energy electron wave (typically 200 keV) that has passed through a material. The phase shift being sensitive to electric and magnetic fields in the sample, local magnetic properties can be mapped and quantitatively compared with micromagnetic simulations.

Thanks to the recent acquisition of a holography-dedicated transmission electron microscope by the CEMES, in the framework of the Equipex project “Mimetic”, a better sensitivity combined with a nanometric lateral resolution allowed us to report the first “magnetic configuration vs size” phase diagram of Fe single-crystalline NCs (Figure 28).<sup>A33</sup>

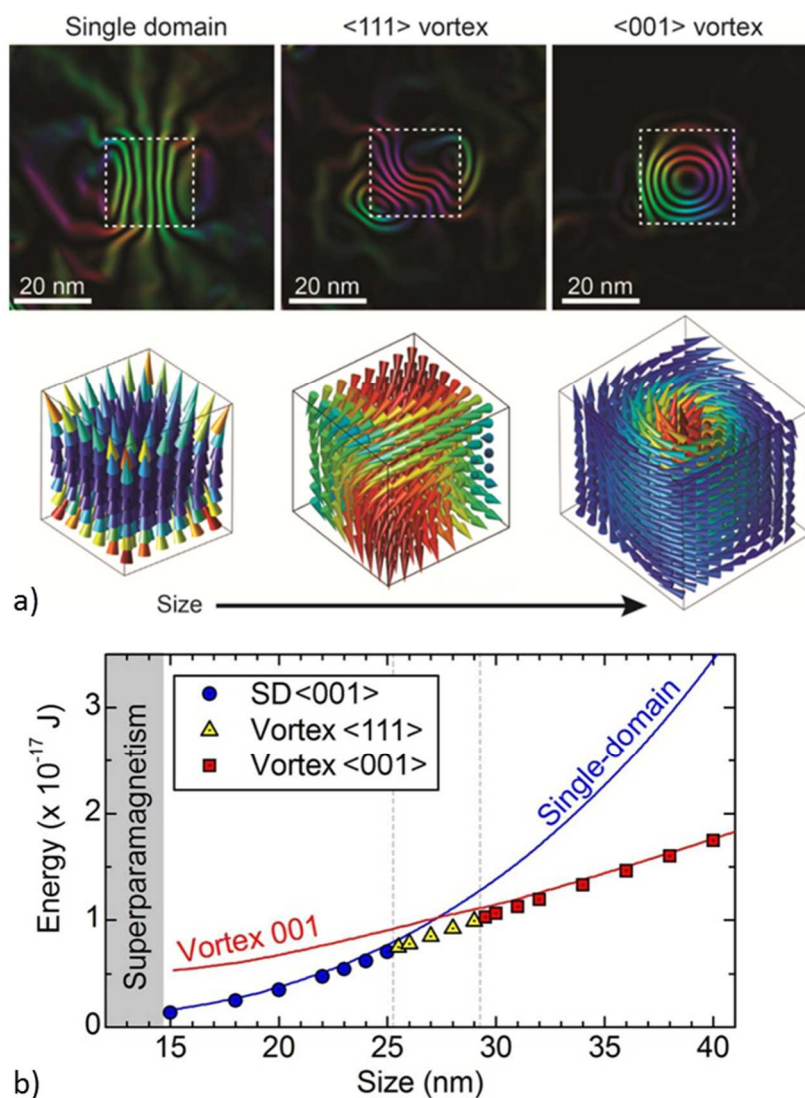


**Figure 28.** a) Magnetic induction flux lines determined by Electron Holography and the corresponding micromagnetic simulations of isolated iron nanocubes of 25, 26 and 27 nm exhibiting a single domain, <111> and <001> vortex states respectively, b) the magnetic phase diagram of a perfect Fe nanocube. The superparamagnetic regime is highlighted in grey.

High sensitivity imaging at room temperature reveals unambiguously how three different spin arrangements can be stabilized within a 3 nm window (between 25 and 27 nm), evidencing the key importance of nanometric size control of magnetic nanoparticles. Moreover, it gives a deeper understanding of the single domain limit, which is more complex than expected. An intermediate spin configuration consisting of an <111> vortex, i.e. of a vortex whose core is oriented along a diagonal of the cube, was for the first time evidenced. The condition of appearance of this <111> vortex was further studied theoretically. Such vortices are only stable in nanocuboids of a given size (around 25 nm) exhibiting a nearly perfect cubic shape (size distortion < 12%) made of Fe or FeCo.<sup>A41</sup> These limited conditions explain why such a configuration was rarely described.

We are currently working on the characterization of the superparamagnetic/ferromagnetic transition on isolated Fe cubes of 15 nm deposited by simple drop-casting. Electrospray deposition is being studied to promote their dispersion on the TEM grid surface.<sup>A35</sup>

## b) Effect of the magnetic interactions

Though optimized sizes for stabilizing single-domain or vortex configuration can be theoretically predicted, inter-particle interactions, mostly dipole-dipole interactions, modify drastically the magnetic configurations within assemblies of NPs.<sup>86</sup> Vortices were no longer stable in interacting 30nm Fe cubes, leading to flux-closure state configurations (Figure 29a-c) or single-domain magnets with the magnetization parallel to the direction of the cube alignment.<sup>A4</sup>

The presence of internal defects in the Fe porous nanocubes synthesized in presence of shorter surfactants, allow anchoring the vortex configuration despite magnetic interactions (Figure 29d-f).

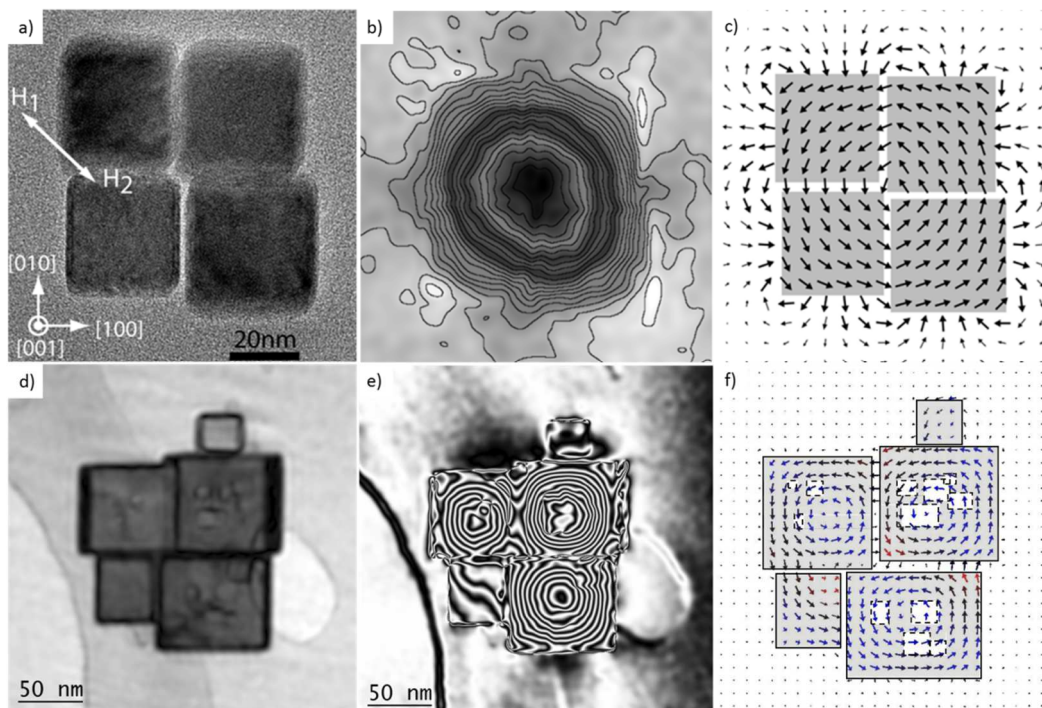


**Figure 29.** a,d) Hologram and the corresponding b,e) experimental and c,f) simulated induction map of interacting a-c) defect free and d-f) porous Fe nanocubes.

To go behind these observations, we are currently working on the controlled deposition of nanoparticles towards large-scale 2D assemblies in order to probe the coupling and the collective behaviour of NPs, for instance the appearance of magnetic domains. Among the different techniques tried, Julien Dugay showed that dip-coating could be successfully used to induce micrometer-size assemblies of FeCo nanoparticles on silica surface. Dip coating technique is based on an evaporation-driven assembly process. We could show that the physico-chemistry of the colloidal solution, i.e. the concentration and the nature of surfactants in excess, was of primary importance to tune the self-assembly (Figure 30).

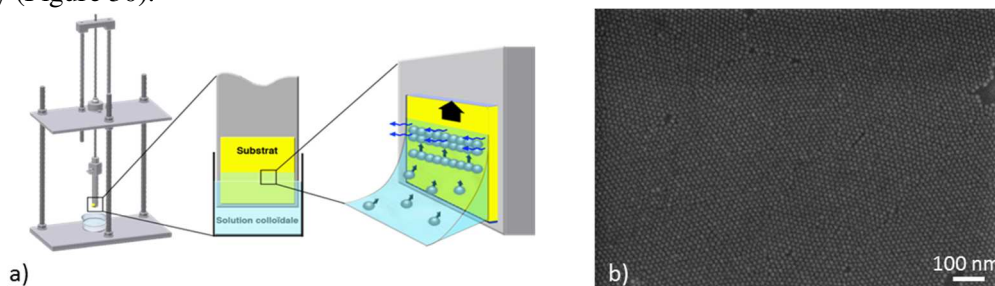


**Figure 30.** a) Schematic view of the dip-coating system developed at LPCNO and b) SEM image of a FeCo assembly obtained on SiO<sub>2</sub> substrate (Reprinted from A27).

Transferring the dip-coating parameters on the porous carbon TEM grids used for electron holography has not yet been convincingly achieved due to their important roughness. Flat Si<sub>3</sub>N<sub>4</sub> grids patterned by Focused-Ion Beam (FIB) are currently investigated by Suhail Usmani.

### c) Magnetic configuration in complex 3D objects

Work performed with Cyril Garnero, Alexandre Pierrot and Thomas Blon, in collaboration with Christophe Gatel (CEMES)

In the last ten years we focused our investigations on model systems such as defect-free Fe nanocubes. We recently started to investigate complex 3D-objects among which FeCo octapods (Figure 31). These single-crystalline objects have been prepared by adapting the synthesis based on the decomposition of silylamide precursors. These objects exhibit high-index {311} facets, conferring them a potential interest for catalytic applications (Figure 31d). Due to the recent development of magnetically-activated catalysis in the laboratory,<sup>A39,87</sup> it was a particular interest and an interesting challenge to further investigate the magnetic configurations of these octapods, which exhibit the bulk magnetization of FeCo alloy (Figure 31e).

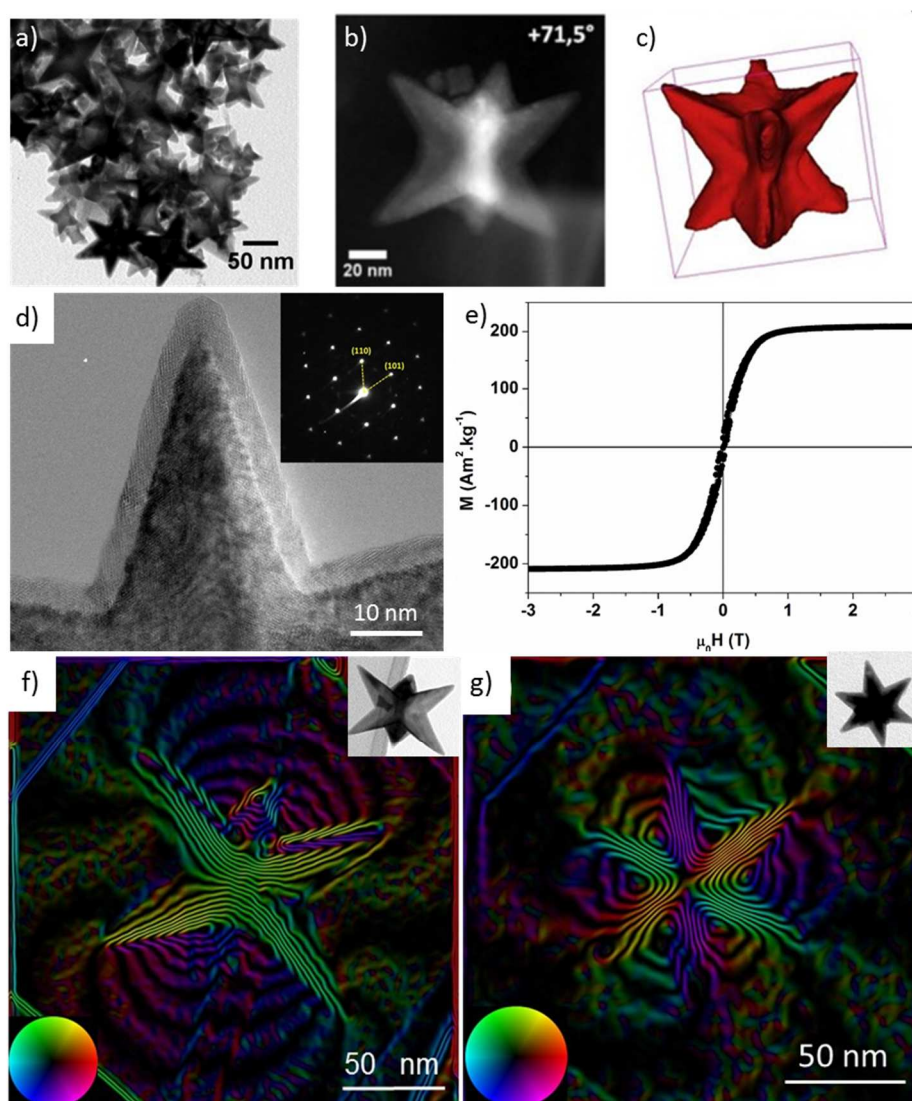


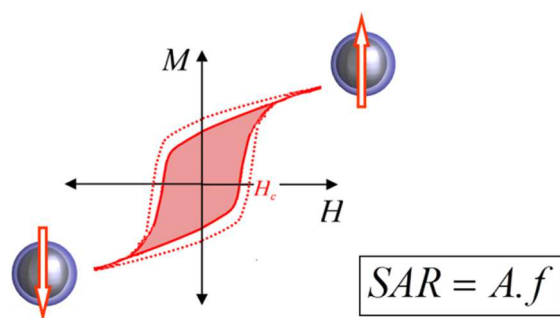
**Figure 31.** a) TEM image, b) HAADF-STEM image obtained during the electron tomography serie, at a tilting angle of  $+71.5^\circ$  and c) the corresponding 3D reconstructed model of the FeCo octapod. d) HRTEM image of an octapod branch observed along the  $\langle 111 \rangle$  zone axis. Inset : SAED pattern. e) Hysteresis cycle measured at 300K of FeCo octapods in random powder state, evidencing a coercivity of 40mT. Magnetic induction flux lines determined by Electron Holography of a single FeCo octapod observed along f) the  $\langle 110 \rangle$  and g) the  $\langle 111 \rangle$  zone axis. The inset color wheel indicates the direction of the magnetic induction.

Isolated octapods exhibit complex magnetic configurations at the remanent state as evidenced by the experimental induction map determined by electron holography (figure 31 f-g), micromagnetic simulations are currently performed to unravel them.

## 2. Magnetic hyperthermia : on the advantage of ferromagnetic losses

phD performed under the supervision of Julian Carrey, in collaboration with Marc Respaud and Gerardo Goya (INA, Saragosse). The work was pursued by Boubkher Mehdaoui and Anca Meffre during their post-doc. These results were reported in 6 papers (AC2, A5, A7, A11, A14 and NA1).

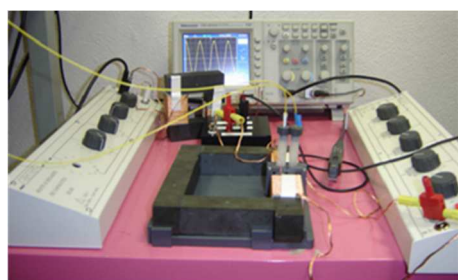
As previously mentioned, one of the potential application of nanomagnets concerns the nanobiomedicine, for both diagnosis, using the nanomagnets as contrast agents for MRI,<sup>A13</sup> or magnetic tag for biosensors,<sup>A17</sup> and for cancer treatment.<sup>A10</sup> Indeed, the sensitivity of cancer cells to heat has spurred the great interest of using magnetic NPs as local heater for cancer therapy. Magnetic field hyperthermia (MFH) is a promising therapeutic method based on the excitation of magnetic NPs, pre-injected in the tumor, under an alternative magnetic field (frequency  $f$ , amplitude  $\mu_0 H_{\max}$ ), leading to a local heating. The temperature increase improves the efficiency of chemotherapy ( $T \sim 42-45^\circ\text{C}$ ) or can even directly kill the tumor cells by necrosis ( $T > 50^\circ\text{C}$ ).



The power generated by the magnetic NPs is directly linked with the area of their magnetic hysteresis loop  $A$  and is evaluated by their specific absorption rate (SAR), the two parameters being linked by the equation  $SAR = A \cdot f$ .

**Figure 32.** Schematic view of the hysteresis cycle of single-domain nanoparticles and the corresponding area  $A$  (in pink).

Exploiting this effect in oncology requires biocompatible NPs with large heating power, thus one of the challenges in this topic is to maximize SAR values. The SAR being an increasing function of  $f$  and  $\mu_0 H_{\max}$ , one could think of increasing these parameters. However, human body cannot be exposed to alternating magnetic field of large  $\mu_0 H_{\max} f$  product, due to medical limitation. Thus, progress in the prediction and optimization of the heating of magnetic nanoparticles in a compatible alternating magnetic field (100 kHz and 20 mT) is highly desirable for their application in magnetic hyperthermia. It was already well established that SAR values could be increased by choosing optimal materials (with high  $M_s$  and moderate anisotropy  $K$ ) and by adjusting the NPs size.<sup>88</sup> Experimental studies were however scarce and quantitative analysis were limited to the linear response theory (LRT), based on the Néel-Brown relaxation, which suffers from a restricted domain of validity.<sup>89</sup> Small NPs exhibiting a superparamagnetic behaviour were considered up to 2008 as optimized for the MFH application.



Thanks to the large panel of NPs obtained by the organometallic approach and the frequency adjustable electromagnet we developed during my PhD (Figure 33)<sup>A5</sup>, we could evidence for the first time that ferromagnetic FeCo NPs were exhibiting higher heating properties than their superparamagnetic counterparts.<sup>A7</sup>

**Figure 33.** Frequency adjustable electromagnet developed at LPCNO

Extensive MFH measurements have been further performed by Boubkher Mehdaoui on iron NPs in a size range going from 5.5 to 27.5 nm (Figure 34a) under alternative applied magnetic field of frequency 54-274 kHz and of amplitude ranging from 8 to 73 mT.<sup>A14</sup> MFH properties measured on our system strongly depend on the NPs size, the optimal size corresponding to the largest specific area ( $A$ , Figure 34b-c). Ferromagnetic single-domain nanoparticles are the best candidates and display the highest specific losses reported in the literature so far ( $11.2 \pm 1 \text{ mJ} \cdot \text{g}^{-1}$ ).

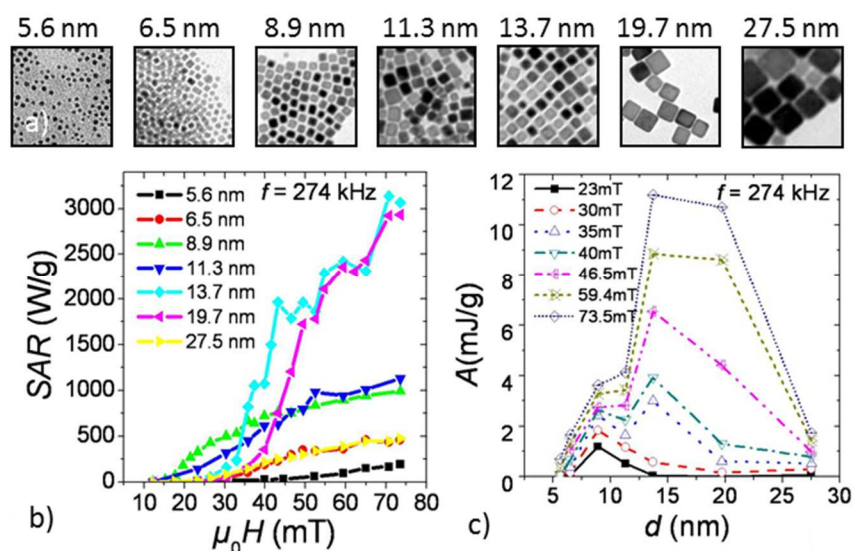


**Figure 34.** a) TEM images of the Fe NPs studied, b) specific absorption rate (SAR) evolution as a function of applied field and c) specific losses ( $A$ ) as a function of the NP mean size.

Measurements were analyzed using analytical formulas and numerical simulations of the hysteresis loops. Several features expected theoretically were observed for the first time experimentally: i) the correlation between the nanoparticle diameter and their coercive field, ii) the correlation between the amplitude of the coercive field and the losses, and iii) the variation of the optimal size with the magnetic field strength. None of these features are predicted by the LRT but are a natural consequence of theories derived from the Stoner–Wohlfarth model. These results opened the path to a more accurate description, prediction, and analysis of magnetic hyperthermia.

*This research activity was actively pursued in the laboratory. A great effort was devoted to the modulation of the magnetic anisotropy of the particle used. Metallic Fe NPs were progressively replaced by  $FeC_x$  NPs for biomedical and catalysis application.<sup>A36,A39,87</sup> The highly crystalline FeCo NPs we developed recently combine a moderate magnetic anisotropy with a high Curie temperature, leading to promising perspectives for high-temperature catalysis reaction. This work is presently undertaken by Julien Marbaix (phD) and Sumeet Kale (engineer).*

### 3. Electronic transport measurements

The control of metallic NPs synthesis opens new routes regarding the bottom-up approach of electronic device fabrication. Indeed, individual NP can be foreseen as active or as interconnecting parts of the next generation of complex logic circuits while arrays of NPs can serve as highly sensitive sensors<sup>90</sup> or for future spintronic-based devices.<sup>91</sup> In both cases, electronic transport studies require the local deposition and the precise addressing of NPs. I will describe the different strategies we have been studying to control the NP deposition and will briefly overview the electronic properties measured in collaboration with the Nanomagnetism group at LPCNO and our colleagues from LNCMI.

#### a) Magnetotransport properties : modulation of the interparticle barrier

*Work initiated during my PhD and pursued after 2009 with Cécile Marcelot, Guillaume Viau, Julian Carrey, Reasmey Tan, Julien Dugay and Marc Respaud. These results were reported in (A8, A15, A24).*

Transport in arrays of metallic NPs is expected to be strongly dependent on the nature of the organic ligands surrounding the nanoparticles (Figure 35). Indeed these ligands act as a tunneling barrier for the electron, therefore their length, their nature and the presence of impurities, such as molecular compounds or paramagnetic species, can drastically affect the conduction property of the assembly through the modification of the barrier resistance  $R_T$ . For instance, a conduction driven by sequential

tunneling event is observed in presence of high barrier resistance while an efficient co-tunneling transport can be encountered for lower barriers, allowing the partial delocalization over a large number of particles.

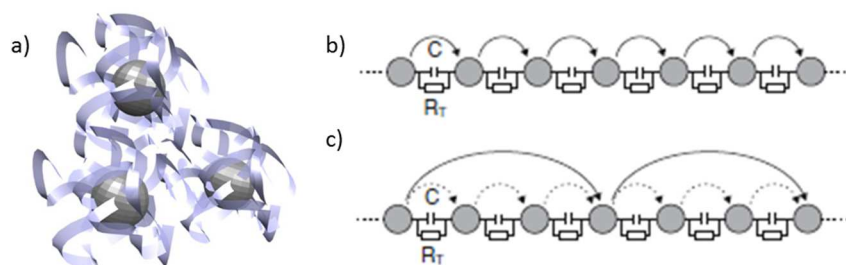


**Figure 35.** a) Schematic view of the chemically grown metallic NPs surrounded by organic surfactants. b-c) Simplified circuit diagrams of a 2D array of NPs (grey dots), having a charging energy  $E_C$  (related to the capacitance  $C$ ), separated by organic surfactants of resistance  $R_T$ . The conduction can occur through b) sequential or c) cooperative tunneling. Derived from reference<sup>92</sup>

The challenges from a chemical point of view consist in controlling the nature of the barrier and the charging energy of the metallic NPs, in order to optimize the conduction properties. The main issue concerns the controlled tailoring of these two parameters which are often intimately coupled.

- Self-assembled supercrystals of FeCo NPs : 3D assemblies

As previously described in section I.2, millimetric supercrystals of amorphous FeCo NPs can be prepared following the synthesis developed by Desvaux et al.<sup>19</sup> The self-assembly occurring at the mean time than the NP growth, the organic barrier can not be easily tuned. Two types of supercrystals can be obtained :

- A dense assembly of 13 nm NPs stabilized by a mixture of hexadecylamine and oleic acid
- A binary assembly of 16 and 27 nm NPs stabilized by a mixture of hexadecylamine, oleic and stearic acid.

In both cases, the supercrystals exhibit complex behaviors at low temperature ( $<10K$ ). A sharp transition between two conduction regimes (Coulomb blockade and conductive) was observed at 1.8K (Figure 36).<sup>A8</sup> The presence of paramagnetic species in the barrier was suspected to be responsible for such results. Theoretical calculations evidenced the possible presence of  $Co^{2+}$  ions. Therefore, we tried to characterize these species using advanced techniques (UV-visible and XPS spectroscopies, magnetic measurements at ultra low temperature). Despite intensive efforts, we could not conclude on the nature of these impurities.

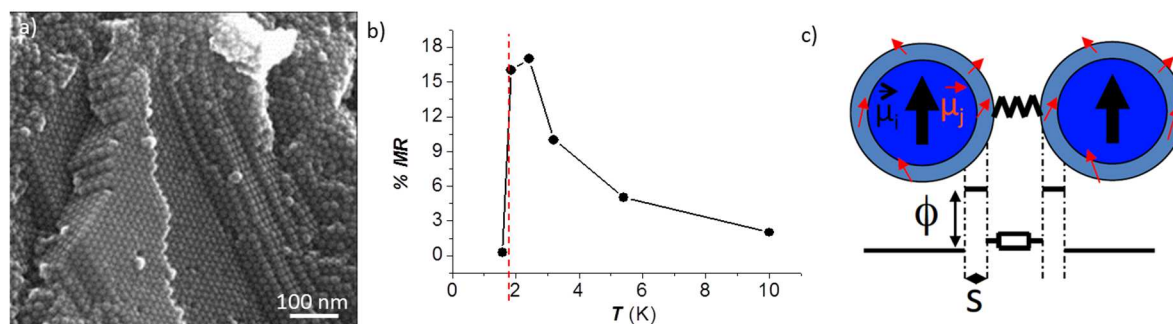


**Figure 36.** a) SEM image of self assembly of 13nm NPs, b) Thermal evolution of the magnetoresistance value and c) Schematic view of the complex tunnel barrier with paramagnetic species present either in the barrier or at the NP surface. Reprinted from reference<sup>93</sup>

To gain a better control of the nature and the length of the organic barrier present within the NP assembly, we progressively moved from the self-assembled supercrystals to controlled assemblies of model objects we could specifically triggered.

- 3D assemblies driven by dielectrophoresis

Dielectrophoresis technique consists in applying a non uniform alternating electric field onto a colloidal solution. Nanoparticles will be attracted by a driving force, the so-called dielectrophoretic force, towards the field gradient (Figure 37). Julien Dugay designed interdigitated Au electrodes with 5  $\mu\text{m}$  spacing. Controlled assembly of nanoparticles into dense arrays could be obtained after a careful optimization of the applied field frequency and strength, and after controlling the physicochemistry of the colloidal solution, by adapting the solvent (viscosity, melting point, evaporation rate) and the NPs concentration. These parameters are dependent of each type of NPs used, requiring a dedicated study.

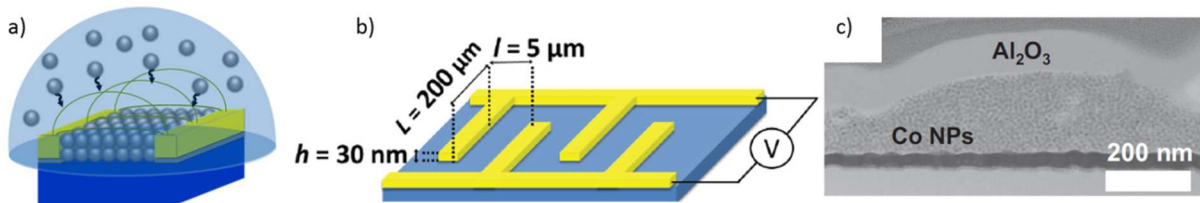


**Figure 37.** a) Schematic view of the dielectrophoresis process, b) dimensions of the Au electrode used and c) examples of dense assembly obtained with 10 nm Co NPs.

- Magnetotransport measurements in Fe and Co assemblies

The effect of the chemical nature of the organic barrier was investigated using Fe NPs as model systems. Fe NPs were carefully purified using classical washing procedure prior to their deposition by dielectrophoresis. For the first time, Tunnel MagnetoResistance (TMR) of few percent was detected at room temperature on these clean assemblies.<sup>A15</sup> Interestingly, similar properties were observed for NPs stabilized by ammonium chloride/amine or carboxylic acid/amine surfactants.

The complex low temperature effects observed on FeCo superlattices were no longer observed. The controlled incorporation of paramagnetic species, suspected to be responsible for such effect, was studied but did not lead to conclusive results so far.

Another key parameter of the organic barrier is its lateral extension. We studied the influence of the interparticle distance on the magnetotransport properties. Ligand exchange could not be satisfactorily made on Fe NPs, due to the strong anchoring of the carboxylate groups. In the framework of our fundamental study on NPs synthesis in pure oleylamine, we could prepare monodisperse Co NPs of 10 nm stabilized solely by amine groups. Thanks to the lability of these ligands we could proceed to a

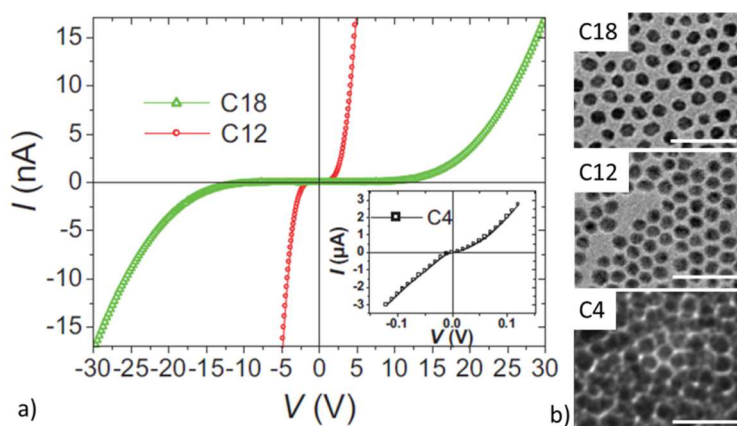


**Figure 37.** a)  $I(V)$  characteristics measured at  $T=2\text{K}$ , b) TEM images of Co NPs surrounded by the different amines.

ligand-exchange process to control the alkyl-chain length of the stabilizing amine, going from oleylamine (C18) to dodecylamine (C12) and butylamine (C4), without affecting the Co NP size. By this mean, the interparticle distance could be tuned from 4 to 2.4 and 0.5 nm, respectively (Figure 37).<sup>A24</sup>

A smaller tunnel barrier length leads to an increased cooperative coupling which is reflected by (i) a spreading of the delocalization length and thus by (ii) a higher conductivity of the assembly.

Magnetotransport studies on the chemically ordered FeCo NPs are currently made by Suhail Usmani (phD).

## b) Electronic properties of single nano-object

### • Pt tripod

Work performed with Bruno Camargo and Benjamin Lassagne, in collaboration with Walter Escoffier (LNCMI Toulouse). These results have been recently published in A44.

Among the different Pt particles we could obtain, planar tripods, whose 3D shape was partly revealed by electron tomography (Figure 38a-c), were of particular interest for electronic transport measurements. Indeed these objects combine a flat surface, allowing the deposition of contact electrodes, and a highly crystalline structure (Figure 38d-e), which is mandatory for a good electronic conduction.

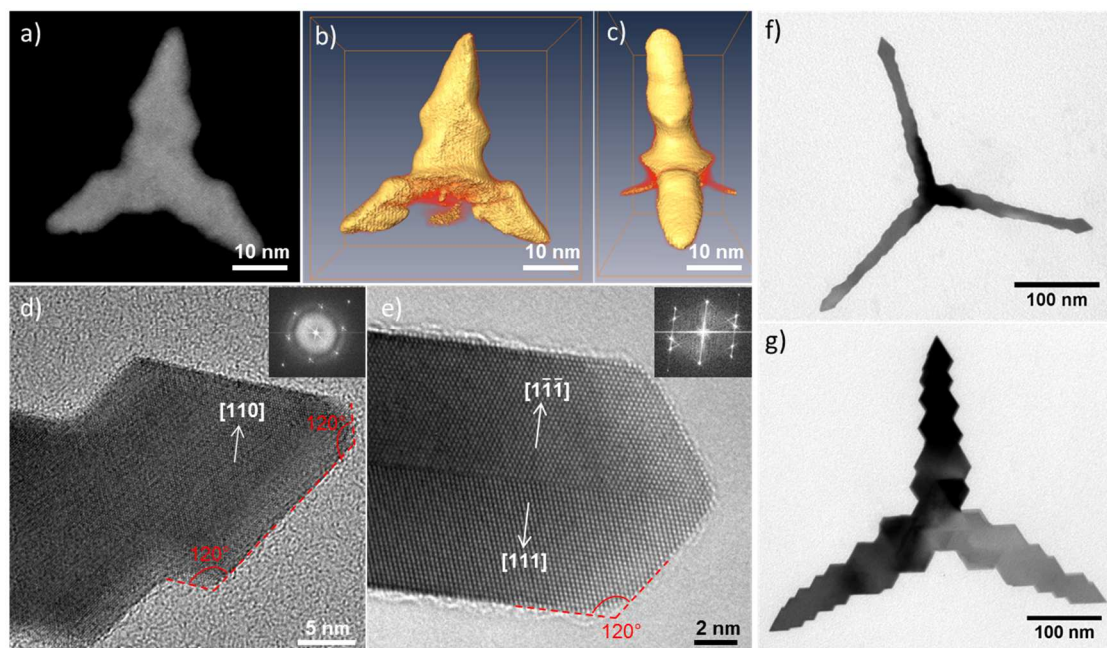


**Figure 38.** a) HAADF-STEM image of planar tripods and b-c) the corresponding 3D reconstruction obtained by electron tomography. HRTEM image of thick Pt tripod arm from d) a top-view and e) a lateral view. The twinning plane is clearly visible. Inset : corresponding FFT images. TEM images of f) thin and g) thick Pt stars

The dimension of the tripods (thickness, arm length and width) could be tuned by adjusting the precursor reactivity. The direct decomposition of the platinum salt ( $\text{H}_2\text{PtCl}_6$ ) led to thin nanostars, exhibiting arms of typical dimensions of 100 nm x 7 nm x 7 nm (length x width x height, Figure 38f). On the contrary, starting from an intermediate Pt-oleylamine complex, thick nanostars were obtained (250 nm x 60 nm x 16 nm, Figure 38g). In both cases the nanostars were composed by two perfect crystals grown symmetrically aside a twinning boundary (Figure 38e).

The chemical synthesis allowed a fine control of the size and the shape of the stars but comes along with the use of organic ligands. In the case of Pt stars, their surface is decorated with oleylamine, and the derived oleylammonium chloride. As previously shown on Co nanoparticles, oleylamine can act as an efficient tunnel barrier. In the case of single object connection we aim at measuring the intrinsic electronic properties of the object without suffering from any important contact resistance. Therefore, an important effort was devoted to the removal of the surfactant prior to the connection.

We first used standard liquid-phase cleaning procedure, consisting in successive precipitation and redispersion steps. The stars were then drop-casted on the  $\text{SiO}_2$ -Si substrate of interest and further exposed to an oxygen plasma treatment. The evolution of the organic content at the star surface was followed using IR spectroscopy in Attenuated Total Reflectance (ATR) configuration, guiding the optimization of the plasma conditions.

Isolated stars were then electrically contacted using standard electron nanolithography techniques (Figure 39a). The contacts exhibit classical ohmic behavior, confirming the removal of the organic barrier. The electrical resistivity of the stars was only one order of magnitude larger than in bulk Pt,

revealing the high purity and high crystallinity of these chemically-grown objects. Interestingly, these objects can withstand very high current densities ( $200 \text{ MA/cm}^2$ ) opening potentiality for power electronics. Moreover, thanks to their reduced sizes, the stars thermalized very efficiently allowing the observation of non-linear effects such as frequency multiplication (Figure 39b).

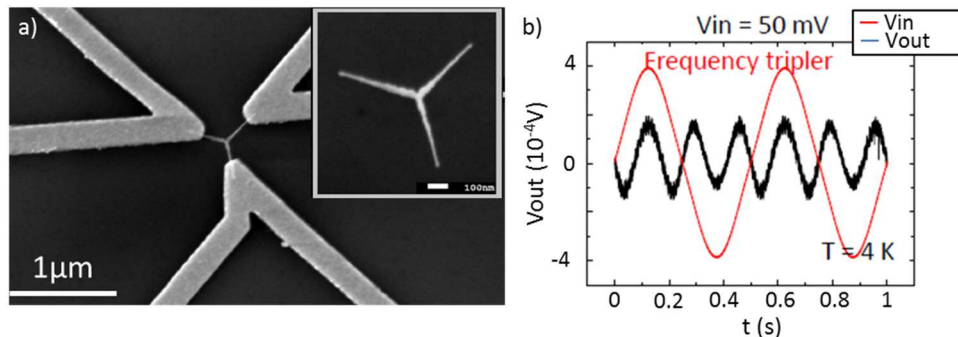


**Figure 39.** a) SEM image of a connected thin Pt nanostar. As inset, the same star before the connection. b) HAADF-STEM image of planar tripods and b-c) the corresponding 3D reconstruction obtained by electron tomography. HRTEM image of thick Pt tripod arm from d) a top-view and e) a lateral view. The twinning plane is clearly visible. Inset : corresponding FFT images. TEM images of f) thin and g) thick Pt stars

- Towards individual Au NW

Work performed with Anaïs Loubat, Said El Nouh, Pierre Moutet, Laurianne Teulon, Laurence Ressler, Etienne Palteau and Guillaume Viau, in collaboration with Bertrand Raquet and Walter Escoffier (LNCMI Toulouse). Results published in A20 and A31.

Our work on the synthesis of ultrathin Au nanowires was motivated by their unique electronic transport properties. Indeed, thanks to their sub-nanometric radius, such wires are likely to display quasi one-dimensional (1D) confinement effects such as non Fermi liquid behavior.<sup>94,95</sup>

A first study was performed on Au nanowires deposited by drop-casted. Solely bundles of few tens of wires could be localized by extensive Atomic Force Microscopy characterizations. Scanning Electron Microscopy, which would have been a much faster mapping technique, was discarded due to the extreme fragility of the wires which tend to brake under the electron beam. The micrometric length of the wires allowed us to use conventional nanolithography technique to connect the bundles (Figure 40a). However, despite the optimization of the process parameters, the wires suffered from the Rayleigh instability and tend to break into shorter rods of  $\sim 100 \text{ nm}$ . A co-tunnelling regime, characteristic of collective effect, was unravelled by low temperature and high magnetic field measurements (Figure 40b).<sup>A20</sup>

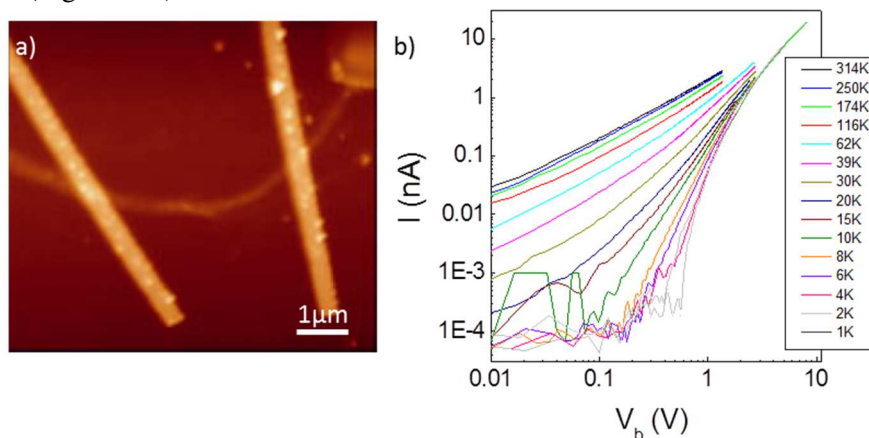


**Figure 40.** a) AFM image of a 20-nm height bundle of Au nanowires after the deposition of Ti/Au electrodes and the corresponding b) Current-Voltage characteristics measured for selected temperatures

To go beyond these measurements and demonstrate experimentally the expected correlations between the high aspect ratio of the nanowires and their conduction properties, the addressing of undamaged individual NW is mandatory. In this aim, highly challenging technological steps must be overcome namely on

- i) the deposition and localisation of individual NWs on pre-defined areas of surface and
- ii) their electrical addressing using stencil as an alternative soft nanopatterning approach.

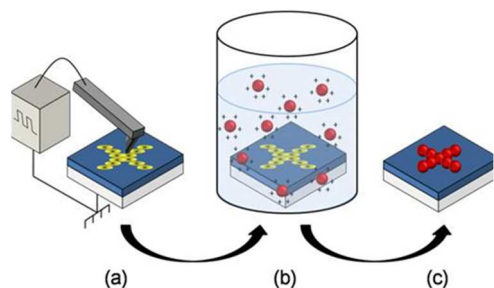


**Figure 41.** Schematic view of the nanoxerography process

Our efforts have mainly focused on the first step of deposition and localization. At LPCNO the Nanotech group developed a nanoscale adaptation of the industrial xerography process used in laser printing. It uses the strong electric fields generated by charge patterns written by atomic force microscopy (AFM) into electret thin films to trap charged and/or polarizable colloidal nano-objects via electrostatic interactions (Coulomb forces and dielectrophoretic forces) at known locations on a substrate (Figure 41).<sup>96,97</sup>

The challenge consisted in adapting the surface chemistry of the nanowires to the nanoxerography requirements. Any surfactant present in excess could be trapped on the charged patterns, resulting in the fading of the electrostatic interactions. Moreover, the use of a highly concentrated solution leads to unspecific deposition onto the substrate and the potential pre-aggregation of the particles in solution. Therefore, important efforts were dedicated to the optimization of the colloidal solution used for nanoxerography experiments.

The wires, initially coated by a bilayer of oleylamine and oleylammonium chloride, were precipitated out from the reaction solution by centrifugation in presence of absolute ethanol. After redispersion in pure hexane, the wires tend to self-assemble into a hexagonal phase exhibiting a much smaller lattice parameter, thus evidencing the presence of a single layer of surfactant at the nanowire surface (Figure 42). XPS analysis confirmed the presence of oleylammonium chloride at the surface of the nanowire.

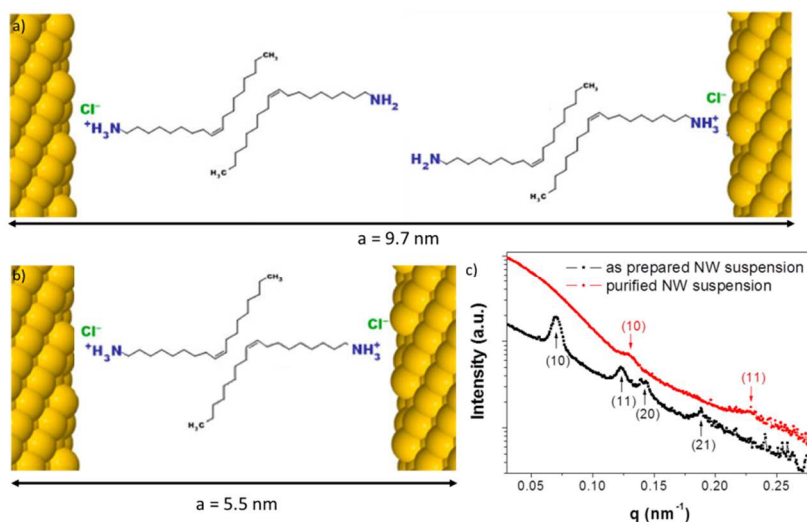


**Figure 42.** Schematic view of the surfactant at the Au nanowire surface a) after synthesis and b) after purification. c) SAXS data of the hexagonal phase formed in solution of as-grown (black) and purified (red) gold nanowires. The peak positions in the reciprocal space relative to the position of the first peak are  $1:\sqrt{3}:\sqrt{4}:\sqrt{7}$  for the as-grown and  $1:\sqrt{3}$  for the purified nanowires.

To prevent the formation of these hexagonal self-assemblies, which are detrimental to the deposition of single nanowires, a drastic dilution of the purified solution was applied, going from a gold concentration of 10 mM down to 20  $\mu$ M.

Interestingly, the diluted solution which contains two nanoparticle populations (the Au wires of interest along with the Au nanospheres that are concomitantly grown, as described in section I.3) shows an impressive shape sorting by nanoxerography. Indeed, Au nanospheres tend to mostly assemble onto negatively charged patterns while the Au nanowires only assembled onto the positively charged patterns (Figure 43a).<sup>A31</sup>

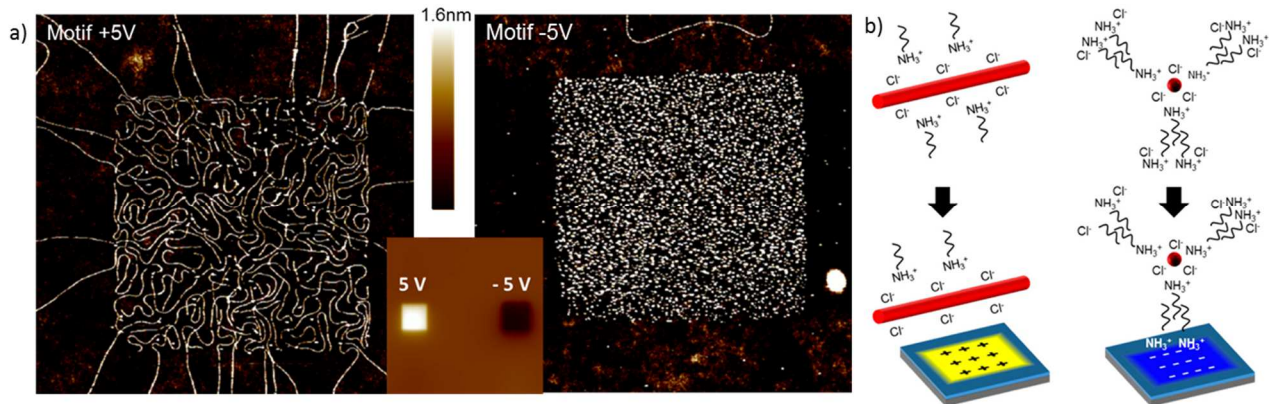


**Figure 43.** a) AFM topographical images of the directed assembly of gold nanowires and nanospheres by AFM nanoxerography on charge patterns of opposite polarities (+/-5V). As inset : Kelvin Force Microscopy image of the two 3 $\mu$ m charged squares of opposite polarities written on a PMMA film. b) Schematic view of the surface stabilization of gold nanowires and nanospheres, far from the charge patterns and near them.

These unexpected results revealed that the Au objects exhibit:

- a negative effective charge for the wires, leading to a specific adsorption onto the positive pattern due to electrostatic forces,
- a slightly positive effective charge for the spheres, leading to a preferential but not selective adsorption on the negative pattern.

Hexane being an apolar solvent, the presence of charged particles is fairly unlikely. The observed effective charges may result from the strong electric field induced by the charged patterns. We believe that the repartitions of chloride anions and oleylammonium are drastically modified by the presence of charge patterns, resulting in effective charges (Figure 43b).

By optimizing the positive pattern design, the controlled deposition of Au nanowires could be tuned from coiling structures to straight alignments down to the controlled deposition of single nanowire deposition (Figure 44).

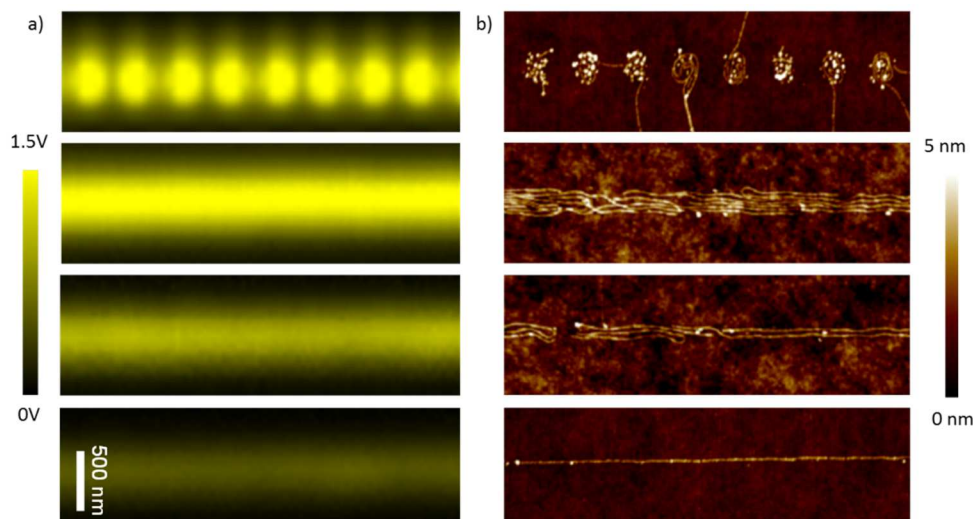


**Figure 44.** a) KFM images of positive patterns and b) the corresponding AFM image after directed assembly.

Connection experiments couldn't be tried so far due the breaking of the wires ~48h after directed assembly. Surface modification is currently studied to expand the wire stability up to a week. This time scale is mandatory to allow the connection by stencil approach and the electronic transport measurements.

### III. Controlled assembly and integration of nanostructured materials : towards applications

In the past 3 years I started to work on the preparation of nanostructured materials starting from the colloidal solution we synthesized. This final step is indeed mandatory for several applications, among which the integration of nanoparticles onto microelectronic devices and the preparation of rare-earth free magnets. Important efforts were devoted to the optimization of the physico-chemical properties of the starting solution to keep the integrity of the nanoparticles in the metamaterial while promoting a high volume fraction, and thus optimized properties.

#### 1. FeCo NPs for RF filters

Work performed with Cyril Garnero, Mathieu Lepasant and Bruno Chaudret, in collaboration with Pierre Fau (LCC, Toulouse), Benjamin Bardet and Gaël Gautier (GREMAN, Tours) and Patrick Poveda (ST, Tours). Two manuscripts are in preparation.

The needs in telecommunications have considerably increased in the past decade, requiring high performance, low power consumption and low cost radiofrequency circuits to support the huge expansion of local exchanges such as video on demand, interconnections with mobile phone applications or shared storage. Among the different passive components present in these circuits, integrated planar inductors plays a key role to properly filter the signal of interest while rejecting the surrounding electromagnetic noise up to the GHz, which is the range of frequency commonly used for cellular phone networks worldwide.

The efficiency of these inductors, evaluated by the value of their inductance, should be constantly increased. However, geometrical features, such as number of spires and diameter of the wires, can no longer be improved without leading to larger inductors. Thus, alternatives are actively sought, the most promising one consisting in improving the environment permeability by embedding the inductors in a soft ferromagnetic material.<sup>98</sup>

An alternative to the thin films commonly used consisted in preparing composite materials composed of optimized magnetic nanoparticles embedded in an insulating matrix. Working with an industrial partner on commercial inductors, we developed two complementary strategies to improve the environment permeability (Figure 45) :

- the filling of porous Si located underneath the inductor, in collaboration with the Greman laboratory.
- The preparation of a composite material further reported on-top of the inductor

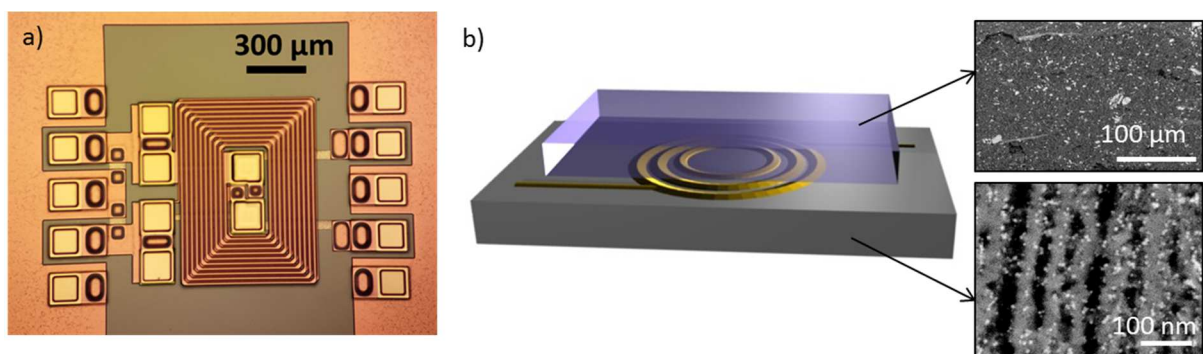


**Figure 45.** a) Optical microscope image of one of the commercial inductor used. b) Schematic view of the integration strategy chosen. As insets : SEM images of filled porous Si (bottom) and composite epoxy resin (top).

FeCo nanoparticles have been chosen for preparing the two metamaterials due to their high saturation magnetization and their low magnetic anisotropy, which are key parameters for radio frequency (RF)-applications. However, the as-prepared particles are highly sensitive to air and prone to oxidize, decreasing drastically their magnetic properties.

### a) Impregnation into porous Si

Porous silicon has recently opened great perspectives for biomedical applications, thanks to its large surface area and biodegradability, and for the microelectronic industry thanks to its excellent isolating properties. Mesoporous Si was prepared by the Greman laboratory and exhibit pores of mean dimension  $25\text{ nm} \times 18\text{ }\mu\text{m}$  (diameter  $\times$  thickness).

Direct synthesis of FeCo nanoparticles within the pores led to relatively small NPs with poor magnetic properties, therefore an impregnation technique was preferred, using preformed 9nm FeCo nanocubes. These nanocubes are highly dispersible in organic solvent, allowing the preparation of stable colloidal solution. Moreover, they exhibit a hydrodynamic diameter of 15 nm, smaller than the mean pore size.

The impregnation technique could be optimized to reach a filling of  $\sim 15\%$  vol. of FeCo NPs. Remarkably, the filling was effective along the whole pore thickness, FeCo NPs being detected at the extreme bottom of the  $18\text{ }\mu\text{m}$  thick mesoporous Si (Figure 46).

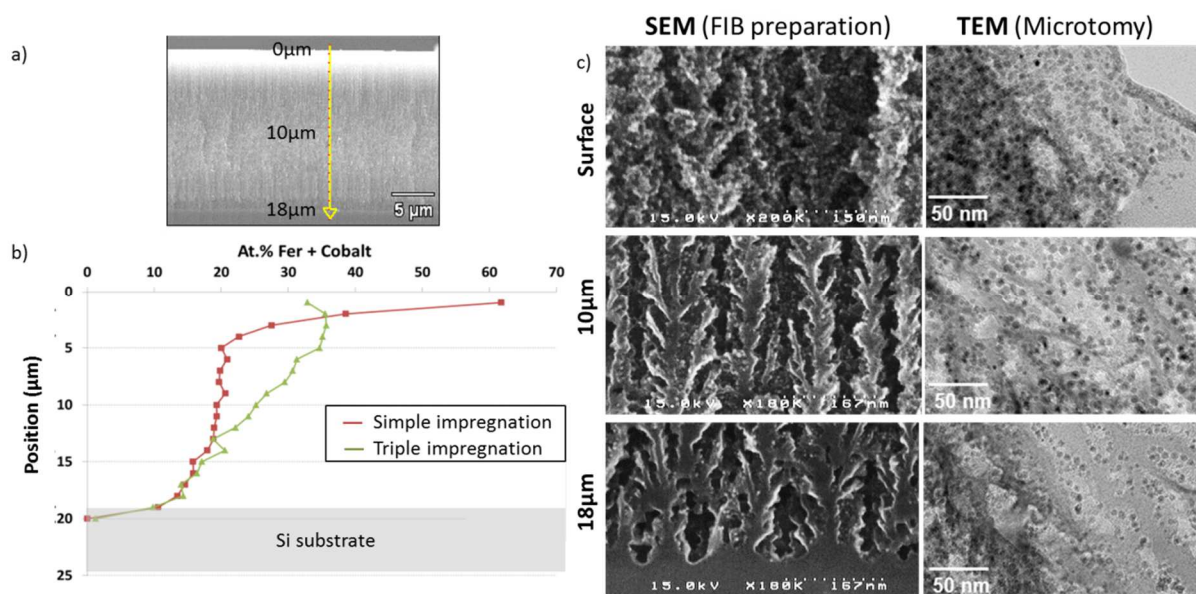


**Figure 46.** a) SEM image of the filled mesoporous Si. b) Evolution of the FeCo atomic content, determined by EDX, as a function of the depth. The position of each EDX spectrum is highlighted on the yellow arrow in a). c) SEM (left column) and TEM (right column) images of the filled pores at the extreme surface (upper row), at a  $10\text{ }\mu\text{m}$  depth (middle row) and at the pores' bottom (bottom row). FeCo NPs can be seen as bright dots on SEM images and dark dots on TEM ones.

### b) Immersion into an epoxy resin

Magnetic composite was prepared by dispersing FeCo nanoparticles into an epoxy resin, already used by our industrial partner. To maximize the magnetic properties of the composite a high metallic loading was mandatory, therefore we focused our investigation on the 12 nm FeCo NPs, which exhibit a high metal content ( $>80\%$  in weight).

Self-supported pellets could be prepared following a simple protocol (Figure 47a-b) with a metal loading varying from 10 to 70% (Figure 47c-f). The nanoparticles are well dispersed along the whole thickness of the pellet and only few aggregates, already observed in the FeCo solution, are observed.

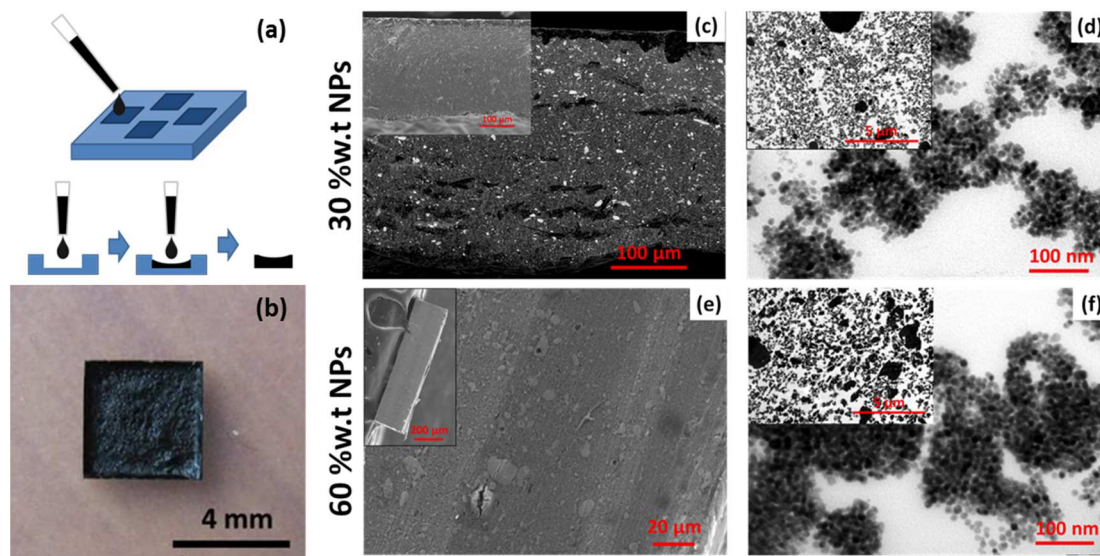


**Figure 47.** a) Schematic view of the pellet preparation and b) the corresponding image. c,e) SEM cross-view image on the pellet thickness and the corresponding d,f) TEM images on pellet'slices prepared by microtomy for c-d)30% and e-f) 60% loaded nanocomposite.

Submillimetric FeCo/epoxy composites have been prepared using a dicing saw and were further reported onto commercial inductors thanks to a pick-and-place approach. Improvements of 18% and 27% were obtained for nanocomposites exhibiting a 30% and a 60% loading respectively (Figure 48).

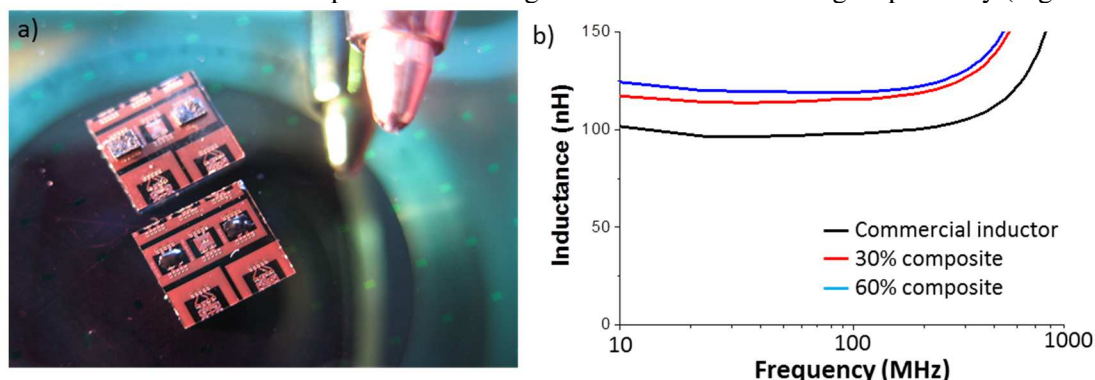


**Figure 48.** a) Image of 30% loaded FeCo/epoxy nanocomposites deposited on commercial inductors by the pick and place approach (upper chip) and by a direct integration using drop casting technique (lower chip). b) evolution of the inductance as a function of the applied current frequency for the commercial inductor as-received (black) and after integration of 30% (red) and 60%-loaded (blue) nanocomposite.

Motivated by the promising results obtained through the pick-and-place approach, preliminary attempts of direct integration of the nanocomposite onto commercial inductor were conducted. Submillimeter deposit of FeCo NPs could be made by simple drop casting of a suspension through a  $400\mu\text{m}\times 400\mu\text{m}$  pitch in a thick PDMS stamp prepared by laser cutting. Some conformity issues were encountered at the edges of the deposit due to the PDMS swelling in presence of the organic solvent used (tetrahydrofurane) and capillary effects.

*Alternative molds are under consideration for local deposition. Functionalization of the mesoporous Si will be tested.*

## 2. Dense assemblies of Co NRs as rare-earth free permanent magnets

Work performed with Evangelia Anagonostopoulou, Marc Pousthomis and Guillaume Viau, in collaboration with Frederic Ott (LLB, Saclay), Semih Ener and Oliver Gutfleisch (TU Darmstadt) in the framework of the European FP7 project Refrepermag. These results have been reported in 5 publications (A29, A32, A34, A42, NA3), 1 book chapter (Ch2), 1 manuscript on consolidation has been submitted.

The increasing demand of permanent magnets and the dependence towards China for the rare earths (RE) supply incite important efforts worldwide to develop next generation magnets requiring either fewer quantities of RE or even to imagine new technologies based on RE free magnets. These new magnets should exhibit an energy product,<sup>100</sup> the so-called  $(BH)_{\max}$ , ranging from  $100 \text{ kJ/m}^3$  to  $200 \text{ kJ/m}^3$ ,<sup>101</sup> intermediate between ferrites ( $< 38 \text{ kJ/m}^3$ ) and rare-earth based magnets ( $>250 \text{ kJ/m}^3$ ) properties.<sup>102</sup>

Single-crystalline Co nanorods (NRs) have been suggested as promising candidates for such alternative RE-free magnets. The great advantage of Co NRs in the field of hard magnetic material is the possibility to add magnetocrystalline and shape anisotropy, providing that the c-axis of their hcp structure is parallel to their long axis (Figure 49), leading to a theoretical intrinsic coercivity  $\mu_0 H_c = 1.6 \text{ T}$  for isolated NR, while experimental values higher than 1T were recently obtained.<sup>103</sup>

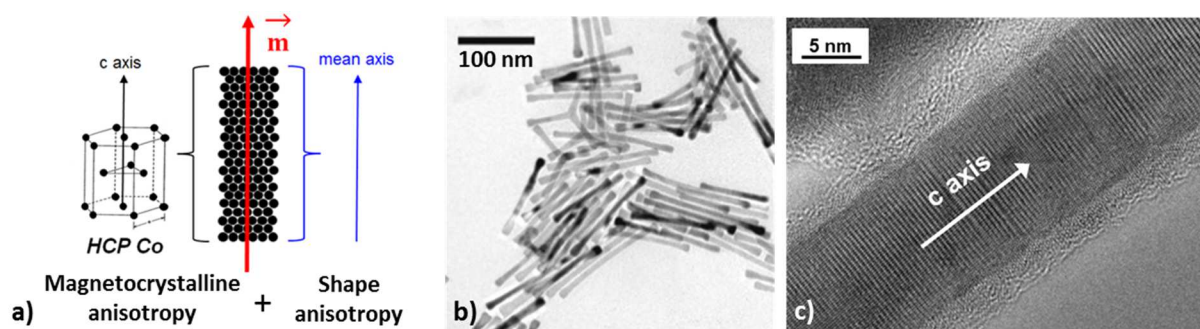
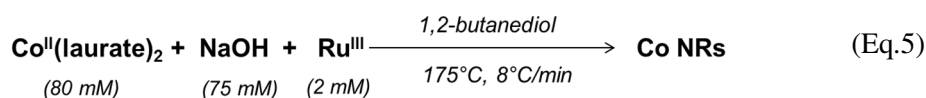


**Figure 49.** a) Schematic representation of a cobalt rod with the c-axis of the hcp structure and the long axis aligned. The vector  $m$  represents the particle magnetization. b) Transmission Electron Microscopy (TEM) image of Co NRs prepared by the polyol process and c) the corresponding High-Resolution TEM (HRTEM) image. The white arrow indicates the c axis of the hcp structure (reprinted from [104]).

Such single-crystalline Co nanorods with high coercivity can be synthesized by the polyol process<sup>103,104</sup> and organometallic chemistry.<sup>105,106</sup> The controlled alignment and compaction of such Co nanorods could theoretically leads to impressive  $(BH)_{\max}$ , (above  $200 \text{ kJ.m}^{-3}$ ), far above the AlNiCo magnets, at the conditions that<sup>107,108</sup> :

- the constitutive Co NRs exhibit high intrinsic coercivity ( $H_c$ ),
- a highly parallel orientation of the rods (misalignment angle  $< 5^\circ$ ),
- a high magnetic volume fraction, *i.e.* packing fraction ( $V_M > 50\%$ ).

We recently demonstrated experimentally the feasibility to elaborate rare-earth free permanent magnets based on cobalt nanorods assemblies with high strength (Figure 50).<sup>A34</sup> Highly crystalline Co NRs exhibiting the hexagonal close pack structure were prepared using the polyol process.<sup>104,109,A29</sup> A cobalt precursor ( $\text{Co(laurate)}_2$ ) is reduced in a basic solution of 1,2-butanediol in presence of a nucleating agent ( $\text{Ru}^{\text{III}}$  salt) (Eq. 5).



We recently succeeded in up-scaling, at the laboratory level, this polyol process, obtaining 5g of well-defined Co NRs in one batch (Figure 50a).<sup>A34</sup> The Co NR aspect ratio (AR), defined as the ratio between the diameter ( $d=8\text{-}40 \text{ nm}$ ) and the length ( $l= 50\text{-}400\text{nm}$ ), could be tuned from 6 to 18 by adjusting the experimental parameters. The intrinsic coercivity being dependent on the exact shape of

the rods,  $^{110, \text{Ch}2}$  values ranging between  $\mu_0 H_c = 0.3$  and  $0.5$  T could be obtained. Their saturation magnetization were evaluated at  $110\text{-}120 \text{ emu/g}_{\text{powder}}$ .

Co NRs could be aligned under external magnetic field, forming centimeter wafers (Figure 50b). Even though no polymer was added to the Co NRs, the wafers obtained exhibit impressive robustness and flexibility, due to strong Van der Waals interaction between the Co NRs. Indeed, dense assemblies were obtained, characterized by important magnetic volume fraction ( $V_M = 0.4 - 0.55$ ) and very small inter-rod distance as confirmed by Scanning electron microscopy (SEM, Figure 50e). Microscopic needles, with submillimeter dimensions (thickness and width  $\sim 100\mu\text{m}$ ), can be separated from these wafers (Figure 50c). They exhibit smooth surfaces without any cracks (Figure 50d) and consist in dense alignments of parallel nanorods along the field direction (Figure 50e).

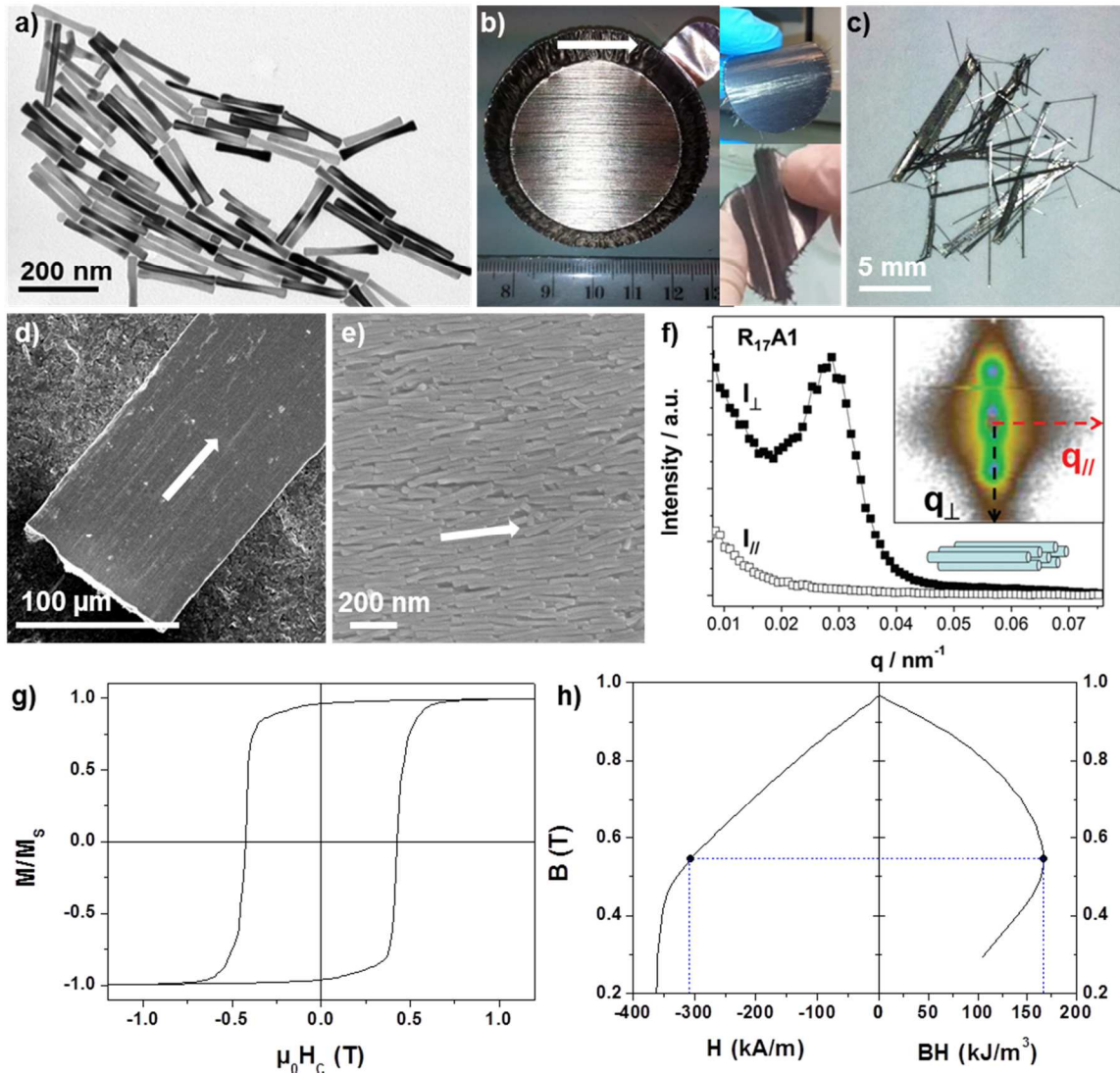


**Figure 50.** a) TEM image of the Co NRs prepared by polyol. Image of b) the nanocomposite magnet aligned in an Al mold by controlled evaporation of a Co suspension under a 1T external magnetic field. Inset shows the 4cm aligned wafer obtained, which exhibits robustness and flexibility. c) Magnetic needles separated from b. d-e) SEM images of the micrometric needle evidencing the Co NRs alignment. f) Small angle neutron intensity profile scattered by Co assemblies, perpendicular (black square) and parallel (open square) to the rod alignment. Inset: corresponding 2D SANS pattern; g) Magnetization loop recorded at 300K, exhibiting a squareness (SQ) of 0.86. h) Second quadrant of an optimized induction loop and the corresponding energy product (BH). Blue point represents the optimized working point, corresponding to a  $(BH)_{\text{max}}$  of  $160 \text{ kJ.m}^{-3}$ . White arrow in b, d) and e) represent the direction of the external magnetic field applied.

The assessment of the magnetic volume fraction allowed extrapolating the induction loop from vibrating sample magnetometry measurements (VSM, Figure 50g) and thus, determining the energy product of these nanostructured alignments (Figure 50h).

$(BH)_{\max}$  ranging from 120 to 165  $\text{kJ}\cdot\text{m}^{-3}$  have been obtained thanks to :

- an impressive alignment of the constitutive Co NRs, as revealed by the very anisotropic Small Angle Neutron Scattering pattern (SANS, Figure 50f) and by the squared hysteresis loops (Figure 50g), characterized by a high squareness (SQ).<sup>A34</sup>
- a high magnetic volume fraction ( $V_M = 0.4 - 0.55$ )

To go further and prepare macroscopic RE-free magnets, consolidation techniques were used in collaboration with S. Ener and O. Gutfleisch (Technical University of Darmstadt). The densification of the cobalt NRs assemblies into a cohesive structure were carried out in absence of any polymer matrix to prevent from a dilution of the active magnetic volume. Images of consolidated Co nanorods with different shapes and obtained by different compaction methods are shown in Figure 51a. As it can clearly be seen from the images, the compacted materials maintain their integrity even after shaping. The ligand layers remaining at the nanorods surface are responsible for the good cohesion of the consolidated materials. Moreover, these surfactants prevent from the rod coalescence during the consolidation steps.

The magnetic volume fraction and the density of the consolidated materials are consistent with a compact microstructure without internal porosity. Magnetic measurement, small angle neutron scattering (SANS) and X-ray diffraction allowed characterizing the rod alignment within the consolidated materials. The best condition to reach a high volume fraction and to preserve the quality of the alignment was the cold compaction under 1 GPa, hot compaction and Spark-plasma sintering (SPS) leading to the rod coalescence.

The magnetic measurement of the resulting bulk consolidated material, shows energy products of 65  $\text{kJ}\cdot\text{m}^{-3}$  (Figure 51b) which can fill the “gap” between the hexaferrites and rare-earth-transition-metal based magnets.

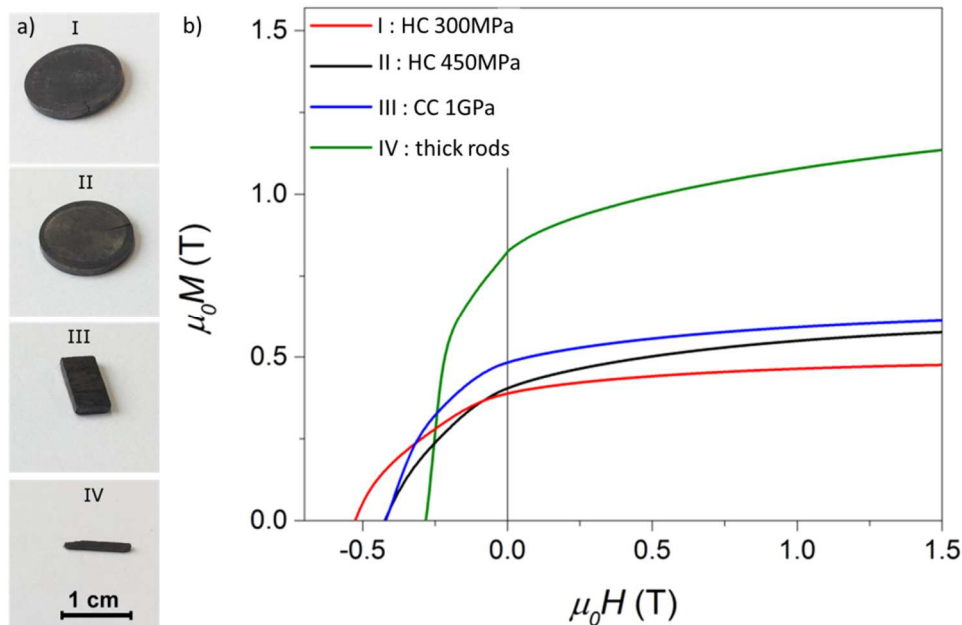


**Figure 51.** a) Images of consolidated Co nanowires in different shapes. Thin nanorods exhibiting a mean diameter of 10.9 nm were compacted at 300 MPa, 180°C (I) ; 450 MPa, 180°C (II) and 1GPa, RT (III). Larger rods (mean diameter of 28.3 nm) were compacted at 450 MPa, 180°C (IV). b) The corresponding demagnetization curves measured at room temperature. HC = hot compaction, CC = cold compaction

Further energy product improvements are expected by reducing the native CoO oxide shell and the surfactant layer present at the Co NRs surface, while maintaining a high coercivity. Therefore we are currently working on the synthesis of non-oxidized thin rods and their further controlled assemblies.

#### IV. Research Project: Submillimetric magnets made of nanoparticles for portable magnetic devices

The expanding market of integrated sensors/actuators in sectors as diverse as the automotive, aerospace or biomedical sectors, requires miniaturized power supplies. The magnetic flux density available being independent from the size, permanent magnets (PM) represent the most attractive choice for such integrated power sources,<sup>111</sup> and would benefit to numerous applications<sup>11</sup> based on Micro-ElectroMechanical Systems (MEMS), such as actuators,<sup>112,113</sup> relays,<sup>114</sup> magnetic sensors,<sup>115,116</sup> micromachines,<sup>117</sup> viscosity sensors<sup>118,119</sup> or biosensors.<sup>120,121</sup> In addition, the unprecedented increase of telecommunications needs leads to very high-speed optical communications on long distance networks as well as within urban infrastructures. All these networks require cheap, efficient and highly integrated systems. In the millions of packages yearly installed, optical isolators, which prevent backward signals from propagating and thus affecting the laser source operation, are discrete magneto-optical materials, which require expensive alignment techniques as well as the application of an external magnetic field, generally provided by external macroscopic rare-earth (RE) based PM.

A major technological challenge therefore consists in providing submillimeter PM with high remanent induction and controlled orientation to address the massive demand for MEMS and optoelectronic components. All these integrated systems share multistep technological processes mastered by semiconducting manufacturers such as implantation, annealing, metallization and reactive etching. To be fully implementable, the PM integration should take place at the very end of the process without altering the complex architecture of the device. This is why high temperature annealing and harsh chemicals must be avoided. Having in mind these technological constraints, we will first present the basics of the physics involved in PM to propose a viable integration solution.

##### 1. State of the art

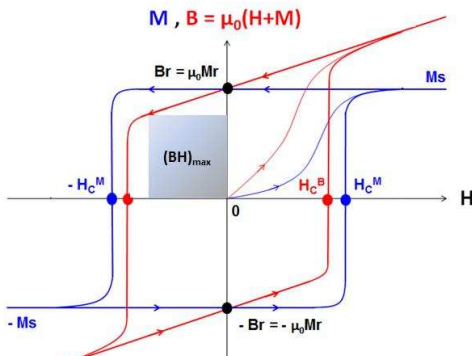


**Figure 52.** Magnetization (in blue) and induction (in red) hysteresis cycle. Grey square :  $(BH)_{max}$

An efficient permanent magnet consists in a material which returns its stored energy, the so-called energy product  $(BH)_{max}$ , under the form of stray fields. This energy product can be, in a first approximation, extrapolated from magnetometry measurements as the maximum area enclosed in the second quadrant of the induction  $(B(H))$  loop (gray square in Figure 52) which directly depends on the remanent induction  $(B_r)$  and the coercivity. Its value is however often reduced compared to the theoretical limit  $(BH)_{MAX} = \mu_0 M_S^2 / 4$  (Eq.6),<sup>20</sup> where  $M_S$  represent the saturation magnetization. Though not directly appearing in Eq.6,  $H_C$  is indeed crucial to fully benefit from the magnetization and prevent any irreversible demagnetization. Coercivity is an extrinsic parameter which depends on the material's size, shape and anisotropy  $(K)$ .<sup>20</sup>

Size reduction stabilizes the single domain configuration in which all spins align along magnetic easy axis direction, imposed by  $K$ . Coercivity raises from 0, for small superparamagnetic NPs, to the maximum value of  $H_c = 2K/M_S$  (Eq. 7) for ferromagnetic NPs close to the single-domain limit (Figure 53).<sup>122,123</sup> This critical size varies between a few tens to a few hundreds of nanometers, depending on the material.<sup>4</sup>

Anisotropy, which should be as large as possible for PM, arises from several contributions, among which the magnetocrystalline anisotropy  $(K_{mc})$ , inherent to the material structure, and the shape contribution  $(K_{sh})$ , which can be increased by favouring rod like particles.

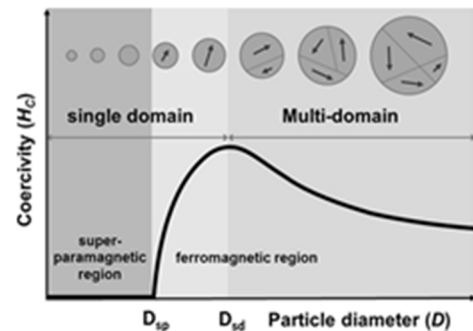


**Figure 53.**  $H_c$  evolution with particle size.  $D_{sp}$  and  $D_{sd}$  : superparamagnetism and single-domain diameter.

Commercially available processed magnets are inherently nanostructured materials, benefiting from the size reduction effect, and are usually prepared following classical metallurgy processes. The sub-micron powders obtained by milling are compacted and magnetically aligned through a high temperature annealing process.

Difficulties are encountered when one wants to reduce the size of the final magnet, due to process incompatibilities. Fully compatible alternative approaches have already been intensively sought. Top-down approaches using sputtering deposition could lead to relatively thick magnetic films, patterned through microelectronics processes<sup>1</sup>, or laser induced thermopatterning,<sup>2,3</sup> but cannot generate a sufficient magnetic flux outside their volume due to their limited thickness.

The bottom-up approach, which consists in assembling single-domain nanoparticles into dense materials,<sup>4,Ch2</sup> is an alternative of primary choice for integrated PM providing that the nanoparticles (NPs) building blocks exhibit a sufficient coercivity.<sup>5</sup> Recently, patterning of magnetic polymers by inkjet,<sup>6</sup> imprinting<sup>7</sup> or photolithography,<sup>8</sup> or electroplating through masks<sup>9,10</sup> have been investigated to design integrated magnets compatible with microelectronic processes.<sup>11</sup> These approaches suffer from a low magnetic fraction, which drastically reduce  $M_S$ , as well as fairly soft magnetic constituents, with low  $K$ .

Thus, one approach to solve the problem of performant integrated PM consists in synthesizing optimized building blocks, assembling them into dense metamaterials through a generic deposition technique. In this respect several fundamental questions must be answered :

- What are the materials of choice for the building blocks?
- How can NPs be chemically synthesized and exhibit the targeted crystallographic phase?
- How can magnetic properties be enhanced by cooperative effects?
- Can the self-assembly of ferromagnetic NPs be controlled?

#### a) Hard magnetic phases

In table 1 are given all the candidates exhibiting a hard magnetic phase. From a magnetic point of view, RE-based alloys are by far the best materials thanks to their high  $M_S$  and  $K$ . However, they suffer from geopolitical, environmental and processing issues, prohibiting their use for integrated PM. Platinum's cost and rarity, combined with the necessary annealing required for reaching the targeted  $L1_0$  phase, discarded Pt-based alloys despite intensive researches. Ferrites, which are widely used, exhibit fairly poor performances. Fe-<sup>101</sup> and Mn-

based alloys<sup>124</sup> have grown as promising phases thanks to their intermediates properties between RE and ferrites. However, a real challenge consists in stabilizing the proper phase, any deviation leading to a drastic decrease of the properties (Figure 54).

For instance, the martensitic  $\alpha''$ -Fe<sub>16</sub>N<sub>2</sub> phase is metastable and can only be partially stabilized at low temperature under strain, yielding limited coercivity.<sup>125</sup> Regarding Mn-based alloys, the bulk phase diagrams are very complex, with up to 11 different phases being observed for MnGe alloys.<sup>126</sup> The  $D0_{22}$  structure of the Mn<sub>3</sub>Ge Heusler, intensively sought for its ferromagnetic

Material	Crystallographic phase	$K_{mc}$ (MJ.m <sup>-3</sup> )	$M_S$ (MA.m <sup>-1</sup> )
Nd <sub>2</sub> Fe <sub>14</sub> B	P4 <sub>2</sub> tetragonal	4.9	1.28
SmCo <sub>5</sub>	D2 <sub>d</sub> hexagonal	17.2	0.85
PtFe	L1 <sub>0</sub> tetragonal	6.6	1.14
Co	hcp	0.41	1.41
MnAl	L1 <sub>0</sub> tetragonal	1.7	0.6
MnBi	B8 <sub>1</sub> -Hexagonal	0.9	0.58
Mn <sub>3</sub> Ge	D0 <sub>22</sub> tetragonal	0.91	0.07
FeNi	L1 <sub>0</sub> tetragonal	1.3	1.26
$\alpha''$ -Fe <sub>16</sub> N <sub>2</sub>	bct	1	1.92
BaFe <sub>12</sub> O <sub>19</sub>	hcp	0.33	0.38

**Table 1.** Intrinsic magnetocrystalline anisotropy ( $K_{mc}$ ) and saturation magnetization ( $M_S$ ) of different materials. Hcp : hexagonal close pack, bct : bodycentered tetragonal

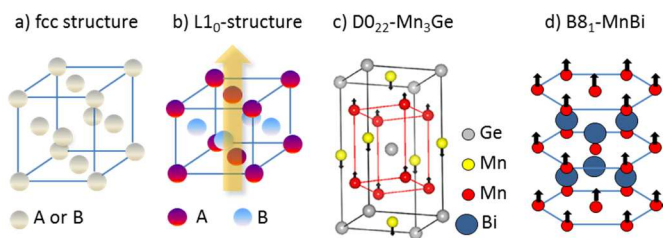


**Figure 54.** Crystallographic structure of a) face-centered cubic, b) L1<sub>0</sub>-tetragonal, c) D0<sub>22</sub> tetragonal and d) B8<sub>1</sub>

and half-metallic character, is the thermodynamic phase expected in a narrow composition window (%Mn = 0.72-0.76). The B8<sub>1</sub>-MnBi phase, which exhibits an unusual increase of coercivity with temperature, is also the thermodynamic phase. However any deviation from the proper stoichiometry leads to antiferromagnetic coupling with the Mn atoms in excess, thus decreasing the magnetization of the whole compound. MnBi and Mn<sub>3</sub>Ge have been obtained by multi-step metallurgy processes (melt-spinning, cryomilling and annealing),<sup>127</sup> or by sputtering on hot surfaces and further annealing,<sup>128</sup> but could never be successfully prepared using a liquid phase approach.

The generic tetragonal L1<sub>0</sub> structure shared by the MnAl, FeNi and PtFe alloys, is also the low temperature phase expected close to the stoichiometry. This structure consists in the regular stacking of chemically pure A (ex: Mn, Fe) and B (ex: Al, Ni, Pt) planes along the *c* axis, leading to a tetragonal distortion. For MnAl, the ferromagnetic L1<sub>0</sub>-phase is however only metastable and requires the addition of C atoms and/or successive thermally-driven phase transitions.<sup>129,130</sup> For FeNi, the difficulty of obtaining synthetic FeNi with the L1<sub>0</sub> structure in comparison with the well mastered L1<sub>0</sub>-FePt phase lays in the reduced temperature of the phase transition (320°C)<sup>131</sup> from the ordered L1<sub>0</sub> to the disordered fcc phase. The phases resulting either from metallurgical processes or from chemical syntheses are generally quenched in a disordered fcc structure, and below 320°C the recrystallization by diffusion is extremely slow, prohibiting the formation of L1<sub>0</sub>-FeNi in a reasonable time.

In conclusion, in addition to optimized Co NRs we will focus on the synthesis of L1<sub>0</sub>-FeNi, which, despite the complexity of the chemical ordering, appears as the most promising candidates for a liquid-phase synthesis approach.

#### b) Controlling the size, shape and crystallographic structure of L1<sub>0</sub>-FeNi NPs

As described in section I.1 and I.2, I have developed a rational approach for the synthesis of Fe(0) NPs by reducing a bis(bis-trimethylsilylamide) Fe complex (referred from now on as Fe(N(TMS)<sub>3</sub>)<sub>2</sub>) under mild conditions (150°C, H<sub>2</sub> pressure).<sup>A6</sup> By tuning precursor-surfactant interactions I could control the relative amount of reactive species, the Fe(N(TMS)<sub>3</sub>)<sub>2</sub> initially introduced, as well as the stable species formed in-situ, and thus finely tailor the nucleation and growth steps through which NPs are formed. Extending this approach to the synthesis of bcc-FeCo NPs by codecomposing Fe and Co silylamide precursors, we could stabilize for the first time the thermodynamic phase B<sub>2</sub>, which can be seen as an analogous to the ordered L1<sub>0</sub> phase in fcc materials.

I propose to tackle the stabilization of the promising magnetic phases of L1<sub>0</sub>-FeNi within nanoparticles using the same organometallic approaches to benefit from a unique control of precursor reactivity, thus addressing the challenges of i) chemical and ii) structural homogeneity.

#### c) Magnetically driven self-assembly

The self-assembly of plasmonic and luminescent NPs has been intensively studied to improve the intrinsic properties of the building blocks thanks to the cooperative effect.<sup>132,133</sup> Often driven by solvent evaporation, the examples of self-assembly on magnetic NPs have been limited to superparamagnetic NPs.<sup>134,135</sup> Indeed, ferromagnetic NPs tend to preform columnar structures in liquid phase due to strong magnetic interactions,<sup>130,136</sup> leading to aggregation phenomena within a short period of time.<sup>137</sup> An alternative consists in promoting the assembly using an external magnetic field, as we have recently reported.

***In summary*** : The candidate of choice for the constituting building blocks has been identified as the L1<sub>0</sub> phase of FeNi but the stabilization of this tetragonal phase remains highly challenging.<sup>5</sup> A backup, less sustainable option would be non oxidized Co NRs. The assembly of ferromagnetic NPs into a dense metamaterial can be magnetically driven providing adequate rheological properties in the solution. In this respect, I propose to tackle the scientific challenges in **chemistry, physical-chemistry and physics to render the bottom-up approach for integrated PM a viable reality.**

## 2. Methodology

Below I outline our approach summarized in Figure 55 to answer the key questions:

- Are the thermodynamic phases of  $L1_0$ -FeNi achievable by chemical means?
- How can dense magnetic metamaterials be prepared from suspensions of magnetically anisotropic though morphologically spherical NPs?
- How can the intrinsic magnetic properties of hard NP be studied? Can the magnetic interactions present in dense metamaterials be tailored?
- Can the metamaterials prepared with this bottom-up-approach be transferred to real devices?

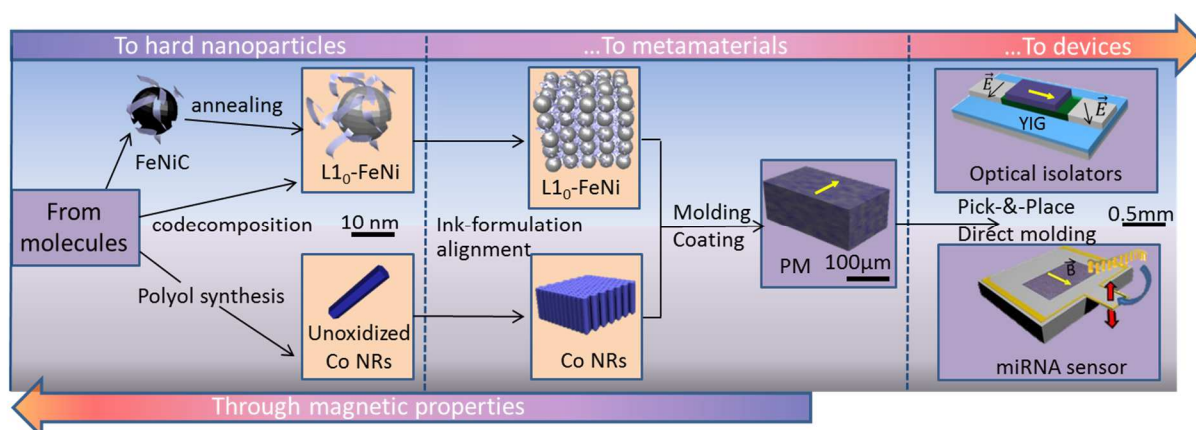


**Figure 55.** Schematic view of the project. Light orange : intermediates studied by structural, chemical and magnetic means.

### a) From molecules to hard nanoparticles

- Synthesis and characterization of  $L1_0$ -FeNi NPs

Natural  $L1_0$ -FeNi crystals were only discovered in meteorites, generally mixed with disordered fcc FeNi alloys but sometimes as main FeNi compounds.<sup>138</sup> Mineralogists generally consider that the ordering occurred over billions of years under mild conditions. While the phase conversion fcc –  $L1_0$  by thermal annealing is not a reasonable option, two strategies have been followed to synthesize artificial  $L1_0$ -FeNi:

- The first approach consists in the successive deposition of Ni and Fe monatomic layers on single crystal substrates.  $AuCu_3$  and Au–Cu–Ni layers with a flat surface can exhibit a good lattice matching with  $L1_0$ -FeNi.<sup>139,140</sup> Very high magnetocrystalline anisotropy has been measured on  $L1_0$ -FeNi thin films but because of a lack of nanostructuration coercivity is limited.
- The second consists in preparing an amorphous FeNi phase. Thanks to the higher atomic diffusivity observed when crystallizing an amorphous phase,  $L1_0$ -FeNi crystallites have been successfully obtained from amorphous FeNi-X (X=Si, B, P, Cu).<sup>141</sup> Interestingly the  $L1_0$ -FeNi phase was obtained after thermal annealing at temperatures varying from 400 to 540°C<sup>142</sup>, thus much higher than the 320°C predicted by the bulk phase diagram. Nevertheless, the  $L1_0$ -FeNi phase has never been obtained in pure form but mixed with Fe- and Ni-rich crystallites. The boron and phosphorous additives actually favor the demixing of Fe and Ni during annealing, thus altering the magnetic properties of the final material.

I therefore propose two different approaches, relying on organometallic chemistry to reach  $L1_0$ -FeNi NPs :

- *Direct synthesis of  $L1_0$ -FeNi NPs by co-decomposition of the silylamide and amidinate precursors.*

Benefiting from our previous expertise on the synthesis of  $B_2$ -FeCo NPs we propose to co-decompose Fe silylamide with an amidinate precursor as the Ni source. Homoleptic N,N'-dialkylacetamidinato metal compounds,<sup>143</sup> could produce thin films using  $H_2$  as the reducing agent through the Atomic

Layer Deposition process.<sup>144</sup> We have recently produced Ni NPs by reducing Ni amidinate under H<sub>2</sub> at 150°C, i.e. in experimental conditions similar to Fe synthesis. The full panel of coordinating surfactants (halides, carboxylates, amines...) and reducing agents (H<sub>2</sub> or alkylamine) will be explored to optimize the relative reactivity of Fe and Ni precursors.

- *Synthesis of amorphous FeNiC<sub>x</sub> NPs and further mild annealing*

The second alternative I propose is inspired from Makino's group idea of benefiting from the higher mobility in amorphous alloys,<sup>141</sup> but limiting the additives to carbon. Demixing issues should be avoided in that case while maintaining a sufficient mobility of Fe and Ni atoms to recrystallize.

We have previously reported that amorphous FeCoC<sub>x</sub> can be obtained by co-decomposition of Fe(CO)<sub>5</sub> and Co(COD)(COT) precursors under mild conditions (150°C, Toluene, 3 bars of H<sub>2</sub>).<sup>19,A8</sup> Wide Angle X-Ray Scattering (WAXS) and High Resolution Transmission Electron Microscopy (HRTEM) have evidenced the amorphous structure of the NPs. Due to interstitial C atoms, the amorphization of the structure is induced by the CO dissociation.<sup>49</sup> A 30 min annealing phase at 500°C under Ar yielded bcc FeCo NPs coated with a 2 nm thick graphitic shell. Even though the B<sub>2</sub> structure was not clearly evidenced at that time, the magnetic properties obtained were in favour of it. I could successfully reproduce these particles while replacing Toluene by Mesitylene, thus diminishing the potential overpressure hazard of the synthesis.<sup>A7,A27</sup>

Benefiting from this experience, I propose to prepare amorphous FeNiC<sub>x</sub> NPs by co-decomposition of Fe(CO)<sub>5</sub> and Ni(COD)<sub>2</sub>,<sup>145</sup> previously used in our group, under mild conditions (Mesitylene, 150°C, H<sub>2</sub>). The reaction of FeNiC<sub>x</sub> → FeNi decarburization will be controlled by playing upon temperature, time and reactive atmosphere (H<sub>2</sub>/CO ratio). We expect that a slow decarburization at a temperature well below the disorder transformation could favour the crystallization of the L1<sub>0</sub> phase. The phase transformation will be followed by in-situ XRD equipped with a high temperature chamber under reactive atmosphere.

In both cases, the crystallographic structure of the obtained NPs will be characterized by XRD. The long range chemical order of the L1<sub>0</sub>-FeNi structure is evidenced by the existence of (100) and (110) superstructure lines in the XRD pattern, while these lines vanish in the pattern of the disordered phase with fcc structure. Therefore, the order parameter *S* can be calculated as follows<sup>140</sup> :

$$S = \sqrt{(I_{100} / I_{111})_{exp.} / (I_{100} / I_{111})_{calc.}}$$
, where (I<sub>100</sub>/I<sub>111</sub>) represents the ratio between the superstructure (100) and the fundamental (111) line intensities, the hardest magnetic properties being expected for *S* = 1.

The difficulty to characterize *S* comes from the very low intensity of the superstructure lines, which is proportional to the difference between the Fe and Ni scattering factors. The difference is generally low except in anomalous diffraction experiments, where the scattering factor contrast can be enhanced using a Co K $\alpha$  radiation whose energy is very close to the Fe absorption edge. We have recently shown that the order in B<sub>2</sub> FeCo phases can be routinely studied using our laboratory diffractometer equipped with Co X-ray source even though the difference of Fe and Co in terms of scattering factors of is even lower than the one between Fe and Ni. In addition, synchrotron experiments will also be helpful to characterize the order thanks to the possibility to select an X-ray energy even closer to the Fe edge, thus further increasing the scattering contrast between Fe and Ni.<sup>146</sup>

Additionally, Mössbauer spectroscopy can be used. Since this technique is highly sensitive to the chemical environment of the <sup>57</sup>Fe nuclei, it can discriminate between the disordered fcc and the L1<sub>0</sub>-phase, as the hyperfine field is slightly reduced in the latter compounds ( $\mu_0 H_{hyp}$  of 32T and 30T respectively), and the presence of an electric field gradient in the L1<sub>0</sub>-structure leads to non-symmetric signatures.<sup>147,148</sup>

- Synthesis of optimized Co NRs

To further improve the magnetic energy stored in the assemblies of Co NRs, we expect to obtain **Co NRs** which exhibit an intrinsic coercive field  $\mu_0 H_C > 0.7T$  at 300K and with  $V_M = 0.6$ . The Co NRs consisting of a metallic Cobalt core surrounded by a cobalt oxide shell (CoO) and a surfactant corona (Figure 56), we propose to optimize each component to reach our goal. Alternatively the addition of a hard magnetic material will also be tried.

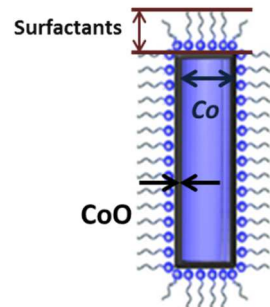


**Figure 56.** Schematic view of a Co NR.

- Improvement of the coercivity in the Co NRs assemblies

Micromagnetic simulations have shown that high coercivities are mandatory to fully benefit from the high remanent induction of dense Co assemblies. A targeted value of  $\mu_0 H_c = 0.7T$  would allow us to search for metallic volume fraction as high as 65%. While we can prepare routinely assemblies exhibiting coercivity of 0.4-0.5T, two different approaches will be followed to improve the assembly hardness.

- i) The refinement of the Co NR shape control.

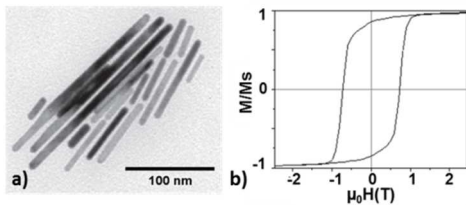


**Figure 57.** a) TEM image of Co NR with rounded tips and the corresponding b) magnetization loop recorded at 300K

shape, a coercivity of 0.72 T at 300 K was measured on aligned rods. These promising results will be reproduced and optimized, by adjusting the stirring and temperature conditions (slope, reaction temperature), to obtain monodispersed NRs.

- ii) The hardening of the Co NRs by addition of  $L1_0$ -FePt

An alternative approach consists in grafting a hard magnetic material at the Co NR tips to prevent the magnetization reversal and thus, boost the coercivity. A first proof of concept has been already obtained (Figure 58).  $L1_0$ -FePt nanoparticles, prepared in LPCNO,<sup>149</sup> were mixed with Co NRs. Binary self-assembly were favored by the addition of 4-mercapto benzoic acid (MBA). The biphasic material was annealed at 400°C to promote intermetallic coupling between the two phases. Magnetization loop recorded at 300K evidenced an enhancement of the coercivity compared to naked Co NRs (up to 2.2T, Figure 58). For a limited Pt content of 25%, a coercivity of 1T could be obtained. Since Pt is a critical material, its content should be further decreased. Moreover the addition of spherical particles onto our Co NRs will lead to a decrease of  $V_M$ . Thus, improvement of the binary assembly is required. We will use an external magnetic field during the MBA addition, to align the easy axis of the particles to promote high squareness and coercivity. Moreover, we will optimize the annealing step, with higher annealing temperature and a reducing atmosphere, to promote  $V_M$ .

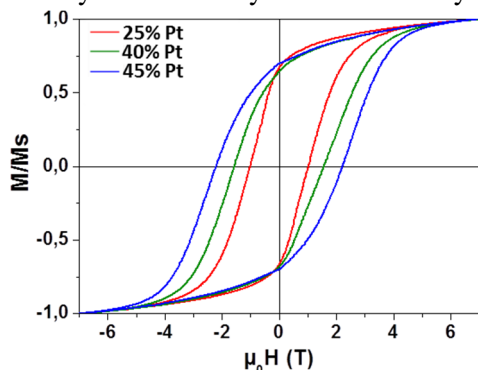


**Figure 58.** Magnetization loop at 300K of FePt-Co composites containing 25 (red), 40 (green) and 45% (blue) of Pt.

- Improvement of the magnetic fraction in the Co NRs assemblies

The improvement of the magnetic volume fraction  $V_M$  in the final nanocomposite magnet, essential for the  $(BH)_{max}$  optimization, can only be obtained if one decreases the two other components of the Co NRs, namely the CoO shell and the surfactants (Figure 56). The Co NRs presently produced exhibit a CoO shell and a surfactant corona with a thickness of approximately  $e=1.2$  and  $L=3.5$  nm, corresponding to twice the carboxylate length, leading to  $V_M = 0.4-0.55$ .<sup>A34</sup> Reducing these thicknesses to  $e=0$  and  $L=2$ nm will allow reaching  $V_M > 0.6$  (Figure 59).

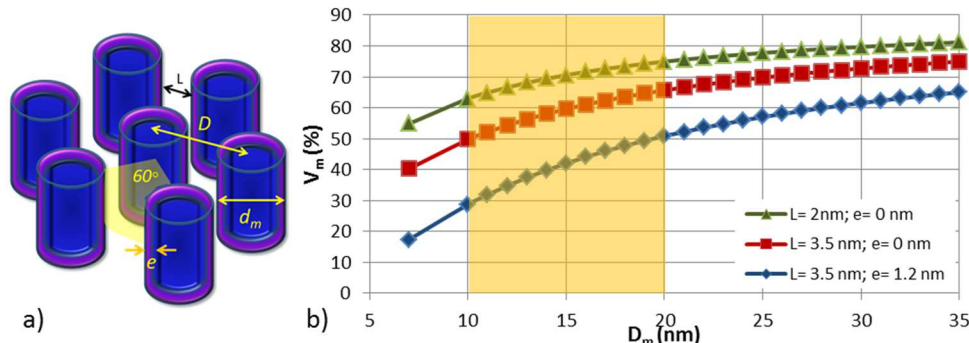


**Figure 59.** a) Model of perfect hexagonal packing of Co NRs with mean diameter  $D_m$ , CoO shell thickness  $e$  and center-to-center distance  $D$ . b) Magnetic volume fraction as a function of  $D_m$  for various CoO and ligand shells. Yellow region : optimum diameter range

i) Reduction of the oxidation

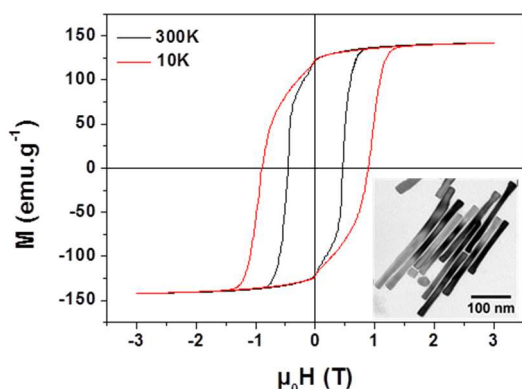


**Figure 60.** Magnetization loop at 300 (black) and 10K (red) recorded on Co NRs assemblies after a 3T field cooling. Inset : TEM image of the Co NRs.

Preliminary results show that by performing the polyol synthesis followed by a magnetic alignment under controlled atmosphere (Ar and vacuum respectively), the **rod oxidation could be limited** : no sign of exchange bias, characteristic of a CoO shell, was observed at low temperature (10K) after a 3T field cooling; the hysteresis cycle remained centered (Figure 60). A **magnetic volume fraction of 0.6** was for the first time measured on such aligned sample. We will use a reducing atmosphere (Ar + 5% H<sub>2</sub>) during the synthesis to totally reduce the CoO shell. The **optimization of the washing procedure** under controlled atmosphere, to remove undesired spheres and unreacted species, will lead to squarer hysteresis cycle and thus larger  $(BH)_{max}$ .

ii) Reduction of the surfactant shell

Two approaches will be followed to maximize our chance of success:

- the **modification of the Co precursor directly during the synthesis**. G. Viau *et al.*<sup>104</sup> have previously shown, at small scale, that Co NRs can be obtained by reduction of **Co(octanoate)<sub>2</sub>** (having 8 carbons, C8) instead of the **Co(laurate)<sub>2</sub>** precursor (C12) classically used. Since the carboxylate stabilizes the lateral facets of the Co NRs,<sup>109</sup> the reduction of their alkyl chain length will reduce the organic matter. We will try to further reduce the alkyl chain of the carboxylate without altering the Co rods morphology.

- **ligand-exchange protocol** performed post-synthesis. An alternative to direct synthesis consists in exchanging, after synthesis, the fatty ligands by shorter molecules. Short bi-functional molecule, the 4-mercaptobenzoic acid (MBA), already used for Co/FePt assembly, will be tried. Preliminary results show that MBA could replace the long carboxylate species at the Co NRs surface, leading to a fast and irreversible self-assembly of the rods. This strategy should be optimized.

Using both approaches, the inter-rod distance will be precisely inferred from the position of the correlation peak observed by Small Angle Neutron Scattering (SANS)<sup>A34</sup> and Small Angle X-Ray Scattering (SAXS).<sup>A26</sup>

## b) From hard nanoparticles to optimized metamaterials

The assembly process, essential to go from a colloidal solution up to a real nanostructure material, should be optimized to yield dense metamaterials by combining :

- a high magnetic volume fraction ( $V_M \sim 50\%$ ), to ensure a high  $M_s$ ,
- a perfect alignment of the magnetic easy-axis of the constituting nanoparticles, to yield high  $H_C$
- sufficient thickness to yield large stray fields.

These requirements can only be met using colloidal solutions with optimized rheology to allow sufficient mobility of the NPs and yield a good alignment of the magnetic easy-axis.

Magnetic alignment takes place thanks to the torque exerted by the external magnetic field on the permanent magnetic moment of the individual cobalt rods. Nearly perfect alignments of the easy axis were obtained. The same phenomenon is expected with  $L1_0$ -FeNi particles even though they have an isotropic shape, on the condition that they exhibit a single domain configuration. In that case, the alignment of the easy axis could even be easier compared to the NRs since the object will encounter fewer frictional forces from the surrounding media.

The optimization of the solution rheology will result from a compromise between NPs stability up to large concentration and evaporation rate. Ferromagnetic NPs tend to preform columnar structures in liquid phase due to strong magnetic interactions,<sup>130,136</sup> leading to aggregation phenomena within a short period of time.<sup>137</sup> Such aggregations drastically decrease the targeted easy axis alignment. Thus, fine tuning the steric hindrance and the solvent/ligand interaction will be needed to prevent aggregation while keeping a high packing fraction in the dried assembly. The metal NPs prepared by organometallic chemistry are generally stabilized with mixtures of long chain surfactants which should be replaced by shorter ones.

## c) Investigations of the magnetic properties: from NPs to the dense assembly

The magnetic behavior of a magnet both depends on the intrinsic properties of its individual constituents and on the interactions (dipolar/exchange) that they experience in the total volume. Following a bottom-up approach, we will thoroughly investigate the magnetic properties from the individual building blocks to the resulting magnet.

### • Intrinsic magnetic behaviour of $L1_0$ -FeNi NPs

The characterization of the intrinsic properties (size, shape, anisotropy, coercivity, thermal stability) of the synthesized  $L1_0$ -FeNi NPs is of prime importance since they have never been previously synthesized. Thus, their expected magnetic properties are only postulated from bulk values, but size reduction effects are known to potentially affect them.<sup>150,AC1</sup> The determination of these intrinsic properties requires studying individual NPs that do not experience any magnetic interactions.

#### - *Magnetometry on assemblies of non-interacting NPs*

Well mastered in my group, magnetometry performed on diluted assemblies of NPs allows measurements of hysteresis loops ( $M(H)$ ) with negligible magnetic interactions.<sup>AC1,AC2 ,A29</sup> We will extract averaged intrinsic values of  $M_s$ ,  $H_c$ ,  $K$ , and their temperature dependence (2-300K). Intrinsic switching field ( $\sim H_c$ ) distribution,<sup>20</sup> which is of high importance for the thermal stability of the targeted magnet, will be investigated thanks to first derivatives of  $M(H)$  loops.

#### - *Direct measurement on isolated NP : Electron Holography (EH)*

The hardest magnetic behaviour is linked to the uniform (single-domain like) magnetic configuration of the isolated particle. Here we will benefit from our previous experience using EH to investigate (i) the magnetic configuration vs structural properties in individual  $L1_0$ -FeNi particles, and (ii) the potential exchange coupling between Co NRs and  $L1_0$ -FePt. Quantitative comparisons between electron holograms and ad-hoc micromagnetic simulations (OOMMF code) will allow quantifying intrinsic  $M_s$  and  $K$  at the NP scale.

- **Magnetic behaviour of metamaterials**

The fundamental objectives consist here in (i) quantifying the respective contribution of exchange vs dipolar interactions and (ii) probing the collective magnetic reversal process at the assembly scale in order to optimize  $BH_{\max}$  values in metamaterials.

- *Macroscopic magnetic behaviour*

The modification of the fundamental macroscopic parameters ( $M_s$ ,  $H_c$ ,  $K$ ) will be determined on powders of randomly oriented NPs and on the final metamaterials obtained from aligned NPs using hysteresis cycle  $M(H)$  at different temperatures. DC Demagnetization (DCD) measurements will be performed to quantify the potential exchange coupling in annealed Co/FePt samples.

- *Microscopic magnetic behaviour*

For PM sake, the switching field distribution, which corresponds in first approximation to the  $H_c$  distribution of the constituting NPs, should exhibit a large mean value (corresponding to a high  $K$ ) with a small standard deviation. It is indeed expected that the magnetic reversal of a NP based PM operates by nucleation and propagation of reversed domains. The weakest NP will behave as low anisotropy centres, thus initiating the reversal process. Thanks to well established collaborations, we propose to use polarized small angle neutron scattering (LLB-CEA Saclay, France)<sup>151</sup> and Kerr microscopy (IPCMS-CNRS, Strasbourg, France) to probe the local magnetic correlations between NPs during the reversal process. The expected result is the description of the correlation lengths (nucleation, domain size, neighbor interactions).

- *Advanced magnetic simulations*

The experimental results obtained on NPs assemblies will be corroborated by dynamic Monte-Carlo simulations, in collaboration with the nanomagnetism group at LPCNO. Each NP is modelled as a single-domain particle considering thermal relaxation and dipolar interactions. Effects of interparticle distance, packing fraction, easy-axis alignment, anisotropy distributions, thermal effects, matrix environment, etc, on  $BH_{\max}$  values will be investigated and will help to drive the synthesis/post-synthesis steps (targeted sizes, shapes, dilutions, etc).

#### d) From the metamaterials to the integration

The two biosensing and optoelectronic devices envisaged in the project are highly demanding in terms of magnetic properties,  $(BH)_{\max}$  values of  $150 \text{ kJ.m}^{-3}$  and remanent induction of 0.5T are indeed mandatory.

- **Preparation of submillimetre magnets**

The optimized rheology of the NPs solution will be used to fill submillimeter molds using generic deposition techniques (ink jet or doctor blade techniques). Since diluted solutions may be used to prevent strong magnetic interactions and aggregation phenomenon, successive steps of deposition/alignment/evaporation may be necessary to yield thick PM. The assemblies being highly insoluble once deposited, their redispersion may not be a drawback. To prevent the constituting NPs from oxidation a passivation layer of epoxy resin will be deposited. We have already demonstrated its efficiency on FeCo NPs.

The induction stray field produced by the PM will be quantitatively mapped using a Hall microprobe (lateral resolution of  $\sim 10\mu\text{m}$ ), obtained thanks to a collaboration with Nora Dempsey, Roman Kramer and Klaus Hasselbach (Neel Institute, Grenoble). The sample will be mounted on a translator stage actuated with piezoelectric motors. Such system is already available in LPCNO; the 3D mapping obtained will be compared with Finite element simulations using COMSOL software. This could give important feedbacks for the chemistry and physical-chemistry part of the project. Moreover, these macroscopic measurements will be compared with the local magnetic characterizations performed.

- Integration onto demo-units : the pick and place approach

The approach, successfully used with FeCo/epoxy metamaterial, will consist in reporting the submillimeter size magnets using micromanipulators.<sup>152</sup> In case of difficulties encountered in the direct preparation of submillimeter PM, larger metamaterials, such as the Co NRs assemblies already mastered,<sup>A34</sup> could be cut using a dicing saw.

- *Test of the demo-units : biosensor*

The electromagnetic actuation of the MEMS resonator will be tested in air and in liquid using integrated piezoresistor and an associated read-out electronic card already developed at LAAS. In the case of encouraging results (acceptable response in liquid with high-enough Q factor), this proof-of-concept device will be functionalized with probe molecules and detection of synthesized miRNAs spiked in diluted serum will be finally carried out.

- *Test of the demo-units : optical isolator*

Optical isolators are generally made of ferrimagnetic garnets (YIG) which exhibit both high transparency in the optical telecommunication wavelength range (1.3 and 1.55 $\mu$ m) and efficient Faraday rotation. However these components require the use of an external magnetic field, generally provided by a bulk PM, to saturate magnetic ions magnetization. In order to provide these garnets in more compact and manipulable configuration, NP PM will be deposited on a test YIG waveguide, with magnetization axis parallel to light propagation. The magnetization magnitude induced by the PM layer will be measured by polarized transmission experiments. The polarization rotation of the transmitted beam will be a direct probe of the PM efficiency. Another promising configuration consists in depositing the PM layer on a semiconductor waveguide capped with a magneto-optical medium, which would make the isolator compatible with photonic integrated circuits (PICs). When the PM magnetization axis is perpendicular to the light propagation, this latter experiences a transverse magneto-optical Kerr effect, which results in non-reciprocal absorption and phase-shift.<sup>153154</sup> Both effects may result in high isolation ratio, opening up new possibilities for a full integration of semiconductor PICs.

*This project will be made in close collaboration with experts in electron microscopy (B. Warot-Fonrose, C. Gatel, CEMES, Toulouse), in nanomagnetism (Thomas Blon, Julian Carrey, Marc Respaud, LPCNO), in Neutron (F. Ott, LLB, Saclay), in biosensors (T. Leïchl , LAAS, Toulouse) and optical applications (A. Monmayrant, LAAS, Toulouse and H. Carr re, LPCNO).*

## References

- (1) Delacour, C.; Bugnicourt, G.; Dempsey, N. M.; Dumas-Bouchiat, F.; Villard, C. Combined Magnetic and Chemical Patterning for Neural Architectures. *J. Phys. Appl. Phys.* **2014**, *47* (42), 425403.
- (2) Walther, A.; Marcoux, C.; Desloges, B.; Grechishkin, R.; Givord, D.; Dempsey, N. M. Micro-Patterning of NdFeB and SmCo Magnet Films for Integration into Micro-Electro-Mechanical-Systems. *J. Magn. Magn. Mater.* **2009**, *321* (6), 590–594.
- (3) Dumas-Bouchiat, F.; Zanini, L. F.; Kustov, M.; Dempsey, N. M.; Grechishkin, R.; Hasselbach, K.; Orlianges, J. C.; Champeaux, C.; Catherinot, A.; Givord, D. Thermomagnetically Patterned Micromagnets. *Appl. Phys. Lett.* **2010**, *96* (10), 102511.
- (4) Poudyal, N.; Ping Liu, J. Advances in Nanostructured Permanent Magnets Research. *J. Phys. Appl. Phys.* **2013**, *46* (4), 43001.
- (5) Skomski, R.; Coey, J. M. D. Magnetic Anisotropy — How Much Is Enough for a Permanent Magnet? *Scr. Mater.* **2016**, *112*, 3–8.
- (6) Song, H.; Spencer, J.; Jander, A.; Nielsen, J.; Stasiak, J.; Kasperchik, V.; Dhagat, P. Inkjet Printing of Magnetic Materials with Aligned Anisotropy. *J. Appl. Phys.* **2014**, *115* (17), 17E308.
- (7) Dempsey, N. M.; Le Roy, D.; Marelli-Mathevon, H.; Shaw, G.; Dias, A.; Kramer, R. B. G.; Viet Cuong, L.; Kustov, M.; Zanini, L. F.; Villard, C.; et al. Micro-Magnetic Imprinting of High Field Gradient Magnetic Flux Sources. *Appl. Phys. Lett.* **2014**, *104* (26), 262401.
- (8) Kandpal, M.; Sharan, C.; Palaparthi, V.; Tiwary, N.; Poddar, P.; Rao, V. R. Spin-Coatable, Photopatternable Magnetic Nanocomposite Thin Films for MEMS Device Applications. *RSC Adv* **2015**, *5* (104), 85741–85747.
- (9) Han, M.; Li, Z.; Sun, X.; Zhang, H. Analysis of an in-Plane Electromagnetic Energy Harvester with Integrated Magnet Array. *Sens. Actuators Phys.* **2014**, *219*, 38–46.
- (10) Myung, N. V.; Park, D.-Y.; Yoo, B.-Y.; Sumodjo, P. T. . Development of Electroplated Magnetic Materials for MEMS. *J. Magn. Magn. Mater.* **2003**, *265* (2), 189–198.
- (11) Niarchos, D. Magnetic MEMS: Key Issues and Some Applications. *Sens. Actuators Phys.* **2003**, *106* (1–3), 255–262.
- (12) Watt, J.; Cheong, S.; Tilley, R. D. How to Control the Shape of Metal Nanostructures in Organic Solution Phase Synthesis for Plasmonics and Catalysis. *Nano Today* **2013**, *8* (2), 198–215.
- (13) Finney, E. E.; Finke, R. G. Nanocluster Nucleation and Growth Kinetic and Mechanistic Studies: A Review Emphasizing Transition-Metal Nanoclusters. *J. Colloid Interface Sci.* **2008**, *317* (2), 351–374.
- (14) LaMer, V. K.; Dinegar, R. H. Theory, Production and Mechanism of Formation of Monodispersed Hydrosols. *J. Am. Chem. Soc.* **1950**, *72* (11), 4847–4854.
- (15) Park, J.; Joo, J.; Kwon, S. G.; Jang, Y.; Hyeon, T. Synthesis of Monodisperse Spherical Nanocrystals. *Angew. Chem. Int. Ed.* **2007**, *46* (25), 4630–4660.
- (16) Shevchenko, E. V.; Talapin, D. V.; Rogach, A. L.; Kornowski, A.; Haase, M.; Weller, H. Colloidal Synthesis and Self-Assembly of CoPt<sub>3</sub> Nanocrystals. *J. Am. Chem. Soc.* **2002**, *124* (38), 11480–11485.
- (17) Henzie, J.; Grünwald, M.; Widmer-Cooper, A.; Geissler, P. L.; Yang, P. Self-Assembly of Uniform Polyhedral Silver Nanocrystals into Densest Packings and Exotic Superlattices. *Nat. Mater.* **2011**, *11* (2), 131–137.
- (18) Goubet, N.; Richardi, J.; Albouy, P.-A.; Pileni, M.-P. Which Forces Control Supracrystal Nucleation in Organic Media? *Adv. Funct. Mater.* **2011**, *21* (14), 2693–2704.
- (19) Desvaux, C.; Amiens, C.; Fejes, P.; Renaud, P.; Respaud, M.; Lecante, P.; Snoeck, E.; Chaudret, B. Multimillimetre-Large Superlattices of Air-Stable Iron–cobalt Nanoparticles. *Nat. Mater.* **2005**, *4* (10), 750–753.
- (20) Coey, J. M. D. *Magnetism and Magnetic Materials*; Cambridge University Press: Cambridge, 2010.
- (21) Huber, D. Synthesis, Properties, and Applications of Iron Nanoparticles. *Small* **2005**, *1* (5), 482–501.
- (22) Farrell, D.; Majetich, S. A.; Wilcoxon, J. P. Preparation and Characterization of Monodisperse Fe Nanoparticles. *J. Phys. Chem. B* **2003**, *107* (40), 11022–11030.
- (23) Peng, S.; Wang, C.; Xie, J.; Sun, S. Synthesis and Stabilization of Monodisperse Fe Nanoparticles. *J. Am. Chem. Soc.* **2006**, *128* (33), 10676–10677.
- (24) Hadjipanayis, C. G.; Bonder, M. J.; Balakrishnan, S.; Wang, X.; Mao, H.; Hadjipanayis, G. C. Metallic Iron Nanoparticles for MRI Contrast Enhancement and Local Hyperthermia. *Small* **2008**, *4* (11), 1925–1929.
- (25) Olmstead, M. M.; Power, P. P.; Shoner, S. C. Three-Coordinate Iron Complexes: X-Ray Structural Characterization of the Iron Amide-Bridged Dimers [Fe (NR<sub>2</sub>)<sub>2</sub>]<sub>2</sub> (R= SiMe<sub>3</sub>, C<sub>6</sub>H<sub>5</sub>) and the Adduct Fe [N (SiMe<sub>3</sub>)<sub>2</sub>]<sub>2</sub> (THF) and Determination of the Association Energy of the Monomer Fe {N (SiMe<sub>3</sub>)<sub>2</sub>]<sub>2</sub> in Solution. *Inorg. Chem.* **1991**, *30* (11), 2547–2551.
- (26) Andersen, R. A.; Faegri Jr, K.; Green, J. C.; Haaland, A.; Lappert, M. F.; Leung, W. P.; Rypdal, K. Synthesis of Bis [Bis (Trimethylsilyl) Amido] Iron (II). Structure and Bonding in M [N (SiMe<sub>3</sub>)<sub>2</sub>]<sub>2</sub>

- (M= Manganese, Iron, Cobalt): Two-Coordinate Transition-Metal Amides. *Inorg. Chem.* **1988**, *27* (10), 1782–1786.
- (27) Kelsen, V.; Wendt, B.; Werkmeister, S.; Junge, K.; Beller, M.; Chaudret, B. The Use of Ultrasmall iron(0) Nanoparticles as Catalysts for the Selective Hydrogenation of Unsaturated C–C Bonds. *Chem. Commun.* **2013**, *49* (33), 3416.
- (28) Park, J.; Lee, E.; Hwang, N.-M.; Kang, M.; Kim, S. C.; Hwang, Y.; Park, J.-G.; Noh, H.-J.; Kim, J.-Y.; Park, J.-H.; et al. One-Nanometer-Scale Size-Controlled Synthesis of Monodisperse Magnetic Iron Oxide Nanoparticles. *Angew. Chem. Int. Ed.* **2005**, *44* (19), 2872–2877.
- (29) Sun, S.; Zeng, H. Size-Controlled Synthesis of Magnetite Nanoparticles. *J. Am. Chem. Soc.* **2002**, *124* (28), 8204–8205.
- (30) Farrell, D.; Cheng, Y.; McCallum, R. W.; Sachan, M.; Majetich, S. A. Magnetic Interactions of Iron Nanoparticles in Arrays and Dilute Dispersions. *J. Phys. Chem. B* **2005**, *109* (28), 13409–13419.
- (31) Meffre, A.; Lachaize, S.; Gatel, C.; Respaud, M.; Chaudret, B. Use of Long Chain Amine as a Reducing Agent for the Synthesis of High Quality Monodisperse iron(0) Nanoparticles. *J. Mater. Chem.* **2011**, *21* (35), 13464.
- (32) Lentijo-Mozo, S.; Tan, R. P.; Garcia-Marcelot, C.; Altantzis, T.; Fazzini, P.-F.; Hungria, T.; Cormary, B.; Gallagher, J. R.; Miller, J. T.; Martinez, H.; et al. Air- and Water-Resistant Noble Metal Coated Ferromagnetic Cobalt Nanorods. *ACS Nano* **2015**, *9* (3), 2792–2804.
- (33) Seo, W. S.; Lee, J. H.; Sun, X.; Suzuki, Y.; Mann, D.; Liu, Z.; Terashima, M.; Yang, P. C.; McConnell, M. V.; Nishimura, D. G.; et al. FeCo/graphitic-Shell Nanocrystals as Advanced Magnetic-Resonance-Imaging and near-Infrared Agents. *Nat. Mater.* **2006**, *5* (12), 971–976.
- (34) Ferrando, R.; Jellinek, J.; Johnston, R. L. Nanoalloys: From Theory to Applications of Alloy Clusters and Nanoparticles. *Chem. Rev.* **2008**, *108* (3), 845–910.
- (35) Ho, D.; Sun, X.; Sun, S. Monodisperse Magnetic Nanoparticles for Theranostic Applications. *Acc. Chem. Res.* **2011**, *44* (10), 875–882.
- (36) Ogawa, T.; Takano, H.; Kura, H.; Takahashi, M. Synthesis of Fe–Co Nanoparticles with High Saturation Magnetization by Low-Temperature Post-Annealing. *J. Appl. Phys.* **2012**, *111* (7), 07B533.
- (37) Chaubey, G. S.; Barcena, C.; Poudyal, N.; Rong, C.; Gao, J.; Sun, S.; Liu, J. P. Synthesis and Stabilization of FeCo Nanoparticles. *J. Am. Chem. Soc.* **2007**, *129* (23), 7214–7215.
- (38) Yan, Q.; Li, S.; Pang, E.; Wang, Y. Fabrication of Hollow Spheres FeCo Alloy through a Hydrothermal Reduction Method. *Mater. Lett.* **2014**, *120*, 185–188.
- (39) Rafique, M. Y.; Pan, L.; Zubair Iqbal, M.; Javed, Q.; Qiu, H.; Rafi-ud-din; Farooq, M. H.; Guo, Z. 3-D Flower like FeCo Alloy Nanostructures Assembled with Nanotriangular Prism: Facile Synthesis, Magnetic Properties, and Effect of NaOH on Its Formation. *J. Alloys Compd.* **2013**, *550*, 423–430.
- (40) Gu, Y.; Cao, Y.; Chi, H.; Liang, Q.; Zhang, Y.; Sun, Y. Facile Synthesis of FeCo/Fe<sub>3</sub>O<sub>4</sub> Nanocomposite with High Wave-Absorbing Properties. *Int. J. Mol. Sci.* **2013**, *14* (7), 14204–14213.
- (41) Wei, X.-W.; Wu, K.-L.; Zhu, G.-X.; Liu, Y.-J.; Shi, W.; Li, X.-Z.; Rong, L.-L.; Chen, L.; Wu, F.-H. Ultrasonic-Assisted Surfactant-Free Synthesis of Highly Magnetized FeCo Alloy Nanocrystallite from Ferric and Cobalt Salt. *J. Alloys Compd.* **2012**, *539*, 21–25.
- (42) Abbas, M.; Islam, M. N.; Rao, B. P.; Abou Aitah, K. E.; Kim, C. Facile Approach for Synthesis of High Moment Fe/ferrite and FeCo/ferrite Core/shell Nanostructures. *Mater. Lett.* **2015**, *139*, 161–164.
- (43) Sun, S.; Murray, C. B.; Weller, D.; Folks, L.; Moser, A. Monodisperse FePt Nanoparticles and Ferromagnetic FePt Nanocrystal Superlattices. *Science* **2000**, *287* (5460), 1989–1992.
- (44) Kim, J.; Rong, C.; Lee, Y.; Liu, J. P.; Sun, S. From Core/Shell Structured FePt/Fe<sub>3</sub>O<sub>4</sub>/MgO to Ferromagnetic FePt Nanoparticles. *Chem. Mater.* **2008**, *20* (23), 7242–7245.
- (45) Wang, C.; Peng, S.; Chan, R.; Sun, S. Synthesis of AuAg Alloy Nanoparticles from Core/Shell-Structured Ag/Au. *Small* **2009**, *5* (5), 567–570.
- (46) Desvaux, C.; Amiens, C.; Fejes, P.; Renaud, P.; Respaud, M.; Lecante, P.; Snoeck, E.; Chaudret, B. Multimillimetre-Large Superlattices of Air-Stable Iron–cobalt Nanoparticles. *Nat. Mater.* **2005**, *4* (10), 750–753.
- (47) Desvaux, C.; Dumestre, F.; Amiens, C.; Respaud, M.; Lecante, P.; Snoeck, E.; Fejes, P.; Renaud, P.; Chaudret, B. FeCo Nanoparticles from an Organometallic Approach: Synthesis, Organisation and Physical Properties. *J. Mater. Chem.* **2009**, *19* (20), 3268.
- (48) Desvaux, C.; Lecante, P.; Respaud, M.; Chaudret, B. Structural and Magnetic Study of the Annealing of Fe–Co Nanoparticles. *J. Mater. Chem.* **2010**, *20* (1), 103.
- (49) Meffre, A.; Mehdaoui, B.; Kelsen, V.; Fazzini, P. F.; Carrey, J.; Lachaize, S.; Respaud, M.; Chaudret, B. A Simple Chemical Route toward Monodisperse Iron Carbide Nanoparticles Displaying Tunable Magnetic and Unprecedented Hyperthermia Properties. *Nano Lett.* **2012**, *12* (9), 4722–4728.
- (50) Halder, A.; Ravishankar, N. Ultrafine Single-Crystalline Gold Nanowire Arrays by Oriented Attachment. *Adv. Mater.* **2007**, *19* (14), 1854–1858.

- (51) Pud, S.; Kisner, A.; Heggen, M.; Belaine, D.; Temirov, R.; Simon, U.; Offenhäusser, A.; Mourzina, Y.; Vitusevich, S. Features of Transport in Ultrathin Gold Nanowire Structures. *Small* **2013**, *9* (6), 846–852.
- (52) Cui, H.; Hong, C.; Ying, A.; Yang, X.; Ren, S. Ultrathin Gold Nanowire-Functionalized Carbon Nanotubes for Hybrid Molecular Sensing. *ACS Nano* **2013**, *7* (9), 7805–7811.
- (53) Kisner, A.; Heggen, M.; Mayer, D.; Simon, U.; Offenhäusser, A.; Mourzina, Y. Probing the Effect of Surface Chemistry on the Electrical Properties of Ultrathin Gold Nanowire Sensors. *Nanoscale* **2014**, *6* (10), 5146.
- (54) Yang, L.; Zhang, Y.; Chu, M.; Deng, W.; Tan, Y.; Ma, M.; Su, X.; Xie, Q.; Yao, S. Facile Fabrication of Network Film Electrodes with Ultrathin Au Nanowires for Nonenzymatic Glucose Sensing and glucose/O<sub>2</sub> Fuel Cell. *Biosens. Bioelectron.* **2014**, *52*, 105–110.
- (55) Xu, J.; Wang, H.; Liu, C.; Yang, Y.; Chen, T.; Wang, Y.; Wang, F.; Liu, X.; Xing, B.; Chen, H. Mechanical Nanosprings: Induced Coiling and Uncoiling of Ultrathin Au Nanowires. *J. Am. Chem. Soc.* **2010**, *132* (34), 11920–11922.
- (56) Xu, J.; Jiang, W. Confinement of Polymer-Tethered Gold Nanowires in Polymeric Colloids. *Macromolecules* **2014**, *47* (7), 2396–2403.
- (57) Chen, Y.; Ouyang, Z.; Gu, M.; Cheng, W. Mechanically Strong, Optically Transparent, Giant Metal Superlattice Nanomembranes From Ultrathin Gold Nanowires. *Adv. Mater.* **2013**, *25* (1), 80–85.
- (58) Sánchez-Iglesias, A.; Rivas-Murias, B.; Grzelczak, M.; Pérez-Juste, J.; Liz-Marzán, L. M.; Rivadulla, F.; Correa-Duarte, M. A. Highly Transparent and Conductive Films of Densely Aligned Ultrathin Au Nanowire Monolayers. *Nano Lett.* **2012**, *12* (12), 6066–6070.
- (59) Lu, X.; Yavuz, M. S.; Tuan, H.-Y.; Korgel, B. A.; Xia, Y. Ultrathin Gold Nanowires Can Be Obtained by Reducing Polymeric Strands of Oleylamine–AuCl Complexes Formed via Auophilic Interaction. *J. Am. Chem. Soc.* **2008**, *130* (28), 8900–8901.
- (60) Huo, Z.; Tsung, C.; Huang, W.; Zhang, X.; Yang, P. Sub-Two Nanometer Single Crystal Au Nanowires. *Nano Lett.* **2008**, *8* (7), 2041–2044.
- (61) Kura, H.; Ogawa, T. Synthesis and Growth Mechanism of Long Ultrafine Gold Nanowires with Uniform Diameter. *J. Appl. Phys.* **2010**, *107* (7), 74310.
- (62) Kisner, A.; Heggen, M.; Fernández, E.; Lenk, S.; Mayer, D.; Simon, U.; Offenhäusser, A.; Mourzina, Y. The Role of Oxidative Etching in the Synthesis of Ultrathin Single-Crystalline Au Nanowires. *Chem. - Eur. J.* **2011**, *17* (34), 9503–9507.
- (63) Imura, Y.; Tanuma, H.; Sugimoto, H.; Ito, R.; Hojo, S.; Endo, H.; Morita, C.; Kawai, T. Water-Dispersible Ultrathin Au Nanowires Prepared Using a Lamellar Template of a Long-Chain Amidoamine Derivative. *Chem. Commun.* **2011**, *47* (22), 6380.
- (64) Feng, H.; Yang, Y.; You, Y.; Li, G.; Guo, J.; Yu, T.; Shen, Z.; Wu, T.; Xing, B. Simple and Rapid Synthesis of Ultrathin Gold Nanowires, Their Self-Assembly and Application in Surface-Enhanced Raman Scattering. *Chem. Commun.* **2009**, No. 15, 1984.
- (65) Kang, Y.; Ye, X.; Murray, C. B. Size- and Shape-Selective Synthesis of Metal Nanocrystals and Nanowires Using CO as a Reducing Agent. *Angew. Chem. Int. Ed.* **2010**, *49* (35), 6156–6159.
- (66) Li, Z.; Tao, J.; Lu, X.; Zhu, Y.; Xia, Y. Facile Synthesis of Ultrathin Au Nanorods by Aging the AuCl(oleylamine) Complex with Amorphous Fe Nanoparticles in Chloroform. *Nano Lett.* **2008**, *8* (9), 3052–3055.
- (67) Wang, C.; Hu, Y.; Lieber, C. M.; Sun, S. Ultrathin Au Nanowires and Their Transport Properties. *J. Am. Chem. Soc.* **2008**, *130* (28), 8902–8903.
- (68) Polte, J.; Erler, R.; Thünemann, A. F.; Sokolov, S.; Ahner, T. T.; Rademann, K.; Emmerling, F.; Kraehnert, R. Nucleation and Growth of Gold Nanoparticles Studied *via in Situ* Small Angle X-Ray Scattering at Millisecond Time Resolution. *ACS Nano* **2010**, *4* (2), 1076–1082.
- (69) Wuithschick, M.; Paul, B.; Bienert, R.; Sarfraz, A.; Vainio, U.; Sztucki, M.; Kraehnert, R.; Strasser, P.; Rademann, K.; Emmerling, F.; et al. Size-Controlled Synthesis of Colloidal Silver Nanoparticles Based on Mechanistic Understanding. *Chem. Mater.* **2013**, *25* (23), 4679–4689.
- (70) Abécassis, B.; Testard, F.; Spalla, O.; Barboux, P. Probing *in Situ* the Nucleation and Growth of Gold Nanoparticles by Small-Angle X-Ray Scattering. *Nano Lett.* **2007**, *7* (6), 1723–1727.
- (71) Hubert, F.; Testard, F.; Thill, A.; Kong, Q.; Tache, O.; Spalla, O. Growth and Overgrowth of Concentrated Gold Nanorods: Time Resolved SAXS and XANES. *Cryst. Growth Des.* **2012**, *12* (3), 1548–1555.
- (72) McKenzie, L. C.; Haben, P. M.; Kevan, S. D.; Hutchison, J. E. Determining Nanoparticle Size in Real Time by Small-Angle X-Ray Scattering in a Microscale Flow System. *J. Phys. Chem. C* **2010**, *114* (50), 22055–22063.
- (73) Sun, Y.; Ren, Y. *In Situ* Synchrotron X-Ray Techniques for Real-Time Probing of Colloidal Nanoparticle Synthesis. *Part. Part. Syst. Charact.* **2013**, *30* (5), 399–419.

- (74) Thünemann, A. F.; Kegel, J.; Polte, J.; Emmerling, F. Superparamagnetic Maghemite Nanorods: Analysis by Coupling Field-Flow Fractionation and Small-Angle X-Ray Scattering. *Anal. Chem.* **2008**, *80* (15), 5905–5911.
- (75) Koerner, H.; MacCuspie, R. I.; Park, K.; Vaia, R. A. In Situ UV/Vis, SAXS, and TEM Study of Single-Phase Gold Nanoparticle Growth. *Chem. Mater.* **2012**, *24* (6), 981–995.
- (76) Wang, W.; Zhang, K.; Cai, Q.; Mo, G.; Xing, X. Q.; Cheng, W. D.; Chen, Z. J.; Wu, Z. H. Real-Time SAXS and Ultraviolet-Visible Spectral Studies on Size and Shape Evolution of Gold Nanoparticles in Aqueous Solution. *Eur. Phys. J. B* **2010**, *76* (2), 301–307.
- (77) Israelachvili, J. N. *Intermolecular and Surface Forces*, 3rd edition.; Elsevier, 2011.
- (78) Gao, J.; Bender, C. M.; Murphy, C. J. Dependence of the Gold Nanorod Aspect Ratio on the Nature of the Directing Surfactant in Aqueous Solution. *Langmuir* **2003**, *19* (21), 9065–9070.
- (79) Wittenberg, N. J.; Haynes, C. L. Using Nanoparticles to Push the Limits of Detection. *Wiley Interdiscip. Rev. Nanomed. Nanobiotechnol.* **2009**, *1* (2), 237–254.
- (80) Antolini, E.; Perez, J. The Renaissance of Unsupported Nanostructured Catalysts for Low-Temperature Fuel Cells: From the Size to the Shape of Metal Nanostructures. *J. Mater. Sci.* **2011**, *46* (13), 4435–4457.
- (81) Chen, J.; Lim, B.; Lee, E. P.; Xia, Y. Shape-Controlled Synthesis of Platinum Nanocrystals for Catalytic and Electrocatalytic Applications. *Nano Today* **2009**, *4* (1), 81–95.
- (82) Tao, A. R.; Habas, S.; Yang, P. Shape Control of Colloidal Metal Nanocrystals. *Small* **2008**, *4* (3), 310–325.
- (83) Sau, T. K.; Rogach, A. L.; Jäckel, F.; Klar, T. A.; Feldmann, J. Properties and Applications of Colloidal Nonspherical Noble Metal Nanoparticles. *Adv. Mater.* **2010**, *22* (16), 1805–1825.
- (84) Parkin, S. S. P.; Hayashi, M.; Thomas, L. Magnetic Domain-Wall Racetrack Memory. *Science* **2008**, *320* (5873), 190–194.
- (85) Pribiag, V. S.; Krivorotov, I. N.; Fuchs, G. D.; Braganca, P. M.; Ozatay, O.; Sankey, J. C.; Ralph, D. C.; Buhrman, R. A. Magnetic Vortex Oscillator Driven by D.c. Spin-Polarized Current. *Nat. Phys.* **2007**, *3* (7), 498–503.
- (86) Bedanta, S.; Kleemann, W. Supermagnetism. *J. Phys. Appl. Phys.* **2009**, *42* (1), 13001.
- (87) Meffre, A.; Mehdaoui, B.; Connord, V.; Carrey, J.; Fazzini, P. F.; Lachaize, S.; Respaud, M.; Chaudret, B. Complex Nano-Objects Displaying Both Magnetic and Catalytic Properties: A Proof of Concept for Magnetically Induced Heterogeneous Catalysis. *Nano Lett.* **2015**, *15* (5), 3241–3248.
- (88) Fortin, J.-P.; Wilhelm, C.; Servais, J.; Ménager, C.; Bacri, J.-C.; Gazeau, F. Size-Sorted Anionic Iron Oxide Nanomagnets as Colloidal Mediators for Magnetic Hyperthermia. *J. Am. Chem. Soc.* **2007**, *129* (9), 2628–2635.
- (89) Carrey, J.; Mehdaoui, B.; Respaud, M. Simple Models for Dynamic Hysteresis Loop Calculations of Magnetic Single-Domain Nanoparticles: Application to Magnetic Hyperthermia Optimization. *J. Appl. Phys.* **2011**, *109* (8), 83921.
- (90) Farcau, C.; Moreira, H.; Viallet, B.; Grisolia, J.; Ressler, L. Tunable Conductive Nanoparticle Wire Arrays Fabricated by Convective Self-Assembly on Nonpatterned Substrates. *ACS Nano* **2010**, *4* (12), 7275–7282.
- (91) Fert, A. Origin, Development, and Future of Spintronics (Nobel Lecture). *Angew. Chem. Int. Ed.* **2008**, *47* (32), 5956–5967.
- (92) Dayen, J.-F.; Devid, E.; Kamalakar, M. V.; Golubev, D.; Guédon, C.; Faramarzi, V.; Doudin, B.; van der Molen, S. J. Enhancing the Molecular Signature in Molecule-Nanoparticle Networks Via Inelastic Cotunneling. *Adv. Mater.* **2013**, *25* (3), 400–404.
- (93) Tan, R. P.; Carrey, J.; Respaud, M. Voltage and Temperature Dependence of High-Field Magnetoresistance in Arrays of Magnetic Nanoparticles. *J. Appl. Phys.* **2008**, *104* (2), 23908.
- (94) Chandni, U.; Kundu, P.; Singh, A. K.; Ravishankar, N.; Ghosh, A. Insulating State and Breakdown of Fermi Liquid Description in Molecular-Scale Single-Crystalline Wires of Gold. *ACS Nano* **2011**, *5* (10), 8398–8403.
- (95) Roy, A.; Pandey, T.; Ravishankar, N.; Singh, A. K. Single Crystalline Ultrathin Gold Nanowires: Promising Nanoscale Interconnects. *AIP Adv.* **2013**, *3* (3), 32131.
- (96) Palleau, E.; Sangeetha, N. M.; Viau, G.; Marty, J.-D.; Ressler, L. Coulomb Force Directed Single and Binary Assembly of Nanoparticles from Aqueous Dispersions by AFM Nanoxerography. *ACS Nano* **2011**, *5* (5), 4228–4235.
- (97) Sangeetha, N. M.; Moutet, P.; Lagarde, D.; Sallen, G.; Urbaszek, B.; Marie, X.; Viau, G.; Ressler, L. 3D Assembly of Upconverting NaYF<sub>4</sub> Nanocrystals by AFM Nanoxerography: Creation of Anti-Counterfeiting Microtags. *Nanoscale* **2013**, *5* (20), 9587–9592.
- (98) Korenivski, V. GHz Magnetic Film Inductors. *J. Magn. Magn. Mater.* **2000**, *215–216*, 800–806.
- (99) Jin, F.-L.; Li, X.; Park, S.-J. Synthesis and Application of Epoxy Resins: A Review. *J. Ind. Eng. Chem.* **2015**, *29*, 1–11.

- (100) Jones, N. The Pull of Stronger Magnets. *Nature* **2011**, *472*, 22–23.
- (101) Coey, J. M. D. Permanent Magnets: Plugging the Gap. *Scr. Mater.* **2012**, *67* (6), 524–529.
- (102) Gutfleisch, O.; Willard, M. A.; Brück, E.; Chen, C. H.; Sankar, S. G.; Liu, J. P. Magnetic Materials and Devices for the 21st Century: Stronger, Lighter, and More Energy Efficient. *Adv. Mater.* **2011**, *23* (7), 821–842.
- (103) Gandha, K.; Elkins, K.; Poudyal, N.; Liu, X.; Liu, J. P. High Energy Product Developed from Cobalt Nanowires. *Sci. Rep.* **2014**, *4*.
- (104) Soumare, Y.; Garcia, C.; Maurer, T.; Chaboussant, G.; Ott, F.; Fiévet, F.; Piquemal, J.-Y.; Viau, G. Kinetically Controlled Synthesis of Hexagonally Close-Packed Cobalt Nanorods with High Magnetic Coercivity. *Adv. Funct. Mater.* **2009**, *19* (12), 1971–1977.
- (105) Dumestre, F.; Chaudret, B.; Amiens, C.; Respaud, M.; Fejes, P.; Renaud, P.; Zurcher, P. Unprecedented Crystalline Super-Lattices of Monodisperse Cobalt Nanorods. *Angew. Chem. Int. Ed.* **2003**, *42* (42), 5213–5216.
- (106) Liakakos, N.; Blon, T.; Achkar, C.; Vilar, V.; Cormary, B.; Tan, R. P.; Benamara, O.; Chaboussant, G.; Ott, F.; Warot-Fonrose, B.; et al. Solution Epitaxial Growth of Cobalt Nanowires on Crystalline Substrates for Data Storage Densities beyond 1 Tbit/in<sup>2</sup>. *Nano Lett.* **2014**, *14* (6), 3481–3486.
- (107) Panagiotopoulos, I.; Fang, W.; Ott, F.; Boué, F.; Ait-Atmane, K.; Piquemal, J.-Y.; Viau, G. Packing Fraction Dependence of the Coercivity and the Energy Product in Nanowire Based Permanent Magnets. *J. Appl. Phys.* **2013**, *114* (14), 143902.
- (108) Toson, P.; Asali, A.; Wallisch, W.; Zickler, G.; Fidler, J. Nanostructured Hard Magnets: A Micromagnetic Study. *IEEE Trans. Magn.* **2015**, *51* (1), 1–4.
- (109) Atmane, K. A.; Michel, C.; Piquemal, J.-Y.; Sautet, P.; Beaunier, P.; Giraud, M.; Sicard, M.; Nowak, S.; Losno, R.; Viau, G. Control of the Anisotropic Shape of Cobalt Nanorods in the Liquid Phase: From Experiment to Theory... and Back. *Nanoscale* **2014**, *6* (5), 2682.
- (110) Ott, F.; Maurer, T.; Chaboussant, G.; Soumare, Y.; Piquemal, J.-Y.; Viau, G. Effects of the Shape of Elongated Magnetic Particles on the Coercive Field. *J. Appl. Phys.* **2009**, *105* (1), 13915.
- (111) Arnold, D. P. Review of Microscale Magnetic Power Generation. *IEEE Trans. Magn.* **2007**, *43* (11), 3940–3951.
- (112) Wilson, S. A.; Jourdain, R. P. J.; Zhang, Q.; Dorey, R. A.; Bowen, C. R.; Willander, M.; Wahab, Q. U.; Willander, M.; Al-hilli, S. M.; Nur, O.; et al. New Materials for Micro-Scale Sensors and Actuators. *Mater. Sci. Eng. R Rep.* **2007**, *56* (1–6), 1–129.
- (113) Lv, X.; Wei, W.; Mao, X.; Chen, Y.; Yang, J.; Yang, F. A Novel MEMS Electromagnetic Actuator with Large Displacement. *Sens. Actuators Phys.* **2015**, *221*, 22–28.
- (114) Schiavone, G.; Desmulliez, M.; Walton, A. Integrated Magnetic MEMS Relays: Status of the Technology. *Micromachines* **2014**, *5* (3), 622–653.
- (115) Lenz, J.; Edelstein, S. Magnetic Sensors and Their Applications. *IEEE Sens. J.* **2006**, *6* (3), 631–649.
- (116) Herrera-May, A. L.; Lara-Castro, M.; López-Huerta, F.; Gkotsis, P.; Raskin, J.-P.; Figueras, E. A MEMS-Based Magnetic Field Sensor with Simple Resonant Structure and Linear Electrical Response. *Microelectron. Eng.* **2015**, *142*, 12–21.
- (117) Özkaya, K. Y.; Beyaz, M. İ. An Investigation on the Electromagnetic Design Optimization of Rotary Micromachines with Double-Layer Permanent Magnets. *Sens. Actuators Phys.* **2015**, *222*, 335–340.
- (118) Cakmak, O.; Elbuken, C.; Ermek, E.; Mostafazadeh, A.; Baris, I.; Erdem Alaca, B.; Kavakli, I. H.; Urey, H. Microcantilever Based Disposable Viscosity Sensor for Serum and Blood Plasma Measurements. *Methods* **2013**, *63* (3), 225–232.
- (119) Dufour, I.; Maali, A.; Amarouchene, Y.; Ayela, C.; Caillard, B.; Darwiche, A.; Guirardel, M.; Kellay, H.; Lemaire, E.; Mathieu, F.; et al. The Microcantilever: A Versatile Tool for Measuring the Rheological Properties of Complex Fluids. *J. Sens.* **2012**, *2012*, 1–9.
- (120) Autebert, J.; Coudert, B.; Champ, J.; Saias, L.; Guneri, E. T.; Lebofsky, R.; Bidard, F.-C.; Pierga, J.-Y.; Farace, F.; Descroix, S.; et al. High Purity Microfluidic Sorting and Analysis of Circulating Tumor Cells: Towards Routine Mutation Detection. *Lab Chip* **2015**.
- (121) Nicu, L.; Leichlé, T. Biosensors and Tools for Surface Functionalization from the Macro- to the Nanoscale: The Way Forward. *J. Appl. Phys.* **2008**, *104* (11), 111101.
- (122) Kneller, E. F.; Luborsky, F. E. Particle Size Dependence of Coercivity and Remanence of Single-Domain Particles. *J. Appl. Phys.* **1963**, *34* (3), 656.
- (123) Sung Lee, J.; Myung Cha, J.; Young Yoon, H.; Lee, J.-K.; Keun Kim, Y. Magnetic Multi-Granule Nanoclusters: A Model System That Exhibits Universal Size Effect of Magnetic Coercivity. *Sci. Rep.* **2015**, *5*, 12135.
- (124) Coey, J. M. D. New Permanent Magnets; Manganese Compounds. *J. Phys. Condens. Matter* **2014**, *26* (6), 64211.
- (125) Jiang, Y.; Dabade, V.; Allard, L. F.; Lara-Curzio, E.; James, R.; Wang, J.-P. Synthesis of  $\alpha'$  - Fe 16 N 2 Compound Anisotropic Magnet by the Strained-Wire Method. *Phys. Rev. Appl.* **2016**, *6* (2).

- (126) Berche, A.; Tedenac, J. C.; Jund, P. Thermodynamic Modeling of the Germanium–manganese System. *Intermetallics* **2014**, *47*, 23–30.
- (127) Rama Rao, N. V.; Gabay, A. M.; Hu, X.; Hadjipanayis, G. C. Fabrication of Anisotropic MnBi Nanoparticles by Mechanochemical Process. *J. Alloys Compd.* **2014**, *586*, 349–352.
- (128) Kurt, H.; Baadji, N.; Rode, K.; Venkatesan, M.; Stamenov, P.; Sanvito, S.; Coey, J. M. D. Magnetic and Electronic Properties of D022-Mn<sub>3</sub>Ge (001) Films. *Appl. Phys. Lett.* **2012**, *101* (13), 132410.
- (129) Fang, H.; Kontos, S.; Ångström, J.; Cedervall, J.; Svedlindh, P.; Gunnarsson, K.; Sahlberg, M. Directly Obtained  $\tau$ -Phase MnAl, a High Performance Magnetic Material for Permanent Magnets. *J. Solid State Chem.* **2016**, *237*, 300–306.
- (130) Skomski, R.; Coey, J. M. D. *Permanent Magnetism*; Institute of Physics Pub.: Bristol, UK; Philadelphia, PA, 1999.
- (131) Paulevé, J.; Dautreppe, D.; Laugier, J.; Néel, L. Une Nouvelle Transition Ordre-Désordre Dans Fe-Ni (50-50). *J. Phys. Radium* **1962**, *23*, 841–843.
- (132) Talapin, D. V.; Shevchenko, E. V.; Kornowski, A.; Gaponik, N.; Haase, M.; Rogach, A. L.; Weller, H. A New Approach to Crystallization of CdSe Nanoparticles into Ordered Three-Dimensional Superlattices. *Adv. Mater.* **2001**, *13* (24), 1868.
- (133) Talapin, D. V.; Lee, J.-S.; Kovalenko, M. V.; Shevchenko, E. V. Prospects of Colloidal Nanocrystals for Electronic and Optoelectronic Applications. *Chem. Rev.* **2010**, *110* (1), 389–458.
- (134) Pileni, M. P. 2D Superlattices and 3D Supracrystals of Metal Nanocrystals: A New Scientific Adventure. *J. Mater. Chem.* **2011**, *21* (42), 16748.
- (135) Cheon, J.; Park, J.-I.; Choi, J.; Jun, Y.; Kim, S.; Kim, M. G.; Kim, Y.-M.; Kim, Y. J. Magnetic Superlattices and Their Nanoscale Phase Transition Effects. *Proc. Natl. Acad. Sci. U. S. A.* **2006**, *103* (9), 3023–3027.
- (136) Varón, M.; Beleggia, M.; Kasama, T.; Harrison, R. J.; Dunin-Borkowski, R. E.; Puentes, V. F.; Frandsen, C. Dipolar Magnetism in Ordered and Disordered Low-Dimensional Nanoparticle Assemblies. *Sci. Rep.* **2013**, *3*.
- (137) Love, J. C.; Urbach, A. R.; Prentiss, M. G.; Whitesides, G. M. Three-Dimensional Self-Assembly of Metallic Rods with Submicron Diameters Using Magnetic Interactions. *J. Am. Chem. Soc.* **2003**, *125* (42), 12696–12697.
- (138) Clarke, R. S.; Scott, E. R. D. Tetrataenite-Ordered FeNi, a New Mineral in Meteorites. *Am. Mineral.* **1980**, *65*, 624.
- (139) Mizuguchi, M.; Sekiya, S.; Takanashi, K. Characterization of Cu Buffer Layers for Growth of L1<sub>0</sub>-FeNi Thin Films. *J. Appl. Phys.* **2010**, *107* (9), 09A716.
- (140) Kojima, T.; Ogiwara, M.; Mizuguchi, M.; Kotsugi, M.; Koganezawa, T.; Ohtsuki, T.; Tashiro, T.-Y.; Takanashi, K. Fe–Ni Composition Dependence of Magnetic Anisotropy in Artificially Fabricated L1<sub>0</sub>-Ordered FeNi Films. *J. Phys. Condens. Matter* **2014**, *26* (6), 64207.
- (141) Makino, A.; Sharma, P.; Sato, K.; Takeuchi, A.; Zhang, Y.; Takenaka, K. Artificially Produced Rare-Earth Free Cosmic Magnet. *Sci. Rep.* **2015**, *5*, 16627.
- (142) Sato, K.; Sharma, P.; Zhang, Y.; Takenaka, K.; Makino, A. Crystallization Induced Ordering of Hard Magnetic L1<sub>0</sub> Phase in Melt-Spun FeNi-Based Ribbons. *AIP Adv.* **2016**, *6* (5), 55218.
- (143) Lim, B. S.; Rahtu, A.; Park, J.-S.; Gordon, R. G. Synthesis and Characterization of Volatile, Thermally Stable, Reactive Transition Metal Amidinates. *Inorg. Chem.* **2003**, *42* (24), 7951–7958.
- (144) Lim, B. S.; Rahtu, A.; Gordon, R. G. Atomic Layer Deposition of Transition Metals. *Nat. Mater.* **2003**, *2* (11), 749–754.
- (145) Margeat, O.; Ciuculescu, D.; Lecante, P.; Respaud, M.; Amiens, C.; Chaudret, B. NiFe Nanoparticles: A Soft Magnetic Material? *Small* **2007**, *3* (3), 451–458.
- (146) Frisk, A.; Lindgren, B.; Pappas, S. D.; Johansson, E.; Andersson, G. Resonant X-Ray Diffraction Revealing Chemical Disorder in Sputtered L1<sub>0</sub> FeNi on Si(001). *J. Phys. Condens. Matter* **2016**, *28* (40), 406002.
- (147) Mibu, K.; Kojima, T.; Mizuguchi, M.; Takanashi, K. Local Structure and Magnetism of L1<sub>0</sub>-Type FeNi Alloy Films with Perpendicular Magnetic Anisotropy Studied through <sup>57</sup>Fe Nuclear Probes. *J. Phys. Appl. Phys.* **2015**, *48* (20), 205002.
- (148) Albertsen, J. F.; Knudsen, J. M.; Roy-Poulsen, N. O.; Vistisen, L. Meteorites and Thermodynamic Equilibrium in Fcc Iron-Nickel Alloys (25-50% Ni). *Phys. Scr.* **1980**, *22* (2), 171.
- (149) Pousthomis, M. From Chemical Synthesis of Nanoparticles to Nano-Structured Magnetic Materials : A Bottom-up Approach for Rare Earth Free Permanent Magnets, Toulouse, INSA, 2016.
- (150) Lu, A.-H.; Salabas, E. L.; Schüth, F. Magnetic Nanoparticles: Synthesis, Protection, Functionalization, and Application. *Angew. Chem. Int. Ed.* **2007**, *46* (8), 1222–1244.
- (151) Anagnostopoulou, E. A New Route for Rare-Earth Free Permanent Magnets: Synthesis, Structural and Magnetic Characterizations of Dense Assemblies of Anisotropic Nanoparticles, Université de Toulouse: Toulouse, 2016.

- (152) Nguyen, T. Y. M. Ferrite-Based Micro-Inductors for Power Systems on Chip: From Material Elaboration to Inductor Optimisation, Universite Toulouse III Paul Sabatier, 2014.
- (153) Shoji, Y.; Miura, K.; Mizumoto, T. Optical Nonreciprocal Devices Based on Magneto-Optical Phase Shift in Silicon Photonics. *J. Opt.* **2016**, *18* (1), 13001.
- (154) Van Parys, W.; Moeyersoon, B.; Van Thourhout, D.; Baets, R.; Vanwolleghem, M.; Dagens, B.; Decobert, J.; Le Gouezigou, O.; Make, D.; Vanheertum, R.; et al. Transverse Magnetic Mode Nonreciprocal Propagation in an Amplifying AlGaInAs/InP Optical Waveguide Isolator. *Appl. Phys. Lett.* **2006**, *88* (7), 71115.



## List of publications

### PATENT

- P1. “Process for controlling surface wettability” (WO/2007/087900)  
P. Colpo, F. Rossi, L.-M. Lacroix, M. Lejeune  
<http://www.wipo.int/pctdb/en/wo.jsp?wo=2007087900>

### PUBLICATIONS

- International publication in peer-reviewed journals

- A44. “Platinum tripods as nanometric frequency multiplexing devices”  
B. Camargo\*, B. Lassagne, R. Arenal, C. Gatel, T. Blon, G. Viau, L.-M. Lacroix\*, W. Escoffier, *Nanoscale in press*
- A43. “Surface-Engineering of Ultrathin Gold Nanowires: Tailored Self-Assembly and Enhanced Stability”  
E. S. A. Nouh, E. A. Baquero, L.-M. Lacroix, F. Delpech, R. Poteau, G. Viau\*,  
*Langmuir*, 3, 5456 (2017)
- A42. “Control of the crystal habit and magnetic properties of Co nanoparticles through the stirring rate.”  
K. Mrad, F. Schoenstein, H. T. T. Nong, E. Anagnostopoulou, A. Viola, L. Mouton, S. Mercone, C. Ricolleau, N. Jouini, M. Abderraba, L.-M. Lacroix, G. Viau, J.-Y. Piquemal\*,  
*Cryst Eng Comm*, 19, 3476 (2017)
- A41. “Magnetic ground states in nanocuboids of cubic magnetocrystalline anisotropy”  
F.J. Bonilla, L.-M. Lacroix, T. Blon\*, *J. Magn. Magn. Mater.* 428, 394-400 (2017)
- A40. “On the advantages of spring magnets compared to pure FePt : strategy for Rare- Earth Free Permanent magnets following a bottom-up approach.”  
M. Pousthomis, C. Garnero, C. Garcia-Marcelot, T. Blon, S. Cayez, C. Cassignol, V.A. Du, M. Krispin, R. Arenal, K. Soulantica, G. Viau, L.-M. Lacroix\*,  
*J. Magn. Magn. Mater.*, 424, 304-313 (2017)
- A39. “Magnetically Induced Continuous CO<sub>2</sub> Hydrogenation Using Composite Iron Carbide Nanoparticles of Exceptionally High Heating Power”  
A. Bordet, L.-M. Lacroix, P.-F. Fazzini, J. Carrey, K. Soulantica\*, B. Chaudret\*.  
*Angew. Chem. Int. Ed.* 55, 15894-15898 (2016)
- A38. “A 3D array of Co(II) cubanes with very strong magnetic anisotropy”  
N. Ben Saber, A. Ben Ali\*, L.-M. Lacroix, P. Gredin, B. Raquet, G. Viau  
*J. Alloys Compd.* 686, 447-452 (2016)
- A37. “Nano-scale to macroscopic-scale Co@CoSb core-shell nanorods: production, characterization and stability”  
U. Sanyal, S. Ener, E. Anagnostopoulou, M. Pousthomis, P.-F. Fazzini, L.-M. Lacroix, K. P. Skokov, O. Gutfleisch, G. Viau\*. *Chem. Mater.* 28, 4982-4990 (2016)

- A36. "A new approach to the mechanism of Fischer-Tropsch Syntheses arising from gas phase NMR and Mass Spectrometry"  
A. Bordet, L.-M. Lacroix, K. Soulantica, B. Chaudret\*. *Chem. Cat. Chem.* 8, 1727-1731 (2016)
- A35. "Electrospray Deposition of Isolated Chemically Synthesized Magnetic Nanoparticles"  
P. Agostini, A. Meffre, L.-M. Lacroix, D. Ugnati, T. Ondarçuhu, M. Respaud, B. Lassagne\*. *J. Nanopart. Res.* 18, 11 (2016)
- A34. "Dense arrays of cobalt nanorods as rare-earth free permanent magnets"  
E. Anagnostopoulou, B. Grindi, L.-M. Lacroix, F. Ott, I. Panagiotopoulos, G. Viau\*, *Nanoscale.* 8, 4020-4029 (2016)
- A33. "Size specific spin configurations in single iron nanomagnet: from flower to exotic vortices"  
C. Gatel\*, F.B. Bonilla, A. Meffre, E. Snoeck, B. Warot-Fonrose, B. Chaudret, L.-M. Lacroix, T. Blon\*, *NanoLett.* 15, 6952-6957 (2015)
- A32. "Towards rare-earth-free permanent magnets : a combinatorial approach exploiting the possibilities of modeling, shape anisotropy in elongated nanoparticles, and combinatorial thin-film approach"  
D. Niarchos\*, G. Giannopoulos, M. Gjoka, C. Sarafidis, V. Psycharis, J. Ruzs, A. Edström, O. Eriksson, P. Toson, J. Fidler, E. Anagnostopoulou, U. Sanyal, F. Ott, L.-M. Lacroix, G. Viau, C. Bran, M. Vazquez, L. Reichel, L. Schultz, S. Fähler, *JOM, The Journal of the Minerals, Metals and Materials Society*, 67, 1318-1328 (2015)
- A31. "Directed assembly of single colloidal gold nanowires by AFM nanoxerography"  
P. Moutet, L. M. Lacroix\*, A. Robert, M. Impéror-Clerc, G. Viau, L. Ressler\*. *Langmuir* 31, 4106-4112 (2015)
- A30. "Ultrathin Au Nanowires: soft-templating vs. liquid phase synthesis, a quantitative study."  
A. Loubat, L.-M. Lacroix\*, A. Robert, M. Impéror-Clerc, R. Arenal, L. Maron, B. Pansu, G. Viau. *J. Phys. Chem. C* 119, 4422-4430 (2015)
- A29. "Localized magnetization reversal processes in cobalt nanorods with different aspect ratios"  
M. Pousthomis, E. Anagnostopoulou, I. Panagiotopoulos, R. Boubekri, W. Fang, F. Ott, K. Ait Atmane, J.-Y. Piquemal, L.-M. Lacroix, G. Viau\*, *Nano Res.* 8, 2231-2241 (2015)
- A28. "Dynamic HAADF STEM observation of single atom chain as transient state of Au ultrathin nanowire breakdown."  
L.-M. Lacroix\*, R. Arenal\*, G. Viau, *J. Am. Chem. Soc.* 136, 13075-13077 (2014)
- A27. "Tuning deposition of magnetic metallic nanoparticles from periodic pattern to thin film by dip coating method"  
J. Dugay\*, R. P. Tan, A. Loubat, L.-M. Lacroix, J. Carrey\*, P. F. Fazzini, B. Chaudret, M. Respaud, *Langmuir*, 30, 9028 (2014)
- A26. "Growth and Self Assembly of Ultrathin Au Nanowires into Expanded Hexagonal Superlattice Studied by in situ SAXS"  
A. Loubat, M. Impéror-Clerc, B. Pansu, F. Meneau, B. Raquet, G. Viau, L.-M. Lacroix\*, *Langmuir* 30, 4005 (2014)

- A25. "Co-Fe Nano-dumbbells: Synthesis, Structure and Magnetic Properties."  
N. Liakakos, C. Gatel, T. Blon, T. Altantzis, S. Lentijo, C. Garcia, L.-M. Lacroix, M. Respaud, S. Bals, G. Van Tendeloo, K. Soulantica\*, *NanoLett*, 14, 2747 (2014)
- A24. "Charge transport and interdot coupling tuned by the tunnel barrier length in assemblies of nanoparticles surrounded by organic ligands".  
J. Dugay, R.P. Tan\*, M. Ibrahim, C. Garcia, J. Carrey\*, L.-M. Lacroix, P.-F. Fazzini, G. Viau, M. Respaud, *Phys. Rev. B*, 89, 041406(R) (2014).
- A23. "Stoichiometry-Controlled FeP Nanoparticles from Single Source Precursor".  
C. Dreher, W.-S. Ojo, S. Bauer, S. Xu, M. Zabel, B. Chaudret, L.-M. Lacroix, M. Scheer, C. Nayral, F. Delpech\*, *Chem. Comm.* 49, 11788 (2013)
- A22. "Carbon Coating, Carburization and High Temperature Stability Improvement of Cobalt Nanorods "  
M. Ibrahim, C. Garcia, K. Ait Atmane, E. Berrichi, L.-M. Lacroix, A. Zwick, B. Warot-Fonrose, S. Lachaize, P. Decorse, J.-Y. Piquemal, G. Viau\*, *J. Phys. Chem. C*, 117, 15808 (2013)
- A21. "New generation of magnetic and luminescent nanoparticles for in-vivo real-time imaging."  
L.-M. Lacroix\*, F. Delpech, C. Nayral, S. Lachaize, B. Chaudret, *Interf. Focus*, 3 (3), 20130014 (2013)  
*Invited paper*
- A20. "Cotunneling transport in ultra-narrow gold nanowire bundles"  
A. Loubat, W. Escoffier, L.-M. Lacroix, G. Viau, R.P. Tan, J. Carrey, B. Warot-Fonrose and B. Raquet\*, *Nano. Res.*, 6, 644 (2013)
- A19. "Stabilizing vortices in interacting nano-objects : a chemical approach"  
L.-M. Lacroix\*, S. Lachaize, F. H ue, C. Gatel, T. Blon, R.P. Tan, J. Carrey, B. Warot-Fonrose, B. Chaudret, *NanoLett*. 12, 3245-3250 (2012)
- A18. "Tuning complex shapes in Pt(0) nanoparticles : from cubic dendrites to five-fold stars"  
L.-M. Lacroix\*, C. Gatel, R. Arenal, C. Garcia, S. Lachaize, T. Blon, B. Warot-Fonrose, E. Snoeck, B. Chaudret, G. Viau, *Angew. Chem. Int. Ed*, 51, 4690-4694 (2012)
- A17. "Magnetic Nanoparticles for Magnetoresistance-Based Biodetection."  
X. Sun, D. Ho, L.-M. Lacroix, Q. Xiao, S. Sun\*, *IEEE Biodetection*, 11, 46-53 (2012)
- A16. "Modeling and Development of a Biosensor Based on Optical Relaxation Measurements of Hybrid Nanoparticles"  
S. Schrittwieser, F. Ludwig, J. Dieckhoff, K. Soulantica, G. Viau, L.-M. Lacroix, S. M. Lentijo, R. Boubekri, J. Maynadi e, A. Huetten, H. Brueckl, J. Schotter\*, *ACS Nano*, 6, 791-801 (2012).
- A15 "Room temperature tunnel magnetoresistance in self-assembled chemically-synthesized metallic iron nanoparticles"  
J. Dugay, R.P. Tan\*, A. Meffre, T. Blon, L.-M. Lacroix, J. Carrey\*, P. F. Fazzini, S. Lachaize, B. Chaudret, M. Respaud, *Nano Lett.*, 11, 5128 - 5134 (2011)
- A14 "Optimal size of nanoparticles for magnetic hyperthermia : a combined theoretical and experimental study"  
B. Mehdaoui, A. Meffre, J. Carrey\*, S. Lachaize, L.-M. Lacroix, M. Gougeon, B. Chaudret, M. Respaud, *Adv. Funct. Mater.*, 21, 4573 - 4581 (2011)

- A13. "Stable single crystalline bcc-Fe nanoparticles"  
L.-M. Lacroix, N. F. Huls, D. Ho, X. Sun, K. Cheng, S. Sun\*, *Nano Lett.*, *11*, 1641-1645 (2011).
- A12. "Internal structure of Al hollow nanoparticles generated by laser ablation in liquid ethanol"  
 G. Viau\*, V. Collière, L.-M. Lacroix, G. A. Shafeev, *Chem. Phys. Lett.*, *501*, 419 - 422 (2011)
- A11. "Large specific absorption rates in the magnetic hyperthermia properties of metallic iron nanocubes."  
 B. Mehdaoui, A. Meffre, L.-M. Lacroix, J. Carrey\*, S. Lachaize, M. Gougeon, M. Respaud, B. Chaudret, *J. Magn. Magn. Mater.*, *322*, L49 (2010)
- A10. "Magnetic Nanoparticles as both Imaging probes and therapeutics agents".  
L.-M. Lacroix, D. Ho, S. Sun\*, *Curr. Top. Med. Chem.*, *10*, 1184 - 1197 (2010)
- A9. "Synthesis of High Moment CoFe Nanoparticles via Interfacial Diffusion in Core/Shell Structured Co/Fe"  
 C. Wang, S. Peng, L.-M. Lacroix, S. Sun\*, *Nano. Res.*, *2*, 380 (2009)
- A8. "Magnetoresistance and collective Coulomb blockade in super-lattices of CoFe nanoparticles"  
 R. P. Tan\*, J. Carrey\*, C. Desvaux, L.-M. Lacroix, P. Renaud, B. Chaudret, M. Respaud\*, *Phys. Rev. B*, *79*, 174428 (2009)
- A7. "Magnetic hyperthermia in single-domain monodisperse FeCo nanoparticles : Evidence for Stoner-Wohlfarth behaviour and large losses"  
L.-M. Lacroix, R. Bel Malaki, J. Carrey, S. Lachaize, G. F. Goya, B. Chaudret, M. Respaud, *J. Appl. Phys.*, *105*, 023911 (2009)
- A6. "Iron Nanoparticles Growth in Organic Super-Structures"  
L.-M. Lacroix, S. Lachaize\*, A. Falqui, M. Respaud, B. Chaudret, *J. Am. Chem. Soc.*, *131*, 549 (2009)
- A5. "A frequency-adjustable electromagnet for hyperthermia measurements on magnetic nanoparticles."  
L.-M. Lacroix, J. Carrey\*, M. Respaud, *Rev. Sci. Instrum.*, *79*, 093909 (2008)
- A4. "Magnetic configurations of 30nm Iron Nanocubes Studied by Electron Holography"  
 E. Snoeck\*, C. Gatel, L.-M. Lacroix, T. Blon, S. Lachaize, J. Carrey, M. Respaud, B. Chaudret, *Nano Lett.*, *8*, 4293 (2008)
- A3. "Deposition of Nanobead Hexagonal Crystals Using Silicon Microcantilevers",  
 A. Valsesia, T. Leichle, L.-M. Lacroix, L. Nicu, F. Bretagnol, P. Colpo\*, F. Rossi, C. Bergaud, *Small*, *2(12)*, 1444 -1447 (2006)
- A2. "Plasma-Based Processes for Surface Wettability Modification",  
 M. Lejeune, L.-M. Lacroix, F. Bretagnol, A. Valsesia, P. Colpo\*, F. Rossi, *Langmuir*, *22(7)*, 3057 - 3061 (2006)
- A1. "Tunable rough surfaces : A new approach for elaboration of superhydrophobic films",  
L.-M. Lacroix, M. Lejeune\*, L. Ceriotti, M. Kormunda, T. Meziani, P. Colpo, F. Rossi, *Surface Science*, *592 (1-3)*, 182 -188 (2005)  
**5th of the top 25 hottest articles Surface Science (2005)**

- [Conference proceedings in peer-reviewed international journals](#)

AC2. “Magnetic anisotropy determination and magnetic hyperthermia properties of small Fe nanoparticles in the superparamagnetic regime”

B. Mehdaoui, A. Meffre, L.-M. Lacroix, J. Carrey\*, S. Lachaize, M. Respaud, M. Gougeon, B. Chaudret, *J. Appl. Phys.*, *107*, 09A324 (2010)

AC1. “Ultra small iron Nanoparticles: effect of size reduction on anisotropy and magnetization”.

L.-M. Lacroix\*, S. Lachaize, A. Falqui, T. Blon, J. Carrey, M. Respaud, F. Dumestre, C. Amiens, O. Margeat, P. Lecante, E. Snoeck, B. Chaudret, *J. Appl. Phys.*, *103*, 07D521 (2008)

- [National publication in peer reviewed journals – Invited papers](#)

NA3. « De nouveaux aimants permanents sans terre rare à base de nanoparticules métalliques anisotropes »

E. Anagnostopoulou, M. Pousthomis, L.-M. Lacroix, F. Ott, J.-Y. Piquemal, G. Viau, *Actualité Chimique*, 408 (2016)

NA2. ”La cristallographie à l’échelle nanométrique : études structurales de nanoparticules, de leur mode de croissance en relation avec leurs propriétés”

B. Chaudret, P. Fazzini, L.-M. Lacroix, P. Lecante, K. Soulantica, G. Viau, *Actualité Chimique*, 387, 153 (2014)

NA1. “Nanoparticules de fer de taille contrôlée pour l’hyperthermie”.

L.-M. Lacroix, S. Lachaize, J. Carrey, M. Respaud, B. Chaudret, *Actualité chimique*, *351*, 28-35 (2011)  
*Article invité*

- [Book chapter](#)

Ch2. “Soft chemistry nanowires for permanent magnet fabrication”

F. Ott, I. Panagiotopoulos, E. Anagnostopoulou, M. Pousthomis, L.-M. Lacroix, G. Viau, J.-Y. Piquemal

*Magnetic nano- and microwires* Ch21: pp 629-651

Edited by Manuel Vazquez, Woodhead publishing Series in Electronic and Optical Materials : Number 80, 2015.

Ch1. “Organometallic Nanoparticles”

P. Lara, K. Philippot, L.-M. Lacroix, S. Lachaize, N. Liakakos, K. Soulantica B. Chaudret  
*Advances in Organometallic Chemistry and Catalysis* Ch31: pp 407-420

Edited by Armando J.L. Pombeiro, John Wiley and Sons 2014.

The Silver/Gold jubilee International Conference on Organometallic Chemistry Celebratory Book

## COMMUNICATIONS (limited to the presentation I gave)

- Invited talks

- 1) **Solution Based Synthesis of Nanomaterials and their Organization for Hybrid Device Structures** (Telluride, 1-4 Aout 16)  
“On the advantage of a bottom-up approach for Nano-structured magnets”  
Evangelia Anagnostopoulou, Marc Pousthomis, Lise-Marie Lacroix, Guillaume Viau, F. Ott
- 2) **ETPMSE** (Toulouse, Juill. 16),  
“Synthèse chimique et auto-assemblage de nanoparticules pour la plasmonique »  
E. Dujardin, L.-M. Lacroix
- 3) **Nanospain 2016** (Logrono, 15-18 Mars 16)  
“Nanoparticles with optimized properties : from chemical synthesis to assembly  
A bottom-up approach for nanostructured materials”  
Lise-Marie Lacroix, Evangelia Anagnostopoulou, Christophe Gatel, Raul Arenal, Guillaume Viau
- 4) **IWMNN 2015**, Internal workshop on Magnetic Nanowire and Nanotubes (Meersburg, 17-20 Mai 15)  
“From High Aspect Ratio Nanoparticles Synthesis to Nano-Structured Permanent Magnets”  
Evangelia Anagnostopoulou, Marc Pousthomis, Billel Grindhi, Cécile Marcelot, Udishnu Sanyal, Lise-Marie Lacroix, Guillaume Viau
- 5) **MNE 2012** (Toulouse, Sept. 12),  
"Synthesis of nanoparticles, self assembly, properties and applications"  
L.-M. Lacroix, J. Carrey, G. Viau, B. Chaudret
- 6) **JSI 2012**, (Saclay, Janv. 12)  
"Synthèse de Nanoparticules Métalliques : Vers un Contrôle de Formes Unique"  
L.-M. Lacroix, S. Lachaize, C. Gatel, R. Arenal, J. Carrey, T. Blon, B. Warot, E. Snoeck, M. Respaud, B. Chaudret, G. Viau
- 7) **SAIAM Workshop**, (Bangkok, Mars. 10),  
"Nanoparticles for biomedical applications : interest of the chemical synthesis"  
L.-M. Lacroix, S. Lachaize, J. Carrey, G. Viau, B. Chaudret
- 8) **JFJPC10**, (Ambleteuse, Oct. 09),  
“Nanoparticules optimisées pour l’hyperthermie : synthèse, caractérisation, mesure de puissance dissipée”  
L.-M. Lacroix, S. Lachaize, J. Carrey, B. Chaudret, T. Blon, C. Gatel, E. Snoeck, M. Respaud.

### **Prix de thèse SCF – DCP**

- Oral presentation

- 9) **Intermag** (Dublin, Irlande, 24-28 Avril 17), *Crystalline Soft Magnetic Materials*  
« Single crystalline FeCo nanoparticles with tuneable size, shape and composition : towards unique magnetic properties”  
C. Garnero, A. Pierrot, R. Arenal, C. Gatel, K. Soulantica, B. Chaudret, T. Blon, L.-M. Lacroix
- 10) **Intermag** (Dublin, Irlande, 24-28 Avril 17), *Magnetic Nanoparticles, Nanowires, and 3D Structures III*  
“Co nanorods : large-scale synthesis and compaction into nano-structured permanent magnets”  
E. Anagnostopoulou, S. Ener, M. Pousthomis, F. Ott, O. Gutfleisch, G. Viau, L.-M. Lacroix

- 11) **EMRS** (Lille, France, 2-6 Mai 16), *Substitution of critical raw materials*  
 "From high aspect ratio nanoparticles synthesis to nano-structured rare-earth free permanent magnets"  
 E. Anagnostopoulou, B. Grindi, F. Ott, L.-M. Lacroix, G. Viau.
  - 12) **EMRS** (Lille, France, 2-6 Mai 16), *In situ studies of functional nano materials at large scale facilities*  
 "Growth and Self Assembly of Ultrathin Au Nanowires into Expanded Hexagonal Superlattice Studied by in situ SAXS"  
 A. Loubat, M. Imp rator-Clerc, B. Pansu, F. Meneau, G. Viau, L.-M. Lacroix.
  - 13) **EMRS** (Lille, France, 2-6 Mai 16), *Established and emerging nanocolloids*  
 "Synthesis of Pt nanoparticles exhibiting complex shapes : new "toys" for electronic transport measurement"  
L.-M. Lacroix, G. Viau, B. Lassagne, B. Camargo, W. Escoffier, C. Gatel, R. Arenal
  - 14) **Euromat** (Warsow, Poland, 21-24 Sept. 15);  
 "Ultrathin Au nanowires : growth and self assembly in liquid-phase"  
L.-M. Lacroix, G. Viau, L. Ressler, M. Imperor-Clerc, R. Arenal.
  - 15) **TNT2015** (Toulouse, 7-11 Sept. 15);  
 "Ultrathin Au nanowires : towards 1D electronic properties"  
L.-M. Lacroix, M. Imperor-Clerc, R. Arenal, B. Pansu, L. Ressler, P. Moutet, G. Viau
  - 16) **AMN7** (Nelson, New Zealand, 8-12 Fev. 15),  
 "Fe nanocubes : synthesis and applications"  
L.-M. Lacroix, F. Bonilla, T. Blon, J. Carrey, A. Meffre, S. Lachaize, M. Respaud, B. Chaudret, C. Gatel, E. Snoeck.
  - 17) **NanoSEA** (Marseille, France, 7-11 Jul. 14), *Metallic nanoparticles*  
 "Synthesis of metallic nanoparticles exhibiting complex shapes : the versatility of liquid phase synthesis"  
L.-M. Lacroix, M. Imp rator-Clerc, C. Gatel, A. Arenal, S. Lachaize, M. Respaud, J. Carrey, T. Blon, B. Raquet, B. Chaudret, G. Viau
  - 18) **EMRS** (Lille, France, 26-31 Mai 14), *Established and emerging nanocolloids*  
 "Ultrathin gold nanowires: growth mechanism and assembly by nanoxerography"  
L.-M. Lacroix, P. Moutet, A. Loubat, M. Imperor-Clerc, L. Ressler, G. Viau
  - 19) **12<sup>th</sup> Joint MMM/ InterMag Conference** (Chicago, USA, Jan. 13), *Magnetic nanoparticles*  
 "Stabilizing vortices in interacting nano-objects: a chemical approach",  
L.-M. Lacroix, C. Gatel, T. Blon, S. Lachaize, R. P. Tan, J. Carrey, F. Hue, B. Chaudret.
  - 20) **ACS Meeting**, (Washington DC, USA, Aout. 09),  
 "Synthesis of air-stable superparamagnetic nanoparticle for highly sensitive bio-detection"  
L.-M. Lacroix, D. Ho, S. Peng, K. Chen, S. Sun
  - 21) **12<sup>eme</sup> Colloque Louis N el**, (La Grande-Motte, Sept. 08), *Nanoparticules, Nanofils, nanostructures*  
 "Nanoparticules de fer pour l'hyperthermie : synth se, propri t s magn tiques, holographie"  
L.-M. Lacroix, S. Lachaize, J. Carrey, B. Chaudret, T. Blon, C. Gatel, E. Snoeck, M. Respaud.
  - 22) **52<sup>nd</sup> Magnetism and Magnetic Materials** (Tampa, USA, Nov. 07), *Nanoparticles and Self-Assembly*  
 "Iron nanoparticles : size and shape control, self assembly and magnetic studies",  
L.-M. Lacroix, S. Lachaize, A. Falqui, J. Carrey, M. Respaud, E. Snoeck, B. Chaudret.
- Student Travel Support**
- 23) **Journ e Chimie-Biologie** (Toulouse, Mai 07)  
 "Synth se de nanoparticules de fer : effet des ligands sur le contr le de la taille et de la forme"  
L.-M. Lacroix, S. Lachaize, A. Falqui, M. Respaud, B. Chaudret

- 24) **Matériaux 2006**, (Dijon, Nov. 06) : *Matériaux magnétiques et leurs applications*.  
"Synthèse et caractérisation de nanoparticules de fer pour l'hyperthermie."  
L.-M. Lacroix, S. Lachaize, J. Carrey, B. Chaudret.
- 25) **10<sup>èmes</sup> Journées de la Matière Condensée**, (Toulouse, août 06) : *Physique des systèmes vivants*.  
"Nano-oncologie : des nanoparticules pour l'hyperthermie."  
L.-M. Lacroix, N. El-Hawi, F. Delpech, S. Lachaize, C. Nayral, J. Carrey, B. Chaudret
- 26) **Journée SFC Jeunes chercheurs** (Toulouse, Avril 06)  
« L'hyperthermie magnétique ou comment des nanoparticules de fer pourraient être utilisées pour le traitement de tumeurs »  
L.-M. Lacroix, N. El-Hawi, F. Delpech, C. Nayral, S. Lachaize, J. Carrey, B. Chaudret  
**Best presentation award**

- **Poster presentation**

- 1) **AMN7** (Nelson, New Zealand, 8-12 Fev. 15),  
"Fe nanocubes : synthesis and applications"  
L.-M. Lacroix, F. Bonilla, T. Blon, J. Carrey, A. Meffre, S. Lachaize, M. Respaud, B. Chaudret, C. Gatel, E. Snoeck.
- 2) **JSI 2015** (Toulouse, 25-27 Janv. 15)  
« Nanofils d'or ultrafins : mécanisme de croissance et étude de stabilité »  
G. Viau, L. Ressler, M. Impéror-Clerc, L.-M. Lacroix.
- 3) **13ème Colloque Louis Néel**, (Albé, Avril 09), *Biotechnologie*  
" Synthèse de nanoparticules de fer stables à l'air : premiers tests pour applications biomédicales."  
L.-M. Lacroix, D. Ho, S. Sun
- 4) **12ème Colloque Louis Néel**, (La Grande-Motte, Sept. 08), *Dynamique*  
" Etude de nanoparticules de FeCo en hyperthermie magnétique"  
L.-M. Lacroix, R. Bel-Malaki, J. Carrey, S. Benderbous, S. Lachaize, M. Respaud, B. Chaudret.  
**Best poster award**
- 5) **NANAX 03** (Lecce, Italie, Mai. 08),  
"Iron nanoparticles synthesis: control of the growth environment anisotropy"  
L.-M. Lacroix, S. Lachaize, J. Carrey, T. Blon, A. Falqui, M. Respaud, E. Snoeck, B. Chaudret.
- 6) **WOMEN in NANO** (Kranjska Gora, SLOVENIE, Fév. 08)  
"Growth mechanism of iron nanoparticles : size and shape control"  
L.-M. Lacroix, S. Lachaize, J. Carrey, A. Falqui, M. Respaud, B. Chaudret.  
**Student Travel Support**
- 7) **11ème Colloque Louis Néel**, (Lyon, Mars. 07), *Nanoparticules et Nanofils*  
" Optimisation de particules magnétiques de fer pour l'hyperthermie"  
L.-M. Lacroix, J. Carrey, S. Lachaize, A. Falqui, M. Respaud, B. Chaudret.  
**Prix du meilleur poster**
- 8) **GALERNE 06** (Bollwiller, Sept. 06)  
"Rôle de la concentration d'acide sur le contrôle de la taille de nanoparticules monodisperses de fer"  
L.-M. Lacroix, N. El-Hawi, J. Carrey, B. Chaudret, S. Lachaize.
- 9) **Journée 2006 de la Division de Chimie de Coordination SFC**, (Toulouse, Avril 06)  
"Synthèse de nanoparticules de fer à forte aimantation : approche organométallique"  
L.-M. Lacroix, N. El-Hawi, S. Lachaize, B. Chaudret.

- 10) **17<sup>th</sup> International Symposium on Plasma Chemistry (ISPC)**, (Toronto, Canada, Août 05)  
 “Plasma-Based Processes for Surface Wettability Modification”,  
L.-M. Lacroix, M. Lejeune, A. Valsesia, P. Colpo, T. Meziani, G. Ceccone, F. Rossi
- 11) **53<sup>rd</sup> AVS International Symposium**, (San Francisco, USA, Nov. 05)  
 “Tuneable rough surfaces : A new approach for elaboration of superhydrophobic films”,  
L.-M. Lacroix, M. Lejeune, L. Ceriotti, P. Colpo, F. Rossi

- [Invited seminars](#)

- 1) **Institut Charles Gerhardt** : Annual meeting INMO (Montpellier, 7 Jul. 17)  
 « Metallic nanoparticles : study of the growth mechanism for size, shape and composition control”
- 2) **Cork University** : Departement of Chemistry (Cork, 22 Fev. 17)  
 « Metallic nanoparticles synthesized by wet-chemistry : new building blocks for nanostructured materials”
- 3) **Institut de Chimie de Toulouse** ; Prix Young Investigator Award (Toulouse, 1 Jui. 16)  
 « Nanoparticules métalliques de formes complexes : étude des mécanismes de croissance».
- 4) **Laboratoire d’Analyse et d’Architecture des Systèmes** – équipe NanoBioSystèmes (Toulouse, 20 Janv. 16)  
 « Synthèse de nanoparticules métalliques de formes complexes».  
L.-M. Lacroix, T. Blon, B. Lassagne, L. Ressler, K. Soulantika, B. Chaudret, G. Viau, C. Gatel, B. Warot-Fonrose, E. Snoeck, R. Arenal, M. Imperor-Clerc, B. Pansu, W. Escoffier,
- 5) **Institut de Sciences et d’Ingénierie Supramoléculaires** - Luisa de Cola (Strasbourg, 17 Avril 15)  
 “Synthesis of metallic nanoparticles exhibiting complex shapes”  
L.-M. Lacroix, T. Blon, C. Gatel, R. Arenal, C. Garnero, P. Moutet, A. Loubat, M. Imperor-Clerc, L. Ressler, B. Chaudret, G. Viau
- 6) **Victoria University** (Wellington, New Zealand, 19 Fev. 15)  
 “Synthesis of metallic nanoparticles with controlled properties”  
L.-M. Lacroix, T. Blon, C. Gatel, R. Arenal, C. Garnero, P. Moutet, A. Loubat, M. Imperor-Clerc, L. Ressler, B. Chaudret, G. Viau
- 7) **LMA User’s day** (Saragossa, Juin 13)  
 “Complexity at the nanoscale : control of nanoparticle shape and composition”  
L.-M. Lacroix, K. Soulantika, C. Gatel, R. Arenal, S. Lachaize, B. Chaudret, G. Viau
- 8) **TALEM Workshop** (Toulouse, Mars 13)  
 “Synthesis of nanoparticles with controlled composition and shape”  
L.-M. Lacroix, K. Soulantika, C. Gatel, R. Arenal, S. Lachaize, B. Chaudret, G. Viau
- 9) **Nanocat Workshop** (Toulouse, Dec. 11)  
 “Synthesis of Pt nanoparticles : From 5 fold-stars to monodisperse cubic dendrites”  
L.-M. Lacroix, C. Gatel, R. Arenal, S. Lachaize, B. Chaudret, G. Viau
- 10) **TEM UCA, Universidad de Cadiz** (Cadiz, Spain, Juill. 10)  
 “Chemical synthesis of magnetic nanoparticles”  
L.-M. Lacroix, S. Lachaize, J. Carrey, T. Blon, M. Respaud, E. Snoeck, C. Gatel, B. Chaudret

- 11) **Instituto de Nanociencia de Aragon INA** (Saragosse, Spain, Fév. 10)  
“From magnetic studies to optimized chemical synthesis”  
L.-M. Lacroix, J. Carrey, T. Blon, B. Lassagne, M. Respaud, C. Gatel, E. Snoeck.

- [Invited Professor](#)

- 1) **Victoria University** (Wellington, New Zealand, Fev. 15)  
A/Prof Richard Tilley. NanoOnco Dumont d’Urville grant.

[Science promotion](#)

- 1) **EREMIP forum CithEtique** (Toulouse, 9 Sept 17)  
Table ronde : Les nanoparticules – vers une démarche éthique
- 2) **Radio France Bleu** (Toulouse, 4 Sept 17)  
Chronique dans le cadre de la nuit européenne des chercheurs
- 3) **Radio Campus FM** (Toulouse, 10 Décembre 16)  
Emission 20 mg de science : « Nano et Société »
- 4) **Chambre de Commerce et d’Industrie du Jura** (Lons-le-Saunier, 17 Mars 17)  
« Les nanoparticules : briques de base pour les technologies du futur ? »
- 5) **Asso Science** (Toulouse, 24 Mars 16)  
« Les nanoparticules dans tous leurs états ! »
- 6) **Ouverture de l’UPS** (Toulouse, 13 Mars 14)  
« Les nanoparticules métalliques dans tous leurs états »
- 7) **50 ans INSA Toulouse** (Toulouse, 21 Mars 13)  
"Nanoparticules : de la synthèse aux applications"

## Iron Nanoparticle Growth in Organic Superstructures

Lise-Marie Lacroix,<sup>†</sup> Sébastien Lachaize,<sup>\*,†</sup> Andrea Falqui,<sup>†,§</sup> Marc Respaud,<sup>†</sup> and Bruno Chaudret<sup>‡</sup>

Université de Toulouse, INSA, UPS, LPCNO, 135 avenue de Rangueil, F-31077 Toulouse, France, CNRS, LPCNO, F-31077 Toulouse, France, and Laboratoire de Chimie de Coordination du CNRS, 205 route de Narbonne, 31077 Toulouse Cedex 4, France

Received July 22, 2008; E-mail: sebastien.lachaize@insa-toulouse.fr

**Abstract:** A tunable synthesis of iron nanoparticles (NPs) based on the decomposition of  $\{\text{Fe}[\text{N}(\text{SiMe}_3)_2]_2\}_2$  in the presence of organic superstructures composed of palmitic acid and hexadecylamine is reported. Control of the size (from 1.5 to 27 nm) and shape (spheres, cubes, or stars) of the NPs has been achieved. An environment-dependent growth model is proposed on the basis of results obtained for the NP morphology under various conditions and a complete Mössbauer study of the colloid composition at different reacting stages. It involves (i) an anisotropic growth process inside organic superstructures, leading to monocrystalline cubic NPs, and (ii) isotropic growth outside these superstructures, yielding polycrystalline spherical NPs.

### Introduction

Many methods that are presently available for the synthesis of metal nanoparticles (NPs) lead to the formation of mono-disperse objects.<sup>1</sup> These nano-objects can further self-organize when deposited on a surface or, in certain cases, directly form large superlattices in solution.<sup>2</sup> However, the processes leading to strict monodispersity of nanoparticles or to the formation of supercrystals in solution are not fully understood. Our group has obtained several metal nanoparticle superlattices composed of either tin, iron, or iron/cobalt.<sup>3</sup> We concentrate in this paper on the process of iron nanoparticle growth, given the present need for highly magnetic nanoparticles.

Magnetic nanoparticles are attractive for various applications provided that strong control of their physical properties can be achieved.<sup>4,5</sup> Metallic iron has a high magnetization at room temperature [ $M_S(\text{bulk}) = 212 \text{ emu g}^{-1}$ ] and a superparamagnetic behavior (for sizes ranging from 1 to 12 nm) that, from a physical point of view, makes it a material of choice for biomedical applications such as magnetic fluid hyperthermia (MFH) and magnetic resonance imaging (MRI).<sup>6</sup> However, its

high reactivity, especially with dioxygen, makes it unusable under these conditions if unprotected. Our research aims at producing magnetic core/shell nanoparticles that take advantage of an iron core whose magnetic properties are preserved from degradation by means of a protective layer.<sup>7</sup> Before taking up this challenge, we first worked on the adjustment of the magnetic properties of the iron core for the above-mentioned applications, that is to say, the adjustment of its size and shape and the nature of surface ligands. Therefore, a good understanding of iron NP formation is a crucial point.<sup>1a,8</sup> Several research groups have already prepared iron NPs of very good quality, but usually with magnetizations lower than that of the bulk, especially at small sizes.<sup>2a,9</sup> In addition, some knowledge has already been reported on size control in different studies: in particular, it has been pointed out that the acid concentration is a key parameter.<sup>9f,10</sup> Our group has previously reported that the reduction of  $\{\text{Fe}[\text{N}(\text{SiMe}_3)_2]_2\}_2$  under  $\text{H}_2$  leads to unoxidized, small iron NPs of homogeneous size near 1.5 nm that exhibit bulk magnetization.<sup>11</sup> The same method leads to larger and well-defined NPs with bulk magnetization when a mixture of long-chain acid and

<sup>†</sup> Université de Toulouse and LPCNO.

<sup>‡</sup> Laboratoire de Chimie de Coordination du CNRS.

<sup>§</sup> Present address: Fondazione Istituto Italiano di Tecnologia (IIT), Via Morego 30, 16163 Genova, Italy.

- (1) (a) Yin, Y.; Alivisatos, A. P. *Nature* **2005**, *437*, 664–670. (b) Park, J.; Joo, J.; Kwon, S. G.; Jang, Y.; Hyeon, T. *Angew. Chem., Int. Ed.* **2007**, *46*, 4630–4660. (c) Hyeon, T. *Chem. Commun.* **2003**, 927, 934.
- (2) (a) Sun, S.; Zeng, H. *J. Am. Chem. Soc.* **2002**, *124*, 8204–8205. (b) Park, J.; An, K.; Hwang, Y.; Park, J. G.; Noh, H. J.; Kim, J. Y.; Park, J. H.; Hwang, N. M.; Hyeon, T. *Nat. Mater.* **2004**, *3*, 891–895. (c) Sun, S.; Murray, C. B. *J. Appl. Phys.* **1999**, *85*, 4325–4330. (d) Soulantica, K.; Maisonnat, A.; Senocq, F.; Fromen, M.-C.; Casanove, M.-J.; Chaudret, B. *Angew. Chem., Int. Ed.* **2001**, *40*, 2984–2986. (e) Legrand, J.; Ngo, A.-T.; Petit, C.; Pileni, M.-P. *Adv. Mater.* **2001**, *13*, 58–61.
- (3) (a) Dumestre, F.; Chaudret, B.; Amiens, C.; Renaud, P.; Fejes, P. *Science* **2004**, *303*, 821–823. (b) Soulantica, K.; Maisonnat, A.; Fromen, M.-C.; Casanove, M.-J.; Chaudret, B. *Angew. Chem., Int. Ed.* **2003**, *42*, 1945–1949. (c) Desvieux, C.; Amiens, C.; Fejes, P.; Renaud, P.; Respaud, M.; Lecante, P.; Snoeck, E.; Chaudret, B. *Nat. Mater.* **2005**, *4*, 750–753.

- (4) (a) Sun, S.; Murray, C. B.; Weller, D.; Folks, L.; Moser, A. *Science* **2000**, *287*, 1989–1992. (b) Toneguzzo, P.; Viau, G.; Acher, O.; Fiévet-Vincent, F.; Fiévet, F. *Adv. Mater.* **1998**, *10*, 1032–1035. (c) Maurer, T.; Ott, F.; Chaboussant, G.; Soumare, Y.; Piquemal, J.-Y.; Viau, G. *Appl. Phys. Lett.* **2007**, *91*, 17501. (d) Jeong, U.; Teng, X.; Wang, Y.; Yang, H.; Xia, Y. *Adv. Mater.* **2007**, *19*, 33–60. (e) Ito, A.; Shinkai, M.; Honda, H.; Kobayashi, T. *J. Biosci. Bioeng.* **2005**, *100*, 1–11.
- (5) (a) Lu, A.-H.; Salabas, E. L.; Schüth, F. *Angew. Chem., Int. Ed.* **2007**, *46*, 1222–1244. (b) Capek, I. *Adv. Colloid Interface Sci.* **2004**, *110*, 49–74. (c) Suslick, S. K.; Fang, M.; Hyeon, T. *J. Am. Chem. Soc.* **1996**, *118*, 11960–11961.
- (6) (a) Hergt, R.; Dutz, S.; Müller, R.; Zeisberger, M. *J. Phys.: Condens. Matter* **2006**, *18*, S2919–S2934. (b) Habib, A. H.; Ondeck, C. L.; Chaudhary, P.; Bockstaller, M. R.; McHenry, M. E. *J. Appl. Phys.* **2008**, *103*, 07A307. (c) Bautista, M. C.; Bomati-Miguel, O.; Zhao, X.; Morales, M. P.; Gonzalez-Carreño, T.; de Alejo, R. P.; Ruiz-Cabello, J.; Veintemillas-Verdaguer, S. *Nanotechnology* **2004**, *15*, S154–S159. (d) Cho, S. J.; Jarrett, B. R.; Louie, A. Y.; Kauzlarich, S. M. *Nanotechnology* **2006**, *17*, 640–644.
- (7) Salgueiriño-Maceira, V.; Correa-Duarte, M. A. *Adv. Mater.* **2007**, *19*, 4131–4144.

amine is added. Using the amido precursor  $\text{Fe}[\text{N}(\text{SiMe}_3)_2]_2(\text{THF})$  ( $\text{Me} = \text{CH}_3$ , THF = tetrahydrofuran) in the presence of oleic acid and hexadecylamine (HDA), Dumestre et al.<sup>3a</sup> have prepared 7 nm iron nanocubes organized into superlattices. The growth process and control of size (in this case limited to 7 nm) and shape (spherical, cubic or anisotropic) were not achieved on this system, however. We have therefore extended the study in order to understand and possibly propose a model for the size and shape control of iron NPs prepared in the presence of such surfactant mixtures. The route we have chosen is the decomposition of  $\{\text{Fe}[\text{N}(\text{SiMe}_3)_2]_2\}_2$  in the presence of HDA and palmitic acid (PA) under mild conditions. Several experimental parameters have been examined and tuned with the aim of understanding their influence on the mean size and shape of the final NPs in order to produce high-quality colloidal samples that could cover the superparamagnetic range of interest. Supported by a complete Mössbauer study of the colloid composition at different reacting stages, this work has led to the proposition of an environment-dependent growth mechanism.

### Materials and Methods

**General Procedures.** Mesitylene (Fluka,  $\geq 99\%$ ) was distilled over sodium according to standard procedures. PA (Sigma,  $\geq 99\%$ ) and HDA (Fluka,  $\geq 99\%$ ) were used without any additional purification. Reactants and products were stored and manipulated in an argon glovebox exclusively. The reactants were mixed together at room temperature, and all of the syntheses were performed in Fischer–Porter bottles.

NPs were obtained by decomposition of the iron dimer  $\{\text{Fe}[\text{N}(\text{SiMe}_3)_2]_2\}_2$ .<sup>12</sup> Both kinds of reactions were performed in the presence of HDA and PA in mesitylene under a reductive atmosphere of dihydrogen (3 bar). The general conditions were adjusted to study the reaction kinetics (reaction time varying from 30 min to 48 h), the influence of temperature (from 100 to 150 °C), and surfactant concentration effects.

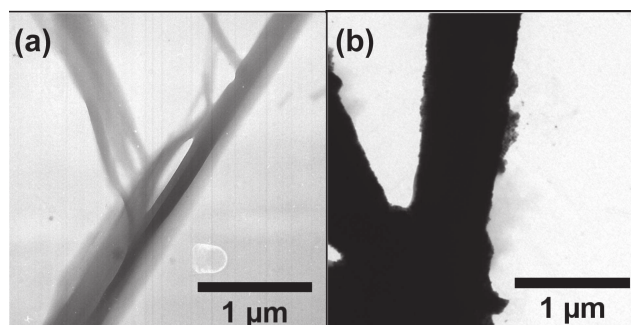


**Figure 1.** TEM pictures of micrometric superstructures observed (a) prior to reaction under  $\text{H}_2$  and (b) after 48 h of reaction.

**Synthesis of Nanocube Superlattices.** A colorless solution of PA (384 mg, 1.5 mmol, 1.5 equiv per mol of iron) in mesitylene (10 mL) was added to a green solution of  $\{\text{Fe}[\text{N}(\text{SiMe}_3)_2]_2\}_2$  (376 mg, 0.5 mmol) in mesitylene (5 mL). The mixture was manually stirred, and its color immediately changed to yellow. After 1 min, a solution of HDA (482 mg, 2.0 mmol, 2.0 equiv) in mesitylene (5 mL) was added to it. The mixture started to darken and became black after 10 min of magnetic stirring at room temperature. The solution was then put under 3 bar of  $\text{H}_2$  and allowed to react in an oil bath at 150 °C for 48 h.

The monitoring of this reaction was performed on the same sample equally distributed into five Fisher–Porter bottles, each of which was placed in the same oil bath (150 °C) for a specified time (0.5, 2, 6, 12, or 25 h).

**Characterization of the NPs.** Microscopy samples were prepared by deposition of a drop of diluted colloidal solution onto a carbon-coated copper grid and observed on a JEOL 6700F microscope for scanning electronic microscopy (SEM), a JEOL 1011 microscope for bright-field transmission electronic microscopy (TEM), or a JEOL-2100F field-emission microscope for high-resolution TEM (HRTEM), the latter two working at 100 and 200 kV, respectively. In the majority of cases, size histograms were obtained by an automatic counting process over 500 particles;<sup>13</sup> on particular samples (stars and large cubes), counting was done manually for at least 100 nanoparticles. Size distributions were fitted by the Gaussian law; the results are expressed in terms of the calculated mean size and the standard deviation ( $\sigma$ ). Magnetic studies were carried out on powder samples by SQUID (Quantum Design MPMS 5.5), and the iron state and environment were analyzed by Mössbauer spectroscopy (WISSEL,  $^{57}\text{Co}$  source). Samples were prepared in the glovebox, and extreme care was taken to avoid oxidation during transfer to the apparatus. Flame-sealed glass tubes of powder were prepared under argon to determine the iron composition from microanalysis measurements performed by inductively coupled plasma (ICP).

### Results

On the basis of the results obtained by Dumestre et al.,<sup>3a</sup> we used a combination of PA and HDA to grow well-defined NPs. We successively monitored the kinetics of the reaction, the influence of the temperature, and finally the influence of the acid/amine ratio, as presented hereafter. The first observation that actually started this study was made before any NPs were formed: a mixture of PA/HDA in a 1.5:2 ratio mixed with  $\{\text{Fe}[\text{N}(\text{SiMe}_3)_2]_2\}_2$  at room temperature led immediately to the formation of organic superstructures in mesitylene, as revealed by TEM (see Figure 1a). Size measurements by dynamic light scattering from the starting solution (after heating at only 50 °C for 10 min) also confirmed the formation of micrometric

- (8) (a) Finney, E. E.; Finke, R. G. *J. Colloid Interface Sci.* **2008**, *317*, 351–374. (b) Dumestre, F.; Chaudret, B.; Amiens, C.; Fromen, M.-C.; Casanove, M.-J.; Renaud, P.; Zurcher, P. *Angew. Chem., Int. Ed.* **2002**, *41*, 4286–4289. (c) Puentes, V. F.; Zanchet, D.; Erdozney, C. K.; Alivisatos, A. P. *J. Am. Chem. Soc.* **2002**, *124*, 12874–12880. (d) Shevchenko, E. V.; Talapin, D. V.; Schnablegger, H.; Kornowski, A.; Festin, O.; Svedlindh, P.; Haase, M.; Weller, H. *J. Am. Chem. Soc.* **2003**, *125*, 9090–9101. (e) Ung, D.; Soumare, Y.; Chakroune, N.; Viau, G.; Vaulay, M.-J.; Richard, V.; Fiévet, F. *Chem. Mater.* **2007**, *19*, 2084–2094. (f) Pei, W.; Kakibe, S.; Ohta, I.; Takahashi, M. *IEEE Trans. Magn.* **2005**, *41*, 3391–3393. (g) Liang, X.; Wang, X.; Zhunang, J.; Chen, Y.; Wang, D.; Li, Y. *Adv. Funct. Mater.* **2006**, *16*, 1805–1813. (h) Casula, M. F.; Jun, Y.-W.; Zaziski, D. J.; Chan, E. M.; Corrias, A.; Alivisatos, A. P. *J. Am. Chem. Soc.* **2006**, *128*, 12675–1682.
- (9) (a) Huber, D. L. *Small* **2005**, *1*, 482–501. (b) Huber, D. L.; Venturini, E. L.; Martin, J. E.; Provencio, P. P.; Patel, R. J. *J. Magn. Magn. Mater.* **2004**, *278*, 311–316. (c) Sun, S.; Zeng, H.; Robinson, D. B.; Raoux, S.; Rice, P. M.; Wang, S. X.; Li, G. *J. Am. Chem. Soc.* **2004**, *126*, 273–279. (d) Peng, S.; Wang, C.; Xie, J.; Sun, S. *J. Am. Chem. Soc.* **2006**, *128*, 10676–10677. (e) Farrell, D.; Majetich, S. A.; Wilcoxon, J. P. *J. Phys. Chem. B* **2003**, *107*, 11022–11030. (f) Farrell, D.; Cheng, Y.; McCallum, R. W.; Sachan, M.; Majetich, S. A. *J. Phys. Chem. B* **2005**, *109*, 13409–13419. (g) Hyeon, T.; Lee, S. S.; Park, J.; Chung, Y.; Na, H. B. *J. Am. Chem. Soc.* **2001**, *123*, 12798–12801. (h) Kim, D.; Park, J.; An, K.; Yang, N.; Park, J.; Hyeon, T. *J. Am. Chem. Soc.* **2007**, *129*, 5812–5813. (i) Yang, H. T.; Ogawa, T.; Hasegawa, D.; Takahashi, M. *Phys. Status Solidi A* **2007**, *204*, 4013–4016. (j) Shavel, A.; Rodriguez-Gonzales, B.; Spasova, M.; Farle, M.; Liz-Marzan, L. M. *Adv. Funct. Mater.* **2007**, *17*, 3870–3876.
- (10) Yang, H.; Ito, F.; Hasegawa, D.; Ogawa, T.; Takahashi, M. *J. Appl. Phys.* **2007**, *101*, 09J112.
- (11) Lacroix, L.-M.; Lachaize, S.; Falqui, A.; Blon, T.; Carrey, J.; Respaud, M.; Dumestre, F.; Amiens, C.; Margeat, O.; Chaudret, B.; Lecante, P.; Snoeck, E. *J. Appl. Phys.* **2008**, *103*, 07D521.
- (12) Olmstead, M. M.; Power, P. P.; Shoner, S. C. *Inorg. Chem.* **1991**, *30*, 2547–2551.

- (13) Rasband, W. S. *ImageJ*; National Institutes of Health: Bethesda, MD, 1997–2007; <http://rsb.info.nih.gov/ij/> (accessed Dec 4, 2008).

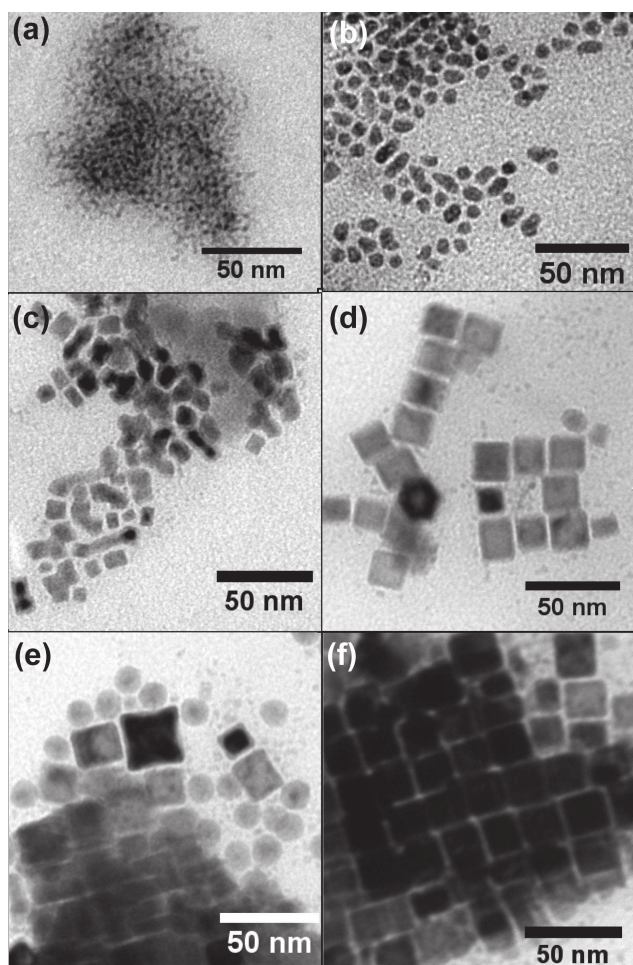


**Figure 2.** TEM pictures of nanoparticles stabilized by a 1.5:2 PA/HDA mixture after (a) 0.5, (b) 2, (c) 6, (d) 12, (e) 25, and (f) 48 h of reaction.

objects (see Figure S1 in the Supporting Information). The nature of the surfactants and the observed shape of these micrometric stable objects are in good agreement with the formation of a mesophase with a lamellar structure.<sup>14,15</sup> Moreover, the TEM picture's contrast on these structures indicates the presence of iron, which is certainly involved in molecular species and/or clusters. The formation of these iron-filled organic superstructures is correlated with the appearance of similar superstructures containing nanocubes observed after heating of the same solution under dihydrogen for 48 h (see Figure 1b), as shown in this article.

**Kinetics of NP Growth.** In order to understand the correlation between the superstructures observed at  $t = 0$  and  $t = 48$  h, the kinetics of the iron dimer decomposition in the presence of 1.5:2 PA/HDA has been monitored. We particularly focused on what happened inside the organic superstructures, and therefore, the TEM pictures in Figure 2 show only these regions (a larger view of each region of interest is available in Figures S2, S3, and S4 in the Supporting Information). After 30 min at 150 °C under dihydrogen, very small ( $<2$  nm) NPs that we will call

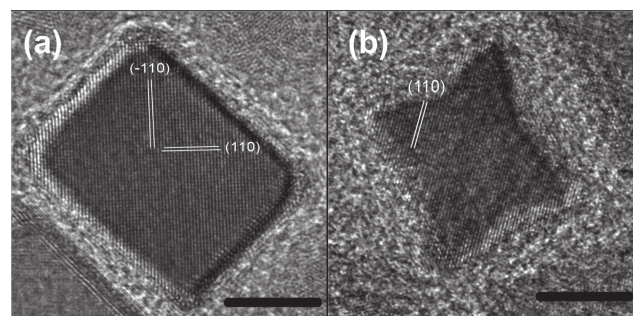


**Figure 3.** HRTEM pictures of monocrystalline octapods and cubic NPs. The {110} planes of the iron bcc crystal structure are highlighted. The scale bar represents 5 nm.

“nuclei” are formed (see Figure 2a). After 2 h, we observed  $\sim 5$  nm spherical NPs and anisotropic NPs displaying a width of  $\sim 5$  nm and a length of  $\sim 10$  nm (see Figure 2b). A majority of the nuclei were still detected around these misshapen NPs. Some were still present even after 6 h, but by this time the sample was predominantly composed of larger NPs (see Figure 2c and Figures S2c and S3 in the Supporting Information). Most of these anisotropic NPs had at least one dimension between 25 and 50 nm ( $32.6$  nm,  $\sigma = 7.4$  nm), and some well-defined facets became apparent. A few cubic NPs displaying round edges ( $11.0$  nm,  $\sigma = 1.0$  nm) were also observed. The anisotropic particles observed at this stage of the reaction result from coalescence. They disappeared with time while particles of cubic shape were formed. As a matter of fact, after 12 h, the cubic NPs became predominant ( $17.0$  nm,  $\sigma = 1.7$  nm; see Figure 2d). After 25 h, large superlattices with lengths of several microns, containing mainly cubic NPs ( $20.7$  nm,  $\sigma = 0.9$  nm) but also some not completely filled octapods, were observed. These objects were on their way to form cubes, indicating that the reaction, though at a very advanced stage, was not yet complete (see Figure 2e and Figures S2e and S4 in the Supporting Information). The spherical NPs observed around the nanocube superlattice (NCS) at this point look well-defined, with a mean diameter of  $13.2$  nm ( $\sigma = 1.2$  nm). Finally, after 48 h of reaction, NCSs composed of cubic NPs ( $20.9$  nm,  $\sigma = 2.7$  nm; see Figures 2f and 1b) were obtained, together with a few spherical NPs outside them ( $12.0$  nm,  $\sigma = 1.0$  nm; see the inset of Figure S2f in the Supporting Information). The system did not change much after 7 days at 150 °C. Consequently, 48 h of reaction was kept as a reference for the other experiments performed at 150 °C.

The crystal structures of the different iron NPs obtained above were investigated by HRTEM (see Figure 3). The octapods and cubic NPs are monocrystalline and exhibit a bcc structure; the cubic NPs expose only {100} planes at their surface, while the octapods also expose {110} planes. Because of air exposure during the transfer of the carbon grid to the microscope chamber, the observed NPs are partially oxidized. The spherical NPs observed outside the organic superstructures are polycrystalline (see Figure S5 in the Supporting Information).

To gain some information on the rate law of this growth process, and especially to shed light on the evolution of the balance between Fe(II) and Fe(0) species, systematic Mössbauer spectroscopy and magnetization measurements were carried out on the raw material at different reaction stages. Figure 4 displays the Mössbauer spectra at  $t = 0, 2, 6, 12,$  and  $48$  h, and Table 1 summarizes the fit parameters (also see Table S1 and Figures S6, S7, and S8 in the Supporting Information for additional details about the Mössbauer and SQUID experiments). As a

(14) Dubois, M.; Lizunov, V.; Meister, A.; Gulik-Krzywicki, T.; Verbavatz, J. M.; Perez, E.; Zimmerberg, J.; Zemb, T. *Proc. Natl. Acad. Sci. U.S.A.* **2004**, *101*, 15082–15087.

(15) (a) Karlsson, S.; Friman, R.; Lindstrom, B.; Backlund, S. *J. Colloid Interface Sci.* **2001**, *243*, 241–247. (b) Abécassis, B.; Testard, F.; Arleth, L.; Hansen, S.; Grillo, I.; Zemb, T. *Langmuir* **2006**, *22*, 8017–8028.

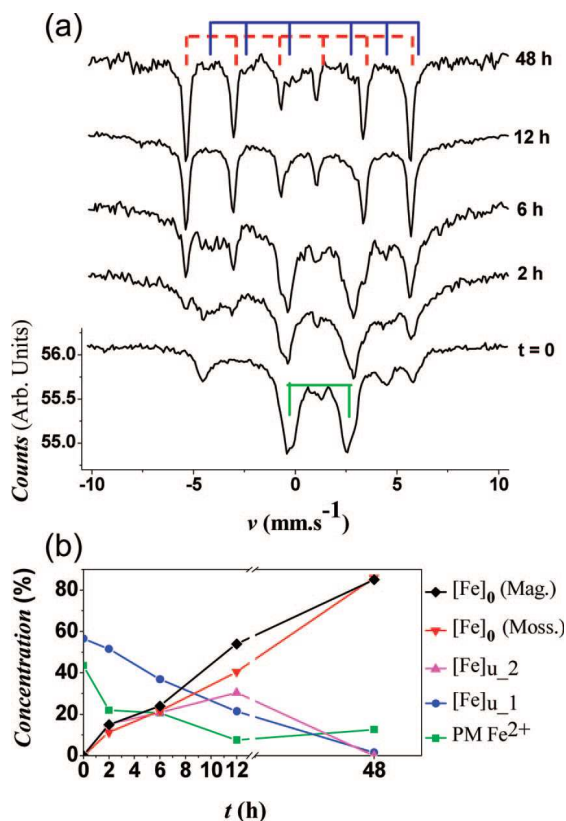


**Figure 4.** (a) Mössbauer spectra of the PA/HDA/iron system at different stages of the reaction. (b) Evolution of the species concentrations as a function of the reaction time, as deduced from fits of the Mössbauer spectra.

**Table 1.** Contribution Parameters Used to Fit the Mössbauer Spectra<sup>a</sup>

species	parameter(s)	contribution at time <i>t</i>				
		0	2 h	6 h	12 h	48 h
PM Fe <sup>2+</sup>	$\delta = 1.16, Q = 2.5$	18.7%	3.7%	2.5%	0.9%	—
	$\delta = 1.2, Q = 3.15$	16.1%	12.9%	14.5%	0.9%	7.7%
	$\delta = 1.16, Q = 3.65$	8.7%	5.3%	3.7%	5.7%	4.9%
	$\langle Q \rangle$	2.97	3.16	3.16	3.45	3.34
[Fe] <sub>u1</sub>	$\delta$	1.14	1.21	1.16	1.14	—
	$Q$	−0.95	−0.95	−0.75	−0.7	—
[Fe] <sub>u2</sub>	$H_{\text{hyp}}^b$	—	249	245	202	—
	$\delta$	—	—	0.45	—	—
	$Q$	—	—	0	—	—
[Fe] <sub>0</sub>	$H_{\text{hyp}}$	—	—	400–450	—	—
	$\delta$	—	0.15	0.1	0.1	0.1
	$Q$	—	0	0	0	0
	$H_{\text{hyp}}$	—	—	330–340	—	—

<sup>a</sup> Units:  $\delta$  and  $Q$  are given in mm s<sup>−1</sup>, and  $H_{\text{hyp}}$  is given in kG. <sup>b</sup> The mean value is given in this case.

general feature, one can notice the gradual change of the absorption up to a sextet consisting of ferromagnetic  $\alpha$ -Fe after 48 h of reaction. Even prior to reaction with H<sub>2</sub> ( $t = 0$ ), the single doublet of the {Fe[N(SiMe<sub>3</sub>)<sub>2</sub>]<sub>2</sub>}<sub>2</sub> precursor does not contribute to the spectrum; thus, the precursor quantitatively reacts with the PA/HDA mixture. Adding either PA or HDA to {Fe[N(SiMe<sub>3</sub>)<sub>2</sub>]<sub>2</sub>}<sub>2</sub> in a 2:1 ligand-to-iron ratio leads to new species of a different nature (Figures S9 and S10 in the Supporting Information display the corresponding spectra and the magnetization curves, respectively). In the case of only HDA, the Mössbauer spectrum evidences a well-defined sextet and the hysteresis curve displays a characteristic weak magnetization with high-field irreversibility. This material behaves as

a well-compensated antiferromagnet. On the contrary, the Mössbauer spectrum evidences a wide doublet in the case of PA: the main contribution is characteristic of molecular iron(II) species, while the small one arises from coupled iron(II) cations. This material has a rather high magnetization and a weak hysteresis curve.

Eventually, reaction of the {Fe[N(SiMe<sub>3</sub>)<sub>2</sub>]<sub>2</sub>}<sub>2</sub> precursor with a 1.5:2 PA/HDA mixture leads to a material with an intermediate spectrum. A wide doublet similar to the one measured in the case of PA again indicates the presence of a paramagnetic iron(II) carboxylate material, denoted as PM Fe<sup>2+</sup>. A second and much more complex contribution, denoted [Fe]<sub>u1</sub>, is characterized by a broad distribution of hyperfine fields ( $H_{\text{hyp}}$ ), a large isomer shift ( $\delta$ ) in the same range as for the PM Fe<sup>2+</sup> species, and a quite large negative quadrupolar effect ( $Q$ ). The measured magnetic moment per Fe atom is weak but still higher than in the case of pure amine system. Although the identification of this material deserves much more work, Mössbauer spectroscopy reveals iron(II) cations in a complex chemical environment that combines carboxylate and amine ligands. We assume this material to mainly compose the large organic superstructures observed by TEM (see Figure 1a), and we will now call it the iron(II) reservoir.

The consumption of the iron(II) reservoir is quite slow; its fingerprint is indeed still observed after 12 h of reaction. Its decrease is accompanied by an increase of an Fe(0) contribution (denoted [Fe]<sub>0</sub>). An intermediate phase (denoted [Fe]<sub>u2</sub>) with large hyperfine contributions of up to 45 T grows in during the first hours of reaction before being totally consumed at the end. After 2 h, the Fe(0) nuclei clearly observed by TEM (see Figure 2b) contribute only 13% of the total spectrum. After 6 h, their contribution increases slightly to 22%, with the iron(II) reservoir still being the majority. After 12 h, the balance is modified in favor of [Fe]<sub>0</sub>, which at this time represents 53%. It increases to 85.9% after 48 h, while the iron(II) reservoir remains only as a small part of the carboxylate iron(II) contribution (14.1%) which is probably due to the equilibrium between Fe<sup>0</sup> and Fe<sup>2+</sup> under these particular conditions (the presence of H<sub>2</sub> and acid) and to the surface coordination of carboxylate groups oxidatively added on the surface of the particles. We also report the evolution of the spontaneous magnetization deduced from the low-temperature magnetic measurements by SQUID (labeled “[Fe]<sub>0</sub> (Mag.)” in Figure 4b). It agrees well with the one deduced from the Mössbauer spectra.

The kinetic study of the reaction, followed by TEM and Mössbauer spectroscopy, evidence a series of complex reaction steps leading to the formation of the iron NCSs. The Mössbauer study shows that the iron(0) NPs are obtained through numerous intermediate phases that slowly feed the growth; their exact identification will require some more work to be done. We assume that at least one of them concerns Fe(II) cations entrapped in the organic superstructures observed by TEM. Thus, in regard to these results, it is possible to decompose the growth inside these organic superstructures into three main steps: (i) nucleation, (ii) isotropic growth and coalescence, which first lead to some anisotropic NPs, and finally (iii) oriented growth and repair mechanisms to form in the end mainly cubic NPs organized into superlattices. Each of these processes is characterized by a different energy barrier. In order to gain some knowledge about these activation energies, various syntheses were performed with the 1.5:2 PA/HDA system at different temperatures.

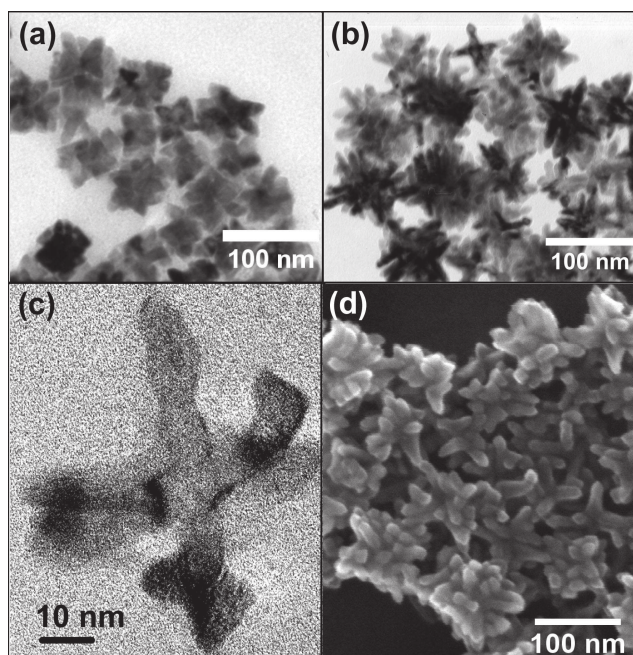


**Figure 5.** TEM pictures of nanoparticles obtained with a 1.5:2 ratio of PA/HDA (a) at 135 °C after 7 days and (b) at 120 °C after 21 days. (c) HRTEM picture of a starlike-shaped NP formed at 120 °C. (d) SEM picture of an aggregate of starlike-shaped NPs.

**Influence of Temperature on NP Growth.** We followed the reactions for 2, 7, 21, and 28 days at three different temperatures: 135, 120, and 100 °C. Since the temperature decrease leads to slower reactions, we adjusted the reaction times to reach the same reaction advancement. At 135 °C, after 7 days we ended up with large objects (46 nm,  $\sigma = 4$  nm) clearly composed of several coalesced but faceted NPs (18.6 nm,  $\sigma = 3.1$  nm) (see Figure 5a). They were stable over 21 days of reaction. Cubic NPs were not observed under these conditions. This result was not just a consequence of the longer reaction time, since as already mentioned above, the NCSs heated to 150 °C for 7 days did not change at all. At 120 °C, we observed the formation of anisotropic particles with starlike shapes after 21 days (see Figure 5b–d). Most of these stars expose six legs, but NPs with fewer branches were also observed (see Figures S11, S12, and S13 in the Supporting Information). Foot-type defects are present at the extremities of some legs (see Figure 5c). These “feet” are triangular and expose both {100} and {110} planes on their surfaces. A mean leg length of 30 nm was estimated from isolated stars. At 100 °C, comparable NPs were produced after 21 days of reaction, but the colloidal solution obtained in this case appeared to be very inhomogeneous, with either small NPs or stars (with leg lengths of  $\sim 60$  nm). These anisotropic particles may result from the growth of coalesced NPs similar to those formed after 6 h at 150 °C. Since the temperature decrease may affect each reaction step differently, one can consider that the coalescence step (ii) is maintained but the rate of the repair mechanism step (iii) is drastically reduced. As a consequence, anisotropic NPs are stabilized at temperatures lower than 150 °C.

**Influence of Acid Concentration on Size and Shape.** To verify the idea of a strong correlation between the initially formed organic superstructures and the NCS, we have looked at a reaction in which the former should not be formed: no organic superstructure was detected in the absence of carboxylic acid, for example. In this case, a 48 h reaction yielded wormlike NPs

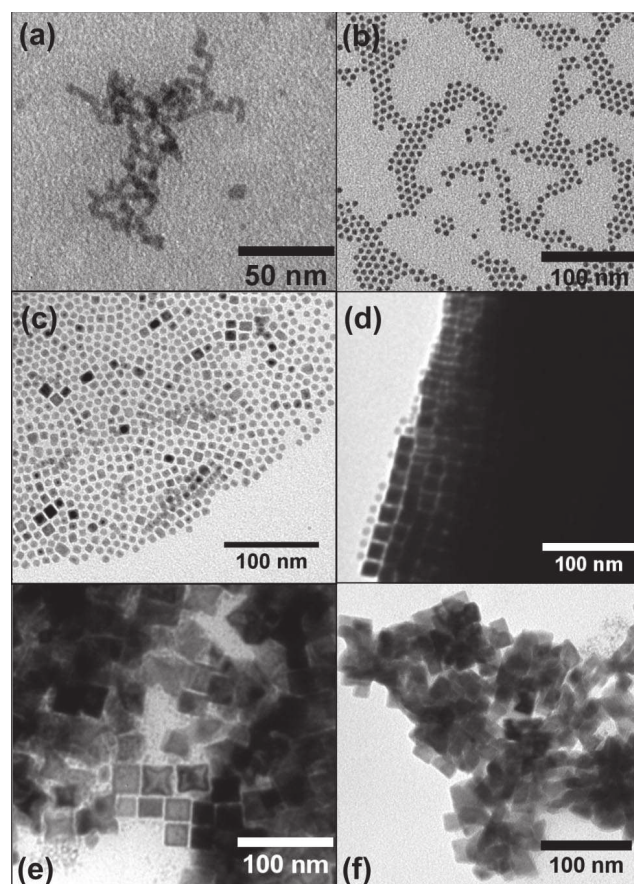


**Figure 6.** TEM pictures of NPs obtained by decomposition at 150 °C for 48 h in the presence of 2 equiv of HDA but different acid concentrations: (a) 0, (b) 1, (c) 1.2, (d) 1.4, (e) 1.6, and (f) 1.8 equiv.

only (see Figure 6a). In order to gain some understanding of the role of the acid, we investigated different acid concentrations. For this purpose, we kept the amine concentration constant at 2 equiv with respect to the iron molarity and varied the acid concentration from 1 to 1.8 equiv (the temperature and reaction time were again 150 °C and 48 h, respectively). Table 2 and Figure 6 sum up the experimental conditions and the results for each reaction (see also Figures S14 and S17 in the Supporting Information). At 1 equiv of PA (reaction A), we detected only spherical NPs with a narrow size distribution centered at 5.4 nm ( $\sigma = 0.5$  nm). These NPs tended to self-organize on the TEM grid because of their narrow size distribution, but no traces of any 3D superstructures were found. Although the NPs were mostly spherical at 1.2 equiv of PA (reaction B), some cubic NPs appeared, generally surrounded by other faceted or spherical NPs inside quite large organizations. At 1.4 equiv of PA (reaction C), most of the NPs were cubic (13.3 nm,  $\sigma = 1.0$  nm) and self-organized into micrometric superlattices. A few spherical NPs were present outside these structures. Furthermore, two size populations were found for them: the minor one was centered at 2.2 nm ( $\sigma = 0.5$  nm) and the major one at 7.6 nm ( $\sigma = 0.7$  nm). At 1.6 equiv of PA (reaction D), a colloidal solution composed of nuclei, octapods, and polydispersed cubic NPs (27.9 nm,  $\sigma = 7.0$  nm) was obtained. The contrast on the TEM picture indicates that they were all entrapped in an amorphous medium, probably an organic shell containing some molecular iron. Finally, at 1.8 equiv (reaction E), the solution was composed of nuclei and large coalesced, faceted NPs ( $> 50$  nm). These coalesced NPs were very similar to the ones obtained at 135 °C for a PA/

**Table 2.** Reaction Summary

	A	B	C	reference	D	E	ref 3a
amine/acid ratio	2:1	2:1.2	2:1.4	2:1.5	2:1.6	2:1.8	2.38:1.19
NP type <sup>a</sup> (average size <sup>b</sup> )	spheres (5.4)	spheres (6.9) cubes (13.3)	cubes (13.0) spheres (8.9)	cubes (20.9) spheres (12.0)	cubes (27.0) filled octapods spheres	coalesced faceted	cubes (7.0)

<sup>a</sup> The major type, as estimated on the basis of TEM pictures, is cited first. <sup>b</sup> Average sizes are given in nm.

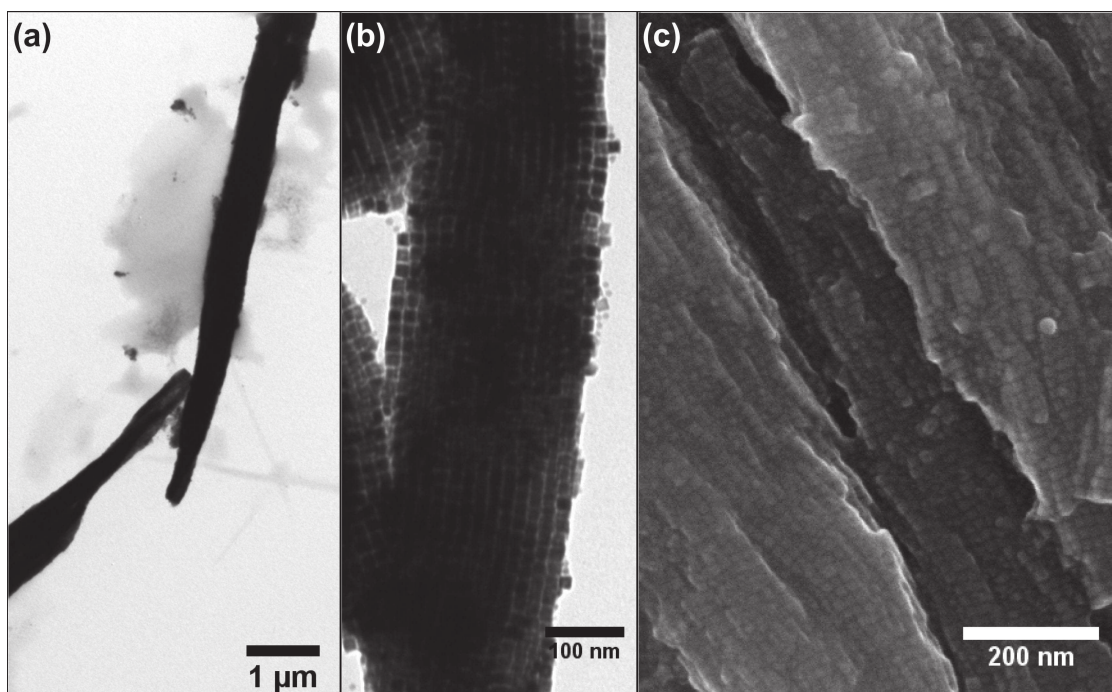


**Figure 7.** Micrometric iron nanocube superlattices formed in reaction C and observed by (a, b) TEM and (c) SEM. The 13.3 nm nanocubes are monodispersed ( $\sigma = 1.0$  nm).

HDA ratio of 1.5:2 (see Figure 5a). Though they were quite large, both of them seemed to be grown under conditions similar to those for the NPs detected after 6 h in the reference reaction (see Figure 2c). Again, these NPs were located inside an amorphous medium.

From 1.4 to 1.8 equiv of PA, the NPs were enclosed in an organic superstructure constituted of HDA and PA. However, it was only for 1.4 and 1.5 equiv of PA (at 150 °C) that micrometric superlattices were detected. They were composed of closely packed monodispersed cubic NPs (13.3 and 20.3 nm, respectively), as revealed by TEM and SEM (see Figure 7). Upon comparison of these two cases, it seems that the smaller the nanocubes are, the larger are the superlattices. This might be correlated to the size distribution getting larger when the mean size increases, indicating that the long-range organization is less favored. The NCSs correspond to extended 3D superstructures formed in solution and not to self-assemblies driven by solvent evaporation. As previously explained by Dumestre et al.,<sup>3a</sup> they can be seen as the result of the concomitant crystallization of the nanoparticles and their ligand shells. This study actually has uncovered new evidence to aid in understanding the mechanism of their formation in solution. In fact, it is

more correct to speak about the growth and shaping of cubic NPs inside a preformed organic superstructure, as discussed below.

## Discussion

The results described above regarding the formation of iron NPs in the presence of PA and HDA suggest that the formation of spherical or cubic NPs depends on the growth environment. Formation of cubes for an acid/amine ratio of 1.4:2 or 1.5:2 is indeed associated with the presence of micrometric superlattices. It can be then inferred that growth of cubic NPs is strongly correlated with the organic superstructures preformed in solution while growth of spherical NPs occurs independently.

On the basis of this observation, the environment-dependent growth mechanism schematically represented in Figure 8 is proposed. This model takes into account the influence of the local acid concentration on every step of the NP synthesis and especially on their faceting. In particular, the model stems from the observations made during the kinetic study of our reference reaction (PA/HDA ratio of 1.5:2), which evidenced the presence of (i) nucleation, (ii) isotropic growth and coalescence, and (iii) oriented growth and repair mechanisms inside organic superstructures.

**Nucleation and Organic Superstructures.** Before decomposition, the solution is composed of several species arising from the reaction of the highly reactive  $\{\text{Fe}[\text{N}(\text{SiMe}_3)_2]_2\}_2$  with PA, HDA, or both. Since the reaction is carried out with less than

(16) Chen, M.; Pica, T.; Jiang, Y.-B.; Li, P.; Yano, K.; Liu, J. P.; Datye, A. K.; Fan, H. *J. Am. Chem. Soc.* **2007**, *129*, 6348–6349.

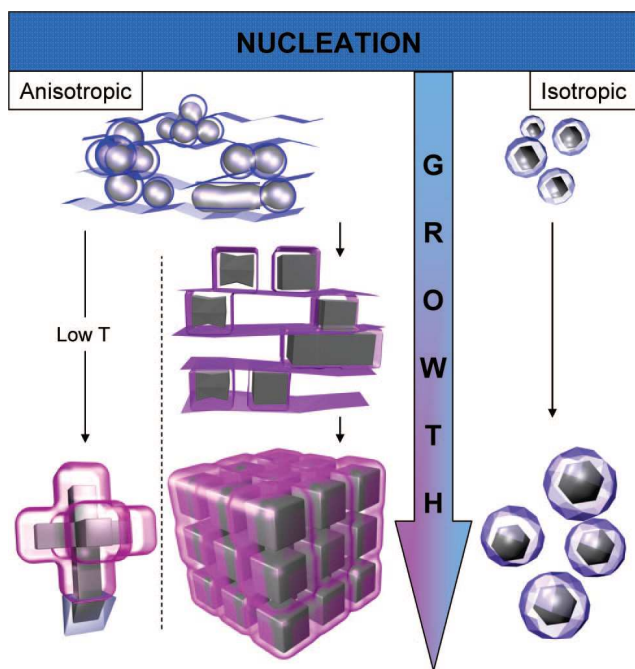


**Figure 8.** Schematic view of the two environment-dependent growth routes (nucleation in two different environments). The blue color indicates an amine-rich environment, and the violet color is used to represent an organic shell composition that preferentially stabilizes the {100} facets of the iron NPs.

2 equiv of PA, we cannot expect that the iron precursor transforms selectively into one species, such as bis(carboxylate)iron(II). This means that the kinetics of the decomposition is likely governed by at least two reactions: the fast decomposition of presumably an amido iron(II) complex/cluster, which feeds the nucleation step, and the slow decomposition of presumably a carboxylate iron(II) complex, which feeds the growth step, in agreement with the difference in stability of amido and carboxylate Fe(II) derivatives. This hypothesis is confirmed by the Mössbauer study: there is still a small contribution of iron(II) complexes after 48 h. Thus, we can consider that nucleation and growth are strictly separated in this reaction as a result of the difference in stability of the two iron sources, at any decomposition temperature from 100 to 150 °C.

Besides acting as stabilizing agents, the PA/HDA surfactant pair has the ability to self-organize into long-range lamellar structures or bilayers. As far as we know, the phase diagram for such a system in an apolar solvent has never been reported in the literature. However, such a phase has previously been observed in water for a surfactant mixture of the same kind.<sup>14</sup> Lamellar self-organization in water, which is typical of salt-free catanionic systems, has been deeply investigated by Zemb et al.<sup>14</sup> They evidenced the formation of stable micrometric objects made up of surfactant bilayers; the objects' shape and stability were dependent upon the acid/amine ratio. By means of calculations, these authors also showed that the bilayers preferentially adopt a close-packed conformation when the acid/amine ratio is 1:2. These observations can also be applied to the acid-concentration dependence in our system, especially in the concentration range of interest where we detect superstructures. A similar oleic acid/oleylamine mixture was shown by Chen et al.<sup>16</sup> to drive the formation of FePt nanorods through the formation of a hexagonal reverse-liquid-crystal mesophase in the organic reaction solution. They assumed that water traces produced by acid-amine condensation were playing a major

role in the stabilization of such a mesophase.<sup>17</sup> This last point highlights the importance of knowing and understanding exactly what composes and strengthens such an organized system. In our case, we have not investigated the presence of water, since we think it would react with the excess hexamethyldisilazane coming from the iron dimer decomposition. We are currently working on the possible role of these light silicon derivatives. However, the organic superstructures' contrast seen in the TEM images suggests an iron upload. Carboxylate iron(II) species here could play the role of a structuring agent. Previous results show that it is possible to take advantage of such a coordination system to grow stable 1D iron(II) structures held together by dicarboxylate ligands.<sup>18</sup> The PA/HDA lamellar phase together with this structuring agent dictate the formation of the iron(II) reservoir and ensure its stability, as shown by the Mössbauer spectra. Evidence that such organic superstructures guide the growth of NPs has been reported very recently in regard to the synthesis of ultrathin Au nanowires.<sup>19</sup> Yang and co-workers<sup>19a</sup> and Xia and co-workers<sup>19b</sup> have explained that an Au<sup>+</sup>-oleylamine complex self-assembles into mesostructures that serve as a template for the anisotropic growth. In our case, after a fast nucleation step, the growth would then take place in an inhomogeneous solution in which two systems have to be considered: the one "inside" the organic superstructures (i.e., in an anisotropic medium) and the one "outside" them (i.e., in an isotropic medium). The iron(II) reservoir would then influence both the kinetics of the growth and its environment.

**Growth inside Organic Superstructures.** The growth mechanism is a complex combination of simultaneous reactions, but we have identified two main successive parts: (a) the coalescence of nuclei when the medium is amine-rich and (b) the growth of the {100} iron facets when the medium becomes acid-rich. In part (a), the ligand shell around the NPs is amine-rich, since most of the acid is stored inside the iron(II) reservoir. These conditions favor the coalescence of nanoparticles, as observed during the initial 6 h of reaction. Coalescence in an amine-rich medium was previously reported in the case of Pt NPs: wormlike NPs stabilized by HDA were formed.<sup>20</sup> In the present case, the decomposition of {Fe[N(SiMe<sub>3</sub>)<sub>2</sub>]<sub>2</sub>}<sub>2</sub> in the presence of HDA alone also yields wormlike iron NPs because of the relatively low binding energy of HDA (see Figure 6a). Therefore, the reaction would produce anisotropic NPs at first, as a result of coalescence in the anisotropic environment provided by the organic superstructures (see the schematic drawing in Figure 8). Some of these NPs display one dimension larger than the size of the final NPs (48 h). The transition between the two growth regimes seems to be effective when the acid concentration around the growing NPs is high enough to significantly stabilize the {100} iron facets. After 12 h of reaction, about half of the acid has been released, since about half of the iron(II) reservoir has been consumed, as shown by the Mössbauer spectra and confirmed by the SQUID measurements. This corroborates the increased number of well-defined facets observed on the TEM pictures (see Figure 2d). The lamellar structure of the ligand self-organization reinforces this effect by preferentially stabilizing the parallel {100} facets. The presence of organic superstructures in this system is therefore

(17) Wu, H.; Yang, Y.; Cao, Y. C. *J. Am. Chem. Soc.* **2006**, *128*, 16522–16523.

(18) Sanselme, M.; Grenèche, J. M.; Riou-Cavellec, M.; Férey, G. *Chem. Commun.* **2002**, 2172–2173.

(19) (a) Huo, Z.; Tsung, C.; Zhang, X.; Yang, P. *Nano Lett.* **2008**, *8*, 2041–2044. (b) Lu, X.; Yavuz, M. S.; Tuan, H.-Y.; Korgel, B. A.; Xia, Y. *J. Am. Chem. Soc.* **2008**, *130*, 8900–8901.

the key point for ensuring the formation of monocrystalline cubic NPs of bcc iron. At the transition between part (a) of the reaction and part (b), we can observe both the formation of cubic nanoparticles resulting from the filling of octapods and the corrosion of large anisotropic particles into cubes. This is in agreement with the concomitant action of oriented growth and repair steps. The first of these processes is evidenced by the presence of monocrystalline filled octapods after 25 h of reaction (see Figures 2e and 3a and Figure S2e in the Supporting Information). Similar objects have been observed in the Pt system studied by Tilley et al.<sup>21</sup> Their presence was assigned to a change in the growth regime from the kinetically controlled growth of the Pt {111} planes to the growth of the more stable {100} planes through a diffusion regime of the adatoms. This change was correlated with a decrease in the Pt atom concentration during the reaction. At the end of the reaction, these particles were then assumed to be nanocubes on their way to completion. This is in quite good agreement with our observations for this Fe system, especially because of the slow consumption of the iron(II) reservoir and the transition from an amine-rich to an acid-rich growth environment. Since we only get nanocubes at the end of the reaction, we can assume that the growth at this stage is governed by the minimization of the total energy of the nanoparticle/ligand system. Since the particles grow in a mesophase that tends to form a stable long-range lamellar structure because of the nature of the aliphatic long-chain ligands, the best energetic compromise is indeed given by the formation of bcc iron particles exposing parallel {100} facets. Moreover, for the same volume, a cubic shape would be preferred over an anisotropic plane-parallel one in order to keep the surface/volume ratio minimal. This means that ripening necessarily occurs to preserve the cubic shape of the growing NPs, which was not obvious a priori in such an anisotropic environment. A digestive ripening process, i.e., the repair step, is evidenced by the corrosion of the large anisotropic NPs, which are not detected anymore at the end of the reaction (see Figures 2f and 3b).

The previous section has emphasized the importance of the variation of the acid/amine ratio during the growth and ripening reactions. However, this ratio can vary even as a function of the organic-shell curvature in the anisotropic reaction medium. Thus, it has been reported by Zemb et al.<sup>13</sup> that the acid/amine ratio inside micrometric objects composed of surfactant bilayers varies as a function of the position in the object (facets, edges, or corners). This difference of acid/amine ratios is governed by the curvature of the objects, the planes/facets being the reference. According to this, we suggest that the curvature around the {110} and {111} facets could be responsible for local fluctuations in the acid concentration. Thus, the ligand shell would present an excess of amine around the edges and the corners of the nanocubes, causing curvature of one sign, but present an excess of acid around two {100} facets, forming an opposite curvature (see Figure 9). Finally, excess amine would favor local growth while excess acid would favor local corrosion, the reference composition being the one stabilizing the {100} facets. These proposed ripening and repair mechanisms are both responsible for the formation of cubic nanoparticles.

**Growth outside the Organic Superstructures.** Outside the organic superstructures, the growth is isotropic. According to the assumption that the organic superstructures must be composed of most of the acid initially introduced into the solution (which was confirmed by the acid-concentration influence; see the Results and also below), we presume that the medium

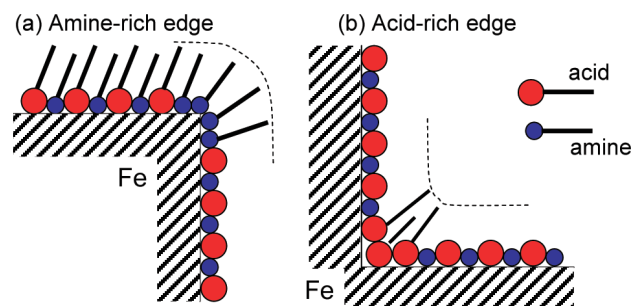


**Figure 9.** Schematic view of the ligand-shell organization along the facets and two kinds of edges of the NPs.

outside these organizations is amine-rich, in agreement with the isotropic shape of the NPs observed in this medium. However, one has to notice that the spherical NPs are polycrystalline (see Figure S5 in the Supporting Information), likely with preferential exposure of only the {100} facets to the solution, which still contains some acid. Finally, there is no further stabilization of only parallel facets, since there is no organic superstructure around.

In summary, the local acid concentration is the key factor that orientates the growth of the nanoparticles, whether we consider it inside or outside the organic superstructures. Thus, since the long-chain acid is incorporated by complexation in the iron(II) reservoir and participates in the organic superstructure, any concentration change has a drastic effect on the environment-dependent growth. At low concentrations of PA (between 1.0 and 1.3 equiv), the stabilization of long-range ligand self-organization is not favored. The nucleation and growth occur in an isotropic environment, yielding small, spherical NPs. These NPs are polycrystalline and expose at their surface {100} facets stabilized by the introduced acid. The narrow size dispersion suggests that nucleation and growth are strictly separated, as we supposed previously. At PA concentrations equal to or higher than 1.4 equiv, a long-range organic lamellar phase, i.e., a significant iron(II) reservoir, is formed. An increase of the PA concentration clearly slows down some of the reaction kinetics (reservoir decomposition, oriented growth, repair mechanism) because of the molecular species stabilization. In addition, the acid concentration changes from the beginning to the end of the reaction because of the slow consumption of the iron(II) reservoir. As the acid rules the stability of the NP surface, this change in concentration modulates the growth of the NPs, which proceeds first by coalescence and then by oriented growth, ripening, and the repair mechanism inside the ligand self-organization.

The influence of the temperature correlates well with the proposed model. As a matter of fact, the ripening and repair processes in particular are slowed when the reaction is performed at lower temperature. After 7 days at 135 °C, the NPs are large (~46 nm) and clearly result from coalescence of smaller ones. They seem to be on their way to completion to become cubic. Because the consumption of the iron(II) reservoir has been slowed, the growth environment remains amine-rich for a long time, and the coalescence is therefore prolonged. The result is a decrease in the number of nuclei, leading then to few but large NPs after 7 days. The SQUID and Mössbauer experiments confirm the reaction is, after 7 days, at a similar stage as the reaction performed at 150 °C after 6 h and 12 h (see Figures S15–S16 and Table S2 in the Supporting Information). After 21 days at 120 °C, we obtain monocrystalline stars that expose {100} facets, as revealed by HRTEM pictures (see Figure

5b–d). The transition from isotropic particles to stars has previously been reported for several systems, such as Rh,<sup>22</sup> CdS,<sup>23</sup> PbS, and Pt systems.<sup>24,25</sup> Interpretations of these temperature-dependent or reduction-kinetics-dependent growths usually invoke a seeded-growth mechanism<sup>24</sup> or a delicate balance between kinetic and thermodynamic regimes.<sup>21</sup> In our case, at 120 °C, nucleation is very slow, growth proceeds through coalescence and preferential {100} facet growth, and the repair mechanism is also presumably very slow. The result is seeded growth, i.e., an oriented growth along the initial directions given by the nuclei, leading to the observed stars for which no effective repair mechanism is available.

## Conclusion

In this paper, we have reported a complete study aimed at understanding the growth of iron NPs by an organometallic route. The effect of several key parameters, including the reaction time, the temperature, and the surfactant concentrations, has been investigated, leading to the development of a model involving an environment-dependent growth mechanism. The presence of organic superstructures filled with iron(II) species at the very beginning of the reaction is a key point in understanding the shape control of the final product. Indeed, the nucleation and growth can occur either outside these

templates (i.e., in an isotropic environment) or inside them (i.e., in an anisotropic environment). In the first case, we obtain spherical polycrystalline NPs having mean sizes that increase with the carboxylic acid concentration, as expected. In the second case, the reaction monitoring reveals several steps: (i) nucleation, (ii) coalescence favored by an amine-rich environment, and (iii) growth and repair mechanisms in an acid-rich environment. These three main steps lead to cubic NPs organized into superstructures: the nanocube superlattices. The evolution of the environment from amine-rich to acid-rich is directly correlated with the decomposition of the iron(II) reservoir, which releases carboxylic acid into the medium. Iron nanocubes are formed inside these templates and then directly assembled into close-packed micrometric superlattices. The growth of anisotropic objects such as stars is obtained by decreasing the reaction temperature, which modifies the relative kinetics of the nucleation, growth, and repair steps. As a whole, this study sheds light on a versatile, complex system, allowing control of the formation of cubic (side length from 13 to 27 nm) and spherical (diameter from 1.5 to 9.4 nm) iron nanoparticles.

**Acknowledgment.** L.-M.L. thanks the French Ministry of National Education and Research for her MENRT grant. We thank A. Mari and J.-F. Meunier for help with the SQUID and Mössbauer measurements and V. Collière for SEM characterization. We also thank K. Soulantica and F. Dumestre for fruitful discussions.

**Supporting Information Available:** Figures S1–S17 and Tables S1 and S2. This material is available free of charge via the Internet at <http://pubs.acs.org>.

JA805719C

- (20) Ramirez, E.; Erades, L.; Philippot, K.; Lecante, P.; Chaudret, B. *Adv. Funct. Mater.* **2007**, *17*, 2219–2228.  
(21) Ren, J.; Tilley, R. D. *J. Am. Chem. Soc.* **2007**, *129*, 3287–3291.  
(22) Hoefelmeyer, J. D.; Niesz, K.; Somorjai, G. A.; Tilley, T. D. *Nano Lett.* **2005**, *5*, 435–438.  
(23) Lee, S.-M.; Cho, S.-N.; Cheon, J. *Adv. Mater.* **2003**, *15*, 441–444.  
(24) Lee, S.-M.; Jun, Y.-W.; Cho, S.-N.; Cheon, J. *J. Am. Chem. Soc.* **2002**, *124*, 11244–11245.  
(25) Chen, J.; Herricks, T.; Xia, Y. *Angew. Chem., Int. Ed.* **2005**, *44*, 2589–2592.



## Stabilizing Vortices in Interacting Nano-Objects: A Chemical Approach

Lise-Marie Lacroix,<sup>\*,†</sup> Sébastien Lachaize,<sup>†</sup> Florian Hue,<sup>‡,||</sup> Christophe Gatel,<sup>§</sup> Thomas Blon,<sup>†</sup> Reamsay P. Tan,<sup>†</sup> Julian Carrey,<sup>†</sup> Bénédicte Warot-Fonrose,<sup>§</sup> and Bruno Chaudret<sup>†</sup>

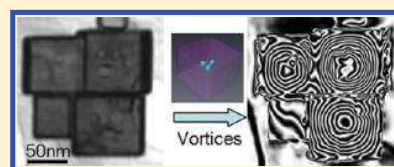
<sup>†</sup>Université de Toulouse, INSA, UPS, LPCNO (Laboratoire de Physique et Chimie des Nano-Objets), F-31077 Toulouse, France; CNRS; UMR 5215 ; LPCNO, F-31077 Toulouse, France

<sup>‡</sup>Department of Materials Science and Metallurgy, University of Cambridge, Pembroke Street, Cambridge, CB2 3QZ, United-Kingdom

<sup>§</sup>CEMES-CNRS, 29 rue J. Marvig, BP4347, 31055 Toulouse, France

### Supporting Information

**ABSTRACT:** We report a chemical method to prepare metallic Fe porous nanocubes. The presence of pores embedded inside the cubes was attested by electron tomography. Thanks to electronic holography and micromagnetic simulations, we show that the presence of these defects stabilizes the vortices in assembly of interacting cubes. These results open new perspectives toward magnetic vortex stabilization at relatively low cost for various applications (microelectronics, magnetic recording, or biological applications).



**KEYWORDS:** Magnetic nanoparticles, bcc-Fe, porous nano-objects, vortex stabilization, electron holography, electron tomography

Magnetic nanoparticles (NPs) are objects of choice for multiple purposes such as magnetic recording,<sup>1,2</sup> which requires high storage density,<sup>3,4</sup> and biomedical applications,<sup>5</sup> such as MRI contrast agents,<sup>6</sup> or therapeutic hyperthermia media.<sup>7,8</sup> Although single-domain magnetic materials are usual targets for these applications,<sup>9,10</sup> vortex configurations, which arise at the transition between multidomain and single-domain materials, could be of particular interest for dedicated purposes.<sup>11</sup> Indeed, vortices are characterized by their polarity, that is, the direction of magnetization in the core (up/down), and their chirality, that is, the direction of rotation around the vortex core (clockwise or counterclockwise).<sup>12</sup> As the vortex polarity and chirality are independent, four magnetic states could be obtained (Supporting Information Scheme 1), thus opening the perspective of two-bit-per-dot media for magnetic storage, providing that they can be manipulated.<sup>13–15</sup> Additionally, the excitation of vortices by a spin-polarized current leads to high-quality radio frequency oscillators, even in the absence of external magnetic field, which is very promising for potential applications.<sup>16–18</sup> Finally, vortices have recently been reported as presenting high potentiality for biomedical applications since they combine high saturation magnetization, required for bioapplications, with negligible remanence magnetization, which is a key feature for stabilizing ferrofluids against aggregation phenomena.<sup>19</sup>

However, in all of these applications, the stabilization of vortices in presence of magnetic dipolar interactions (for closely packed nanostructures or highly concentrated ferrofluids) is crucial. We have previously reported that an isolated 30 nm Fe nanocube exhibits a vortex state.<sup>20</sup> However, ferromagnetic coupling appeared between self-assembled nano-

cubes, leading to the disappearance of individual vortex in favor of more stable flux closure configurations across several cubes.<sup>20</sup> For dipoles of Fe<sub>3</sub>O<sub>4</sub> nanorings, theoretical works have also shown a magnetic coupling leading to the disappearance of vortices.<sup>19</sup> In order to overpass this limitation, one should improve the stability of the vortex within a single object. Two options may be considered: an increase of the object size, which will be a drawback for applications, or the introduction of internal vacancies and defects within small object which could pin the vortex core.<sup>21,22</sup> Up to now, the experimental preparation of such artificial pinning sites (defects, holes) requires costly multistep patterning processes.<sup>21,23</sup> An alternative method for the preparation of magnetic objects with embedded defects could be liquid-phase chemical reactions.

Though synthesis of magnetic nanoparticles with high magnetization values has been a long-sought goal, researches were mainly focused on defect-free particles.<sup>9</sup> Except from hollow Fe<sub>3</sub>O<sub>4</sub> spheres or rods,<sup>19,24</sup> synthesis of metallic nanoparticles with pores embedded has never been reported. On the basis of our know-how in the size and shape control of iron nanoparticles,<sup>25</sup> we have succeeded in the growth of porous particles. Our method is based on a mediated-growth that proceeds through three distinct steps: (i) nucleation; (ii) growth/coalescence, (iii) growth/ripening. The control of the growth/coalescence step has recently received lots of interest yielding nanoparticles with unique features.<sup>26,27</sup> Here, its

**Received:** April 3, 2012

**Revised:** April 23, 2012

**Published:** April 26, 2012

control allows us to force the presence of holes within nanocubes.

**Method. Synthesis of Porous Cubes.** A colorless solution of lauric acid (300 mg, 1.5 mmol, 1.5 equivalent per mole of iron) in mesitylene (10 mL) was added to a green solution of  $\{\text{Fe}[\text{N}(\text{SiMe}_3)_2]_2\}_2$  (376 mg, 0.5 mmol) in mesitylene (5 mL) under Ar atmosphere. The mixture was manually stirred and its color immediately turned to yellow. One minute later, a solution of dodecylamine (370 mg, 2.0 mmol, 2.0 equiv) in mesitylene (5 mL) was added to it. The mixture started to darken and it became black after 10 min of magnetic stirring at room temperature. The solution was then put under 3 bar of  $\text{H}_2$  and let to react in an oil bath at 150 °C for 48 h. See Supporting Information for further details.

**Characterization of the NPs.** Microscopy samples were prepared by deposition of a diluted colloidal solution drop on a carbon-coated copper grid and observed on a JEOL-1011 for bright-field transmission electronic microscopy (TEM) and JEOL-2100F field emission microscope for high-resolution TEM (HRTEM) working with 100 and 200 kV respectively. In the majority of cases, size histograms were obtained by manual counting process over at least 100 particles, using ImageJ software.<sup>28</sup> Size distributions have been fitted by Gaussian law; the results are expressed by the calculated mean size and standard deviation  $\sigma$ . Magnetic studies were carried out on powder samples by SQUID (MPMS Quantum Design 5.5) and the iron state and environment were analyzed by Mössbauer spectroscopy (WISSEL, <sup>57</sup>Co source). Samples were prepared into the glovebox and extreme care was taken to avoid oxidation during transfer to the apparatus. Flame-sealed glass tubes of powder were prepared under argon to determine the iron composition from microanalysis measurements performed by ICP (inductively coupled plasma).

**Electron Tomography.** To study the morphology of these Fe cubes, we use electron tomography in scanning transmission electron microscopy (STEM) mode using high-angle annular dark-field (HAADF) detector. This technique is well suited to obtain size and morphology information of crystalline materials without suffering from Fresnel fringes and diffraction contrast. A full three-dimensional (3D) analysis is then possible. We acquire HAADF-STEM tilt series on a FEI Tecnai F20 microscope fitted with a Fischione high-tilt tomography holder. The holder is designed to allow a  $\pm 80^\circ$  tilt without being limited by the pole piece gap of the microscope. The only restriction comes from the specimen itself and its support (400 mesh grid, in our case). We acquired two tilt series with two different camera lengths. The first tilt series was taken between  $-66$  and  $+70^\circ$  with an angular step of  $2^\circ$  between each acquisition. The tilt maximum leads to a missing wedge of information that induces an artifact of elongation in the  $z$  direction. In our case, the global missing wedge is  $44^\circ$  and induces an elongation with a ratio of 1.1 in  $z$ .<sup>29</sup> The second tilt series was acquire with a  $-45$  +  $56$  tilt range that leads to a strong elongation in  $z$  (ratio of 1.35) but the camera length was more appropriate and the contrast of the projections as well as the quality of the 3D object were improved. In both cases, the projections were sorted out under inspect3D software and aligned by cross-correlations, using an appropriate spatial filter.

**Electron Holography.** The structures of the different layers and interfaces were investigated by transmission electron microscopy (TEM) both in conventional and in high-resolution mode using a FEI Tecnai-F20 microscope fitted with a spherical aberration (Cs) corrector (CEOS) whose point resolution is

0.12 nm. We use off-axis EH in the same microscope to study the remnant magnetic state of the Fe porous nanocubes at room temperature. Holograms were digitally acquired with switching off the conventional objective lens and using the first transfer lens of the Cs corrector and the projectors to reach a maximum magnification of about  $\times 300\,000$ . The phase images were obtained by reconstruction the hologram using Fourier transformation and removing any additional phase shift using a reference hologram obtained in vacuum. The spatial resolution of the phase images is determined by the fringe spacing, which depends on the voltage applied to the biprism (2,3 nm at 135 V) and the diameter of the spatial-frequency filter (6 nm) applied in the Fourier space when reconstructing the holograms. The magnetic contribution to the phase shift was extracted by recording holograms in two opposite directions (sample up/down).

**Micromagnetic Calculations.** We used the three-dimensional version of the micromagnetic code OOMMF to determine the magnetic configuration in the samples.<sup>30</sup> The 3D nanocube shapes and sizes introduced for the calculations are deduced from the 2D TEM images with the assumption that the Fe cubes are perfectly cubic. Each iron nanocube is discretized in 3D cells with 4 nm side length. We used bulk magnetic parameters for iron: saturation magnetization  $M_S = 1.72 \times 10^6$  A/m, exchange stiffness  $A = 2.1 \times 10^{-11}$  J/m, and cubic anisotropy constant  $K_1 = 4.8 \times 10^4$  J/m<sup>3</sup>. A damping parameter of  $\alpha = 0.5$  was used to reach equilibrium remnant state rapidly. To fit the simulations with the experimental procedure, we applied magnetic fields of the same amplitude and direction as were applied experimentally. The nanoparticles have been deposited onto the TEM grid in presence of a 250mT magnet, generating a field along [001] direction. Then, the objective lens, though switched off, induces a residual magnetic field of ca. 20 mT parallel to the optic axis due to the remanence of polar pieces. Thus, we included in the simulations this small magnetic field parallel to [001]. Electron holography provides a 2D induction map of the magnetic nanocubes. In order to compare our simulations with experimental results, we add the magnetization and total field vector coordinates in each cell to obtain a 3D induction map. Then, the calculated induction vectors are averaged along the  $z$  direction to obtain a 2D map of the simulated induction integrated along the sample thickness.

**Results and Discussion.** The reduction of  $(\text{Fe}\{\text{N}[\text{Si}(\text{CH}_3)_2]_2\}_2)$  in mesitylene under a dihydrogen atmosphere at 150 °C leads to nanoparticles of 1.5 nm of diameter.<sup>31</sup> Adding surfactants with a long alkyl chain and a polar head ( $-\text{NH}_2$ ,  $-\text{COOH}$ ) to the initial mixture has the following effects: (i) they stabilize the nanoparticles formed, (ii) they react with the precursor to form more stable species such as iron(II) carboxylate complexes, and (iii) at large concentration, they tend to self-organize leading to a mediated-growth.<sup>25</sup> For acid/amine ratio below 1.4:2 equivalents (equiv) per mole of iron, nano-objects grow in an isotropic environment, leading after 2 days of reaction to spherical nanoparticles with mean diameters ranging from 1.5 to 9 nm (Supporting Information Figure S1).

For acid/amine ratio of 1.5:2 eq., self-assemblies of surfactants are observed concomitant with the growth of cubic nanoparticles (Supporting Information Figure S2). These self-assemblies seem a prerequisite for the synthesis of cubes through a mediated-growth. By modifying the alkyl chain length of surfactants from 16 to 12 carbons, we could tune this mediated-growth. Polydisperse cubes (42 nm,  $\sigma = 16$  nm) were

obtained after 2 days of reaction with C12 surfactants (Figure 1a, Supporting Information Figure S3). Within these objects,

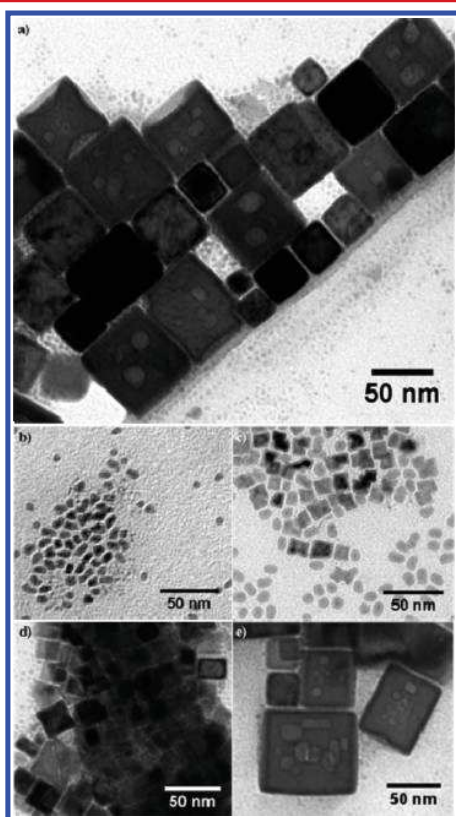


**Figure 1.** TEM images of (a) porous nanocubes obtained at 150 °C under 3 bar of H<sub>2</sub> with an acid/amine ratio of 1.5:2 with alkyl chain C12, and the intermediate nanoparticles observed after (b) 2, (c) 6, (d) 24, and (e) 48 h of reaction.

regions with brighter contrast are observed in transmission electron microscopy (TEM, Figure 1a) and in high-resolution TEM (HRTEM, Supporting Information Figure S4). Such contrast could be due to local variations of thickness or of material. However, metallic Fe was the only material detected by HRTEM, thus, the thickness variation could more likely arise from local defects at the surface or embedded within the cubes.

Since TEM only provide a 2D projection of the objects, electron tomography has been performed in order to determine more precisely the localization of these defects. Tomography leads to a complete 3D reconstruction of the objects based on a series of 2D TEM images acquired by HAADF scanning TEM (HAADF-STEM) from different tilting angles.<sup>32</sup> An *xy*-orthoslice of the 3D view of packed nanocubes is presented in Figure 2a. The presence of darker regions, corresponding to the voids, is clearly visible. Such inversion of contrast compared to previous TEM images (Figure 1a) is due to the HAADF signal, which is directly related to the sample thickness. In order to extract quantitative information on pores, an additional manual segmentation is performed.<sup>33</sup> Gray levels are segmented all along the reconstruction volume in order to reveal the edges of the cubes and pores. After such treatment, 3D visualization is obtained with pores being represented in light blue and surfaces of cubes by a violet envelope (Figure 2b,c, Supporting Information Video 1). The presence of internal pores is clearly

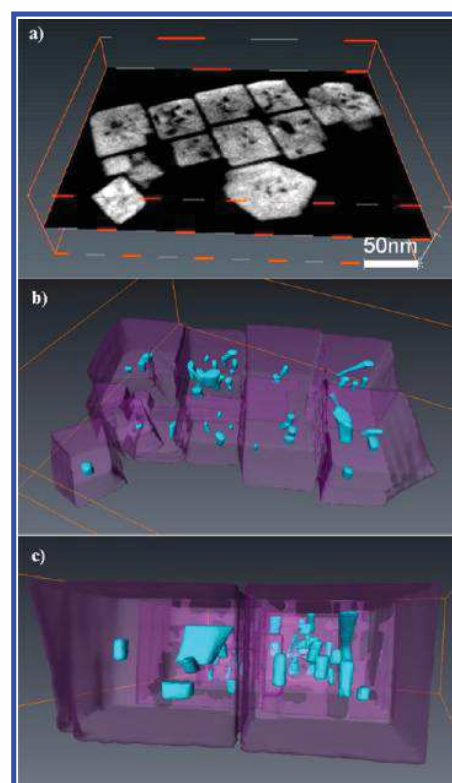


**Figure 2.** Three-dimensional reconstruction of porous nanocubes obtained by electron tomography (a) *xy*-orthoslice through the 3D reconstruction; (b) top view and (c) lateral view of the 3D reconstruction, pores are represented in blue while external envelope of the cubes are in transparent violet.

attested with the defects being in a large majority (>90%) embedded within the cube.

The presence of internal defects within cubes rises the question of their formation and nature. Below a critical size of 30 nm, no defects are observed while above, more than 90% of cubes exhibit holes. A strong correlation between the lateral size of cubes and the number of defects could be seen: the bigger the cubes, the more defects are embedded (Supporting Information Figure S5). A kinetic study was performed by monitoring the reaction, combining iron precursor with 1.5:2 equiv of acid/amine. This reaction was equally distributed into four Fisher-Porter bottles, allowed to react at 150 °C for 2, 6, 24, and 48 h, respectively (Figure 1). Anisotropic nanoparticles with mean lateral sizes of 10 × 6 nm are observed after 2 h of reaction. After 6 h, this anisotropic shape is retained but facets start to appear. Coalescence of cubes through edges leads to the presence of large octapods (18 nm,  $\sigma = 5$  nm) and embedded pores. Finally, after 48 h large and polydisperse porous cubes (42 nm,  $\sigma = 25$  nm) are obtained. This monitoring, based on TEM images, seems fairly similar to the one previously reported with C16 surfactants.<sup>25</sup> Thus a similar growth mechanism, based on successive nucleation, growth-coalescence and growth-ripening steps, seems to control the synthesis of these cubes. Ripening appears after 6 h, as revealed by the faceting of anisotropic objects, which is in agreement with the observation for C16 surfactants.<sup>25</sup> However, coalescence does not end at the appearance of ripening but lasts at least 24 h. Such variation in the coalescence step duration could explain the difference in cube sizes (21 nm for C16, up to 80 nm for

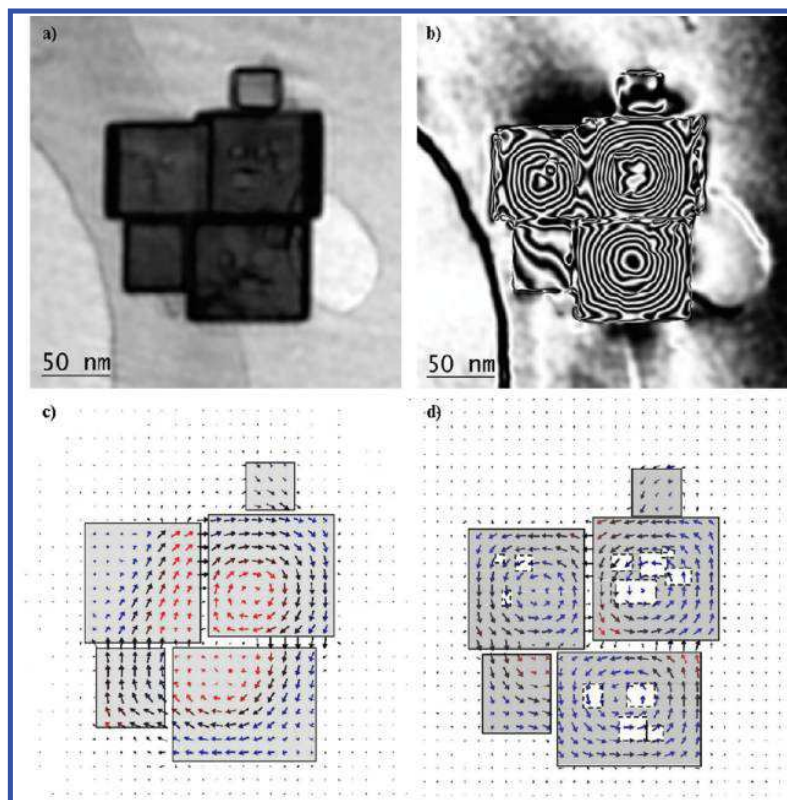


**Figure 3.** Electron holography and micromagnetic simulations for a compact assembly of 5 Fe nanocubes. (a) TEM image reveals the cubic structure and the internal defects within larger cubes. (b) Cosinus of the magnetic phase image corresponding to the magnetic contribution to the phase shift with  $\pi/4$  rad isophase contours. Note the cylindrical symmetry of the magnetic induction flux line in the three larger cubes. Micromagnetic simulation (with bulk Ms) of the in-plane induction (the location and the number of arrows are not related with the discretization points) for (c) defect-free objects (visualized in gray) and (d) porous cubes. Dashed white boxes are a guide to the eye to indicate the lateral extent and the in-plane position of the defects.

C12) and the presence of defects embedded within the cubes. The reason for that extent is not known yet, but it could be linked to the difference in the stability of cube edges due to a lower steric hindrance for C12 compared to C16 alkyl chains. Though it will be difficult to conclude on the chemical species trapped within pores, their size distribution, extracted from the projected lateral size observed by TEM, give some clues (Supporting Information Figure S6). Indeed, the minimum pore size is above 4 nm, that is, twice the surfactant alkyl chain length. Since the defects are formed during a coalescence process, we propose that the cavities are filled with surfactants, which would explain this minimum size and the facets observed,  $\{100\}$  faces being stabilized by acid.<sup>25</sup>

Magnetic characterization performed on raw powders at 2 and 300 K reveals that these porous nanocubes exhibit a magnetization of respectively 220 and 216  $\text{Am}^2/\text{kg}_{\text{Fe}}$  close to the bulk value of bcc-Fe and are ferromagnetic at room temperature ( $\mu_0 H_C = 15\text{mT}$ , Supporting Information Figure S7). The local study of the magnetic behavior of these cubes has been performed by electron holography (EH).<sup>32</sup> Off-axis EH allows measuring the phase shift of the high-energy electron wave that has passed through a material.<sup>34</sup> Since the phase shift is sensitive to electric and magnetic fields in the sample, local magnetic properties in nanoscale materials can be mapped after having isolated the magnetic part. The nanocubes observed have been deposited onto the TEM grid in presence of a 250mT magnet, generating a field along  $[001]$  direction. As

expected from the size of the object above the single-domain/vortex transition ( $\sim 28\text{ nm}$ ),<sup>11,20</sup> isolated nanocubes exhibit a vortex state (Supporting Information Figure S8). Perturbations of the vortex core are observed at the vicinity of pores, but the out-of-plane component of the magnetization is still clearly observed. The induction state in interacting nanocubes could also be determined (Figure 3). Contrarily to the observation previously performed on interacting 30 nm nanocubes,<sup>20</sup> vortices are retained within each cube presenting defects. Such a peculiar magnetic configuration could be reproduced by micromagnetic calculations (OOMMF code).<sup>30</sup> In order to address the stability question of the vortices, we have compared the numerical simulation obtained for defect-free (Figure 3c) and porous (Figure 3d) interacting cubes. Porous objects have been simulated by introducing voids within the cubes. The lateral sizes and in-plane position of the defects were extracted from TEM images. Their height was extrapolated from a cubic shape since mainly isotropic defects are observed by tomography. Finally the out-of-plane position of the defects was arbitrary taken within the cubes, equally distributed apart from the median position. Since the position of isotropic defects was reported as not affecting the vortex nucleation field,<sup>35</sup> we did not explore the effect of the  $z$  position on the stability of the vortices. While a flux closure state is observed for arrangements of defect-free objects (Figure 3c), vortices are observed for porous cube as evidenced in the integrated induction map (Figure 3d) and in the 3D magnetic moment

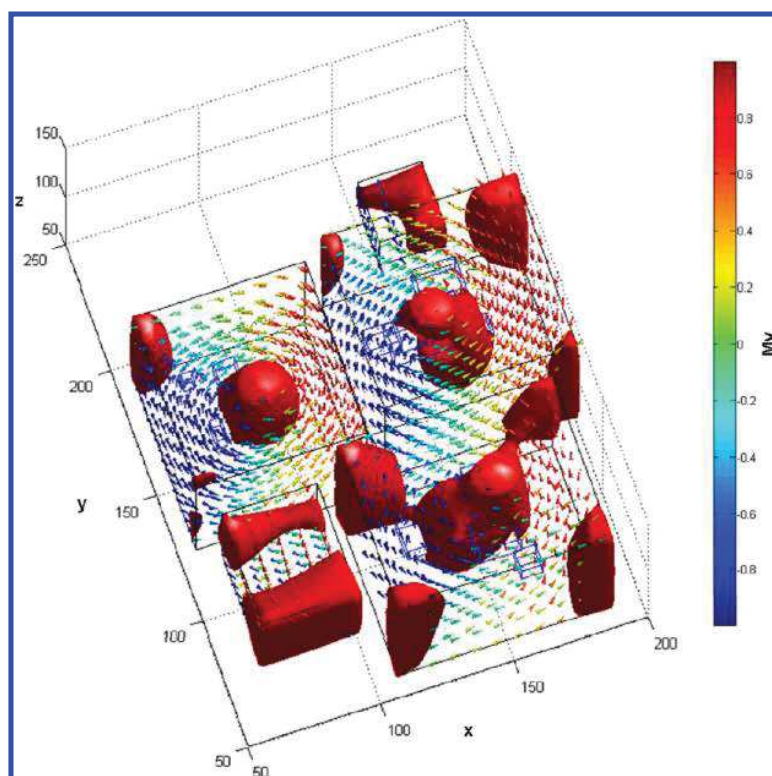


**Figure 4.** Three-dimensional visualization of the magnetic moment within an assembly of 5 Fe nanocubes. The presence of defects within the three larger cubes is represented with blue boxes. The red surface displays the surface of spins with  $M_z = 0.6$  (we reduced the number of arrows for a better visualization).

cartography (Figure 4). Thus, in the presence of internal defects vortices become the configuration of minimum energy due to the overall reduction of the exchange energy.<sup>23,36</sup> However, most of the results previously reported have been handled on permalloy nanodisks with single lithography-defined defect of same thickness than the object.<sup>21,23,35</sup> In such cases, the vortex core is stabilized within the void, resulting in the total disappearance of the out-of-plane singularity, and thus to an onion configuration rather than a vortex configuration. In our case, where multiple voids are smaller and randomly distributed within the materials, the vortex core is still observed within the cubes. Thus, the detailed mechanism of vortex stabilization could be more complicated and would benefit from deeper investigations with cross-correlated electronic tomography–holography measurements and micromagnetic simulations.

In conclusion, a fine-tuning of the growth environment and the use of appropriate aliphatic surfactants allowed us to synthesize quantitatively Fe nanocubes above 30 nm and incorporating voids. The presence of internal defects embedded within cubes has been characterized by electron tomography. These defects have been for the first time evidenced as stabilizing vortex magnetic states within nanoparticle interacting assemblies. In this respect, we provided experimental proof for the potential interest of metallic porous cubes as stable vortices structures. These vortices are particularly important for advanced fundamental studies and might eventually become new building blocks for dedicated applications (spintronics, magnetic recording, and nanomedicine). Subsequent optimizations need however to be undertaken, such as stabilizing defects within smaller objects, reducing the overall size

dispersity of the Fe cubes, and controlling their self-assembly on large 2D areas.

## ■ ASSOCIATED CONTENT

### 📄 Supporting Information

(1–2) Schematic view of the four states of the magnetic vortex (3–4) and the corresponding size distribution of the cubes and the defects. TEM images of nanoparticles obtained under various experimental conditions (ligands, temperature, and concentration). Characterization of porous cubes by (5) HRTEM, and (6) TEM. (7) Magnetic characterization of bcc-Fe porous NPs ( $M(H)$  at 2 and 300 K). (8) Electron holography on a single porous nanocube. A video of the electron tomography reconstruction is also available. This material is available free of charge via the Internet at <http://pubs.acs.org>.

## ■ AUTHOR INFORMATION

### Corresponding Author

\*E-mail: [lmacroi@insa-toulouse.fr](mailto:lmacroi@insa-toulouse.fr). Phone: +33561559652. Fax: +33561559697.

### Present Address

<sup>†</sup>Université de Rouen, UMR 6634 CNRS, F-76801 Saint-Etienne du Rouvray, France.

### Notes

The authors declare no competing financial interest.

## ■ ACKNOWLEDGMENTS

L.-M.L. thanks the French Ministry of “National Education and Research” for MENRT grant. The authors thank the METSA

and ESTEEM networks for microscopy studies, Alain Mari for magnetic measurements, and Marc Respaud for fruitful discussions.

## REFERENCES

- (1) Sun, S.; Murray, C. B.; Weller, D.; Folks, L.; Moser, A. Monodisperse FePt nanoparticles and ferromagnetic FePt nanocrystal superlattices. *Science* **2000**, *287*, 1989–1992.
- (2) Wetz, F.; Soulantica, K.; Respaud, M.; Falqui, A.; Chaudret, B. Synthesis and magnetic properties of Co nanorod superlattices. *Mater. Sci. Eng., C* **2007**, *27*, 1162–1166.
- (3) Lau, J. W.; Shaw, J. M. Magnetic nanostructures for advanced technologies: fabrication, metrology and challenges. *J. Phys. D: Appl. Phys.* **2011**, *44* (2011), 303001.
- (4) Lim, F.; Wilson, B.; Wood, R. Analysis of shingle-write readback using magnetic-force microscopy. *IEEE Trans. Magn.* **2010**, *46*, 1548–1551.
- (5) Gao, J.; Gu, H.; Xu, B. Multifunctional magnetic nanoparticles: design, synthesis and biomedical applications. *Acc. Chem. Res.* **2009**, *42*, 1097–1107.
- (6) Bouchard, L.-S.; et al. Picomolar sensitivity MRI and photo-acoustic imaging of cobalt nanoparticles. *Proc. Natl. Acad. Sci. U.S.A.* **2009**, *106*, 4085–4089.
- (7) Lacroix, L.-M.; Ho, D.; Sun, S. Magnetic Nanoparticles as Both Imaging Probes and Therapeutic Agents. *Curr. Top. Med. Chem.* **2010**, *10*, 1184–1197.
- (8) Mehdaoui, B.; et al. Optimal size of nanoparticles for magnetic hyperthermia: a combined theoretical and experimental study. *Adv. Funct. Mater.* **2011**, *21*, 4573–4582.
- (9) Lu, A.-H.; Salabas, E. L.; Schüth, F. Magnetic nanoparticles: synthesis, protection, functionalization, and application. *Angew. Chem., Int. Ed.* **2007**, *46*, 1222–1244.
- (10) Jeong, U.; Teng, X.; Wang, Y.; Yang, H.; Xia, Y. Superparamagnetic colloids: controlled synthesis and niche applications. *Adv. Mater.* **2007**, *19*, 33–60.
- (11) Rave, W.; Fabian, K.; Hubert, A. Magnetic states of small cubic particles with uniaxial anisotropy. *J. Magn. Magn. Mater.* **1998**, *190*, 332–348.
- (12) Milat, J.; Thiaville, A. Vortex cores—smaller than small. *Science* **2002**, *298*, 555.
- (13) Van Waeyenberge, B.; et al. Magnetic vortex core reversal by excitation with short bursts of an alternating field. *Nature* **2006**, *444*, 461–464.
- (14) Keavney, D. J.; Cheng, X. M.; Buchanan, K. S. Polarity reversal of a magnetic vortex core by a unipolar, nonresonant in-plane pulsed magnetic field. *Appl. Phys. Lett.* **2009**, *94*, 172506.
- (15) Choi, Y.-S.; et al. Out-of-plane current controlled switching of the fourfold degenerate state of a magnetic vortex in soft magnetic nanodots. *Appl. Phys. Lett.* **2010**, *96*, 072507.
- (16) Yu, X. W.; et al. Images of spin-torque-driven magnetic nano-oscillator. *Phys. Rev. Lett.* **2011**, *106*, 167202.
- (17) Dussaux, A.; et al. Large microwave generation from D.C. driven magnetic vortex oscillators in magnetic tunnel junctions. *Nat. Commun.* **2010**, *1*, 8.
- (18) Vogel, A.; et al. Coupled vortex oscillations in spatially separated permalloy squares. *Phys. Rev. Lett.* **2011**, *106*, 137201.
- (19) Yang, Y.; Liu, X.-L.; Yi, J.-B.; Yang, Y.; Fan, H.-M.; Ding, J. Stable vortex magnetite nanorings colloid: micromagnetic simulation and experimental demonstration. *J. Appl. Phys.* **2012**, *111*, 044303.
- (20) Snoeck, E.; et al. Magnetic Configurations of 30 nm Iron Nanocubes Studied by Electron Holography. *Nano Lett.* **2008**, *8*, 4293–4298.
- (21) Rahm, M.; Biberger, J.; Umansky, V.; Weiss, D. Vortex pinning at individual defects in magnetic nanodisks. *J. Appl. Phys.* **2003**, *93*, 7429–7431.
- (22) Goll, D.; Berkowitz, A. E.; Bertram, H. N. Critical sizes for ferromagnetic spherical hollow nanoparticles. *Phys. Rev. B* **2004**, *70*, 184432.
- (23) Uhling, et al. Shifting and pinning of a magnetic vortex core in a permalloy dot by a magnetic field. *Phys. Rev. Lett.* **2005**, *95*, 237205.
- (24) Peng, S.; Sun, S. Synthesis and characterization of monodisperse hollow Fe<sub>3</sub>O<sub>4</sub> nanoparticles. *Angew. Chem., Int. Ed.* **2007**, *46*, 4155–4158.
- (25) Lacroix, L.-M.; Lachaize, S.; Falqui, A.; Respaud, M.; Chaudret, B. Iron Nanoparticle Growth in Organic Superstructures. *J. Am. Chem. Soc.* **2009**, *131*, 549–557.
- (26) Huo, Z.; Tsung, C.-K.; Huang, W.; Zhang, X.; Yang, P. Sub-Two Nanometer Single Crystal Au Nanowires. *Nano Lett.* **2008**, *8*, 2041–2044.
- (27) Lu, X.; Yavuz, M. S.; Tuan, H.-Y.; Korgel, B. A.; Xia, Y. Ultrathin Gold Nanowires Can Be Obtained by Reducing Polymeric Strands of Oleylamine-AuCl Complexes Formed via Auophilic Interaction. *J. Am. Chem. Soc.* **2008**, *130*, 8900–8901.
- (28) Rasband, W. S.; Image, J. Research Services Branch, U.S. National Institutes of Health, Bethesda, Maryland, <http://rsb.info.nih.gov/ij/>, 1997–2007.
- (29) Kawase, N.; Kato, M.; Nishioka, H.; Jinnai, H. Transmission electron microtomography without the “missing wedge” for quantitative structural analysis. *Ultramicroscopy* **2007**, *107*, 8–15.
- (30) Donahue, M. J.; Porter, D. G. *OOMMF User's Guide, Version 1.0, Interagency Report NISTIR 6376*; National Institute of Standards and Technology: Gaithersburg, MD, 1999. We used version 1.2a3 of this public code that can be found at the URL <http://math.nist.gov/oommf/>.
- (31) Lacroix, L.-M.; et al. Ultrasmall iron nanoparticles: Effect of size reduction on anisotropy and magnetization. *J. Appl. Phys.* **2008**, *103*, 07D521.
- (32) Midgley, P. A.; Dunin-Borkowski, R. E. Electron tomography and holography in materials science. *Nat. Mater.* **2009**, *8*, 271–280.
- (33) Biermans, E.; Molina, L.; Batenburg, K. J.; Bals, S.; Van Tendeloo, G. Measuring Porosity at the Nanoscale by Quantitative Electron Tomography. *Nano Lett.* **2010**, *10*, 5014–5019.
- (34) Thomas, J. M.; Simpson, E. T.; Kasama, T.; Dunin-Borkowski, R. E. Electron holography for the study of magnetic nanomaterials. *Acc. Chem. Res.* **2008**, *41*, 665–674.
- (35) Liu, Y.; Du, A. Arrangement effects of triangular defects on magnetization reversal process in a permalloy dot. *J. Magn. Magn. Mater.* **2011**, *323*, 461–464.
- (36) Vaz, C. A. F.; Athanasiou, C.; Bland, J. A. C.; Rowlands, G. Energetics of magnetic ring and disk elements: uniform versus vortex state. *Phys. Rev. B* **2006**, *73*, 054411.

# Tuning Complex Shapes in Platinum Nanoparticles: From Cubic Dendrites to Fivefold Stars\*\*

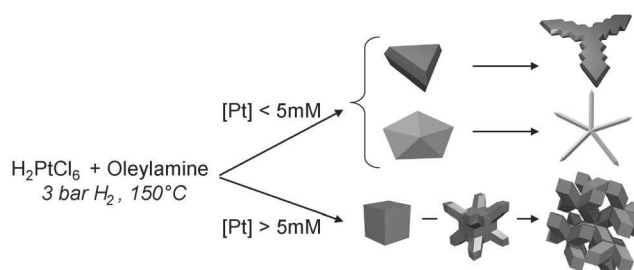
Lise-Marie Lacroix,\* Christophe Gatel, Raul Arenal, Cécile Garcia, Sébastien Lachaize, Thomas Blon, Bénédicte Warot-Fonrose, Etienne Snoeck, Bruno Chaudret, and Guillaume Viau

The synthesis of nanoparticles (NPs) exhibiting large surface-area-to-volume ratios has been a long-sought goal in developing various applications such as ultrasensitive sensors<sup>[1]</sup> or highly active catalysts.<sup>[2]</sup> In addition to a large specific area, crystallographic planes exposed on the surface of the NPs are key parameters for the reactivity and selectivity of NPs in catalytic processes.<sup>[3]</sup> Thus, intense research has been devoted to the shape control of noble-metal nanocrystals.<sup>[4]</sup> For example, for Pt-based nanoparticles, dendritic nanostructures,<sup>[5]</sup> branched-NPs,<sup>[6]</sup> or multipods<sup>[7]</sup> exhibit enhanced catalytic activities relative to their spherical counterparts.<sup>[8]</sup> Such shape control could be obtained by manipulating the reduction kinetics<sup>[6]</sup> through temperature,<sup>[6a,9]</sup> pH,<sup>[10]</sup> ligands,<sup>[11]</sup> or the addition of small amounts of nucleating agents.<sup>[6b]</sup> Interestingly, in this variety of shapes, only few groups reported multiply twinned Pt nanoparticles,<sup>[12]</sup> whereas decahedrons are fairly common for most of the noble metals (e.g. Au, Ag, Rh).<sup>[13]</sup> However, these twinned NPs could offer significant benefits toward catalysis because they have mainly their {111} faces exposed.<sup>[14]</sup>

Herein, we report complex platinum nanoobjects of unprecedented shapes (monodisperse cubic dendrites and fivefold stars) and the fine-tuning between two growth mechanisms. The platinum concentration is finely tuned in a fairly simple reaction of  $\text{H}_2\text{PtCl}_6$  in oleylamine under dihydrogen pressure. Amine plays the role of solvent and stabilizer and can assist the reduction process. Previous work has shown that the room-temperature reduction of  $\text{HAuCl}_4$  by neat oleylamine yielded unique Au nanowires.<sup>[15]</sup> However, in the same conditions, Pt required higher temperature to be

reduced (250 °C).<sup>[9]</sup> In the present study, addition of dihydrogen, a well-known reducing agent,<sup>[16]</sup> lowered the reduction temperature and, at the same time, played an important role in the shape control of NPs. Indeed,  $\text{H}_2$  can “clean” the NP surface by temporarily removing weak coordinating ligands, such as amines, leading to coalescence or ripening.<sup>[17]</sup>  $\text{H}_2$  can also generate surface hydrides, which stabilize the NP and perform hydrogenation reactions.<sup>[18]</sup>

An ex situ kinetic study, followed by high-resolution transmission electron microscopy (HRTEM), has evidenced two growth mechanisms based respectively on cubic or decahedral seeds (see Scheme 1) leading to monodisperse cubic dendrites or fivefold stars.



**Scheme 1.** General overview of the versatile synthesis of Pt<sup>0</sup> NPs. Shape could be controlled by the platinum concentration and the nature of the seeds formed.

Pt NPs were produced by reduction of  $\text{H}_2\text{PtCl}_6$  in oleylamine under an  $\text{H}_2$  atmosphere (3 bar) at 150 °C (see the Experimental Section and Scheme 1). The shape of the Pt NPs could be easily tuned by varying the experimental parameters, in particular the Pt concentration from low (2 mM) to high (10 mM) values. For example, dendritic growth was observed at high Pt concentration ( $[\text{Pt}] > 5 \text{ mM}$ ) (Figure 1 a,b and Figures S1 and S2 in the Supporting Information). The resulting objects were obtained quantitatively with a Pt yield over 95%. The most striking feature, relative to previously reported dendrites,<sup>[5]</sup> was their cubic contour.

Figure 2a shows a high-magnification transmission electron microscopy (TEM) image of a single dendrite exhibiting dense organization of branches with defined orientations. The outer faces of the cubes coincided with the {100} planes of the crystallographic structure of fcc-Pt. The selective-area electron diffraction (SAED) pattern on a single cube (Figure 2b) shows fourfold symmetry, which is characteristic of a single-crystalline fcc crystal observed along the  $\langle 100 \rangle$  zone axis. The elongation of the diffraction spots {200} and {220} indicates a slight misorientation between the branches (ca. 10°). These

[\*] Dr. L.-M. Lacroix, Dr. C. Garcia, Dr. S. Lachaize, Dr. T. Blon, Prof. B. Chaudret, Prof. G. Viau

LPCNO, Université de Toulouse, INSA, UPS, CNRS  
135 avenue de Rangueil, 31077 Toulouse (France)

E-mail: lmlacroix@insa-toulouse.fr

Homepage: <http://lpcno.insa-toulouse.fr/>

Dr. C. Gatel, Dr. B. Warot-Fonrose, Prof. E. Snoeck  
CEMES, CNRS, 29 rue Jeanne Marvig, 31077 Toulouse (France)

Dr. R. Arenal  
Laboratorio de microscopias avanzadas (LMA), Instituto de Nanociencia de Aragon (INA), U. Zaragoza  
C/Mariano Esquillor s/n, 50018 Zaragoza (Spain)

Dr. R. Arenal  
Fundacion ARAID, 50004 Zaragoza (Spain)

[\*\*] This work was supported by the European FP7-Train2 project and the French network METSA. We thank G. Antorrena for XPS measurements.

Supporting information for this article is available on the WWW under <http://dx.doi.org/10.1002/anie.201107425>.

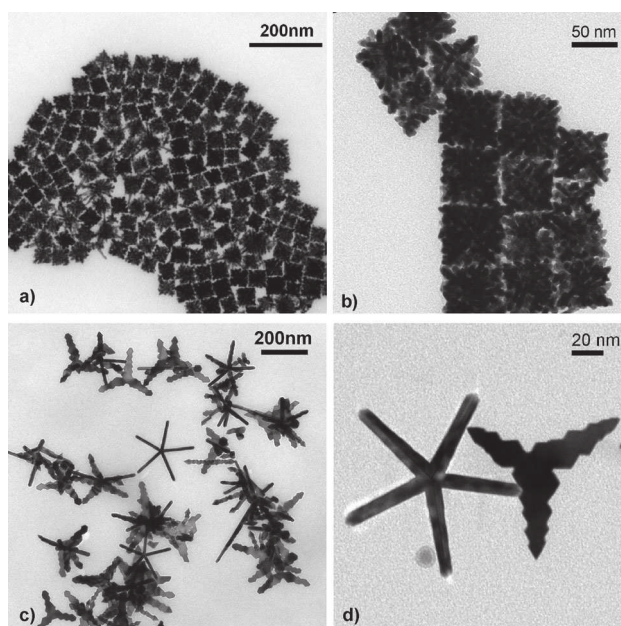


**Figure 1.** TEM images of Pt nanocrystals prepared at various concentrations of platinum: a,b) dendritic cubes obtained at  $[Pt] = 10 \text{ mM}$ ; c,d) Pt stars obtained at  $[Pt] = 2 \text{ mM}$ .

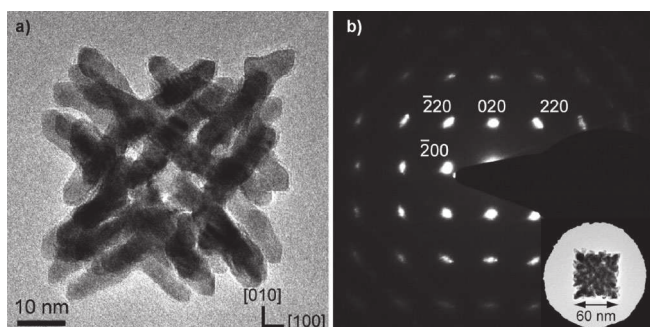


**Figure 2.** a) HREM image of a single Pt dendritic cube obtained after reaction for 1 h. b) SAED pattern along the  $[001]$  axis on a 60-nm-cube obtained after reaction for 2 h, as shown in the inset.

results demonstrate that cubic dendrites adopt a slightly distorted single-crystalline structure.

The growth mechanism of such peculiar dendrites was investigated by stopping the reaction at various stages (Figure 3 and Figure S3). The reaction is very fast, as shown by the octapods already observed after 1 min of reaction at  $150^\circ\text{C}$ . These octapods result from a growth on the  $\langle 111 \rangle$  directions on cubic seeds. The  $\{100\}$  facets are observed, concomitant with closing  $\{110\}$  facets. After 3 min of reaction, the selected growth on  $\{100\}$  facets leads to the appearance of bifurcations, and new branches start to grow along three different  $\langle 111 \rangle$  growth directions. Such selected growth is repeated until the platinum precursor is completely consumed. Although the diameter of the branches was rather constant at approximately 5.5 nm, the mean size of the cubic dendrites could be tuned from 30 to 100 nm by varying the reaction time between 10 min and 2 h (Figure S4). The dendrites finally obtained exhibit a high proportion of  $\{100\}$

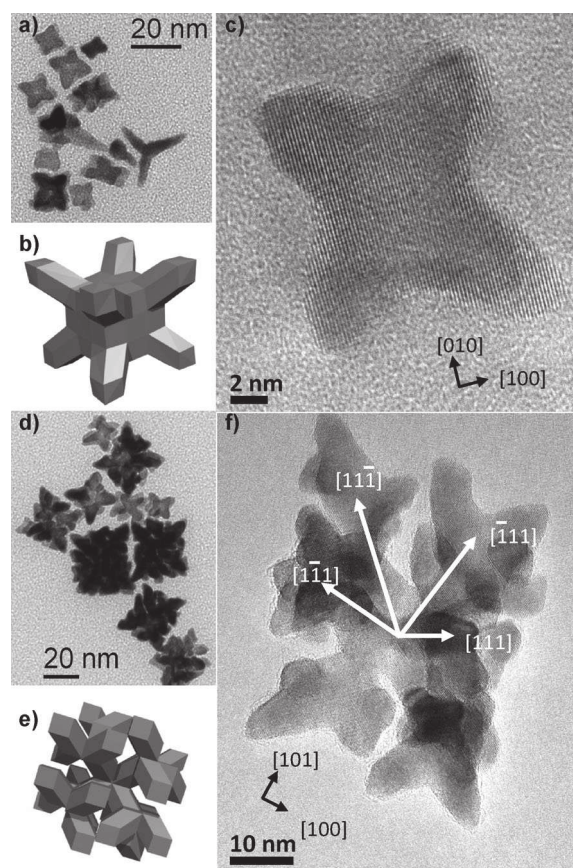


**Figure 3.** Nanoparticles obtained after reaction for a–c) 1 min and d–f) 3 min. a,d) TEM micrograph and the corresponding c,f) HREM micrographs. The  $\{100\}$  facets are highlighted along the  $\langle 111 \rangle$  growth directions. b,e) Schematic view of the objects at this growth stage.

and  $\{110\}$  facets, as in the earlier growth stage (Figure S5). Such dendritic structures, which have no precedent, were stable at  $150^\circ\text{C}$  for days; the complex branches architecture did not collapse into denser crystals.

Star-shaped NPs were obtained at low Pt concentration ( $[Pt] = 2 \text{ mM}$ ; Figure 1c,d and Figure S6). Samples were composed of nanocrystals exhibiting a well-defined morphology with around 20% fivefold stars, 70% threefold stars (planar tripods), and 10% multipods or undefined shapes. This ratio could vary: the proportion of multipods increased with the  $[Pt]$  concentration. Threefold stars were obtained previously by using a different approach (reduction of  $\text{Pt}(\text{acac})_2$  by a diol at  $160^\circ\text{C}$ ).<sup>[7a]</sup> However, the present fivefold Pt stars are unique. Their arm length could be tuned from 30 nm to 120 nm by varying the reaction time between 6 and 48 h (Figure S7).

Figure 4 shows a high magnification image of a single fivefold star and the corresponding SAED pattern along the  $\langle 110 \rangle$  zone axis. The complex pattern displays fivefold symmetry of the fcc structure spots, which is similar to the SAED pattern obtained on Au decahedra.<sup>[19]</sup> The HRTEM image of the core clearly shows the noncrystallographic fivefold axis and the five resulting twinning boundaries. Periodic lattice fringes could be clearly resolved for three families of planes.

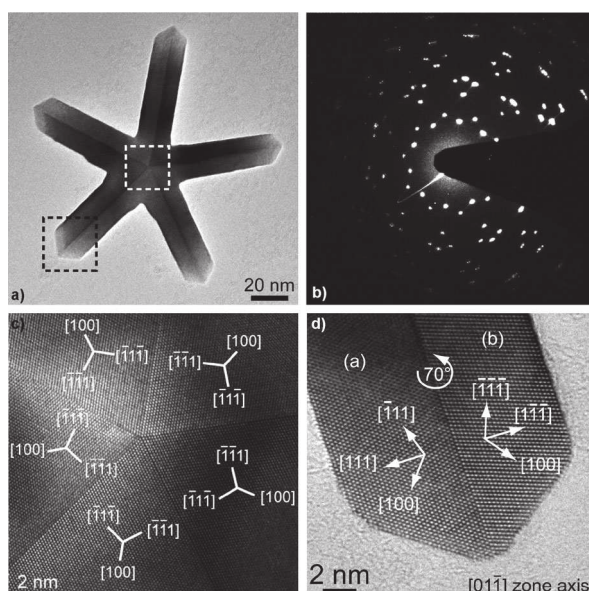


**Figure 4.** a) TEM micrograph of a single Pt fivefold star and b) its corresponding ED pattern. HRTEM images of c) the core and d) a branch tip as shown in (a) by white and black boxes, respectively.

Lattice spacings of 2.26 Å and 1.96 Å correspond to the {111} and {100} planes of fcc-Pt, respectively. The rotation of these planes along the fivefold axis is evidenced in Figure 4c: single-crystalline tetrahedra were observed between two successive twin boundaries.

Figure 4d shows a HRTEM image of the branch tip. The branches are highly crystalline, exposing mainly {111} facets (Figures S8–10). These branches grow symmetrically along the twinning plane from each corner of the central decahedra, as revealed by TEM images taken after different growth stages (Figure 5). Such growth on decahedra corners was

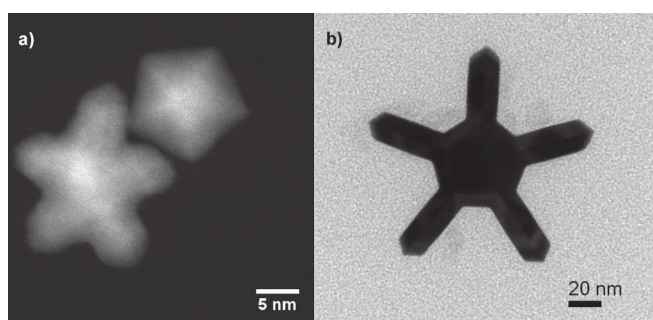


**Figure 5.** High-angle annular dark field and TEM images of Pt NPs obtained for [Pt] = 2 mM after reaction for a) 2 h and b) 4 h.

recently reported by Zhang et al. on Rh starfishlike NPs, but the crystallinity of the branches was not clearly evidenced.<sup>[13c]</sup> If Pt decahedra are fairly rare objects, highly crystalline fivefold Pt stars represent a unique result to the best of our knowledge.

X-ray photoelectron spectroscopy (XPS) and energy-dispersive X-ray spectroscopy (EDS) analyses were performed on cubic dendrites and stars. As expected, the Pt NPs

resulting from the different syntheses consisted of pure Pt<sup>0</sup> (Figures S11–12). The surface of the particles was stabilized mostly by amine groups, although chloride anions and ammonium groups could be detected as traces.

It is noteworthy that reaction times were considerably longer at low [Pt] concentration compared with the few minutes required for high [Pt] concentration synthesis. At 2 mM, the yellow color, which is characteristic of the Pt precursor, vanished after at least 24 h of reaction. The shape control in this versatile synthesis then looked strongly correlated with the reaction rates. Three experimental parameters can be adjusted to increase the reaction rate: [Pt] concentration, temperature ( $T$ ), and dihydrogen pressure ( $p_{\text{H}_2}$ ). Increasing the temperature and pressure yield cubic dendrites after only 1 hour (Figure S13), even at low [Pt] concentration (2 mM). Thus, we could induce a dendritic growth by increasing the reaction rate. An illustration of this difference of kinetic between cubic dendrites and stars is given by the variation of dihydrogen pressure profile with time (Figure S14). Fast consumption of dihydrogen was observed for dendritic growth, while no abrupt drop was detected in the case of star-shaped growth. These two hydrogenation profiles combine multiple reactions (reduction of platinum, corresponding to ca. 0.3 bar of H<sub>2</sub>, and hydrogenation catalyzed by Pt NPs or molecular species) in various experimental conditions. Thus, the catalytic activities of dendrites vs. stars cannot be directly compared. However, we can conclude that very catalytically active species were quickly formed at high temperature and pressure, whereas this was not the case under conditions of lower temperature and pressure.

The shape control reported herein for Pt<sup>0</sup> NPs (planar tripods, fivefold stars, and cubic dendrites) was achieved by varying the reaction conditions in a relatively narrow range of concentration or temperature. The nature of the seeds—cubic (exposing noncompact faces) or triangular and decahedral (exposing {111} faces)—is determinant in the final morphology reached (Scheme 1).

At fast reaction rates, cubic seeds, exhibiting fcc structure, are quickly formed as shown by ex situ HREM study and the evolution of H<sub>2</sub> pressure as a function of time. The very fast consumption of H<sub>2</sub> is due to fast reduction of Pt precursor and to the hydrogenation of oleylamine by reactive seeds. Noncompact faces ({100} and {110}) are known to be active towards the reduction of internal olefins for Pd.<sup>[20]</sup> These cubic seeds, although very reactive, are relatively limited in number. The stability of the H<sub>2</sub>PtCl<sub>6</sub> precursor is indeed a determinant factor in this dendritic growth. The reduction of Pt(acac)<sub>2</sub> under similar conditions yielded multiple seeds and thus multiarmed NPs (Figure S15). Few seeds and fast reduction is characteristic of an autocatalytic process, previously reported for Pt.<sup>[3]</sup> Such autocatalytic processes combines a surface reaction between the precursor and preferential faces, leading here to a growth direction along {111} directions. The outer cubic shape of these nearly single-crystalline cubic dendrites, so peculiar, results from the strong crystallographic driving force combined with the tendency of dihydrogen to repair surfaces. The large cubic dendrites obtained at the end of the reaction expose noncompact faces,

which are not energetically favored. Such structures represent kinetic products and result from a growth limited by the diffusion of adatoms at the surface. Such diffusion-limited process is also known to be responsible for the size mono-dispersity of the final objects.<sup>[21]</sup>

When the reaction rates were decreased, by lowering either the platinum concentration or the reaction temperature, the reduction of the platinum precursor occurred over a longer period of time and yielded seeds exhibiting compact {111} faces. The profile of dihydrogen consumption is drastically modified compared to dendritic growth, as a result of the formation of a very limited number of seeds and of their nature. Indeed, under these conditions, stable twinned decahedra or triangular seeds could grow, resulting from the minimization of surface energy. These objects expose only {111} compact crystallographic planes. The successive growth of decahedra seeds into fivefold stars could be explained through multiple nucleation events. Decahedra are composed of five tetrahedra. However, these tetrahedra cannot fill the entire space and leave an empty angle of 7.3°, unless they adopt a highly strained structure, as reported for Au decahedra.<sup>[19]</sup> Since strain increases with the particle size, above a critical size, corresponding to the highest strain in Pt decahedron, the structure relaxes. In our case, this relaxation corresponds to the nucleation and growth of the arms at each corner of the decahedra core (Figure 5). Further crystallographic studies will be performed on these fivefold stars to determine the structural strain contained in the vicinity of the core and of the arms to confirm our growth model hypothesis. Such a multistep process has already been proposed by Maksimuk et al.<sup>[12a]</sup> for the growth of planar tripods. According to their model, branches grow at the corner of triangular twinned seeds, which act as preferential nucleation sites for a second growth process. In our reaction, fivefold stars and planar tripods coexist, giving strength to our growth hypothesis.

In summary, we have demonstrated that quasi-single-crystalline Pt nanoparticles with peculiar morphologies—cubic dendrites, planar tripods, and fivefold stars—can be obtained selectively and in high yield from a very simple procedure by tuning the reduction kinetics of a platinum salt under a dihydrogen atmosphere in the presence of an amine. The control of experimental parameters such as Pt concentration, reaction temperature, and dihydrogen pressure, leads to fine-tuning of the kinetics of the reaction and of the nature of seeds formed during the nucleation step. Although the reason for such an abrupt transition between cubic or twinned seeds is still unknown, numerical simulations of the energy of the seeds could give some important insights.

A slow reaction leads to twinned seeds, which evolve into planar tripods (threefold stars) and fivefold stars. Such multiply twinned NPs are unique for Pt and could open new perspectives for fundamental research on strained materials. In addition to this fundamental interest, catalytic activities could benefit from the presence of almost exclusively crystallographic surface orientation {111} for selectivity purposes.

A fast reaction leads to cubic seeds and thus to a dendritic growth. The peculiarity of these objects is their outer cubic

shape and an unprecedented size control of their envelope. Such dendritic cubes display a high surface-to-volume ratio, while their cubic shape enables their self-assembly on surfaces, which should be of high interest in catalysis. Structural characterization of the exposed surfaces, the reactivity, and the catalytic activity of these novel species will be evaluated to attest the potential of these unique cubic dendrites.

## Experimental Section

Typical synthesis of dendritic NPs : H<sub>2</sub>PtCl<sub>6</sub> (Alfa Aesar, 51 mg, 0.1 mmole) and oleylamine (Aldrich, 10 mL) were mixed in a vial and placed for 15 min in an ultrasonic bath to dissolve the Pt precursor. The 10 mM solution was transferred in a Fisher–Porter bottle and pressurized up to 3 bar with H<sub>2</sub>. The bottle was then allowed to react at 150°C in a preheated oil bath for 1 h. At the end of the reaction, a black precipitate was obtained while the supernatant is transparent. Typical yellow Pt precursor traces were no longer observed. The bottle was then cooled to room temperature, resulting in solidification of the supernatant. Hexanes (40 mL, Aldrich) was added to solubilize the NPs. The suspension, after the addition of 40 mL of absolute ethanol (VWR), was then centrifuged (4000 rpm, 6 min) to separate the NPs. The process is repeated three times to remove the excess of surfactants. The final product (ca. 25 mg) was kept in powder form or diluted in 5 mL toluene (Carlo Erba) for further use.

Multiply twinned NPs were synthesized by a similar procedure except that the Pt concentration was decreased below 5 mM. The reaction time was extended to 48 h, because the reaction rate is drastically reduced.

Characterization: Samples for TEM analysis were prepared by depositing few drops of diluted solution on an amorphous carbon-coated copper grid. Low-resolution images were obtained with a JEOL-1400 microscope, operating at 120 kV. HRTEM images were obtained with a Tecnai F20 (200 kV) instrument equipped with a spherical aberration corrector. X-ray photoelectron spectra were recorded using a Kratos Analytical Limited Axis ultralimited system fitted with a microfocused monochromatic Al<sub>Kα</sub> X-ray source (1486.6 eV, 12 kV × 120 W). The pass energy was set at 160 eV and 20 eV for the survey and the regions spectra, respectively.

Received: October 21, 2011

Revised: March 7, 2012

Published online: March 30, 2012

**Keywords:** crystal growth · nanostructures · platinum · solid-state structures

- [1] N. J. Wittenberg, C. L. Haynes, *WIREs Nanomed. Nanobiotech.* **2009**, *1*, 237–254.
- [2] a) R. J. White, R. Luque, V. L. Budarin, J. H. Clark, D. J. Macquarrie, *Chem. Soc. Rev.* **2009**, *38*, 481–494; b) E. Antolini, J. Perez, *J. Mater. Sci.* **2011**, *46*, 4435–4457.
- [3] J. Chen, B. Lim, E. P. Lee, Y. Xia, *Nano Today* **2009**, *4*, 81–95.
- [4] a) A. R. Tao, S. Habas, P. Yang, *Small* **2008**, *4*, 310–325; b) T. K. Sau, A. L. Rogach, *Adv. Mater.* **2010**, *22*, 1781–1804.
- [5] a) Y. Song, Y. Yang, C. J. Madforth, E. Pereira, A. K. Singh, H. Xu, Y. Jiang, C. J. Brinker, F. Van Swol, J. A. Schelutt, *J. Am. Chem. Soc.* **2004**, *126*, 635–645; b) X. Zhong, Y. Feng, I. Lieberwirth, W. Knoll, *Chem. Mater.* **2006**, *18*, 2468–2471.
- [6] a) J. Ren, R. D. Tilley, *Small* **2007**, *3*, 1508–1512; b) J. Chen, T. Herricks, Y. Xia, *Angew. Chem.* **2005**, *117*, 2645–2648; *Angew. Chem. Int. Ed.* **2005**, *44*, 2589–2592.

- [7] a) M. A. Mahmoud, C. E. Tabor, M. A. El-Sayed, Y. Ding, Z. L. Wang, *J. Am. Chem. Soc.* **2008**, *130*, 4590–4591; b) S. Sun, G. Zhang, D. Geng, Y. Chen, R. Li, M. Cai, X. Sun, *Angew. Chem.* **2011**, *123*, 442–446; *Angew. Chem. Int. Ed.* **2011**, *50*, 422–426.
- [8] a) Z. Peng, H. Yang, *Nano Today* **2009**, *4*, 143–164; b) B. Lim, Y. Xia, *Angew. Chem.* **2011**, *123*, 78–87; *Angew. Chem. Int. Ed.* **2011**, *50*, 76–85.
- [9] H.-T. Zhang, J. Ding, G.-M. Chow, *Langmuir* **2008**, *24*, 375–378.
- [10] H. Lee, S. E. Habas, S. Kwekin, D. Butcher, G. A. Somorjai, P. Yang, *Angew. Chem.* **2006**, *118*, 7988–7992; *Angew. Chem. Int. Ed.* **2006**, *45*, 7824–7828.
- [11] M. R. Axet, K. Philippot, B. Chaudret, M. Cabié, S. Giorgio, C. R. Henry, *Small* **2011**, *7*, 235–241.
- [12] a) S. Maksimuk, X. Teng, H. Yang, *J. Phys. Chem. C* **2007**, *111*, 14312–14319; b) N. V. Long, M. Ohtaki, M. Uchida, R. Jalem, H. Hirata, N. D. Chien, M. Nogami, *J. Colloid Interface Sci.* **2011**, *359*, 339–350.
- [13] a) D. Seo, C. I. Yoo, I. S. Chung, S. M. Park, S. Ryu, H. Song, *J. Phys. Chem. C* **2008**, *112*, 2469–2475; b) W. Zhang, Y. Liu, R. Cao, Z. Li, Y. Zhang, Y. Tang, K. Fan, *J. Am. Chem. Soc.* **2008**, *130*, 15581–15588; c) H. Zhang, X. Xia, W. Li, J. Zeng, Y. Dai, D. Yang, Y. Xia, *Angew. Chem.* **2010**, *122*, 5424–5428; *Angew. Chem. Int. Ed.* **2010**, *49*, 5296–5300.
- [14] a) A. Guerrero-Martínez, S. Barbosa, I. Pastoriza-Santos, L. M. Liz-Marzan, *Curr. Opin. Colloid Interface Sci.* **2011**, *16*, 118–127; b) H. Hofmeister, *Z. Kristallogr.* **2009**, *224*, 528–538.
- [15] a) Z. Huo, C.-K. Tsung, W. Huang, X. Zhang, P. Yang, *Nano Lett.* **2008**, *8*, 2041–2044; b) X. Lu, M. S. Yavuz, H.-Y. Tuan, B. A. Korgel, Y. Xia, *J. Am. Chem. Soc.* **2008**, *130*, 8900–8901.
- [16] a) F. Dumestre, B. Chaudret, C. Amiens, M. Respaud, P. Fejes, P. Renaud, P. Zurcher, *Angew. Chem.* **2003**, *115*, 5371–5374; *Angew. Chem. Int. Ed.* **2003**, *42*, 5213–5216; b) L.-M. Lacroix, S. Lachaize, A. Falqui, M. Respaud, B. Chaudret, *J. Am. Chem. Soc.* **2009**, *131*, 549–557; c) C. Desvaux, C. Amiens, P. Fejes, P. Renaud, M. Respaud, P. Lecante, E. Snoeck, B. Chaudret, *Nat. Mater.* **2005**, *4*, 750–753.
- [17] E. Ramirez, L. Eradès, K. Philippot, P. Lecante, B. Chaudret, *Adv. Funct. Mater.* **2007**, *17*, 2219–2228.
- [18] a) T. Pery, K. Pelzer, G. Buntkowsky, K. Philippot, H.-H. Limbach, B. Chaudret, *ChemPhysChem* **2005**, *6*, 605–607; b) J. García-Antón, M. R. Axet, S. Jansat, K. Philippot, B. Chaudret, T. Pery, G. Buntkowsky, H.-H. Limbach, *Angew. Chem.* **2008**, *120*, 2104–2108; *Angew. Chem. Int. Ed.* **2008**, *47*, 2074–2078.
- [19] C. L. Johnson, E. Snoeck, M. Ezcurdia, B. Rodriguez-Gonzalez, I. Pastoriza-Santos, L. M. Liz-Marzan, M. J. Hÿtch, *Nat. Mater.* **2008**, *7*, 120–124.
- [20] a) L. Piccolo, A. Valcarel, M. Bausach, C. Thomazeau, D. Uzio, G. Berhault, *Phys. Chem. Chem. Phys.* **2008**, *10*, 5504–5506; b) D. Uzio, G. Berhault, *Catal. Rev. Sci. Eng.* **2010**, *52*, 106–131.
- [21] J. Park, J. Joo, S. G. Kwon, Y. Jang, T. Hyeon, *Angew. Chem.* **2007**, *119*, 4714–4745; *Angew. Chem. Int. Ed.* **2007**, *46*, 4630–4660.



# Growth and Self-Assembly of Ultrathin Au Nanowires into Expanded Hexagonal Superlattice Studied by in Situ SAXS

Anaïs Loubat,<sup>†,‡,§</sup> Marianne Impéror-Clerc,<sup>||</sup> Brigitte Pansu,<sup>||</sup> Florian Meneau,<sup>⊥</sup> Bertrand Raquet,<sup>§</sup> Guillaume Viau,<sup>†,‡</sup> and Lise-Marie Lacroix<sup>\*,†,‡</sup>

<sup>†</sup>INSA, UPS, LPCNO (Laboratoire de Physique et Chimie des Nano-Objets), Université de Toulouse, F-31077 Toulouse, France

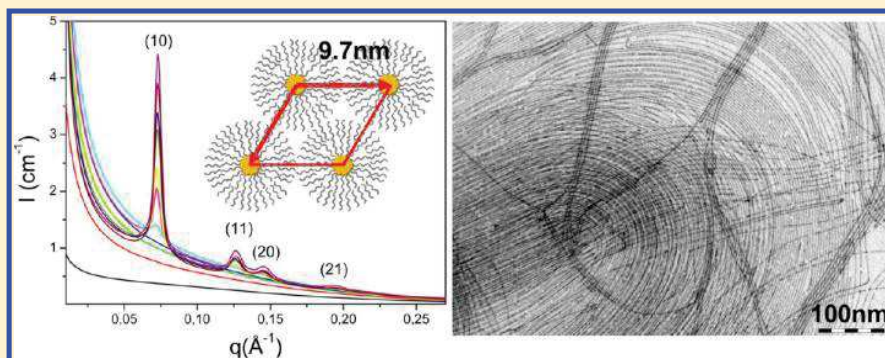
<sup>‡</sup>UMR 5215; LPCNO CNRS, F-31077 Toulouse, France

<sup>§</sup>Laboratoire National des Champs Magnétiques Intenses, CNRS-INSA-UJF-UPS, UPR 3228, 143 Avenue de Rangueil, F-31400 Toulouse, France

<sup>||</sup>Laboratoire de Physique de Solides, UMR 8502, Bat. 510, Université Paris-Sud, F-91405 Orsay, France

<sup>⊥</sup>SWING, Synchrotron Soleil, BP 48, F-91192 Gif-sur-Yvette, France

## Supporting Information



**ABSTRACT:** We report the self-assembly of gold nanowires into hexagonal superlattices in liquid phase followed by in situ small-angle X-ray scattering and give new insights into their growth mechanism. The unprecedented large interwire distance of 8 nm strongly suggests the stabilization of the ultrathin gold nanowires by a ligand's double layer composed of oleylamine and oleylammonium chloride. The one-dimensional growth is discussed, opening perspectives toward the control growth and self-assemblies of metallic nanowires.

## 1. INTRODUCTION

In the past 20 years, improvement in liquid-phase synthesis opened the way toward controlled nanoparticles with adjustable size and very narrow size dispersion ( $\sigma < 10\%$ ).<sup>1</sup> Though leading to a fine-tuning of the physical properties, the shape control of the nanoparticles is still under investigation. Anisotropic metallic nanoparticles, which exhibit modified plasmonic resonance or stable magnetization compared to their spherical counterparts,<sup>2,3</sup> arisen from nonisotropic growth processes.<sup>4</sup> Au nanorods, prepared in aqueous media, were one of the most studied systems due to the inertness of the materials and the multiple potential applications ranging from catalysis to biomedical applications.<sup>5</sup> However, several hypotheses are often invoked for such anisotropic growth: the nature of the seeds,<sup>6</sup> the preferential adsorption of surfactant on peculiar crystallographic faces,<sup>7,8</sup> or the existence of templates such as anisotropic micelles in which the growth occurred.<sup>9</sup>

Recently, ultrathin gold nanowires which exhibit a mean diameter in the range 1.5–2 nm and a micrometer length attracted lots of interest due to their size homogeneity and their

potential application as SERS probes,<sup>10</sup> lightweight foldable optoelectronics membranes,<sup>11,12</sup> or elastic coiled springs.<sup>13</sup> Their unique 1D feature confers them remarkable conductivity properties, such as quantum phenomena at room temperature, opening innovative routes in nanoelectronic.<sup>14–16</sup> Several strategies have been followed to synthesize these ultrathin nanowires. A gold salt ( $\text{HAuCl}_4$  or  $\text{AuCl}$ ) is reduced in pure oleylamine (OY)<sup>17–19</sup> or in a solution containing OY and an additional reducing agent.<sup>10,20,21</sup> Self-assembly of these ultrathin nanowires into very nice parallel arrays was observed on the TEM carbon grids,<sup>10,17</sup> or at the water interface,<sup>12</sup> opening perspectives for artificially designed metamaterials.<sup>22</sup>

Though exiting, the reported synthesis did not univocally address the question of the growth mechanism, which is of prime interest to tune the size of the wires and thus their physical properties. If the presence of OY was reported

**Received:** February 10, 2014

**Revised:** March 21, 2014

**Published:** March 25, 2014

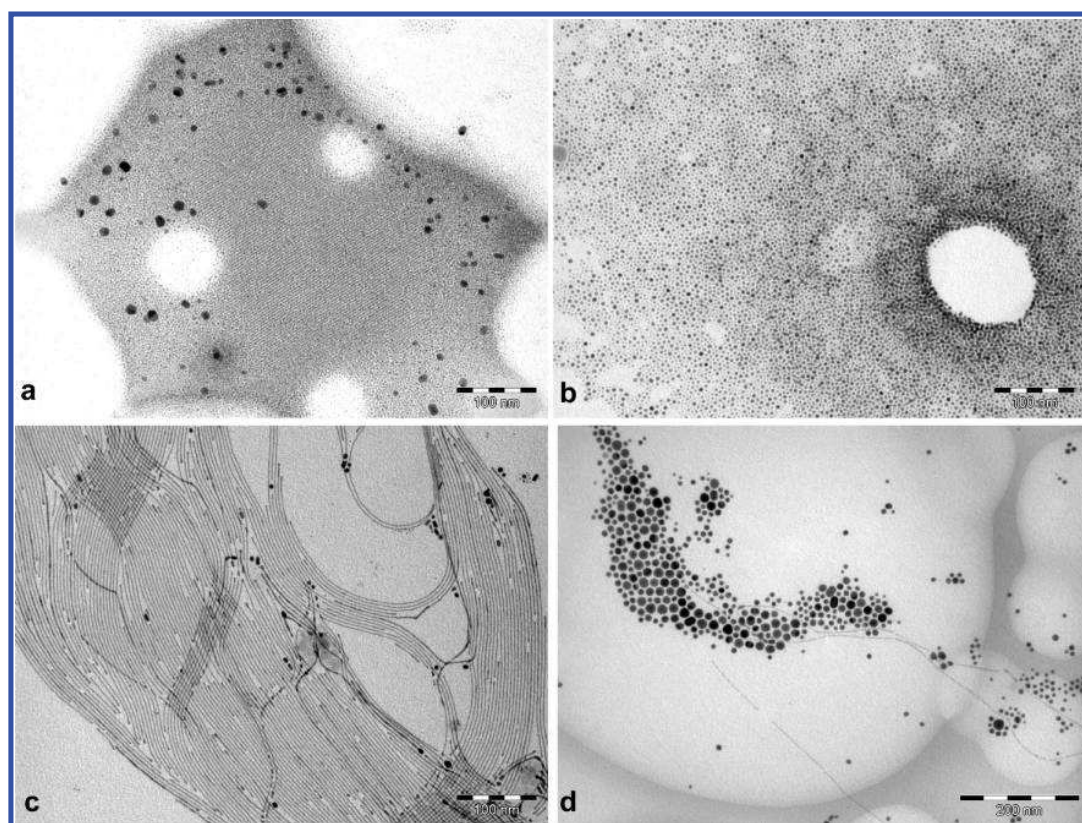


**Figure 1.** TEM image of Au NPs obtained after 24 h at 40 °C for TIPS/Au = 100 and [OY] = (a) 20, (b) 50, (c) 100, and (d) 2000 mM.

consensually as crucial for the 1D growth, Hadler et al. proposed an oriented attachment and ripening process of small seeds,<sup>21</sup> while Pazos-Pérez et al. invoked a micellar growth.<sup>19</sup> Moreover, the driving force of the self-assembly, which could be tuned to control the final metamaterial obtained, was not clearly evidenced. The potential preassembly in solution, prior to solvent evaporation which is known as a strong driving force toward crystallization,<sup>23,24</sup> requires in situ characterizations based on dynamic light scattering with conventional DLS<sup>25,26</sup> or small-angle X-ray scattering (SAXS).

Real-time SAXS enables to address both the study of the growth mechanism of nanoparticles in liquid phase,<sup>27</sup> thanks to their specific scattering profile, and the in situ crystallization,<sup>28</sup> through additional Bragg peaks, similarly to conventional X-ray diffraction (XRD). On the basis of SAXS, we report here for the first time the formation of hexagonal superlattices of ultrathin gold nanowires in the liquid phase. The present in situ study gives new information about the driving force that originates the self-assembly in solution. The unprecedented interwire distance of 8 nm suggests a bilayer stabilization of Au nanowires leading to new perspective on their growth mechanism.

## 2. EXPERIMENTAL SECTION

**2.1. Au NWs Synthesis.** The ultrathin gold nanowires (NWs) were prepared following a synthesis adapted from Xing and co-workers.<sup>10</sup> Typically, a 10 mM solution of gold was prepared: 40 mg of HAuCl<sub>4</sub>·3H<sub>2</sub>O was dissolved in a solution containing 1.32 mL of oleylamine (OY, 400 mM, OY/Au = 40) in 6.60 mL of hexane. 2.05 mL of triisopropylsilane (TIPS, 1 M, TIPS/Au = 100) was added to initiate the gold reduction. Though the exact mechanism is still unclear, TIPS acts as a strong reducing agent, fastening the reaction

from several days to few hours. The solution was then kept undisturbed at 40 °C for few hours. Magnetic stirring did not drastically change the morphology of the final nanowires as shown in Figure S1.

The effect of OY concentration on the growth of Au NWs was studied following the same procedure. OY was varied from 20 to 2000 mM, corresponding to 66 μL and 6.60 mL respectively. The volume of hexane was adjusted from 7.85 to 0 mL in order to keep a gold concentration of 10 mM.

**2.2. Characterization.** A kinetic study of the growth mechanism of ultrathin gold nanowires coupling ex situ (TEM) and in situ (SAXS) was performed. The 10 mL solution was splitted into a 15 mL glass vial and a sealed glass capillary tube for the SAXS analysis. Both conditioners were placed at 40 °C for 30 h. Aliquots were taken regularly with time to perform an ex situ TEM study of the evolution of the nanoparticles. To limit artifacts, aliquots were directly deposited, without any dilution or purification, on copper grids. TEM images were obtained with a JEOL-1011F microscope, operating at 100 kV.

In situ SAXS measurements were performed on the same solution at 40 °C every 5 min for the first 3 h and every 30 min from 3 to 30 h. The experiments were performed at the SWING beamline at the SOLEIL synchrotron using a monochromatic X-ray beam (10 keV). The reaction solution was introduced inside a glass capillary (1.5 mm in diameter), and the SAXS intensity was recorded on a CCD bidimensional detector placed inside a vacuum tube. The accessible  $q$ -range was between  $6 \times 10^{-3}$  and  $0.6 \text{ \AA}^{-1}$ . For background subtraction, the capillary was measured first filled with the pure solvent (hexane) before introducing the reaction solution (inside the same capillary) to perform the in situ experiment. The SAXS intensities were experimentally normalized in absolute units ( $\text{cm}^{-1}$ ) using water as a standard. This allowed quantifying the volume fractions in solution of the spheres and the nanowires from the modeling results (Supporting Information for details), assuming a known value for the scattering contrast between gold and the solvent of  $4420 \pm 20 \text{ e/nm}^3$ .

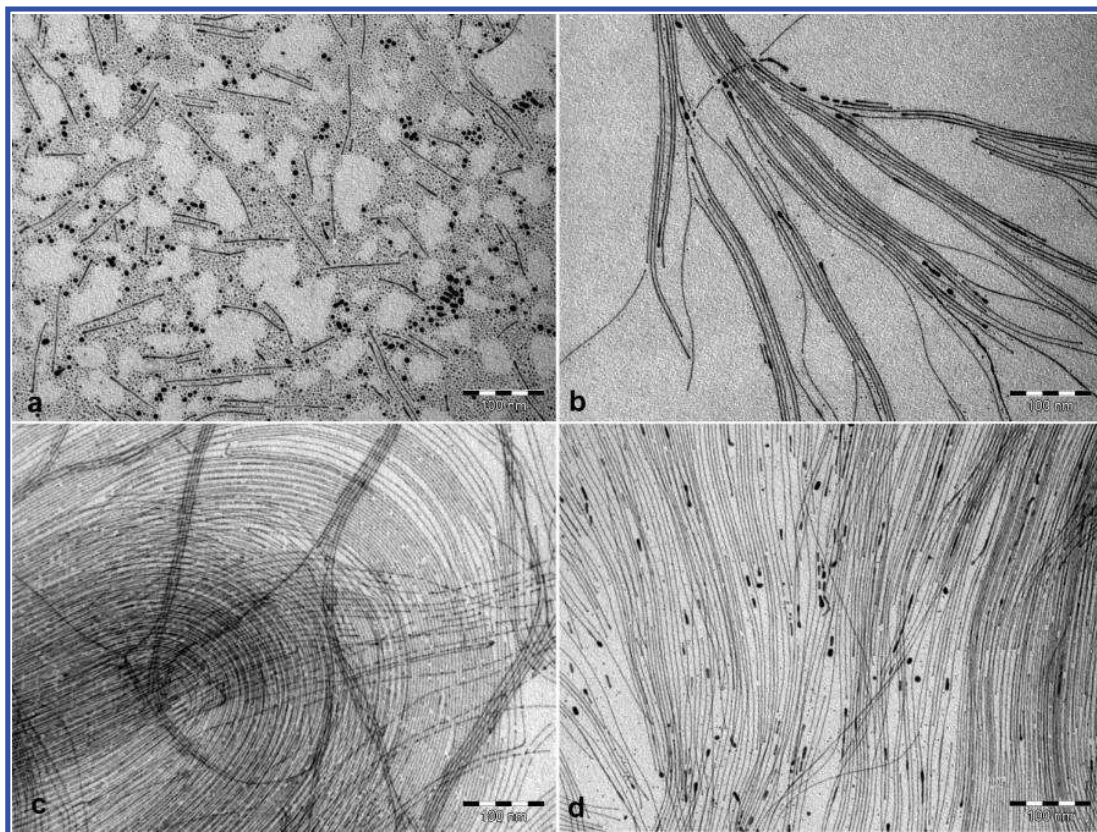


**Figure 2.** TEM images of Au nanoparticles obtained after (a) 15 min, (b) 45 min, (c) 3 h, and (d) 27 h of reaction at 40 °C with  $[\text{Au}] = 10 \text{ mM}$  and  $[\text{OY}] = 400 \text{ mM}$ .

The final Au NWs were characterized by X-ray photoelectron spectroscopy (XPS) and solid state nuclear magnetic resonance (NMR) after a purification process. Briefly, 20 mL of absolute ethanol was added (Technical grade, VWR). Centrifugation at 4000 rpm for 5 min was performed. Au NWs were then redispersed in 5 mL of hexane, and the precipitation was repeated twice. X-ray photoelectron spectra were recorded using a Kratos Analytical Limited Axis ultra limited system fitted with a microfocused monochromatic Al  $K\alpha$  X-ray source (1486.6 eV, 12 kV, 120 W). The pass energy was set at 160 and 20 eV for the survey and the regions spectra, respectively. The solid state NMR experiment of  $^1\text{H}$  at magic angle spinning (MAS) was recorded on a Bruker Advance 400 spectrometer. The sample was packed into a 2.5 mm zirconia rotor and was spun at 24 kHz at room temperature.

### 3. RESULTS AND DISCUSSION

**3.1. Synthesis and Characterization of Au NWs.** We first tried to optimize the experimental condition for the synthesis of ultrathin Au NWs adapted from Xing et al.<sup>10</sup> We evidenced the strong influence of the OY concentration over the shape and size of the gold NPs. Solutions with  $[\text{Au}] = 10 \text{ mM}$ ,  $\text{TIPS}/\text{Au} = 100$  and OY concentration varying from 20 to 2000 mM ( $\text{OY}/\text{Au} = 2$  to 200) were prepared following the protocol previously described and placed at 40 °C for 24 h. Aliquots were taken after 5 h (Figure S2) and 24 h (Figure 1) directly deposited, without any dilution or purification, on copper grids for TEM characterization. For  $[\text{OY}] = 20 \text{ mM}$ , only small spheres exhibiting a diameter  $\sim 1.5 \text{ nm}$  were observed. These spheres self-organize on TEM grids, exhibiting an interparticle distance of  $\sim 2 \text{ nm}$ . For  $[\text{OY}] = 50 \text{ mM}$ , very short rods were observed after 5 h but evolved toward spheres after 24 h (Figure 1b). Long wires were obtained and remained

stable for oleylamine concentration in the range 100–1000 mM. At 2000 mM, the reaction was drastically slowed down, and after 12 h a white precipitate was observed. This precipitate could be identified as a lamellar phase composed of Au–Cl–oleylamine complexes, as previously described by Yang and co-workers.<sup>17</sup> After 24 h, Au nanowires were finally obtained concomitantly with  $\sim 8 \text{ nm}$  spheres. Since the increase of oleylamine concentration favors the stabilization of Au NWs but decreases the reaction kinetics, a compromise should be found. In the following experiments, the oleylamine concentration was kept constant at 400 mM, in agreement with Xing et al.<sup>10</sup>

We then follow the evolution of ultrathin gold nanowires with time for  $[\text{OY}] = 400 \text{ mM}$ . After 15 min, the TEM images showed two populations of spheres with mean diameter of 1.5 and 5 nm, respectively. Short wires exhibiting a mean diameter of  $\sim 1.5 \text{ nm}$  and a length of  $\sim 100 \text{ nm}$  were also observed in a smaller proportion (Figure 2a). After 45 min, the proportion of nanowires increased and their diameter remained constant at  $\sim 1.5 \text{ nm}$  while their length increased to  $\sim 500 \text{ nm}$  (Figure 2b). No sign of size evolution could be detected for the spheres. After 3 h of reaction, parallel assemblies of micrometric-long ( $l \geq 2 \mu\text{m}$ ) nanowires were mostly observed (Figure 2c). After 27 h of reaction (Figure 2d and Figure S3), micrometric wires were still observed in coexistence with a reduced amount of the two populations of spheres (1.5 and 5 nm).

Final gold nanowires, precipitated from the hexane solution by addition of absolute ethanol, were characterized by XPS and solid state NMR. The main peaks observed in the XPS survey scan were Au 4f, C 1s, N 1s, and Cl 2p peaks centered at ca. 84,

285, 400, and 198 eV, respectively (Figure S4). The Au  $4f_{7/2}$  and  $4f_{5/2}$  high-resolution spectra were fitted with only one component corresponding to Au(0) peaks (Figure S5a). The N 1s high-resolution spectrum revealed two peaks centered at 399 and 401 eV (Figure S5b), corresponding to the binding energy of N 1s of nitrogen atom in the oleylamine (OY) and in the oleylammonium cation (referred to as OY<sup>+</sup>), respectively.<sup>29</sup> The molar ratio N(OY<sup>+</sup>)/Cl, determined from the integrated peak areas, was found very close to 1 as expected for an ammonium chloride. The molar ratio N(OY)/N(OY<sup>+</sup>) was also close to 1, indicating that the stabilization of purified Au nanowires was ensured fairly equally by long chain amine and ammonium. The important presence of ammonium at the surface of Au NWs was confirmed by <sup>1</sup>H MAS NMR spectra of pure Au NWs (Figure S6). A signal at 7.7 ppm typical of NH<sub>3</sub><sup>+</sup> group of OY<sup>+</sup> could be observed. Thus, the ammonium chloride, resulting from the protonation of oleylamine by the gold precursor HAuCl<sub>4</sub>, is strongly attached to the gold NWs.

**3.3. SAXS Growth Study.** We performed a kinetic study of the Au NWs growth obtained at 40 °C from a 10 mM gold solution with [OY] = 400 mM thanks to in situ SAXS. The variation of the SAXS intensity during the first 150 min is reported in Figure 2a. The successive scattering curves were analyzed using the form factors of a mixture of polydisperse spheres and nanowires, in agreement with the simultaneous ex-situ TEM study (Figure 2). The SAXS profiles were nicely fitted (inset Figure 3a) with the following adjustable parameters: diameter, polydispersity, and volume fraction of gold spheres, diameter, polydispersity on the diameter and volume fraction of gold nanowires, and a small constant background contribution (details in Supporting Information).

At  $t = 0$ , the scattering profile fitting indicates only the presence of spheres, with a diameter of 1.7 nm and a large polydispersity (>30%). The larger spheres (5–10 nm) that appeared on the TEM grid (Figure 2a) were not detected with SAXS, revealing that their volume fraction in solution is very low compared to the ones of the small spheres. During the reaction, an additional scattering profile is observed; its intensity increased up to 80 min, following a  $q^{-1}$  law in the low- $q$  region (Figure 3a), indicating the presence of more and more nanowires in solution. The diameter of the wires was found constant at 1.7 nm with a polydispersity on the diameter distribution of only 2%, in good agreement with the TEM observations. The length of the gold nanowires was always too large to be estimated from the SAXS signals during the kinetics and was fixed to an effective value of 100 nm for all fits, corresponding to the size resolution of the SAXS experimental setup.

The variation of the volume fraction of the 1.7 nm spheres and of the nanowires with time is plotted in Figure 3b. While only few variation of the sphere volume fraction was observed with time, the nanowires were actually detected by SAXS after 20 min, in good agreement with the TEM observations. At 30 min, the sphere volume fraction reached a maximum, and concomitantly, the rate of growth of the nanowires was the highest. Between 80 and 150 min the SAXS intensity hardly varied and was still fitted by a mixture of small spheres and ultrathin nanowires with nearly constant volume fractions. At 150 min these fractions were  $5.3 \times 10^{-5}$  and  $1.8 \times 10^{-5}$  for the wires and the spheres, respectively. The total volume fraction of  $7.1 \times 10^{-5}$  derived from SAXS at 150 min is in good agreement with the  $10^{-4}$  value expected from a 10 mmol L<sup>-1</sup> solution, taking into account the overall precision of the calibration

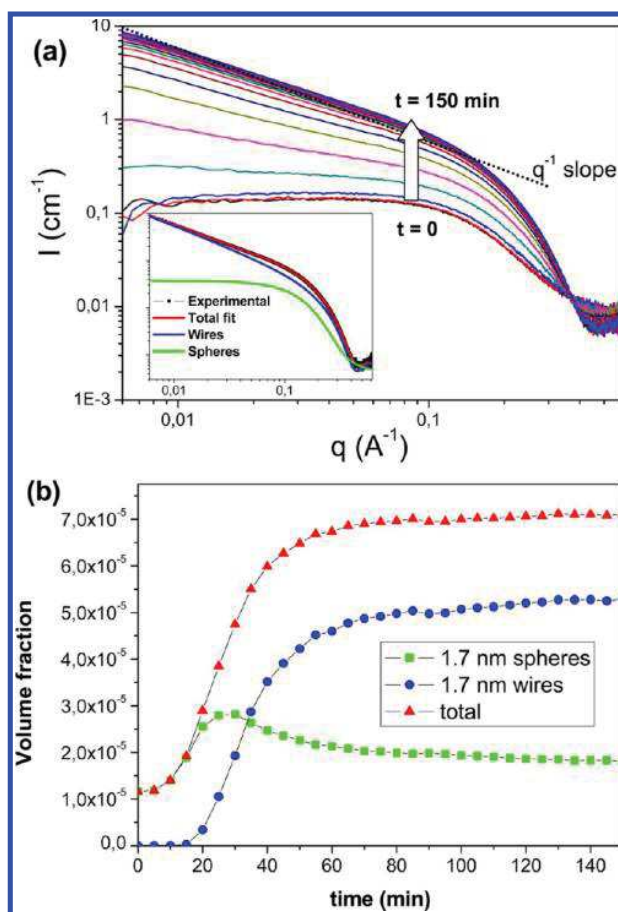


**Figure 3.** (a) Small-angle X-ray scattering results measured at 40 °C every 5 min. Inset: comparison with the experimental data at 150 min and the fitting curve as a sum of nanowires and spheres contributions. The  $q^{-1}$  slope in the dashed line is a guide to the eyes. (b) Volume fraction calculated from the SAXS modeling at different times.

procedure of the SAXS intensity. Thus, we can conclude that after only 80 min of reaction (i) essentially all Au atoms were contained either in the small spheres or in the nanowires and (ii) the proportion of the wires was large, corresponding to 73% of the initial Au introduced.

A similar kinetic study, coupling TEM (Figure S7) and SAXS (Figure S8), was performed at 25 °C. A growth following the same trend as at 40 °C was observed. Spheres were already present at  $t = 0$ , and their volume fraction remained fairly constant with time. The wires growth was slow down compared to the reaction at 40 °C. After 5 h, the reaction was just completed as evidenced by the evolution of their respective volume fraction (Figure S9). Thus, as expected, reaction temperature has a drastic effect on the kinetic of the nanowires growth.

#### 3.4. Self-Assembly of Au NWs in Liquid Phase.

Whereas no significant difference was detected on the TEM images between 3 and 28 h (Figure 2c,d), the SAXS profiles revealed four well-resolved Bragg peaks, showing the presence of a long-range positional order between the nanowires after a few hours (Figure 4). The peak positions in the reciprocal space relative to the position of the first peak were  $1:\sqrt{3}:\sqrt{4}:\sqrt{7}$ , characterizing a bidimensional hexagonal positional order in the plane normal to the wires. The lattice

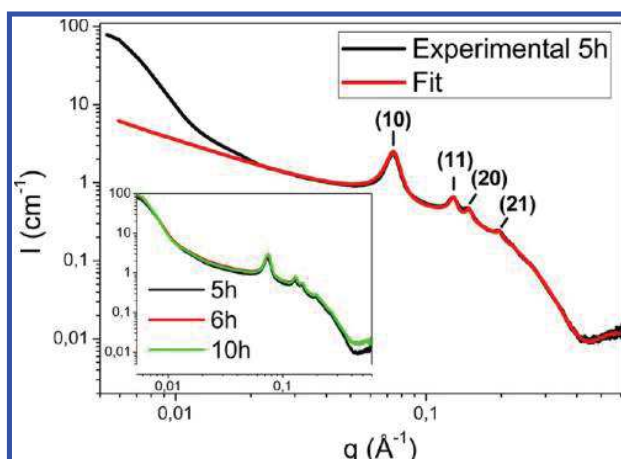


**Figure 4.** SAXS data of the hexagonal phase of nanowires at 5 h; the fitting curve is a sum of the signal of the hexagonal phase (Bragg peaks) and of free nanowires remaining in solution. Inset: SAXS profile at different times.

parameter of this hexagonal phase inferred from the peak positions was  $a = 9.7 \pm 0.1$  nm. The estimated domain size for the hexagonal phase derived from the width of the Bragg peaks was of 64 nm after 5 h and 73 nm after 10 h. Along with the increase in the intensity at small angles (characterized by a small oscillation near  $q = 0.015 \text{ \AA}^{-1}$ ), this indicated that the hexagonal phase could grow in a morphology of elongated fibers, with a typical diameter of 70 nm. The isotropic SAXS signal on the 2D detector shows that these NW hexagonal organizations are randomly oriented in the capillary, evidencing an homogeneous nucleation of the self-assembly in liquid phase and not at the surface of the capillary glass tube. The experimental SAXS spectra could be completely fitted (for  $q$  values greater than  $0.02 \text{ \AA}^{-1}$ ) by a model curve including the hexagonal phase of nanowires (Bragg peaks) in coexistence with free nanowires in solution (details in Supporting Information). Interestingly, the form factor of the nanowires was equal for both contributions, with a diameter of  $d = 1.7 \pm 0.05$  nm, constant with time, indicating that the same type of nanowires was present in solution and inside the hexagonal phase. Quantitatively, the volume fraction of the free nanowires is found equal to  $3.0 \times 10^{-5}$  after 10 h, corresponding to a proportion of 60% of nanowires, the other 40% being embedded within the hexagonal phase. Since the diameter  $d$  of the nanowires in the hexagonal phase was characterized, the interwire distance in the plane normal to the wires could be calculated as  $a - d = 8$  nm (Figure 5). The oleylamine chain length being 2.1 nm,<sup>30</sup> the interwire distance is then approximately 4 times the oleylamine length. The hexagonal phase could thus be described as a parallel assembly of 1.7 nm gold NWs coated with an oleylamine/oleylammonium bilayer (Figure 5). The hypothesis of an hexagonal phase composed of Au NWs coated with a monolayer of ligands, and the vacancies filled with solvent, was at the present time discarded due to the large interwire distance inferred from TEM (from 5.2 to 6.1 nm, Figure S10); of course, this assumption would only be validated by further characterizations, such as small-angle neutron scattering (SANS).<sup>31</sup> After solvent evaporation, Au NWs coated by a monolayer would indeed lead to interwire distance in the range 2–4 nm due to the partial interdigitation of alkyl chain upon solvent evaporation.<sup>32</sup>

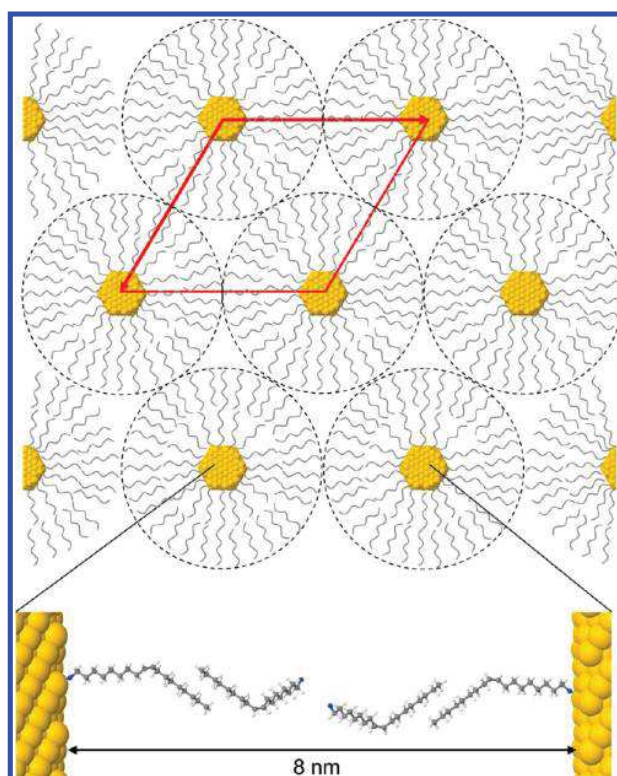


**Figure 5.** Scheme of the hexagonal phase unit cell (arrows); we considered a 1.7 nm AuNW with an hexagonal cross section, as suggested by Roy et al.<sup>49</sup> The double layer around each nanowire is represented with a dashed circle, and a possible arrangement of the four OY and/or OY<sup>+</sup> molecules is shown in the enlarged view. For simplification, only one type of isomer, corresponding to the fully extended molecules, is shown.

The same kinetic study was performed by SAXS at 25 °C (Figure S8). The hexagonal phase appeared after 6 h with a very similar lattice parameter,  $9.9 \pm 0.1$  nm, taken into account the modification of the alkyl chain configuration with temperature.

Hexagonal phases of elongated objects in solution like DNA,<sup>33</sup> carbon nanotubes<sup>34</sup> or viruses,<sup>35</sup> and self-assemblies of inorganic rods and wires were already characterized by SAXS<sup>36</sup> or on by TEM,<sup>20</sup> but to our knowledge, this is the first report of a well-organized hexagonal phase in solution of metallic nanowires. Interestingly, our in situ study reveals that the nucleation of the hexagonal phase required an incubation time of nearly 3 h after the formation of the NWs. In contrast, only a few seconds was needed for the self-assembly into superlattices of 11.6 nm spherical Au nanoparticles at a similar volume fraction.<sup>27</sup> Such discrepancy can be explained by diffusion and orientation requirements prior to the nanowire organization and thus a slower dynamics of the nucleation/growth in solution. The formation of nanoparticle superlattices results from the delicate balance of attractive and repulsive forces.<sup>37,38</sup> In most cases, the driving force toward self-assembly is a strong van der Waals attraction between the particles, which increases with nanoparticle polarizability and diameter. In such superlattices, interdigitated ligands leading to short interparticle distances are generally found.<sup>39,40</sup> In the case of water suspensions of charged anisotropic nanoparticles with strong electrostatic repulsion, entropic effects are inducing parallel

organizations with crystal liquid behavior (Onsager theory).<sup>41</sup> Depletion attraction through excess of surfactants can also be at the origin of nanoparticles organizations.<sup>37</sup>

In the present case, the small diameter and the very large interwire distance ensured by the ligand bilayer around each nanowire raise the question of the driving force of such self-assembly. Considering that the wire radius ( $R = 0.85$  nm) is much smaller than the interaxial distance ( $a = 9.7$  nm) and negligible compared to the wire length ( $L = 1000$  nm), the van der Waals energy between two parallel Au nanowires can be estimated according to eq 1 (approximate expression valid for  $R \ll a \ll L$ ).<sup>42,43</sup>

$$E_{\text{vdw}} = -\frac{3A}{8\pi} \frac{(\pi R)^4}{a^5} L \quad (1)$$

Because of comparable Hamaker constants of hexane and oleylamine,<sup>44,45</sup> the classical value of  $75 kT$  usually considered for the Hamaker constant of gold nanoparticles in hexane<sup>46,47</sup> is certainly a good approximation in our system, leading to  $E_{\text{vdw}} = -5.3 k_B T$ . This value has the same order of magnitude as in the case of spherical gold particle superlattices already reported.<sup>38</sup> The steric repulsion appears with ligands interdigitation and thus for interwire distances lower than the full extend of two oleylamine bilayers, i.e. below  $4 \times 2.1$  nm = 8.4 nm. This steric repulsion ensured by the bilayer at the surface of Au NWs could be responsible for the stabilization of the hexagonal superlattices with an interwire distance as large as 8 nm.

**3.5. Nanowire Growth Mechanism.** Regarding the growth mechanism, we observed that the wire growth, at 40 or 25 °C, did not induce a diminution of the number of spheres, as revealed by the time evolution of the volume fraction of each type of particle (Figure 3b and Figure S9). Such observation is in contradiction with a growth mechanism based on oriented attachment of small spheres, where the wire growth would consume the initial 1.7 nm spheres. These small spheres appear mainly as side product, but the slight decrease of their volume fraction after 30 min at 40 °C, concomitant with the highest nanowire growth rate, may stress their role as seeds.<sup>48</sup> The unprecedented large interwire distance in the hexagonal superlattice suggests a bilayer stabilization of the Au nanowires. One can infer that this bilayer stabilization may be also present at the surface of the free NWs and not only inside the hexagonal superlattice. The XPS and NMR analysis showed that the stabilization of purified Au nanowires is ensured fairly equally by oleylamine and oleylammonium chloride. Such charged stabilization reminds the CTAB bilayer, recently characterized by SANS,<sup>31</sup> at the surface of Au nanorods in water. We have also observed that the shape of the Au nanoparticles was strongly dependent on the oleylamine concentration initially introduced. This concentration effect reminds the phase diagram of surfactants like CTAB in aqueous media<sup>44</sup> and the critical micellar concentration associated with the transition from spherical to cylindrical micelles. All these observations suggest that a micellar growth mechanism drives the one-dimensional growth.

## 4. CONCLUSION

Owing to an in situ SAXS study, we were able to describe precisely for the first time the self-assembly of ultrathin Au NWs into a hexagonal superlattice in apolar solvent. This superlattice exhibits a very large lattice parameter correspond-

ing to an interwire distance of 8 nm. Such a large value can be explained by the presence of a bilayer at the surface of each nanowire, composed of oleylamine and oleylammonium, as revealed by NMR and XPS. Along with the strong influence of the oleylamine concentration on the final shape of the Au nanoparticles, all these results suggest a micellar growth mechanism for the NWs. To have a deeper understanding of the supramolecular organization of OY and OY<sup>+</sup>/Cl<sup>-</sup>, both at the surface of the nanowires and in the second layer, and their impact on the growth of Au nanoparticles, coupled SANS and SAXS studies will be performed, while NMR, periodic-DFT, and Monte Carlo theoretical studies should give new insight into the chemical organization of these micelles. The unprecedented hexagonal self-assembly of micrometer long Au nanowires opens new perspectives for dedicated applications such as catalysis or electronic nanocontact.

## ■ ASSOCIATED CONTENT

### Supporting Information

Model for the SAXS intensity, XPS survey and high-resolution scans and <sup>1</sup>H MAS NMR spectrum of purified Au NWs; TEM and SAXS characterization of the kinetic study at 25 °C and the corresponding volume fraction evolution with time. TEM images of Au NWs obtained under magnetic stirring. This material is available free of charge via the Internet at <http://pubs.acs.org>.

## ■ AUTHOR INFORMATION

### Corresponding Author

\*E-mail [lmalcroi@insa-toulouse.fr](mailto:lmalcroi@insa-toulouse.fr); ph +33561559652; fax +33561559697 (L.-M.L.).

### Notes

The authors declare no competing financial interest.

## ■ ACKNOWLEDGMENTS

Patrick Davidson (LPS, Orsay), Bruno Chaudret, and Romuald Poteau (LPCNO, Toulouse) are warmly thanked for fruitful discussions. We thank Y. Coppel (LCC, Toulouse) for RMN measurements and G. Antorrena (INA, Saragossa) for XPS measurements. A. Robert is thanks for his help in the experimental section. Jan Skov Pedersen (University of Aarhus, Denmark) is especially thanked for his advice concerning the SAXS modeling. The authors acknowledge the financial support of the Midi-Pyrénées region, of the university of Toulouse, PRES, of the Labex NEXT, No. 11 LABX 075, of the French GDR Or-Nano and of the French network METSA.

## ■ REFERENCES

- (1) Kwon, S. G.; Hyeon, T. Colloidal chemical synthesis and formation kinetics of uniformly sized nanocrystals of metals, oxides, and chalcogenides. *Acc. Chem. Res.* **2008**, *41*, 1696–1709.
- (2) Pérez-Juste, J.; Pastoriza-Santosa, I.; Liz-Marzán, L. M.; Mulvaney, P. Gold nanorods: Synthesis, characterization and applications. *Coord. Chem. Rev.* **2005**, *249*, 1870–1901.
- (3) Lu, A.-H.; Salabas, E. L.; Schüth, F. Magnetic nanoparticles: synthesis, protection, functionalization, and application. *Angew. Chem., Int. Ed.* **2007**, *46*, 1222–1244.
- (4) Sau, T. K.; Rogach, A. L. Nonspherical noble metal nanoparticles: colloid-chemical synthesis and morphology control. *Adv. Mater.* **2010**, *22*, 1781–1804.
- (5) Grzelczak, M.; Perez-Juste, J.; Mulvaney, P. A.; Liz-Marzán, L. M. Shape control in gold nanoparticle synthesis. *Chem. Soc. Rev.* **2008**, *37*, 1783–1791.

- (6) Lofton, C.; Sigmund, W. Mechanisms controlling crystal habits of gold and silver colloids. *Adv. Funct. Mater.* **2005**, *15*, 1197–1208.
- (7) Murphy, C. J.; Thompson, L. B.; Alkilany, A. M.; Sisco, P. N.; Boulos, S. P.; Sivapalan, S. T.; Yang, J. A.; Chernak, D. J.; Huang, J. The many faces of gold nanorods. *J. Phys. Chem. Lett.* **2010**, *1*, 2867–2875.
- (8) Katz-Boon, H.; Rossouw, C. J.; Weyland, M.; Funston, A. M.; Mulvaney, P.; Etheridge, J. Three-dimensional morphology and crystallography of gold nanorods. *Nano Lett.* **2011**, *11*, 273–278.
- (9) Gao, J.; Bender, C. M.; Murphy, C. J. Dependence of the gold nanorod aspect ratio on the nature of the directing surfactant in aqueous solution. *Langmuir* **2003**, *19*, 9065–9070.
- (10) Feng, H.; Yang, Y.; You, Y.; Li, G.; Guo, J.; Yu, T.; Shen, Z.; Wu, T.; Xing, B. Simple and rapid synthesis of ultrathin gold nanowires, their self assembly and application in surface-enhanced Raman scattering. *Chem. Commun.* **2009**, 1984.
- (11) Chen, Y.; Ouyang, Z.; Gu, M.; Cheng, W. Mechanically strong, optically transparent, giant metal superlattice nanomembranes from ultrathin gold nanowires. *Adv. Mater.* **2013**, *25*, 80–85.
- (12) Sanchez-Iglesias, A.; Rivas-Murias, B.; Grzelczak, M.; Perez-Juste, J.; Liz-Marzan, L. M.; Rivadulla, F.; Correa-Duarte, M. A. Highly transparent and conductive films of densely aligned ultrathin Au nanowire monolayers. *Nano Lett.* **2012**, *12*, 6066–6070.
- (13) Xu, J.; Wang, H.; Liu, C.; Yang, Y.; Chen, T.; Wang, Y.; Wang, F.; Liu, X.; Xing, B.; Chen, H. Mechanical nanosprings: induced coiling and uncoiling of ultrathin Au nanowires. *J. Am. Chem. Soc.* **2010**, *132*, 11920–11922.
- (14) Pud, S.; Kisner, A.; Heggen, M.; Belaine, D.; Temirov, R.; Simon, U.; Offenhäuser, Mourzina, Y.; Vitusevich. Features of transport in ultrathin gold nanowire structures. *Small* **2013**, *9*, 846–852.
- (15) Loubat, A.; Escoffier, W.; Lacroix, L.-M.; Viau, G.; Tan, R.; Carrey, J.; Warot-Fonrose, B.; Raquet, B. Cotunneling transport in ultra-narrow gold nanowire bundles. *Nano Res.* **2013**, *6*, 644–651.
- (16) Chandni, U.; Kundu, P.; Kundu, S.; Ravishankar, S.; Ghosh, A. Tunability of electronic states in ultrathin gold nanowires. *Adv. Mater.* **2013**, *25*, 2486–2491.
- (17) Huo, Z.; Tsung, C.-K.; Huang, W.; Zhang, X.; Yang, P. Sub-two nanometer single crystal Au nanowires. *Nano Lett.* **2008**, *8*, 2041–2044.
- (18) Lu, X.; Yavuz, M. S.; Tuan, H.-Y.; Korgel, B. A.; Xia, Y. Ultrathin gold nanowires can be obtained by reducing polymeric strands of oleylamine-AuCl complexes formed by aurophilic interaction. *J. Am. Chem. Soc.* **2008**, *130*, 8900–8901.
- (19) Pazos-Pérez, N.; Baranov, D.; Irsen, S.; Hilgendorff, M.; Liz-Marzán, L. M.; Giersig, M. Synthesis of flexible, ultrathin gold nanowires in organic media. *Langmuir* **2008**, *24*, 9855–9860.
- (20) Kang, Y.; Ye, X.; Murray, C. B. Size- and shape-selective synthesis of metal nanocrystals and nanowires using CO as a reducing agent. *Angew. Chem., Int. Ed.* **2010**, *49*, 6156–6159.
- (21) Halder, A.; Ravishankar, N. Ultrafine single-crystalline gold nanowire arrays by oriented attachment. *Adv. Mater.* **2007**, *19*, 1854–1858.
- (22) Nie, Z.; Petukhova, A.; Kumacheva, E. Properties and emerging applications of self-assembled structures made from inorganic nanoparticles. *Nat. Nanotechnol.* **2009**, *5*, 15–25.
- (23) Rabani, E.; Reichman, D. R.; Geissler, P. L.; Brus, L. E. Drying-mediated self-assembly of nanoparticles. *Nature* **2003**, *426*, 271–274.
- (24) Park, J.; Zheng, H.; Lee, W. C.; Geissler, P. L.; Rabani, E.; Alivisatos, A. P. Direct observation of nanoparticle superlattice formation by using liquid cell transmission electron microscopy. *ACS Nano* **2012**, *6*, 2078–2085.
- (25) Miszta, K.; de Graaf, J.; Bertoni, G.; Dorfs, D.; Brescia, R.; Marras, S.; Ceseracciu, L.; Cingolani, R.; van Roij, R.; Dijkstra, M.; Manna, L. Hierarchical self-assembly of suspended branched colloidal nanocrystals into superlattice structures. *Nat. Mater.* **2011**, *10*, 872–876.
- (26) Pagès, C.; Coppel, Y.; Kahn, M. L.; Maisonnat, A.; Chaudret, B. Self-assembly of ZnO nanocrystals in colloidal solutions. *ChemPhysChem* **2009**, *10*, 2334–2344.
- (27) Abécassis, B.; Testard, F.; Spalla, O. Gold nanoparticles superlattice crystallization probed in situ. *Phys. Rev. Lett.* **2008**, *100*, 115504.
- (28) Abécassis, B.; Testard, F.; Spalla, O.; Barboux, P. Probing in situ the nucleation and growth of gold nanoparticles by small-angle X-ray scattering. *Nano Lett.* **2007**, *7*, 1723–1727.
- (29) Kumar, A.; Mandal, S.; Selvakannan, P. R.; Pasricha, R.; Mandale, A. B.; Sastry, M. Investigation into the interaction between surface-bound alkylamines and gold nanoparticles. *Langmuir* **2003**, *19*, 6277–6282.
- (30) Mourdikoudis, S.; Liz-Marzán, L. M. Oleylamine in nanoparticle synthesis. *Chem. Mater.* **2013**, *25*, 1465–1476.
- (31) Gomez-Grana, S.; Hubert, F.; Testard, F.; Guerrero-Martinez, A.; Grillo, I.; Liz-Marzán, L. M.; Spalla, O. Surfactant (bi)layers on gold nanorods. *Langmuir* **2012**, *28*, 1453–1459.
- (32) Ge, G.; Brus, L. E. Fast surface diffusion of large disk-shaped nanocrystals aggregates. *Nano Lett.* **2001**, *1*, 219–222.
- (33) Livolant, F.; Levelut, A. M.; Doucet, J.; Benoit, J. P. The highly concentrated liquid-crystalline phase of DNA is columnar hexagonal. *Nature* **1989**, *339*, 724–726.
- (34) Thess, A.; Lee, R.; Nikolaev, P.; Dai, H.; Petit, P.; Robert, J.; Xu, C.; Lee, Y. H.; Kim, S. G.; Rinzler, A. G.; Colbert, D. T.; Scuseria, G. E.; Tománek, D.; Fischer, J. E.; Smalley, R. E. Crystalline ropes of metallic carbon nanotubes. *Science* **1996**, *273*, 483–487.
- (35) Grelet, E. Hexagonal order in crystalline and columnar phases of hard rods. *Phys. Rev. Lett.* **2008**, *100*, 168301.
- (36) Hamon, C.; Postic, M.; Mazari, E.; Bizien, T.; Dupuis, C.; Even-Hernandez, P.; Jimenez, A.; Courbin, L.; Gosse, C.; Artzner, F.; Marchi-Artzner, V. Three-dimensional self-assembly of gold nanorods with controlled macroscopic shape and local smectic B order. *ACS Nano* **2012**, *6*, 4137–4146.
- (37) Henzie, J.; Grünwald, M.; Widmer-Cooper, A.; Geissler, P. L.; Yang, P. Self-assembly of uniform polyhedral silver nanocrystals into densest packings and exotic superlattices. *Nat. Mater.* **2012**, *11*, 131–137.
- (38) Goubet, N.; Richardi, J.; Albouy, P.-A.; Pileni, M.-P. Which forces control supercrystal nucleation in organic media? *Adv. Funct. Mater.* **2011**, *21*, 2693–2704.
- (39) Jiang, Z.; Lin, X.-M.; Sprung, M.; Narayanan, S.; Wang, J. Capturing the crystalline phase of two-dimensional nanocrystal superlattices in action. *Nano Lett.* **2010**, *10*, 799–803.
- (40) Lee, B.; Podsiadlo, P.; Rupich, S.; Talapin, D. V.; Rajh, T.; Schevchenko, E. Comparison of structural behaviour of nanocrystals in randomly packed films and long-range ordered superlattices by time-resolved small angle X-ray scattering. *J. Am. Chem. Soc.* **2009**, *131*, 16386–16388.
- (41) Lekkerkerker, H. N.W.; Vroege, G. J. Liquid crystal phase transitions in suspensions of mineral colloids: new life from old roots. *Philos. Trans. R. Soc. A* **2013**, *371*, 20120263.
- (42) Parsegian, V. A. *Van der Waals Forces*; Cambridge University Press: New York, 2006.
- (43) Russel, W. B.; Saville, D. A.; Scholwalter, W. R. *Colloidal Dispersions*; Cambridge University Press: New York, 1989.
- (44) Israelachvili, J. N. *Intermolecular and Surface Forces*, 3rd ed.; Elsevier: Amsterdam, 2011.
- (45) Jia, G.; Sitt, A.; Hitin, G. B.; Hadar, I.; Bekenstein, Y.; Amit, Y.; Popov, I.; Banin, U. Couples of colloidal semiconductor nanorods formed by self-limited assembly. *Nat. Mater.* **2014**, *13*, 301–307.
- (46) Bargeman, D.; Van Voorst Vader, F. Van der Waals forces between immersed particles. *J. Electroanal. Chem.* **1972**, *37*, 45–52.
- (47) Pansu, B.; Lecchi, A.; Constantin, D.; Impéror-Clerc, M.; Veber, M.; Dozov, I. Insertion of gold nanoparticles in fluid mesophases: Size filtering and control of interactions. *J. Phys. Chem. C* **2011**, *115*, 17682–17687.
- (48) Azulai, D.; Cohen, E.; Markovich, G. Seed concentration control of metal nanowire diameter. *Nano Lett.* **2012**, *12*, 5552–5558.

(49) Roy, A.; Pandey, T.; Ravishankar, N.; Singh, A. K. Single crystalline ultrathin gold nanowires: Promising nanoscale interconnects. *AIP Adv.* **2013**, *3*, 032131.



Cite this: *Nanoscale*, 2016, **8**, 4020

## Dense arrays of cobalt nanorods as rare-earth free permanent magnets†

E. Anagnostopoulou,<sup>a</sup> B. Grindi,<sup>a</sup> L.-M. Lacroix,<sup>a</sup> F. Ott,<sup>b</sup> I. Panagiotopoulos<sup>c</sup> and G. Viau<sup>\*a</sup>

We demonstrate in this paper the feasibility to elaborate rare-earth free permanent magnets based on cobalt nanorods assemblies with energy product  $(BH)_{\max}$  exceeding  $150 \text{ kJ m}^{-3}$ . The cobalt rods were prepared by the polyol process and assembled from wet suspensions under a magnetic field. Magnetization loops of dense assemblies with remanence to a saturation of 0.99 and squareness of 0.96 were measured. The almost perfect  $M(H)$  loop squareness together with electron microscopy and small angle neutron scattering demonstrate the excellent alignment of the rods within the assemblies. The magnetic volume fraction was carefully measured by coupling magnetic and thermogravimetric analysis and found in the range from 45 to 55%, depending on the rod diameter and the alignment procedure. This allowed a quantitative assessment of the  $(BH)_{\max}$  values. The highest  $(BH)_{\max}$  of  $165 \text{ kJ m}^{-3}$  was obtained for a sample combining a high magnetic volume fraction and a very large  $M(H)$  loop squareness. This study shows that this bottom-up approach is very promising to get new hard magnetic materials that can compete in the permanent magnet panorama and fill the gap between the ferrites and the NdFeB magnets.

Received 14th October 2015,

Accepted 8th January 2016

DOI: 10.1039/c5nr07143g

www.rsc.org/nanoscale

## Introduction

Permanent magnets have become essential to daily-life products. Ranging from electronic power generation to energy conversion and transportation, the domain of the application of magnets is growing exponentially. This huge market is mostly supplied by rare earth-based magnets, which exhibit the best performances, and the ferrite based-magnets, which are by far the cheapest.<sup>1</sup> The fear of a rare-earth supply limitation has recently motivated numerous efforts on rare-earth free permanent magnets.<sup>2,3</sup> A reasonable objective is to find new hard magnetic materials that could fill the gap between the Ba(Sr) hexaferrites and the powerful NdFeB magnets. The first approach consists of playing with crystal structures in order to find new highly magneto-crystalline compounds such as manganese compounds,<sup>4</sup> iron–nickel,<sup>5</sup> and iron–cobalt borides with tetragonal structures,<sup>6</sup> or cobalt carbide  $\text{Co}_2\text{C}$ /

$\text{Co}_3\text{C}$  nanocomposites.<sup>7,8</sup> An alternative approach consists of assembling single domain nanoparticles with a high anisotropy into dense materials and to exploit nano-structuration.<sup>9,10</sup> This bottom-up approach has the advantage over the classic metallurgy processes as it is scalable down to submillimeter sizes and could address the demand for microscale permanent magnets with high added value.<sup>11</sup>

Recently, several processes were developed to synthesize hard magnetic particles with a very good size control in the nanometer range. One feature of nanoparticles is that metastable and/or new structures can appear for sub 10 nm sizes. For example, Balasubramanian *et al.* showed that intermetallic  $\text{Zr}_x\text{Co}_{100-x}$  nanoparticles prepared by cluster deposition crystallized in the high-anisotropy rhombohedral  $\text{Zr}_2\text{Co}_{11}$  structure for a broad composition range.<sup>12</sup> Moreover, the size control allows a fine control of the magnetic properties and enables these particles to be suitable for spring magnet elaboration.<sup>13,14</sup> Finally, nanoparticles with a great variety of shapes can be obtained by chemical processes, offering the possibility to get nanoparticles with anisotropic shapes. This is the case of magnetic nanorods (NRs) and nanowires (NWs) the synthesis of which has been developed both by electrochemistry and wet-chemistry.<sup>15</sup> Liquid phase syntheses of FeCo,<sup>16</sup> Ni,<sup>17</sup> and CoNi<sup>18</sup> high aspect ratio particles were developed. Nevertheless, the coercivity of these compositions was limited compared to those measured on cobalt high aspect ratio particles. The great advantage of Co NWs and NRs in the field of hard magnetic material is the possibility to add magnetocrystalline

<sup>a</sup>Université de Toulouse, Laboratoire de Physique et Chimie des Nano-Objets, UMR 5215 INSA, CNRS, UPS, 135 avenue de Rangueil F-31077 Toulouse cedex 4, France. E-mail: guillaume.viau@insa-toulouse.fr

<sup>b</sup>Laboratoire Léon Brillouin CEA/CNRS UMR12, Centre d'Etudes de Saclay, 91191 Gif sur Yvette, France

<sup>c</sup>Department of Materials Science and Engineering, University of Ioannina, Ioannina 45110, Greece

†Electronic supplementary information (ESI) available: Transmission electron microscopy images of the cobalt nanorods; thermogravimetric analysis of a dense array of cobalt nanorods; Table S1 details on the rod washing and alignment procedure. See DOI: 10.1039/c5nr07143g

and shape anisotropy. For cobalt wires with the hcp structure and the  $c$  axis parallel to the wire long axis, a theoretical coercivity  $\mu_0 H_C = \mu_0 M_S/2 + K_1/2M_S = 0.89 + 0.58 = 1.47$  T is expected, provided that the Stoner–Wohlfarth model applies.

Co NWs and NRs with high coercivity were first synthesized by the polyol process<sup>19</sup> and organometallic chemistry.<sup>20,21</sup> These last few years several experimental works were devoted to Co NWs and NRs for permanent magnet applications with main objectives a better shape control and an improvement of their magnetic properties. Co NRs with enhanced coercivity,  $\mu_0 H_C$  higher than 1 T, were obtained by Gandha *et al.* thanks to a modified polyol synthesis in solvothermal conditions.<sup>22</sup> A detailed study of the polyol synthesis mechanism clearly identified the role of the laurate ion concentration on the growth of hcp cobalt, parallel or perpendicular to the  $c$  axis.<sup>23</sup> A scale-up of high aspect ratio nanoparticle synthesis by the polyol process was developed.<sup>24</sup> Parallel alignments of cobalt nanorods prepared by organometallic chemistry and characterized by magnetization loops with remanence to a saturation ratio close to 1 were obtained by grafting liquid crystals at their surface.<sup>25</sup> High temperature stability of cobalt nanorods was improved by a thin carbon coating.<sup>26,27</sup>

Furthermore, several theoretical works were recently devoted to the magnetic properties of isolated or assembled Co NWs and NRs. The effects of the particle shape on the coercivity and on the magnetization reversal were described by micromagnetic modelling.<sup>28</sup> The role of the dipolar interactions in rod assemblies on the coercivity<sup>29</sup> and the calculation of the energy product as a function of the wire packing fraction<sup>30,31</sup> allowed an assessment of the performance of permanent magnets based on Co NR assemblies.

The last issue, which has not yet been addressed experimentally, is the elaboration of dense arrays of parallel nanorods. An easy axis alignment is of paramount importance in order to obtain a high energy product.<sup>32,33</sup> Nevertheless, high energy products require also high magnetic induction, namely, for rods assemblies, a high packing fraction.

In this paper we describe the elaboration of dense assemblies of Co NRs with different diameters and morphologies prepared by the polyol process. The rod alignment and the magnetic volume fraction were characterized by electron microscopy, neutrons scattering, thermal analysis and magnetic measurements. This is the first time that energy products of nanorods assemblies have been assessed. We show that the performance of these new magnetic materials makes them very good candidates to compete in the new rare-earth free permanent magnet panorama.

## Experimental

### Synthesis and characterization of Co NRs

Cobalt nanowires were produced by the polyol process following a procedure described previously.<sup>19</sup> Cobalt acetate was purchased from Alfa Aesar, sodium hydroxide, lauric acid and 1,2-butanediol from Acros, and hydrated ruthenium chloride from

Sigma-Aldrich (ref. Sigma Aldrich 84050). All the raw chemicals were used without additional purification.

Cobalt laurate was prepared by mixing equimolar aqueous solutions of cobalt acetate and sodium laurate. The pink precipitate was washed with de-ionized water and was dried at 50 °C in order to remove the water excess. The cobalt laurate was characterized by thermogravimetric analysis (TGA) in air from room temperature to 600 °C. The TGA showed a first mass loss of about 6% at 100 °C followed by a second mass loss of 76–77 in the temperature range from 200 to 450 °C. The total mass loss was between 82 and 83%. These mass losses are in a good agreement with a di-hydrated cobalt laurate (calculated mass losses: 7.3% for the loss of the two water molecules at 100 °C and 83.7% for the total mass loss corresponding to the transformation of the di-hydrated cobalt laurate to Co<sub>3</sub>O<sub>4</sub>).

The cobalt laurate was dispersed in a sodium hydroxide solution of 1,2-butanediol. The concentration of cobalt was  $8 \times 10^{-2}$  mol L<sup>-1</sup> in all experiments. The NaOH concentration was  $7.5 \times 10^{-2}$  mol L<sup>-1</sup>. Ruthenium chloride was added in the medium to control the nucleation step. The ratio [Ru]/[Co] = 2.5% was fixed in all experiments. The suspension of cobalt laurate in the basic solution of butanediol containing the ruthenium chloride was heated up to 175 °C for 30 min under mechanical stirring in the range of 80 to 240 rpm. The solution turned black, indicating the cobalt reduction. A classic heating mantle was used as the heating system. The temperature slope was fixed at 8 K min<sup>-1</sup>. Small and large scale experiments were performed in 100 mL and 1 L of 1,2 butanediol leading to the formation of 0.47 g and 4.7 g of cobalt respectively.

The cobalt particles were characterized by transmission electron microscopy (TEM), using a 100 kV Jeol JEM 1011. The cobalt particles were recovered by centrifugation, washed twice with absolute ethanol and once with chloroform. A drop of the colloidal solution of Co nanorods in chloroform was deposited on a carbon coated copper grid. Their mean diameter ( $d_m$ ) and mean length ( $L_m$ ) were measured from the image analysis on *ca.* 200 rods using the ImageJ software<sup>34</sup> (image magnification 250k). X-ray diffraction (XRD) patterns were recorded on a PANalytical Empyrean diffractometer using the Co K $\alpha$  radiation.

### Assembly of Co NRs into dense anisotropic nanomaterials

Co NRs were washed in chloroform or in toluene prior to their alignment and after washing they were dispersed under sonication in chloroform. Dispersions containing approximately 1 g of powder in 10 mL of solvent were allowed to dry under air at room temperature in a homogenous magnetic field of 1 T generated by an electro-magnet. The different assemblies are noted as R $_d$ A $_j$  for rods, exhibiting the mean diameter  $d$ , aligned following the procedure A $_j$ . The alignments A1 and A3 correspond to rods washed in chloroform, A2 and A4 to rods washed in toluene. For A1 and A2 (standard procedures) three successive washings were realized, for A3 an extended washing was carried out. A4 corresponds to alignment of large scale samples for which the washing was limited in comparison to the standard samples.

The rod assemblies  $R_dA_j$  were characterized by scanning electron microscopy (FEG-SEM) using a JEOL JSM 6700F. Thermogravimetric Analysis (TGA) was performed on a Mettler-Toledo balance in air and under  $H_2/Ar$  atmosphere.

The Small-Angle Neutron Scattering (SANS) experiments were carried out on the spectrometer PAXY at the Laboratoire Léon Brillouin.<sup>35</sup> The neutron wavelength was set at 5 Å. The amount of magnetic material put in the beam was on the order of 10–20 mg ( $5 \times 5 \times 0.1 \text{ mm}^3$ ).

The magnetic properties of the assemblies were characterized using a Quantum Design Physical Property Measurement System (PPMS) with the Vibrating Sample Magnetometer (VSM) configuration.

### Magnetic measurements

The saturation magnetization values were measured on sample mass larger than 10 mg.  $M(H)$  loops were measured on small needles of dimensions *ca.*  $5 \times 0.5 \times 0.1 \text{ mm}$  with the applied field parallel to the needle long axis.

### Volume fraction measurements

The assessment of the magnetic volume fraction,  $V_M$ , in the dense assemblies is necessary for the calculation of the energy product  $(BH)_{\text{max}}$ . Assuming the absence of internal porosity in the assemblies, it is arguable that they consist of three components: the Co metal cores, a cobalt oxide shell around each core, since the drying and alignment of the Co nanorods were carried out under air, and an outer ligand shell, *i.e.* the organic molecules remaining at the rod surface and occupying the inter-rod spacing. These organic molecules include the ligands and remaining solvent.

The volume fraction of the three components noted,  $V_M$ ,  $V_{\text{CoO}}$  and  $V_L$ , respectively were calculated from the mass fraction inferred from the VSM and TGA measurements.

The magnetic mass fraction was deduced from the saturation magnetization,  $M_S$ , of the samples measured by magnetometry:

$$\% w(\text{Co}_{\text{metal}}) = \frac{M_S}{M_{S \text{ cobalt}}} \quad (1)$$

with  $M_S$  expressed in  $\text{emu g}^{-1}$  and  $M_{S \text{ cobalt}} = 160 \text{ emu g}^{-1}$ .

In order to determine the mass fraction of the Co oxide and the ligands in the NR assemblies, a sample of mass  $m_0$  was heated in air at 700 °C for 2 hours, in order to remove all the organics and to fully oxidize the cobalt core, resulting in a mass gain  $\Delta m_1 > 0$ . After cooling at room temperature in the thermo-balance, the sample was then heated at 700 °C under a mixture of  $H_2/Ar$  for 2 hours in order to reduce the cobalt oxide in metal cobalt, resulting in a mass loss  $\Delta m_2 < 0$ . The final mass of the sample is  $m_3$  and consists purely of metal Co.

The mass fraction of the total Co,  $\%w(\text{Co}_{\text{total}})$ , corresponding to the cobalt involved both in the metal core and in the oxide shell, was calculated from eqn (2) (see an example in Fig. S2 of the ESI†).

$$\% w(\text{Co}_{\text{total}}) = \frac{m_3}{m_0} = 1 + \frac{\Delta m_1 + \Delta m_2}{m_0} \quad (2)$$

This allows us to deduce the mass fraction of the cobalt involved in the oxide shell:

$$\% w(\text{Co}^{\text{II}}) = \% w(\text{Co}_{\text{total}}) - \% w(\text{Co}_{\text{metal}}) \quad (3)$$

Assuming that the cobalt oxide at the surface of the cobalt rods is cobalt monoxide,  $\text{CoO}$ , as previously reported,<sup>36</sup> its mass fraction can be calculated from the mass fraction of  $\text{Co}^{\text{II}}$  according to:

$$\% w(\text{CoO}) = \% w(\text{Co}^{\text{II}}) \times \frac{M_{\text{Co}} + M_{\text{O}}}{M_{\text{Co}}} \quad (4)$$

with the molar weight  $M_{\text{Co}} = 58.9 \text{ g mol}^{-1}$  and  $M_{\text{O}} = 16 \text{ g mol}^{-1}$ .

Finally, the mass fraction of the ligands can be obtained by:

$$\%w(\text{L}) = 1 - \%w(\text{Co}_{\text{metal}}) - \%w(\text{CoO}) \quad (5)$$

Then, assuming that the density of Co, CoO and the ligands are similar to their bulk values, namely  $\rho_{\text{Co}} = 8.9$ ,  $\rho_{\text{CoO}} = 6.4$  and  $\rho_{\text{L}} = 0.9 \text{ g cm}^{-3}$ , respectively, their volume fraction could be deduced as follows:

$$V_{\text{Co}} = \frac{\% w(\text{Co}_{\text{metal}})/\rho_{\text{Co}}}{[\% w(\text{Co}_{\text{metal}})/\rho_{\text{Co}}] + [\% w(\text{CoO})/\rho_{\text{CoO}}] + [\% w(\text{L})/\rho_{\text{L}}]} \quad (6a)$$

$$V_{\text{CoO}} = \frac{\% w(\text{CoO})/\rho_{\text{CoO}}}{[\% w(\text{Co}_{\text{metal}})/\rho_{\text{Co}}] + [\% w(\text{CoO})/\rho_{\text{CoO}}] + [\% w(\text{L})/\rho_{\text{L}}]} \quad (6b)$$

$$V_{\text{L}} = \frac{\% w(\text{L})/\rho_{\text{L}}}{[\% w(\text{Co}_{\text{metal}})/\rho_{\text{Co}}] + [\% w(\text{CoO})/\rho_{\text{CoO}}] + [\% w(\text{L})/\rho_{\text{L}}]} \quad (6c)$$

In this paper  $V_{\text{Co}}$  is noted as  $V_M$  for the magnetic volume fraction.

Assuming an ideal core-shell structure for the cobalt nanorods consisting of a metal cobalt cylinder core and a CoO shell, the thickness,  $e$ , of the CoO shell was calculated using:

$$e = \frac{d_m}{2} \times \left[ 1 - \sqrt{\frac{V_{\text{Co}}}{V_{\text{Co}} + V_{\text{CoO}}}} \right] \quad (7)$$

with  $d_m$  the external mean diameter of the rods determined by TEM.

## Results and discussion

### Nanorod alignment characterization

The cobalt nanorods prepared by the polyol process exhibited a mean diameter in the range 17–31 nm and a mean length in the range from 120 to 200 nm as observed on the transmission electron microscopy (TEM) images. Fig. 1a shows a TEM image of representative rods exhibiting a mean diameter  $d_m = 22 \text{ nm}$ . The TEM images of the different rods used in this study are given in the ESI (Fig. S1†). The thinner rods ( $d_m$  below 24 nm) have a regular diameter except at the tips while the larger ones exhibit irregularities along their length. The irregular rods

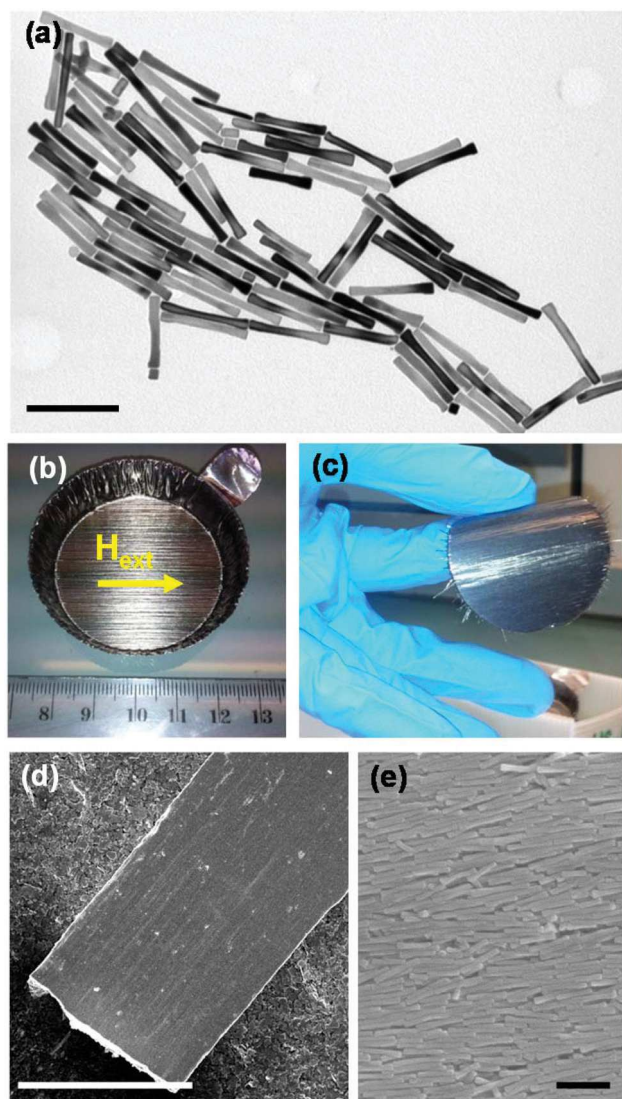


**Fig. 1** (a) TEM image of cobalt nanorods prepared by the polyot process prior to their alignment; (b) and (c) wafer of cobalt nanorods obtained by drying a suspension in chloroform under an external magnetic field of 1 T; (d) SEM image of a millimeter size parallelepiped made of aligned cobalt nanorods; (e) SEM image of the surface of a parallelepiped. Scale bars denote (a) 200 nm, (d) 100  $\mu\text{m}$  and (e) 200 nm.

with the larger mean diameters were obtained with a higher stirring rate (>160 rpm). Decreasing the stirring rate to 80 rpm improved the rod morphology and decreased the mean diameter. X-ray diffraction shows that the cobalt rods crystallize with the hcp structure with the  $c$  axis parallel to the long axis as previously reported.<sup>23</sup> After being washed in organic solvents (chloroform or toluene) the nanorods were dispersed in chloroform. Large wafers of parallel assemblies of rods were obtained by drying the rod dispersions in a uniform magnetic field of 1 T (Fig. 1b). Although no additional polymer was used for the rod consolidation, the dried assemblies exhibited robustness along the axis parallel to the applied field during the solidification and flexibility perpendicular to it (Fig. 1c).

Individual millimeter long needles with a parallelepiped shape could be separated from these wafers for further characterizations (Fig. 1d). Scanning electron microscopy (SEM) of the needles showed smooth surfaces without any cracks (Fig. 1d) and dense alignments of parallel nanorods with their rod long axis parallel to the needle long axis (Fig. 1e).

Small angle neutron scattering (SANS) patterns were recorded on different rod assemblies. The patterns of assemblies  $R_{17A1}$  and  $R_{17A2}$  are shown in Fig. 2 as examples. The alignment procedures of these two samples were different. In procedure A1, the rods were washed with chloroform, while in the procedure A2 they were washed with toluene (see Experimental section). Very anisotropic scattering patterns are observed. The intensity scattered perpendicular to the rod direction measures the correlations between the rods: the better aligned, the higher the intensity. In the direction parallel to the rods the scattering is very low. From the 2D scattering patterns, it is possible to extract the scattered intensity parallel,  $I_{\parallel}$ , and perpendicular,  $I_{\perp}$ , to the rods. These two intensities are plotted in Fig. 2a and b. On the  $I_{\perp}$  curves, a well-defined peak can be observed. It corresponds to the rod-rod distance in the correlation function. The intensity of this correlation peak is a measure of the quality of the alignment. It can be observed that, depending on the alignment procedure (A1 or A2), the quality of the alignment varies significantly. The  $q$  position of the correlation peak provides a measure of the mean center to center distance between rods,  $D_m$ , according to  $q_{\perp\text{max}} = 2\pi/D_m$ . For the assembly  $R_{17A1}$  (Fig. 2a), the mean distance deduced from the correlation peaks at the wave vector  $q_{\perp} = 0.295 \text{ nm}^{-1}$  is  $D_m = 21.3 \text{ nm}$ . Considering the rod mean diameter  $d_m = 17.5 \text{ nm}$  inferred from TEM images, the mean inter-rod distance is approximately  $h = D_m - d_m = 3.8 \text{ nm}$ . This value is in agreement with an inter-rod spacing occupied by organic molecules like the laurate ions remaining at the surface of the Co NRs and solvent molecules trapped by capillary forces. The strong van der Waals forces that apply at very small inter-rod distances explain the robustness of the assemblies. The van der Waals energy between two parallel nanorods of radius  $R$ , length  $L$  and separated by a distance  $h$  can be estimated according to eqn (8) (approximate expression valid for  $h < R$ ).<sup>37</sup>

$$E_{\text{vdw}} = -\frac{A_H \times L \times R^{1/2}}{24 \times h^{3/2}} \quad (8)$$

with  $A_H$  the Hamaker constant. Assuming  $A_H = -50k_B T$  for metallic cobalt dispersed in organic medium,<sup>37</sup> the van der Waals energy between two rods in the assembly  $R_{17A1}$  is estimated to  $E_{\text{vdw}} = -100k_B T$ .

The better alignment in the assembly  $R_{17A1}$  compared to  $R_{17A2}$  observed on the SANS patterns is corroborated by the hysteresis cycle measurement, which shows a squarer hysteresis loop for  $R_{17A1}$  than for  $R_{17A2}$  (Fig. 2c). The squareness SQ of the magnetization curve, measured with the field parallel to the rod long axis, was calculated as follows:

$$\text{SQ} = \frac{A}{H_C \times M_S} \quad (9)$$

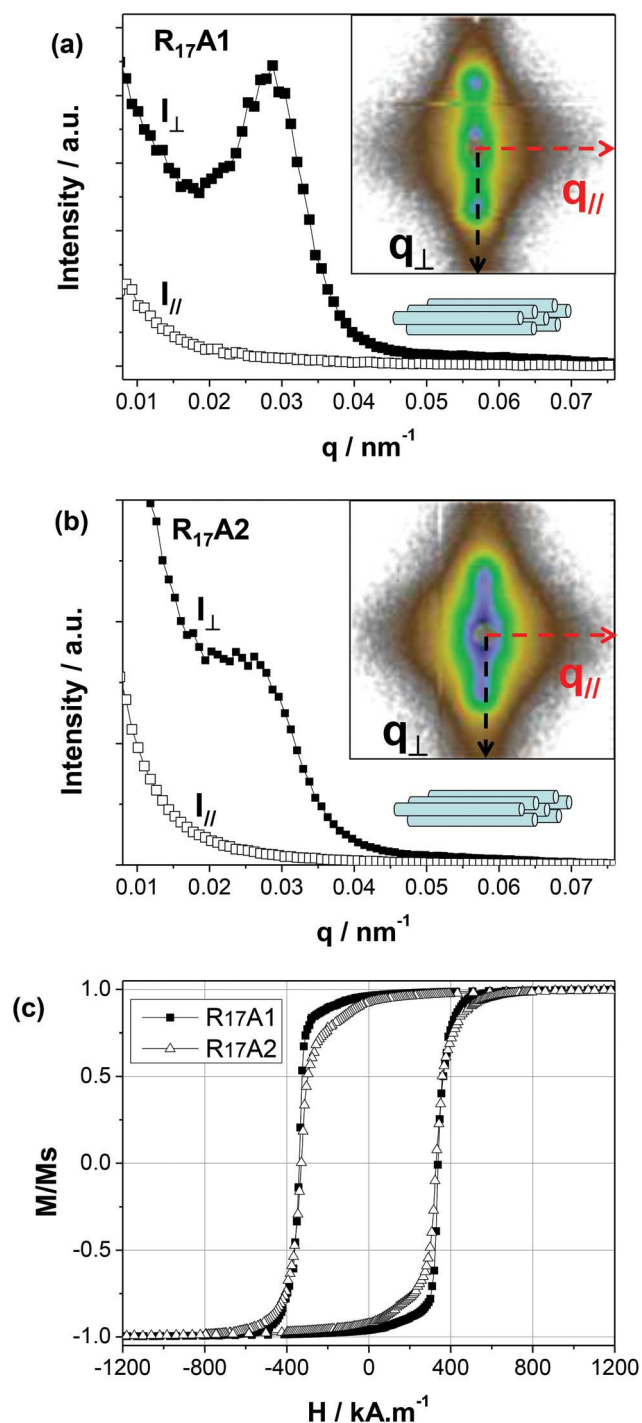


**Fig. 2** (a) and (b) Small angle neutron intensity profile scattered by two cobalt nanorod assemblies (R<sub>17</sub>A1 and R<sub>17</sub>A2), perpendicular (black squares) and parallel (open squares) to the rod alignment. Inset: corresponding 2D SANS pattern; (c) magnetization curves in the parallel configuration of the assemblies R<sub>17</sub>A1 (black squares) and R<sub>17</sub>A2 (open triangles).

with  $A$  the area below the  $M(H)$  loops in the second quadrant area, *i.e.* from  $H = 0$  to  $H = -H_C$ , and  $H_C \times M_S$  corresponding to the area of the ideal rectangle loop obtained for a fully parallel configuration. The SQ values of the  $M(H)$  loops of samples

R<sub>17</sub>A1 and R<sub>17</sub>A2 were found equal to 0.86 and 0.75, in agreement with a sharper SANS peak recorded for sample R<sub>17</sub>A1. The squareness appears to be a more sensitive criterion than the remanence to saturation ratio, usually used, to describe the rod ordering. Indeed, despite the difference of alignment quality, fairly close values of  $M_R/M_S = 0.96$  and  $0.93$  were found for samples R<sub>17</sub>A1 and R<sub>17</sub>A2, respectively.

Magnetic measurement being more accessible than SANS, the squareness parameter can be routinely used to characterize the different assemblies, noted R<sub>d</sub>A<sub>j</sub>, obtained with rods R<sub>d</sub> exhibiting the mean diameter  $d$  aligned following the procedure A<sub>j</sub> (see Experimental section). The squareness of several R<sub>d</sub>A<sub>j</sub> samples is given in Table S1 of the ESI.† The best rod alignments in the dried assemblies were obtained with rods washed with chloroform (SQ > 0.86) rather than toluene (SQ < 0.81) (Table S1†). We could observe experimentally that the rods R<sub>22</sub> exhibited the best shape homogeneity (low diameter dispersion, smooth surface) and led to the best orientations. Successive chloroform washings also improved the quality of the alignment (Table S1†).

Considering the absence of cracks in the needles and assuming no void inside, as suggested by the SEM images, the volume fractions of the magnetic core ( $V_M$ ), the oxide shell ( $V_{\text{CoO}}$ ), and the remaining organic molecules ( $V_L$ ) were calculated using the saturation magnetization values and thermal analysis (see Experimental section). The results for different rod assemblies are gathered in Table 1. The magnetic volume fraction  $V_M$  values were found in the range from 45 to 56%, the ligand volume fraction  $V_L$  in the range from 25 to 40% and the cobalt oxide volume fraction  $V_{\text{CoO}}$  was found in the range from 11 to 19% (Table 1). The thickness of the cobalt oxide shell, calculated using eqn (7) (see Experimental section), was found in the range from 1.1 to 1.4 nm for three samples (Table 1). The oxidation, which results from the air exposure of the Co NRs during the post-treatment process, remained rather limited, in good agreement with previous electron microscope observations on similar cobalt and cobalt–nickel nanorods.<sup>36,38</sup> However, one sample, R<sub>28</sub>, suffered an additional undesired oxidation with an oxide shell thickness of about 1.8 nm. The thin oxide shell around the Co rods protects them from any further oxidation. When the rods were handled at room temperature in dry air, the CoO shell thickness was found constant.

### Magnetic properties and $(BH)_{\text{max}}$ assessment

The magnetization curves  $M(H)$  of the different assemblies were measured at room temperature. In Table 1 are given the main magnetic properties, remanence to saturation ratio ( $M_R/M_S$ ), squareness (SQ), coercivity ( $H_C$ ) and induction remanence ( $B_R$ ), of several assemblies. The  $H_C$  values were found in the range from 270 to 360  $\text{kA m}^{-1}$  ( $\mu_0 H_C$  from 0.34 to 0.47 T). All the rods of this study exhibited an aspect ratio between 6 and 8. As expected, the highest  $H_C$  values were obtained with the thinnest nanorods, in agreement with previous experimental studies and micro-magnetic modelling.<sup>39</sup>

**Table 1** Summary of the morphological, chemical and magnetic properties of densely packed assemblies of cobalt nanorods:  $d_m$ , mean diameter and  $L_m$ , mean length of the rods;  $V_M$  is the magnetic volume fraction,  $V_{CoO}$  the cobalt oxide volume fraction and  $V_L$  the ligand volume fraction;  $e$  is the cobalt oxide shell thickness around the rods calculated from eqn (7);  $M_R/M_S$  is the remanence to saturation ratio and  $\mu_0 H_C$  the coercivity;  $B_R = V_M \times B_{Co\ bulk}$  is the remanence of the  $B(H)$  loops and  $(BH)_{max}$  the energy product; SQ is the squareness of the  $M(H)$  loops,  $\alpha$  is the slope of the model curve calculated from eqn (11) and  $B_R/2(1 + \alpha)$  is the critical magnetic field of eqn (13). The sample noted  $R_{d_m}A_j$  corresponds to the washing protocol and alignment  $A_j$  of the rods  $R$  of mean diameter  $d_m$

Sample	$d_m/L_m$ (nm)	$V_M$ (%)	$V_{CoO}$ (%)	$V_L$ (%)	$e$ (CoO) (nm)	$M_R/M_S$	$\mu_0 H_C$ (T)	$B_R$ (T)	$(BH)_{max}$ (kJ m <sup>-3</sup> )	SQ	$\alpha$	$\frac{B_R}{2(1 + \alpha)}$ (T)
R <sub>22</sub> A1	22/166	48.7	14.0	37.3	1.3	0.98	0.436	0.85	125	0.93	0.27	0.334
R <sub>22</sub> A2	22/166	47.9	15.2	36.9	1.4	0.92	0.451	0.79	92	0.79	0.74	0.228
R <sub>22</sub> A3	22/166	54.4	12.0	33.6	1.1	0.99	0.465	0.96	165	0.96	0.165	0.412
R <sub>24</sub> A1	24/190	48.7	11.0	40.3	1.2	0.92	0.410	0.80	82	0.74	1.02	0.198
R <sub>28</sub> A2	28/190	55.1	19.3	25.6	1.9	0.96	0.345	0.95	106	0.81	1.05	0.232
R <sub>28</sub> A4	28/190	48.8	15.6	35.6	1.8	0.89	0.363	0.78	51	0.57	1.85	0.137
R <sub>31</sub> A4	31/190	56.8	11.6	31.6	1.4	0.94	0.339	0.95	81.5	0.69	1.735	0.174

The remanence to saturation ratio was between  $M_R/M_S = 0.89$  and  $0.99$ ; a value above  $0.9$  is generally considered a criterion of a good alignment. Nevertheless, the squareness was observed to vary in a broader range with values between  $0.57$  and  $0.96$  (Table 1). It is noteworthy that the highest value  $SQ = 0.96$ , obtained for sample  $R_{22}A4$ , corresponds to a nearly perfect alignment and is, as far as we know, the best value for an anisotropic particle assembly.

The energy product  $(BH)_{max}$  is the figure of merit of a magnet performance. The working point is the value of the  $B(H)$  loop corresponding to the maximum of the  $B \times H$  product. The determination of the magnetic volume fraction ( $V_M$ ) within the assemblies allowed us to plot the  $B(H)$  loops and to assess the  $(BH)_{max}$ . In Fig. 3 are plotted the second quadrant of the  $B(H)$  loop and the  $B \times H$  product over the second quadrant of a representative sample ( $R_{22}A1$ ). An energy product of  $125 \text{ kJ m}^{-3}$  was determined for this assembly that exhibited a magnetic volume fraction  $V_M = 48.7\%$  and a  $M(H)$  loop squareness  $SQ = 0.93$ . The  $(BH)_{max}$  values, calculated following the same method for the different assemblies, were found in the range from  $50$  to  $165 \text{ kJ m}^{-3}$  (Table 1) depending on the magnetic volume fraction and on the quality of the alignment.

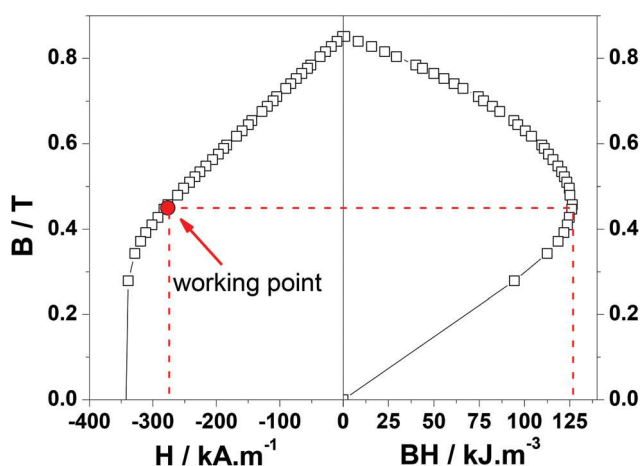


**Fig. 3** Second quadrant of the  $B-H$  loop and energy product  $(BH)_{max} = 125 \text{ kJ m}^{-3}$  of the Co NR assembly  $R_{22}A1$ .

In Fig. 4 are plotted the  $B(H)$  curves of three assemblies exhibiting the same magnetic volume fraction ( $\sim 48.8\%$ ) but prepared with different rod batches. The squareness of the

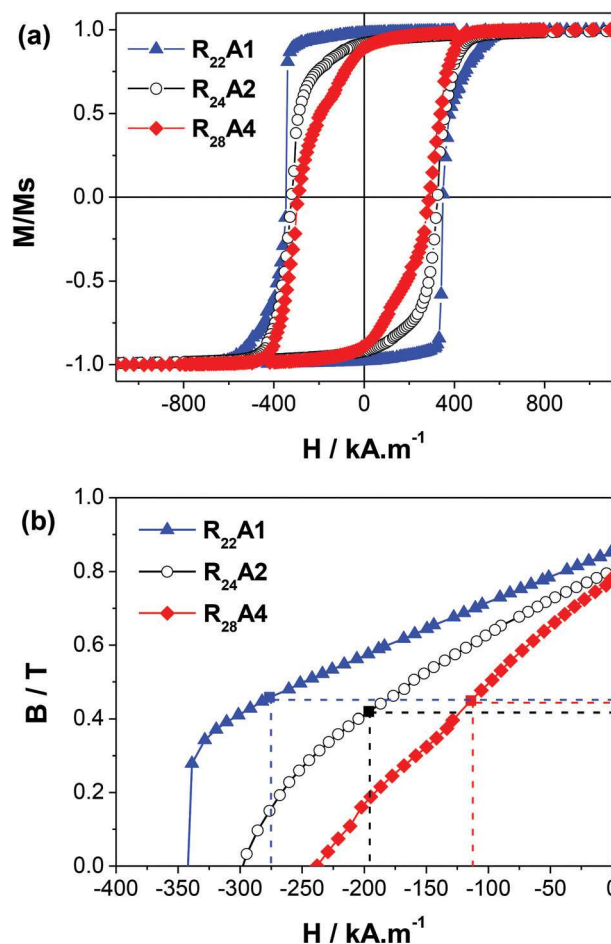


**Fig. 4** Normalized  $M(H)$  loops (a) and second quadrant of the corresponding  $B(H)$  loops (b) of three rod alignments exhibiting the same magnetic volume fraction: sample  $R_{22}A1$  (blue triangles):  $V_M = 48.7\%$ ,  $SQ = 0.93$ ,  $(BH)_{max} = 125 \text{ kJ m}^{-3}$ ; sample  $R_{24}A2$  (black circles):  $V_M = 48.7\%$ ,  $SQ = 0.74$ ,  $(BH)_{max} = 82.5 \text{ kJ m}^{-3}$ ; sample  $R_{28}A4$  (red diamonds):  $V_M = 48.8\%$ ,  $SQ = 0.57$ ,  $(BH)_{max} = 51 \text{ kJ m}^{-3}$ .

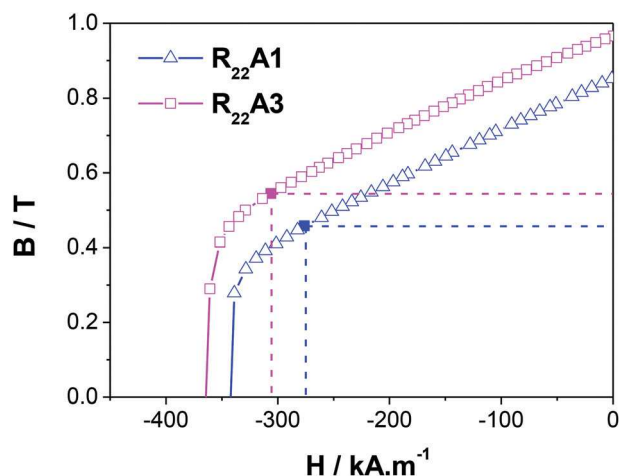


Fig. 5 Second quadrant of the  $B(H)$  loops and working points of the assemblies  $R_{22}A1$  and  $R_{22}A3$  prepared with cobalt nanorods of mean diameter  $d_m = 22$  nm. Sample  $R_{22}A1$  (blue triangles):  $V_M = 48.7\%$ ,  $SQ = 0.93$ ,  $(BH)_{\max} = 125$   $\text{kJ m}^{-3}$ ; sample  $R_{22}A3$  (magenta squares):  $V_M = 54.4\%$ ,  $SQ = 0.96$ ,  $(BH)_{\max} = 165$   $\text{kJ m}^{-3}$ .

$M(H)$  loops of these samples varied from 0.57 to 0.93, showing strong differences in the quality of the rod alignment. The opening of the hysteresis loop has, as a consequence, increased the energy product from 51 to 125  $\text{kJ m}^{-3}$  (Fig. 5b).

The other parameter that has a strong influence on the value of the energy product is the magnetic volume fraction within the assembly. In Fig. 5 are plotted the  $B(H)$  curves of two samples prepared with the same rods and exhibiting similar squareness (0.93 and 0.96). Increasing the magnetic volume fraction from 48.7% to 54.4% increases the  $(BH)_{\max}$  from 125 to 165  $\text{kJ m}^{-3}$ .

## Discussion

The results gathered in Table 1 show that the highest  $(BH)_{\max}$  was obtained for the sample that combined a high magnetic volume fraction and a squared  $M(H)$  loop with a very large  $SQ$ , which indicates a very good alignment of the nanorods.

The energy product of a sample exhibiting a perfectly square magnetization curve is:<sup>31</sup>

$$(BH)_{\max} = B_R^2/4\mu_0 \text{ if } \mu_0 H_C \geq B_R/2 \quad (10a)$$

$$(BH)_{\max} = H_C(B_R - \mu_0 H_C) \text{ if } \mu_0 H_C \leq B_R/2 \quad (10b)$$

In order to describe the effect of partial order in the rod assembly we consider schematically a linear variation of the magnetization in the second quadrant of the  $M(H)$  loop as follows:

$$M = M_R + \alpha H$$

with  $\alpha$  the slope of the  $M(H)$  loop at remanence (Fig. 6). The parameter  $\alpha$  can be deduced from the squareness defined above by:

$$\alpha = \frac{2M_R(1 - SQ)}{H_C} \quad (11)$$

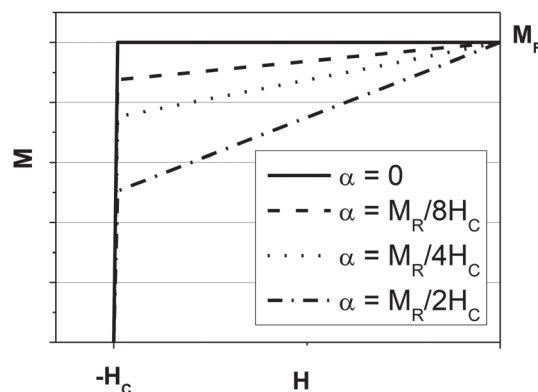


Fig. 6 Second quadrant of model  $M(H)$  loops with  $M = M_R + \alpha \times H$  for different values of the slope  $\alpha$ . The squareness of the four loops is 1, 0.9375, 0.875 and 0.75.

$\alpha$  is between 0 and  $M_R/H_C$ ,  $\alpha = 0$  for a perfect parallel orientation and  $\alpha > 0$  characterizes a degree of disorder in the assembly.

For such  $M(H)$  loops the energy product can be written as:

$$(BH)_{\max} = \frac{B_R^2}{4\mu_0(1 + \alpha)} \text{ if } \mu_0 H_C \geq \frac{B_R}{2(1 + \alpha)} \quad (12a)$$

$$(BH)_{\max} = H_C[B_R - \mu_0(1 + \alpha)H_C] \text{ if } \mu_0 H_C \leq \frac{B_R}{2(1 + \alpha)} \quad (12b)$$

For a magnetic volume fraction  $V_M$ , in the assembly the remanence is  $B_R = V_M \times B_{\text{Co bulk}}$  (with  $B_{\text{Co bulk}} = 1.79$  T). So, in the case of a coercivity higher than the critical field  $\frac{B_R}{2(1 + \alpha)}$  the energy product becomes:

$$(BH)_{\max} = \frac{B_{\text{Co bulk}}^2}{4\mu_0} \times \left[ \frac{V_M^2}{(1 + \alpha)} \right] \quad (13)$$

The magnetic field and induction of the working point are:

$$H = -\frac{B_R}{2\mu_0(1 + \alpha)} \text{ and } B = \frac{B_R}{2} \quad (14)$$

In Table 1 are given the  $\alpha$  values calculated from the squareness following eqn (11). All the samples studied exhibited coercivity higher than the critical field  $B_R/2(1 + \alpha)$  (Table 1) showing that the experimental data have to be compared with the formula of eqn (13) and (14).

According to eqn (13) the energy product varies as a quadratic function of the magnetic volume fraction. It describes well the important improvement of  $(BH)_{\max}$  observed in Fig. 5 when the volume fraction was increased from 48.7% in sample  $R_{22}A1$  to 54.4% in sample  $R_{22}A3$  (Table 1). Such a dependence on the magnetic volume fraction also explains why, despite a poor squareness, the assemblies prepared with the thicker rods ( $R_{31}A4$  and  $R_{28}A2$  in Table 1) exhibit a rather good  $(BH)_{\max}$ .

Eqn (13) predicts also that the energy product varies as an inverse function of the slope of the  $M(H)$  loop. In Fig. 4 are

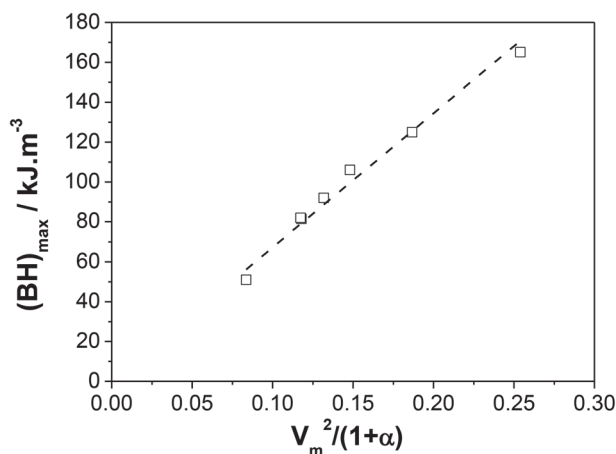


Fig. 7 Experimental energy product vs.  $V_M^2/(1 + \alpha)$  with  $V_M$  the magnetic volume fraction and  $\alpha$  the slope of the model  $M(H)$  curve at remanence (dashed line: linear fit).

compared samples R<sub>22</sub>A1, R<sub>24</sub>A2 and R<sub>28</sub>A4 that contained almost the same magnetic volume fraction (Table 1) and that exhibited  $M(H)$  loops with different squareness, 0.93, 0.74 and 0.57, respectively (Table 1). For these three samples the  $B$  value of the working point are found almost constant (Fig. 4b) and close to  $B_R/2$  as predicted by eqn (14). The decreasing of the  $(BH)_{\max}$  value is only due to the decreasing of the  $H$  value of the working point (Fig. 4b) as predicted by eqn (14). The  $\alpha$  values corresponding to the model  $M(H)$  curves calculated according to eqn (11) were found equal to 0.27, 1 and 1.85 for samples R<sub>22</sub>A1, R<sub>24</sub>A2 and R<sub>28</sub>A4, respectively (Table 1). The energy products calculated with these values according to eqn (13) were found equal to 53, 75 and 119  $\text{kJ m}^{-3}$ , very close to the experimental energy products (51, 82 and 125  $\text{kJ m}^{-3}$ ).  $(BH)_{\max}$  increases linearly with the ratio  $V_M^2/(1 + \alpha)$  (Fig. 7). The slope of the linear fit is 670  $\text{kJ m}^{-3}$ , very close to  $B_{\text{Cobulk}}^2/4\mu_0 = 638 \text{ kJ m}^{-3}$  as expected from eqn (13), showing that our simple model applies quite well.

### Magnet performance optimization

The  $(BH)_{\max}$  value of 165  $\text{kJ m}^{-3}$  obtained with a dense assembly of parallel cobalt nanorods is higher than the  $(BH)_{\max}$  of classical ferrites and AlNiCo magnets and comes close to the energy product of bonded NdFeB magnets.<sup>40</sup> This is the first proof of concept that such dense arrays can compete in the magnet panorama. The best assembly described in this paper exhibited a squareness  $SQ = 0.96$  showing that there is quasi no more room to improve the alignment quality. So, in order to increase the  $(BH)_{\max}$ , the next goal is to increase the magnetic volume fraction. In Fig. 8 are plotted the magnetic volume fraction and the energy product of perfect hexagonal arrays of nanorods as a function of the rod diameter for an inter-rod distance fixed at 3.5 nm. Non-oxidized and oxidized rods with a CoO shell thickness of 1.2 nm were considered. For a given ligand amount in the assemblies, the magnetic volume fraction increases when the rod diameter increases,

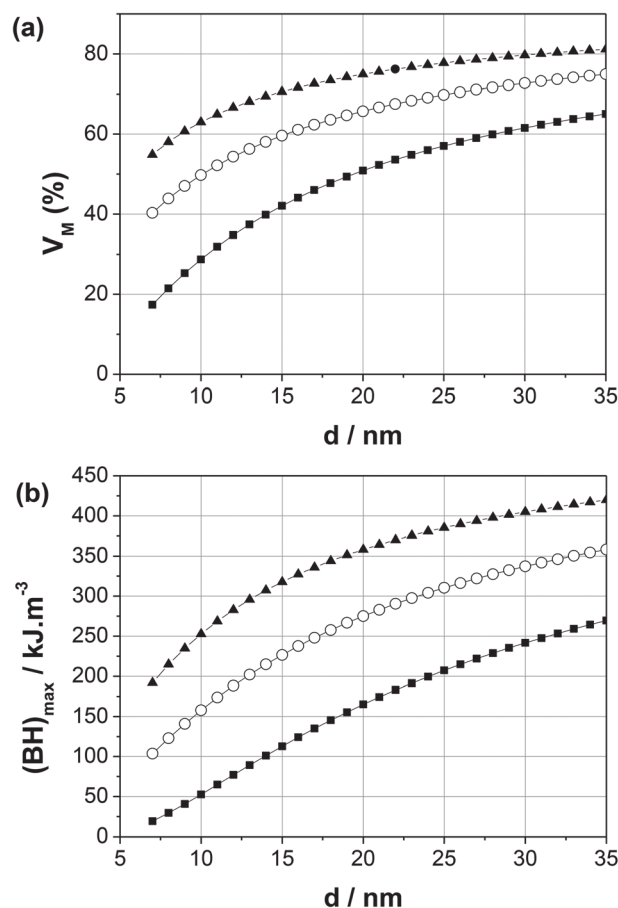


Fig. 8 Magnetic volume fraction (a) and energy product (b) of perfectly aligned hexagonal arrays of cobalt nanorods of mean diameter  $d$  separated by a ligand shell of 3.5 nm, of oxidized rods with a CoO shell thickness of 1.2 nm (full squares) and of non-oxidized rods (open circles); non oxidized rods separated by a ligand shell of 2 nm (full triangles).

explaining why it is easier to reach a higher volume fraction with thicker rods. Nevertheless, even if a significant increase of  $(BH)_{\max}$  is expected, an increase of the rod diameter must be discarded for permanent magnet applications due to the decrease of coercivity, which may potentially drop below the critical field (eqn (12)). Another way to increase the magnetic volume fraction would be to avoid the rod oxidation. For a rod diameter in the range from 10 to 20 nm the oxidation dramatically decreases the magnetic volume fraction (Fig. 8a). Magnetic volume fractions of 60% and 65% are expected for non-oxidized rods of diameter 15 and 20 nm, respectively, while only 42 and 51% are expected for oxidized ones (Fig. 8a). Finally, a significant increase of volume fraction could also be reached by lowering the organic amount. With non-oxidized rods separated by only a ligand shell of only 2 nm, the magnetic volume fraction could reach 70 and 75% for 15 and 20 nm rods (Fig. 8a).<sup>‡</sup> The effect of oxidation and inter-rod

<sup>‡</sup>Note that spacing between the rods is necessary to avoid a magnetic exchange and the loss of the shape anisotropy.

spacing on the energy product is even more important since it varies as the square of the magnetic volume fraction (Fig. 8b). According to eqn (13), the magnetic volume fraction in the range from 60 to 75% could lead to  $(BH)_{\max}$  values from 230 to 360 kJ m<sup>-3</sup>, providing a perfectly square hysteresis loop, and from 180 to 280 kJ m<sup>-3</sup> for a more realistic squareness, SQ = 0.93 ( $\alpha = 0.27$ ). Such an energy product would require a coercivity  $\mu_0 H_C$  higher than  $B_R/2$ , *i.e.* above 0.54 T and 0.67 T for a magnetic volume fraction of 60% and 75%, respectively. Such values of coercivity have already been obtained with thin cobalt nanorods,<sup>22,39</sup> showing that there is still room to improve the  $(BH)_{\max}$  of Co NRs assemblies.

## Conclusions

This is the first time that the energy products of nanorod assemblies have been assessed experimentally. Good alignment and high magnetic volume fraction are the two requirements to obtain important  $(BH)_{\max}$  values. We have shown that cobalt nanorods synthesized by the polyol process, washed and re-dispersed in chloroform are very well suited to get highly packed assemblies with a nearly perfect rod alignment. Very homogeneous Co NRs (low standard deviation on the diameter, no roughness) lead to  $M(H)$  loop squareness in the range from 0.93 to 0.96, indicative of a very good parallel order, while magnetic volume fractions were found in the range from 45 to 55%. The highest volume fraction combined with a nearly perfect alignment (SQ = 0.96) allowed us to reach a  $(BH)_{\max}$  of 165 kJ m<sup>-3</sup>, a value much higher than the energy product of barium ferrite and AlNiCo magnets. The road map for a  $(BH)_{\max}$  improvement is now clear. The next goal will be to increase the magnetic volume fraction by avoiding the rod oxidation and by decreasing the ligand amount in the final material, while maintaining a rod mean diameter below 15–20 nm in order to keep a high coercivity. A  $(BH)_{\max}$  increase of a factor 1.5 is a reasonable goal for the near future, opening up perspectives for rare earth free permanent magnets of 250 kJ m<sup>-3</sup> competing with bounded SmCo and NdFeB magnets. Furthermore, the bottom-up approach should allow us to down-size magnets to the millimeter and submillimeter scale and open up perspectives for an integration into micro-devices.

## Acknowledgements

This work was supported by the European Commission FP7 for the REFREPERMAG (EU NMP3-SL-2012-280670) project.

## Notes and references

- O. Gutfleisch, M. A. Willard, E. Brück, C. H. Chen, S. G. Sankar and J. P. Liu, *Adv. Mater.*, 2011, **23**, 821.
- J. M. D. Coey, *Scr. Mater.*, 2012, **67**, 524.

- L. H. Lewis and F. Jiménez-Villacorta, *Metall. Mater. Trans. A*, 2013, **44**, 2.
- J. M. D. Coey, *J. Phys.: Condens. Matter*, 2014, **26**, 064211.
- (a) L. H. Lewis, A. Mubarok, E. Poirier, N. Bordeaux, P. Manchanda, A. Kashyap, R. Skomski, J. Goldstein, F. E. Pinkerton, R. K. Mishra, R. C. Kubic Jr. and K. Barmak, *J. Phys.: Condens. Matter*, 2014, **26**, 064213; (b) Y. Hayashi, S. Gotou, M. Mizuguchi, M. Kotsugi, Y. Kitou, E. Okuno and K. Takanashi, *J. Magn. Soc. Jpn.*, 2013, **37**, 198; (c) A. Makino, P. Sharma, K. Sato, A. Takeuchi, Y. Zhang and K. Takenaka, *Sci. Report*, 2015, **5**, 16627.
- M. D. Kuz'min, K. P. Skokov, H. Jian, I. Radulov and O. Gutfleisch, *J. Phys.: Condens. Matter*, 2014, **26**, 064205.
- V. G. Harris, Y. Chen, A. Yang, S. Yoon, Z. Chen, A. L. Geiler, J. Gao, C. N. Chinnasamy, L. H. Lewis, C. Vittoria, E. E. Carpenter, K. J. Carroll, R. Goswami, M. A. Willard, L. Kurihara, M. Gjoka and O. Kalogirou, *J. Phys. D: Appl. Phys.*, 2010, **43**, 165003.
- K. J. Carroll, Z. J. Huba, S. R. Spurgeon, M. Qian, S. N. Khanna, D. M. Hudgins, M. L. Taheri and E. E. Carpenter, *Appl. Phys. Lett.*, 2012, **101**, 012409.
- N. Poudyal and J. P. Liu, *J. Phys. D: Appl. Phys.*, 2013, **46**, 043001.
- R. Skomski, P. Manchanda, P. Kumar, B. Balamurugan, A. Kashyap and D. J. Sellmyer, *IEEE Trans. Magn.*, 2013, **49**, 3215.
- D. P. Arnold, *IEEE Trans. Magn.*, 2007, **43**, 3940.
- B. Balasubramanian, B. Das, R. Skomski, W. Y. Zhang and D. J. Sellmyer, *Adv. Mater.*, 2013, **25**, 6090.
- B. Balasubramanian, P. Mukherjee, R. Skomski, P. Manchanda, B. Das and D. J. Sellmyer, *Sci. Rep.*, 2014, **4**, 6265.
- J. S. Jiang and S. D. Bader, *J. Phys.: Condens. Matter*, 2014, **26**, 064214.
- M. Vazquez, *Magnetic Nano- and Microwires, Design, Synthesis, Properties and Applications*, Woodhead Publishing, 1st edn, 2015.
- K. Gandha, P. Tsai, G. Chaubey, N. Poudyal, K. Elkins, J. Cui and J. Ping Liu, *Nanotechnology*, 2015, **26**, 075601.
- Y. Soumare, A. Dakhlaoui-Omrani, F. Schoenstein, S. Mercone, G. Viau and N. Jouini, *Solid State Commun.*, 2011, **151**, 284.
- Y. Soumare, J.-Y. Piquemal, T. Maurer, F. Ott, G. Chaboussant, A. Falqui and G. Viau, *J. Mater. Chem.*, 2008, **18**, 5696.
- Y. Soumare, C. Garcia, T. Maurer, G. Chaboussant, F. Ott, F. Fiévet, J.-Y. Piquemal and G. Viau, *Adv. Funct. Mater.*, 2009, **19**, 1971.
- K. Soulantica, F. Wetz, J. Maynadié, A. Falqui, R. P. Tan, T. Blon, B. Chaudret and M. Respaud, *Appl. Phys. Lett.*, 2009, **95**, 152504.
- N. Liakakos, T. Blon, C. Achkar, V. Vilar, B. Cormary, R. P. Tan, O. Benamara, G. Chaboussant, F. Ott, B. Warot-Fonrose, E. Snoeck, B. Chaudret, K. Soulantica and M. Respaud, *Nano Lett.*, 2014, **14**, 3481.

- 22 K. Gandha, K. Elkins, N. Poudyal, X. Liu and J. P. Liu, *Sci. Rep.*, 2014, **4**, 5345.
- 23 K. Aït Atmane, C. Michel, J.-Y. Piquemal, P. Sautet, P. Beaunier, M. Giraud, M. Sicard, S. Nowak, R. Losno and G. Viau, *Nanoscale*, 2014, **6**, 2682.
- 24 N. Ouar, S. Farhat, S. Mercone, F. Zighem, F. Schoenstein, N. Jouini, I. Hinkov, G. Wang and C. Ricolleau, *AIChE J.*, 2015, **61**, 304.
- 25 O. Riou, B. Lonetti, P. Davidson, R. P. Tan, B. Cormary, A.-F. Mingotaud, E. Di Cola, M. Respaud, B. Chaudret, K. Soulantica and M. Mauzac, *J. Phys. Chem. B*, 2014, **118**, 3218.
- 26 M. Ibrahim, C. Garcia, K. Aït Atmane, E. Berrichi, L.-M. Lacroix, A. Zwick, B. Warot-Fonrose, S. Lachaize, J.-Y. Piquemal and G. Viau, *J. Phys. Chem. C*, 2013, **117**, 15808.
- 27 K. Aït Atmane, F. Zighem, Y. Soumare, M. Ibrahim, R. Boubekri, T. Maurer, J. Margueritat, J.-Y. Piquemal, F. Ott, G. Chaboussant, F. Schoenstein, N. Jouini and G. Viau, *J. Solid State Chem.*, 2013, **197**, 297.
- 28 F. Ott, T. Maurer, G. Chaboussant, Y. Soumare, J.-Y. Piquemal and G. Viau, *J. Appl. Phys.*, 2009, **105**, 013915.
- 29 I. Panagiotopoulos, W. Fang, K. Ait-Atmane, J.-Y. Piquemal, G. Viau, F. Dalmas, F. Boué and F. Ott, *J. Appl. Phys.*, 2013, **114**, 233909.
- 30 I. Panagiotopoulos, W. Fang, F. Ott, F. Boué, K. Aït-Atmane, J.-Y. Piquemal and G. Viau, *J. Appl. Phys.*, 2013, **114**, 143902.
- 31 P. Toson, A. Asali, W. Wallisch, G. Zickler and J. Fidler, *IEEE Trans. Magn.*, 2015, **51**, 7400104.
- 32 T. Maurer, F. Ott, G. Chaboussant, Y. Soumare, J.-Y. Piquemal and G. Viau, *Appl. Phys. Lett.*, 2007, **91**, 172501.
- 33 B. Balamurugan, B. Das, V. R. Shah, R. Skomski, X. Z. Li and D. J. Sellmyer, *Appl. Phys. Lett.*, 2012, **101**, 122407.
- 34 W. S. Rasband, *ImageJ*, U. S. National Institutes of Health, Bethesda, Maryland, USA, 1997–2007, <http://rsb.info.nih.gov/ij/>.
- 35 <http://www-llb.cea.fr/spectros/pdf/paxy-llb.pdf>.
- 36 T. Maurer, F. Zighem, F. Ott, G. Chaboussant, G. André, Y. Soumare, J.-Y. Piquemal, G. Viau and C. Gatel, *Phys. Rev. B: Condens. Matter Mater. Phys.*, 2009, **80**, 064427.
- 37 J. N. Israelachvili, *Intermolecular and Surface Forces*, Academic Press, 1985.
- 38 S. Liébana-Viñas, U. Wiedwald, A. Elsukova, J. Perl, B. Zingsem, A. S. Semisalova, V. Salgueiriño, M. Spasova and M. Farle, *Chem. Mater.*, 2015, **27**, 4015.
- 39 M. Pousthomis, E. Anagnostopoulou, I. Panagiotopoulos, R. Boubekri, W. Fang, F. Ott, K. Aït Atmane, J.-Y. Piquemal, L.-M. Lacroix and G. Viau, *Nano Res.*, 2015, **8**, 2231.
- 40 J. M. D. Coey, *IEEE Trans. Magn.*, 2011, **47**, 4671.